

PROCEEDINGS

8TH INTERNATIONAL CONFERENCE ON
COMMUNICATIONS, ELECTROMAGNETICS AND MEDICAL
APPLICATIONS (CEMA'13)

Organized by:



FACULTY OF TELECOMMUNICATIONS
TECHNICAL UNIVERSITY OF SOFIA, BULGARIA



NATIONAL TECHNICAL UNIVERSITY OF ATHENS, GREECE,
SCHOOL OF ELECTRICAL AND COMPUTER ENGINEERING

NATIONAL TECHNICAL
UNIVERSITY OF ATHENS,
GREECE



SCHOOL OF ELECTRICAL
AND COMPUTER
ENGINEERING

Sofia, Bulgaria
17th - 19th October, 2013

KING

Edited by Prof. Dr. Eng. **Dimiter Tz. Dimitrov**

All rights reserved. This book, or parts there of, may not be reproduced in any form or by any means, electronic or mechanical, including photocopying or any information storage and the retrieval system now known or to be invented without written permission from the Publisher.

ISSN: 1314-2100

Printed in Bulgaria
KING 2001, Sofia



D. Dimitrov

Dear Colleagues,

It's my privilege to thank you all for your contributions submitted at 8th regular International Conference on 'Communication, Electromagnetic and Medical Applications' CEMA'13. This is one conference which should help future collaboration between engineering, especially communication technologies and medicine. This is an important scientific event not only in Balkan region, but in Europe, also. The International Conference on Communication, Electromagnetism and Medical Application CEMA'13 is dedicated to all essential aspects of the development of global information and communication technologies and their impact for medicine. The objective of Conference is to bring together lecturers, researchers and practitioners from different countries, working on the field of communication, electromagnetism and medical applications, computer simulation of electromagnetic field, in order to exchange information and bring new contribution to this important field of engineering design and application in medicine. The Conference will bring you the latest ideas and development of the tools for the above mentioned scientific areas directly from their inventors. The objective of the Conference is also to bring together the academic community, researchers and practitioners working in the field of Communication, Electromagnetic and Medical Applications, not only from all over Europe, but also from America and Asia, in order to exchange information and present new scientific and technical contributions. Many well known scientists took part in conference preparation as members of International Scientific Committee or/and as reviewers of submitted paper. I would like to thank you all for their efforts, for their suggestions and advices.

On behalf of the International Scientific Committee, I would like to wish you successful presentations of your papers, successful discussions and new collaborations for your future scientific investigations. Engineering and medicine should provide high level of live for all people.

Dimiter Tz. Dimitrov
Conference Chairman

INTERNATIONAL SCIENTIFIC COMMITTEE

Chairman:

Prof. D. TZ. DIMITROV, Technical University of Sofia, Bulgaria

Vice Chairman:

Prof. P. FRANGOS, National Technical University of Athens, Greece

Members:

Prof. N. AMPILOVA,	University of Perersburg, Russia
Prof. A. BEKJARSKY,	Technical University of Sofia, Bulgaria
Prof. B. DEKERIS,	Kaunas University of Technology, Lithuania
Prof. V. DEMIREV,	Technical University of Sofia, Bulgaria
Prof. N. DIB,	Jordan University of Science and Technology, Jordan
Prof. K. DIMITROV,	Technical University of Sofia, Bulgaria
Prof. M. DONTSCHEWA,	University of Applied Sciences, Dornbirn, Austria
Prof. V. DUMBRAVA,	Kaunas University of Technology, Lithuania
Prof. D. EIDUKAS,	Kaunas University of Technology, Lithuania
Prof. N. ESCUDEIRO,	ISEP, Porto, Portugal
Prof. E. GAGO-RIBAS,	University of Oviedo, Spain
Prof. G. GOUSSETIS,	Heriot - Watt University, United Kingdom
Prof. A. GRIGORIEV,	St. Petersburg University, Russia
Prof. S. Ver HOEYE,	University of Oviedo, Spain
Prof. M. HOFMANN,	University of Ulm, Germany
Prof. I. ILIEV,	Technical University of Sofia, Bulgaria
Prof. L. JORDANOVA,	Technical University of Sofia, Bulgaria
Prof. R. KRIVICKAS,	Kaunas University of Technology, Lithuania
Prof. G. MALLET,	University "Sophia Antipolis", Nice, France
Prof. G. MATSOPOULOS,	National Technical University of Athens, Greece
Prof. V. MARINKEV,	Medical University of Plovdiv, Bulgaria
Prof. M. MARTINS,	Instituto Superior Técnico, Lisboa, Portugal
Prof. M. MORALES-GONZALES,	University of Valladolid, Spain
Prof. K. NIKITA,	National Technical University of Athens, Greece
Prof. M. NIKOLOVA,	High Naval School, Varna, Bulgaria
Prof. J. PETROVSKA,	Medical University of Sofia, Bulgaria
Prof. F. PRATO,	University of Western Ontario, Canada
Prof. H. ROTH,	University of Siegen, Germany
Prof. S. SAUTBEKOV,	Euroasian University, Astana, Kazakhstan
Prof. A. SAVOV,	Medical University of Sofia, Bulgaria
Prof. S. SAVOV,	Technical University of Varna, Bulgaria
Prof. H-P. SCHADE,	Technical University of Ilmenau, Germany
Prof. L. SONG,	Technical University of Harbin, China
Prof. A. USHEVA,	University of Boston, USA

REVIEWERS

Q. BALZANO,	University of Maryland, USA
H. BERG,	Technical University of Jena, Germany
E. BOEMO,	Technical University of Madrid, Spain
M. DONTSCHEWA,	University of Applied Sciences, Dornbirn, Austria
D. DIMITROV,	Technical University of Sofia, Bulgaria
M. HOFMANN,	University of Ulm, Germany
F. KLETT,	Franhofer Institute, Ilmenau, Germany
G. MALLET,	University "Sophia Antipolis", Nice, France
M. MARINKEV,	Medical University of Plovdiv, Bulgaria
M. MARTINS,	Instituto Superior Técnico, Lisboa, Portugal
M. MORALES-GONZALES,	University of Valladolid, Spain
J. PETROVSKA,	Medical University of Sofia, Bulgaria
H. ROTH,	University of Siegen, Germany
A. SAVOV,	Medical University of Sofia, Bulgaria
H-P. SCHADE,	Technical University of Ilmenau, Germany
L. SONG,	Technical University of Harbin, China
A. USHEVA,	University of Boston, USA

Sponsor: INTRACOM-Bulgaria

REGISTRATION

October, 17th, 09h - 16h

Conference registration desk:

International Meeting Centre of Technical University – Sofia

CONFERENCE PROGRAM

17th October

*Technical University of Sofia
International Meetings Center "Helmut Boehme"*

OPENING CEREMONY

09h – 09h 30

INVITED PRESENTATION

09h 30 – 10h

Picture Archiving and Communication Systems in E-Health

Yassen Spassov, INTRACOM-Bulgaria

BREAK

10h – 10h 30

FIRST SESSION

10h 30 – 12h

Chairman: Prof. V. Demirev, Technical University of Sofia, Bulgaria

1. **Evaluation of EEG measurement noise during clinical research of epilepsy in multiple sclerosis patients between adjacent electrodes**, Viktor Mihaylov¹, Faculty of Telecommunications, Technical University of Sofia, Bulgaria, Dr. Filip Alexiev², Medical University of Sofia, Bulgaria. Kalin Dimitrov¹, ¹Faculty of Telecommunications, Technical University of Sofia, Bulgaria
2. **Post-processing of EEG recordings during clinical research of epilepsy in multiple sclerosis patients**, Viktor Mihaylov¹, Faculty of Telecommunications, Technical University of Sofia, Bulgaria, Dr. Filip Alexiev², Medical University of Sofia, Bulgaria, Kalin Dimitrov¹, ¹Faculty of Telecommunications, Technical University of Sofia, Bulgaria,
3. **The Research of Drops Sensors of Peristaltic Pumps**, V. Markevicius, D. Navikas, D. Andriukaitis, A. Valinevicius, N. Dubauskiene, Department of Electronics Engineering, Kaunas University of Technology, Kaunas, Lithuania
- 4...**Experimental investigation on space configuration and influence of electromagnetic field of microwave apparatuses in medical therapy**, Veska M. Georgieva, Antoniya P. Petrova, Faculty of Telecommunications, Technical University of Sofia, Bulgaria
5. **GUI for Contrast Enhancement in Medical Images**, Veska M. Georgieva, Faculty of Telecommunications, Technical University of Sofia, Bulgaria, Virginia A. Mileva, Faculty of German Engineering Education and Industrial Management, Technical University of Sofia, Bulgaria
6. **Deactivation of Staphylococcus aureus and Escherichia coli using plasma needle at atmospheric pressure**, ¹Hamad Raheem H., ²Maha Adel Mahmood, ¹Department

of Physics, College of Science, Baghdad University, Baghdad, Iraq, ²Department of Basic Science, College of Dentistry, Baghdad University, Baghdad, Irak

LUNCH
12h - 13h

SECOND SESSION
13h - 14h30

Chairman: Prof. Lina Narbutaite, Kaunas University of Technology, Lithuania

1. **Method for design of system for magnetotherapy using “running” random low frequency series of signal**, Atanas Dimitrov, Kalin Dimitrov, Faculty of telecommunication, Technical University of Sofia, Bulgaria
2. **An algorithm for visualization of low-frequency magnetic signals in systems for magnetotherapy**, Bogdan Kudrin, St. Petersburg State University, Faculty of Math. & Mech., Rossia, Atanas Dimitrov, Faculty of Telecommunication, Technical University of Sofia, Bulgaria
3. **Computer visualization of low frequency magnetic signals in systems for magnetotherapy with variable parameters**, Bogdan Kudrin, St. Petersburg State University, Faculty of Math. & Mech., Rossia, Atanas Dimitrov, Faculty of Telecommunication, Technical University of Sofia, Bulgaria
4. **Experimental investigation on space configuration and influence of electromagnetic field of short wave apparatuses in medical therapy**, Antoniya P.Petrova, Dimitar Dimitrov, Faculty of telecommunication, Technical University of Sofia, Bulgaria
5. **Structural entropy based processing of colorectal polyp images**, András Fehér, Ádám Békefi, Szilvia Nagy, Széchenyi István University, Győr, Hungary
6. **Mathematical investigation on calculation of magnetic induction of low frequency magnetic field in systems for magnetotherapy**, Nataly. Ampilova, St. Petersburg State University, Faculty of Math.& Mech., Rossia, Dimitar Dimitrov, Faculty of telecommunication, Technical University of Sofia, Bulgaria, Bogdan Kudrin, St. Petersburg State University, Faculty of Math. & Mech., Rossia

BREAK
14h 30 - 15h

THIRD SESSION
15h - 16h 30

Chairman: Prof. Kalin Dimitrov, Technical University of Sofia, Bulgaria

1. **A novel closed - form analytical solution to the radiation problem from a vertical short dipole antenna above flat ground using spectral domain approach**, S. Sautbekov**, P. Frangos* Ch. Christakis* and K. Ioannidi*, *School of Electrical and

Computer Engineering, National Technical University of Athens, Athens, Greece,
**Eurasian National University, Astana, Kazakshtan

2. **Flicker Noise in Harmonic Rejecting Current Commutating Passive FET Mixers**, Ludwig Lubich, Faculty of Telecommunications, Technical University of Sofia, Bulgaria
3. **White Noise in Harmonic Rejecting Current Commutating Passive FET Mixers**, Ludwig Lubich, Faculty of Telecommunications, Technical University of Sofia, Bulgaria
4. **Recent Trends and Future Developments of Vehicle Mounted Satellite Tracking Communications Systems**, Veselin Demirev, Faculty of Telecommunication, Technical University of Sofia, Bulgaria
5. **The Investigation of Optical - WiMAX Hybrid Access Network**, Lina Narbutaitė, Rasa Brūzgienė, Tomas Adomkus, Mindaugas Ruočkus, Kaunas University of Technology Department of Telecommunications, Lithuania
6. **Experimental study on the atmospheric attenuation effective on audio signals in Free Space Laser Communication Links**, Jassim Mohammed Jassim, Babylon University - College of Science for Women, Iraq

18th October

Technical University of Sofia

International Meetings Center "Helmut Boehme"

FOURTH SESSION

09h – 10h 30

Chairman: Prof. Dimitar Dimitrov, Technical University of Sofia, Bulgaria

1. **On some aspects of the fractal signature method**, N. B. Ampilova, Faculty of Math.& Mech., Starii Peterhof, Russia, I. P. Soloviev, Faculty of Math.& Mech., Starii Peterhof, Russia, Y. V. Shupletsov, Faculty of Math.& Mech., Starii Peterhof, Russia
2. **On a natural-science investigation of the ultralow doses effect**, E. Y. Gurevich, Sofia & Jacobs Foundation, St. Petersburg, Russia, N. B. Ampilova, St. Petersburg State University, Faculty of Math. & Mech, Russia, I. P. Soloviev, St. Petersburg State University, Faculty of Math. & Mech., Russia
3. **System for measurement of magnetic induction of low frequency magnetic field**, Vladimir Nikolov, Faculty of Telecommunication, Technical University of Sofia, Bulgaria
4. **Application of Speech to Text as Criterion of Audio Quality Estimation in Multimedia Communication Systems**, Snejana Pleshkova, Kalina Peeva, Faculty of Telecommunication, Technical University of Sofia, Bulgaria

5. **Microphone Arrays Beamforming Methods with Least Mean Square Spatial Filtration for Noise Suppression**, Snejana Pleshkova, Faculty of Telecommunication, Technical University of Sofia, Bulgaria

BREAK
10h 30 - 11h

FIFTH SESSION
11h - 12h

Chairman: Prof. Snejana Pleshkova, Technical University of Sofia, Bulgaria

1. **Mathematical Methods and Algorithms Based on Analysis of ECG and EEG Signals and Noise Removal from ECG and EEG Signals**, Dimiter Dimitrov, Deyan Milev, Faculty of Telecommunications, Technical University of Sofia, Bulgaria
2. **A Real Time ECG and EEG Data Transmission for Remote Patient Monitoring System**, Dimiter Dimitrov, Deyan Milev, Faculty of Telecommunications, Technical University of Sofia, Bulgaria
3. **Application of an Autofocusing Algorithm for SAR Image Quality Improvement and Application of the Modified Fractal Signature (MFS) Method for SAR Image Classification for the case of Real Radar Data**, A. Malamou, C. Pandis, A. Karakasiliotis, P. Stefaneas, D. Kodokostas and P. Frangos, National Technical University of Athens, Greece
4. **PRAXIS: the European Centre for Project/Internship Excellence**, Nuno Escudeiro¹, Paula Escudeiro² ^{1,2}Instituto Superior de Engenharia do Porto, Portugal
5. **The evolution of active prosthetics**, Viktor A. Nedialkov, Faculty of Telecommunication, Technical University of Sofia, Bulgaria

CLOSING SESSION
12h- 12h 30

LUNCH
12h 30 - 13h 30

SOCIAL PROGRAM

Banquet
October, 17th, 19h 30

Trip
to Koprivstizza
October 19th

CONTACT US:

GENERAL INFORMATION AND SUBMISSION OF CONTRIBUTIONS

Prof. Dr. D. Dimitrov

Faculty of Telecommunications
Technical University of Sofia
8, Kliment Ohridsky str.
1756 Sofia, Bulgaria
Phone/Fax: ++359 2 9652278
E-mail: dcd@tu-sofia.bg

Prof. Dr. P. Frangos

National Technical University of Athens
School of Electrical and Computer Engineering
9, Iroon Polytechniou Str.,
157 73 Zografou, Athens, Greece
Phone: 00 30 210 772 3694
Fax: 00 30 210 772 2281
E-mail: pfrangos@central.ntua.gr

TABLE OF CONTENTS

Evaluation of EEG measurement noise during clinical research of epilepsy in multiple sclerosis patients between adjacent electrodes	1
<i>Viktor Mihaylov, Filip Alexiev, Kalin Dimitrov</i>	
Post-procesing of EEG recordings during clinical research of epilepsy in multiple sclerosis patients	4
<i>Viktor Mihaylov, Filip Alexiev, Kalin Dimitrov</i>	
The Research of Drops Sensors of Peristaltic Pumps	7
<i>V. Markevicius, D. Navikas, D. Andriukaitis, A. Valinevicius, N. Dubauskiene</i>	
Experimental investigation on space configuration and influence of electromagnetic field of microwave apparatuses in medical therapy.....	13
<i>Veska M. Georgieva, Antoniya P. Petrova</i>	
GUI for Contrast Enhancement in Medical Images	17
<i>Veska M. Georgieva, Virginia A. Mileva</i>	
Deactivation of Staphylococcus aureus and Escherichia coli using plasma needle at atmospheric pressure	21
<i>Hamad Raheem H., Maha Adel Mahmood</i>	
Method for design of system for magnetotherapy using “running” random low frequency series of signal	26
<i>Atanas Dimitrov, Kalin Dimitrov</i>	
An algorithm for visualization of low-frequency magnetic signals in systems for magnetotherapy.....	31
<i>Bogdan Kudrin, Atanas Dimitrov</i>	
Computer visualization of low frequency magnetic signals in systems for magnetotherapy with variable parameters	36
<i>Bogdan Kudrin, Atanas Dimitrov</i>	
Experimental investigation on space configuration and influence of electromagnetic field of short wave apparatuses in medical therapy.....	40
<i>Antoniya P. Petrova, Dimitar Dimitrov</i>	
Structural entropy based processing of colorectal polyp images	44
<i>András Fehér, Ádám Békefi, Szilvia Nagy</i>	
Mathematical investigation on calculation of magnetic induction of low frequency magnetic field in systems for magnetotherapy.....	48
<i>Nataly Ampilova, Dimitar Dimitrov, Bogdan Kudrin</i>	
A novel closed – form analytical solution to the radiation problem from a vertical short dipole antenna above flat ground using spectral domain approach	52
<i>S. Sautbekov, P. Frangos, Ch. Christakis, K. Ioannidi</i>	

Flicker Noise in Harmonic Rejecting Current Commutating Passive FET Mixers	56
<i>Ludwig Lubich</i>	
White Noise in Harmonic Rejecting Current Commutating Passive FET Mixers	61
<i>Ludwig Lubich</i>	
Recent Trends and Future Developments of Vehicle Mounted Satellite Tracking Communications Systems	66
<i>Veselin Demirev</i>	
The Investigation of Optical – WiMAX Hybrid Access Network	70
<i>Lina Narbutaitė, Rasa Brūzgienė, Tomas Adomkus, Mindaugas Ruočkus</i>	
Experimental study on the atmospheric attenuation effective on audio signals in Free Space Laser Communication Links	75
<i>Jassim Mohammed Jassim</i>	
On some aspects of the fractal signature method	80
<i>N. B. Ampilova, I. P. Soloviev, Y. V. Shupletsov</i>	
On a natural-science investigation of the ultralow doses effect	85
<i>E. Y. Gurevich, N. B. Ampilova, I. P. Soloviev</i>	
System for measurement of magnetic induction of low frequency magnetic field	89
<i>Vladimir Nikolov</i>	
Application of Speech to Text as Criterion of Audio Quality Estimation in Multimedia Communication Systems	92
<i>Snejana Pleshkova, Kalina Peeva</i>	
Microphone Arrays Beamforming Methods with Least Mean Square Spatial Filtration for Noise Suppression	96
<i>Snejana Pleshkova</i>	
Mathematical Methods and Algorithms Based on Analysis of ECG and EEG Signals and Noise Removal from ECG and EEG Signals	100
<i>Dimiter Dimitrov, Deyan Milev</i>	
A Real Time ECG and EEG Data Transmission for Remote Patient Monitoring System	104
<i>Dimiter Dimitrov, Deyan Milev</i>	
Application of an Autofocusing Algorithm for SAR Image Quality Improvement and Application of the Modified Fractal Signature (MFS) Method for SAR Image Classification for the case of Real Radar Data	108
<i>A. Malamou, C. Pandis, A. Karakasiliotis, P. Stefaneas, D. Kodokostas, P. Frangos</i>	
PRAXIS: the European Centre for Project/Internship Excellence	112
<i>Nuno Escudeiro, Paula Escudeiro</i>	
The evolution of active prosthetics	116
<i>Viktor A. Nedialkov</i>	

AUTHOR INDEX

ADOMKUS, T.	70	MAHMOOD, M. A.	21
ALEXIEV, F.	1,4	MALAMOU, A.	108
AMPILOVA, N.	48,80,85	MARKEVICIUS, V.	7
ANDRIUKAITIS, D.	7	MIHAYLOV, V.	1,4
BÉKEFI, Á.	44	MILEV, D.	100,104
BRŪZGIENĖ, R.	70	MILEVA, V.	17
CHRISTAKIS, CH.	52	MOHAMMED J. J.	75
DEMIREV, V.	66	NAGY, S.	44
DIMITROV, A.	26,31,36	NARBUTAITĖ, L.	70
DIMITROV, D.	40,48,100,104	NAVIKAS, D.	7
DIMITROV, K.	1,4,26	NEDIALKOV, V.	116
DUBAUSKIENE, N.	7	NIKOLOV, V.	89
ESCUDEIRO, N.	112	PANDIS, C.	108
ESCUDEIRO, P.	112	PEEVA, K.	92
FEHÉR, A.	44	PETROVA, A.	13,40
FRANGOS, P.	52,108	PLESHKOVA, SN.	92,96
GEORGIEVA, V.	13,17	RAHEEM H., H.	21
GUREVICH, E.	85	RUOČKUS, M.	70
IOANNIDI, K.	52	SAUTBEKOV, S.	52
KARAKASILIOTIS, A.	108	SHUPLETSOV, Y.	80
KODOKOSTAS, D.	108	SOLOVIEV, I.	80,85
KUDRIN, B.	31,36,48	STEFANEAS, P.	108
LUBICH, L.	56,61	VALINEVICIUS, A.	7

EVALUATION OF EEG MEASUREMENT NOISE DURING CLINICAL RESEARCH OF EPILEPSY IN MULTIPLE SCLEROSIS PATIENTS BETWEEN ADJACENT ELECTRODES

Viktor Mihaylov¹, Dr. Filip Alexiev², Kalin Dimitrov¹

¹Faculty of Telecommunications, Technical University of Sofia,
8 Kliment Ohridski Blvd., 1000 Sofia, Bulgaria, vmihaylov@abv.bg, kld@tu-sofia.bg

²1st Faculty of Medicine, Charles University in Prague, alexiev.eeg@gmail.com

Abstract

Data recorded with modules for processing of EEG signals for diagnostics of multiple sclerosis is highly susceptible to various forms and sources of noise especially in environments in close proximity to high power electrical equipment. It is the case when recording has to be done in emergencies in the intensive care units of the hospital. A number of strategies are available to handle the noise effectively at the time of EEG recording as well as post preprocessing of recorded data. The aim of the paper is to evaluate the noise artifacts of EEG data gathered by measurement equipment.

1. INTRODUCTION

It is not always the case that EEG can be recorded in a well set environment, avoiding strictly jamming and interference. This often happens in evaluating symptomatic epilepsy induced seizures when on time measurement is of utmost importance in patients with multiple sclerosis [1]. It is frequent that the same cannot be transferred to a better shielded location. Measurements in intensive care units have the disadvantage of the low preparation time and overexposure to a large variety of electrical equipment [2]. Having so there are many sources of noise, to most of which the available EEG equipment is highly susceptible. Biological, electrical and environmental artefacts are seen more frequently. Dealing with the issue of noise in EEG is a task significantly laboured by the stochastic character of the recorded signal. In [3] several strategies are investigated both at recording time and during preprocessing. A basic approach in eliminating unnecessary sources of EM noise is by separately measuring the noise source and then subtracting its components from the biosignal. A wide range and principle circuit diagrams of some of the major sources of interference presented in [4], show a firm dependence of noise from the measurement device's input impedance and wiring. Thus obtaining information for the measurement device, its main characteristics, noise sources, recording methodology and interdependence is crucial for noise reduction. Employing a separate device for a simultaneous measurement with methodology might thus

increase the signal-to-noise ratio of the recorded signal.

2. METHODS AND MATERIALS

2.1. Multiple Sclerosis and ictal events

The methodology is highly dependent on the nature of the problem. And in our line of work close collaboration with a neurologist was done in order to evaluate the problem's specifics.

Multiple sclerosis (MS) is a chronic inflammatory disease of the immune system that affects the central nervous system, including the brain, spinal cord and optic nerves. It is considered an autoimmune disease, which means it occurs as a result of the body's immune system attacking and damaging its own nervous system. More specific consequences subside to epilepsy seizures. Although not often manifested, they are more frequent than in the general population [5], with the average 2-2.5% [6]. Those types of seizures are called symptomatic. EEG helps determine seizure type and epilepsy syndrome in patients with epilepsy, and thereby choice of antiepileptic medication and prediction of prognosis. EEG findings contribute to the multi-axial diagnosis of epilepsy [7][8], in terms of whether the seizure disorder is focal or generalised, idiopathic or symptomatic, or part of a specific epilepsy syndrome.

2.2. EEG signal acquisition

In accordance with the above mentioned we have used as part of our investigation a universal analog to digital converter with broad software compatibility. The conversion involves quantization of the input, so it necessarily introduces a small amount of error. Instead of doing a single conversion, the ADC performs the conversions ("samples" the input) periodically. The result is a sequence of digital values that have converted a continuous-time and continuous-amplitude analog signal to a discrete-time and discrete-amplitude digital signal. This greatly reduces and simplifies the medical and engineering analysis.

2.3. EEG signal acquisition

The event logging with multipurpose ADC converter has the great benefit when combined with National Instruments LabView software. Being an efficient and cost effective solution that assists greatly in the communication with specialists and the consecutive signal processing.

3. EXPERIMENTS

3.1. Definition of specific characteristic parameters and equipment composites

The measurements are done in a standard EEG lab. Two types of recordings are made with differentiation in the electrode to electrode comparison. NRSE (detect the ground voltage provided by the signal for all EEG leads) and differential voltage between the electrodes. 3 to four leads are chosen for the measurement – Z (for ground), Cz, C4, T4. All are placed on the EEG cap and linked to bridge electrodes.

3.2 Materials

For the purpose of the benchmark measurement device we have chosen National Instruments USB-6211 bus-powered USB M Series multifunction data acquisition (DAQ) module (Figure 1). This was led by a consideration and discussion with a neurologist and evaluating EEG signal specifics. The module offers 16 analog inputs; 250 kS/s single-channel sampling rate and four programmable input ranges (± 0.2 to ± 10 V) per channel. Most important being the Minimum Voltage Range (from -200 mV to -200 mV) and Minimum Voltage Range Sensitivity - 4.8 μ V, well in the limits of normal EEG signals. Input impedance for the analog input is >10 G Ω in parallel with 100 pF.



Figure 1. NI USB-6211 DAQ with 4 electrodes

3.2. Recorded signals

The measurements in Figure 2 is done with the ground reference provided by external signal being measured - the setup is called non-referenced single-ended mode NRSE.

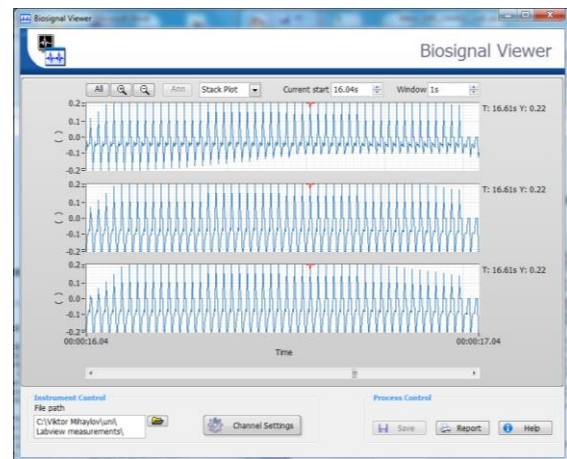


Figure 2. NRSE recording of Cz, C3 and T3

Second differential measurement is in Figure 3. Differential input connections are particularly well-suited for low-level signal and when the signal leads travel through noisy environments

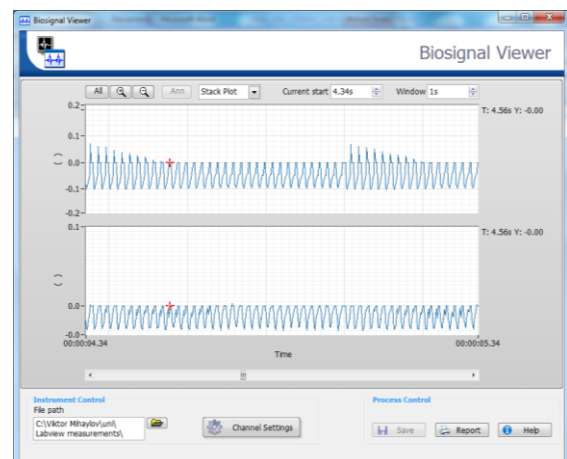


Figure 3. Differential recording of Cz-Z and C3-T3

4. ANALYSIS AND CONCLUSION

As visible on the graphics, the signals are in a good tolerance with standard EEG recording. Average signal amplitude is in between 6 μ V to 100 μ V, thus meaning that NI USB-6211 could be utilized as a separate device for a simultaneous measurement and implemented methodology for the increase of the signal-to-noise ratio of the signal. Also easily observable is the 50 Hz component, mainly to the electrical grid magnetic induction.

As an extension the experiment several more approaches should be applied such as increasing the number of patient subjects, leads measured and inclusion of signal postprocessing.

5. APPENDIX AND ACKNOWLEDGMENTS

The paper was supported by Proposition for Funding for Scientific Research Project for Doctoral studies (Session 2013) № 132PD0053-07 (132ПД0053-07) – Module for processing of EEG signals for diagnostics of multiple sclerosis.

References

- [1] C.F., Lucchinetti. "Advances in the neuropathy of multiple sclerosis: evolving pathogenic insights." *Continuum*, 2007; 13(5):86-116
- [2] Kenneth G. Jordan. "Continuous EEG Monitoring in the Neuroscience Intensive Care Unit and Emergency Department"
- [3] Repovs, Grega, "Dealing with noise in EEG recording and data analysis" *Infor Med Slov*: 2010; 15(1): 18-25
- [4] T. C. Ferree, P. L. Luu, G. S. Russell and D. M. Tucker (2001). Scalp electrode impedance, infection risk and EEG data quality. *Clinical Neurophysiology* 112/3: 536-544.
- [5] Ghezzi A., et al. Epilepsy in multiple sclerosis. *Eur Neurol*, 1990;30(4):218-23.
- [6] Catenox H., et al. Multiple sclerosis and epileptic seizures. *Mult Scler*, 2011;17(1):96-102.
- [7] Prof. Alexander D. Alexandrov, "Clinical Encephalography", Sofia, 2003
- [8] Christoph M. Michel, *Electrical Neuroimaging*, Cambridge University Press, New York, 2009r

POST-PROCESSING OF EEG RECORDINGS DURING CLINICAL RESEARCH OF EPILEPSY IN MULTIPLE SCLEROSIS PATIENTS

Viktor Mihaylov¹, Dr. Filip Alexiev², Kalin Dimitrov¹

¹Faculty of Telecommunications, Technical University of Sofia,
8 Kliment Ohridski Blvd., 1000 Sofia, Bulgaria, vvmihaylov@abv.bg, kld@tu-sofia.bg

²1st Faculty of Medicine, Charles University in Prague, alexiev.eeg@gmail.com

Abstract

Data recorded with modules for processing of EEG signals for diagnostics of multiple sclerosis needs to be further post processed since its highly susceptibility to various forms and sources of noise. Investigation of the EEG with different filters and software tools is done in order. to handle the noise effectively. Aim is the evaluation of the noise artifacts of EEG data by employing separate benchmark software with highly universal capabilities benefiting from the rapid prototyping environment for developing, testing and processing biosignals

1. INTRODUCTION

EEG recording has a major drawback when considering the environment built, as interferences from adjacent electrical equipment can easily compromise measurements. It often happens that in evaluating symptomatic epilepsy induced seizures on time measurement is of utmost importance in patients with multiple sclerosis [1]. Very often patients cannot be transferred to a better shielded location. Measurements in intensive care units have the disadvantage of the low preparation time and over-exposure to a large variety of electrical equipment [2]. Having so there are many sources of noise, to most of which the available EEG equipment is highly susceptible. Biological, electrical and environmental artifacts are seen more frequently. In [3] strategies for signal decomposition and filtering are investigated recommending and outlining changes in classical filtering approaches due to the inadequacy of previously used ones. Dealing with the issue of noise in EEG is a task significantly labored by the stochastic character of the recorded signal. A wide range of adaptive filtering methods of some of the major sources of interference are presented in [4], showing a significant reduction in unwanted artifacts. Thus employing separate software for a simultaneous processing increases the probability of a high signal-to-noise ratio of the recorded signal.

2. METHODS AND MATERIALS

2.1. Clinical basis

Multiple sclerosis (MS) is a chronic inflammatory disease of the immune system that affects the cen-

tral nervous system, including the brain, spinal cord and optic nerves. An observed symptom is epilepsy seizures. Although not very frequently manifested, they can be observed more than in the general population [5], with the average 2-2.5% [6]. EEG helps determine seizure type and epilepsy syndrome in patients with epilepsy, and thereby choice of antiepileptic medication and prediction of prognosis. EEG findings contribute to the multi-axial diagnosis of epilepsy [7][8], in terms of whether the seizure disorder is focal or generalised, idiopathic or symptomatic, or part of a specific epilepsy syndrome.

2.2. EEG recording processing

Having the above mentioned we have used as part of our investigation a universal analog to digital converter jointly with LabView software and the add on Biomedical Workbench Toolkit. This an efficient and cost effective solution that assists in the communication with specialists and the consecutive signal processing. The Biomedical Toolkit includes – file management, biosignal calibrator, viewer, logger and player. A time saving feature is the file format converter, which diminishes the need for additional processing for the conversion of recorded data. This helps for the simultaneous comparison of EEG files from Neurowerk EEG, Nihon Kohden EEG 9100 and the independent National Instruments DAQ 6211. The file conversion utility imports many widely used biomedical data logger formats into NI Technical Data Management Streaming (TDMS) format including Biopac .ACQ, iWorx, .MAT, EDF, and HL7. Another important feature is

the EEG signal simulation which could help in noise evaluation.

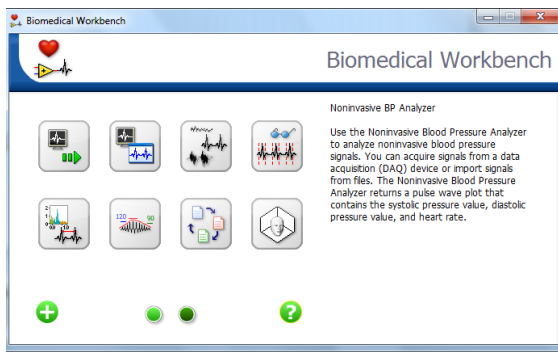


Figure 1. Biomedical Toolkit Workbench initial screen

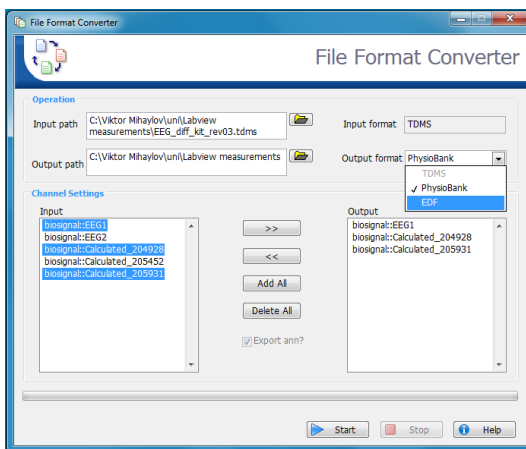


Figure 2. Biomedical Toolkit File Format converter

2.3. Acquisition methodology

As a basis for the measurement evaluation algorithm it is assumed the ANOVA statistical hypothesis measurement.

Two types of recordings are made with differentiation in the electrode to electrode comparison and filtering of the system is done. Initial spectral analysis is made in order to have a rough estimate on the noise levels in the signal. Lead connection is done in NRSE (detect the ground voltage provided by the signal for all EEG leads) and differential voltage between the electrodes. 3 to four leads are chosen for the measurement – Z (for ground), Cz, C4, T4. For recoding of the signal the Biomedical toolkit Logger is used, with three preset filters. A low pass Butterworth filter, a band stop Butterworth filter, and a Chebyshev low pass. Both band stop filters target a frequency of 50 Hz.

3. EXPERIMENTS

3.1. Equipment

For the purpose of the benchmark measurement device we have chosen National Instruments USB-6211 bus-powered USB M Series multifunction data acquisition (DAQ) module. All post processing is done with LabView and Biomedical Toolkit Logger.

3.2. Compatibility of the system components

Test were made in order to evaluate the compatibility of the module and software.

3.3. Evaluation of signals

The measurements in Figure 3 are a differential recording of two scalp electrodes, and the 3rd, 4th and 5th graphs represent low pass and two band stop filter applied to the C4 – T4 couple.

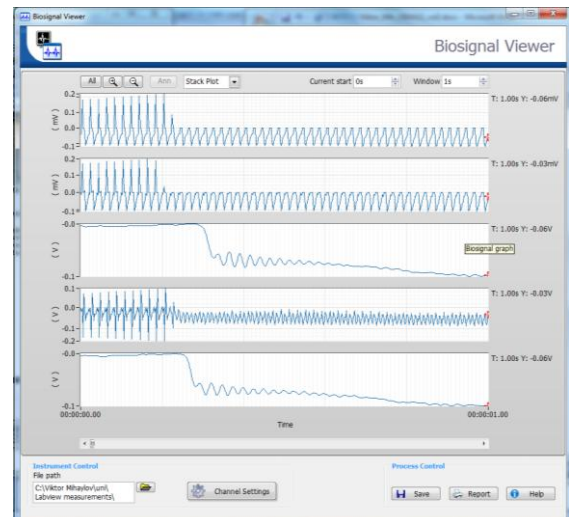


Figure 3. Differential measurement between Z-Cz, and C4-T4

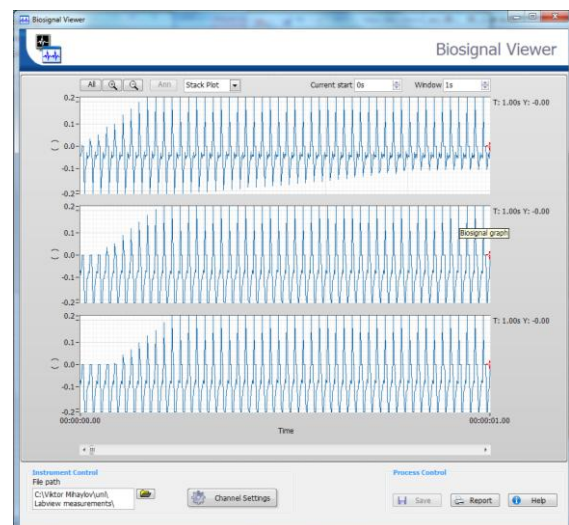


Figure 3. Non-referenced single-ended mode NRSE measurement between Z-Cz, and C4-T4

4. ANALYSIS AND CONCLUSION

Visible from the graphics is the large amount of noise in both in NRSE and Differential setup. After basic processing with the Biomedical Toolkit we strip the differential signal from the 50Hz component and its harmonics. Thus the signal can be prepared for future examination.

The NRSE on the other hand is more prone to noise artifacts, and its removal should be based on similar feature extraction from the adjacent electrodes, as share common noise source. As an extension the experiment increasing the number of patient subjects, leads measured and inclusion independent component analysis should be applied.

5. APPENDIX AND ACKNOWLEDGMENTS

The paper was supported by Proposition for Funding for Scientific Research Project for Doctoral studies (Session 2013) № 132PD0053-07 (132ПД0053-07) – Module for processing of EEG signals for diagnostics of multiple sclerosis.

References

- [1] C.F., Lucchinetti. "Advances in the neuropathy of multiple sclerosis: evolving pathogenic insights." *Continuum*, 2007; 13(5):86-116
- [2] Kenneth G. Jordan. "Continuous EEG Monitoring in the Neuroscience Intensive Care Unit and Emergency Department"
- [3] J.B Nitschke, G.A. Miller, "Digital Filtering in EEG/ERP analysis: Some technical and empirical comparisons", *Behaviour Research Methods, Instruments and Computers*:1998, 30(1), 54-67
- [4] A. G.Correa, E Laciari, H D Patiño, M E Valentinuzzi, "Artifact removal from EEG signals using adaptive filters in cascade", *Journal of Physics: Conference Series* **90** (2007)
- [5] Repovš, Grega, "Dealing with noise in EEG recording and data analysis" *Infor Med Slov*: 2010; 15(1): 18-25
- [6] T. C. Ferree, P. L. Luu, G. S. Russell and D. M. Tucker (2001). Scalp electrode impedance, infection risk and EEG data quality. *Clinical Neurophysiology* 112/3: 536-544.
- [7] Ghezzi A., et al. Epilepsy in multiple sclerosis. *Eur Neurol*, 1990;30(4):218-23.
- [8] Catenoix H., et al. Multiple sclerosis and epileptic seizures. *Mult Scler*, 2011;17(1):96-102.
- [9] Prof. Alexander D. Alexandrov, "Clinical Encephalography", Sofia, 2003
- [10] Christoph M. Michel, *Electrical Neuroimaging*, Cambridge University Press, New York, 2009 r.

THE RESEARCH OF DROPS SENSORS OF PERISTALTIC PUMPS

V. Markevicius, D. Navikas, D. Andriukaitis, A. Valinevicius, N. Dubauskiene

Department of Electronics Engineering, Kaunas University of Technology,
Studentu St. 50-418, LT-51368 Kaunas, Lithuania
T. +370 37 300518; E: vytautas.markevicius@ktu.lt

Abstract

Due to its simplicity and efficiency peristaltic drips [1] are widely used in a wide variety of treatments in medical practice [2]. Drip sensors used along with the drips provide step-infusion of medications and reduce the influence of the human factor. Infusion rate of medication plays one of the key roles in the treatment process [3], [4], so it is necessary to ensure that the drops sensor adequately detects the state of the drip camera when dripping speed is from a few ml/h to a few hundred ml/h. Three types of drop detectors are examined. Their main advantages and disadvantages are given.

1. INTRODUCTION

Drops sensors are used as a protective measure for peristaltic drips to reduce the likelihood of termination of the infusion, drug overdose, or infusion into a human circulatory system acceleration or slowdown due to external (e.g., suppressed drug supply hose) and internal (e.g. peristaltic pump failure) causes. These sensors capture the dripping fact, but do not count the drops.

Modern peristaltic pumps can administer medication at very different speeds - from a few ml/h to a few hundred ml/h [1]. The speed depends on the design of the pump and the size of the drops camera, and drops sensors have to be versatile and be able to detect infusions at any speed. It should be noted that the higher the infusion rate, the more difficult it is to capture the drops due to the transition of a dripping on to a weak continuous stream of flowing fluid (Fig. 1).

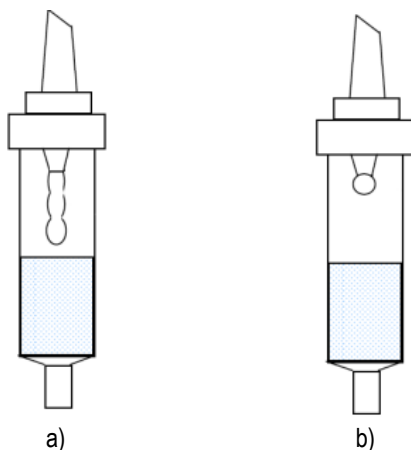


Figure 1. a) High drip rate; b) low drip rate

This paper presents analysis of several drop sensors of different manufacturers and patents related, identifying their strengths and weaknesses.

2. DROP SENSORS

Drop sensors of peristaltic pumps are designed to protect patients from drug overdose or accidental drug supply disruptions and help doctors timely find deviations from the norm in the level of medicine in drug containers.

Currently the market is dominated by three types of drop sensors with IR LEDs and IR sensors. In general, the sensors can be classified as:

1. Operating on the basis of optical lenses;
2. Without specialized optics;
3. Operating on the basis of mirror optics.

Drops sensors of the first type are made with a sophisticated optical system of lenses. Such a sensor typically consists of one IR LED, which is covered by a complex lens, focusing rays and directing them straight to the IR sensor, which is often also covered with a focusing lens.

Drops sensor of the second type does not have any complex optical systems. In it the IR LEDs and IR sensors are covered with a simple protective filter, which does not focus rays and performs as a simple safety feature, to keep out dust, liquids, and so on. In these, only electronics-based drops sensors, comparators, repeaters and pulse generators are commonly used, but not all drops sensors have all of these microchips.

Drops sensors of the third type have a complex optical system based on mirrors. These drops sen-

sors are quite difficult to produce because mirror calibration and adjusting means is a complex process. Without optics electronic parts are also required in such systems. Therefore, in order to produce such accurate drops sensors require precise mechanics, optics and electronics.

2.1. Lens Optics based Drop Sensors

Optical sensor based drops sensor LED directivity diagram study was carried out in the horizontal (Fig. 2) and the vertical (Fig. 3) planes, with IR-sensor $\Phi\Delta$ 263-01, and built-in IR sensor.

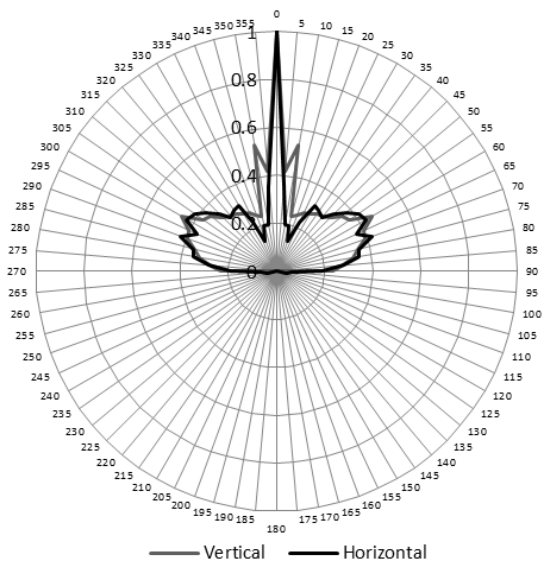


Figure 2. IVAC LED directivity diagram in the vertical and horizontal planes, measured with $\Phi\Delta$ -263-01 IR sensor (values normalized by the maximum value)

The study found that the directivity diagram width is about 5° (Fig. 2). After normalizing by the maximum voltage value it indicates that at small deviations (up to 5°) directivity diagrams have the same profile. At the higher (30°–90°) deviations similar shape of lateral leaves (Fig. 2 (b)) is obtained. The maximum directivity diagram discrepancies are observed in the measurements of the vertical plane at 10° deviations.

Figure 3 shows the directivity diagram obtained by measurements when the lens centre distance is 2.7 cm (which corresponds to the actual distance between the LEDs and the sensor in the IVAC drop detector), and 7.5 cm. This (Fig. 3) directivity diagram shows that the optics in the IVAC drop sensor is able to focus the IR beam into a narrow strip. During the measurements in the horizontal or vertical plane width of the directivity diagrams obtained is 10°–30°.

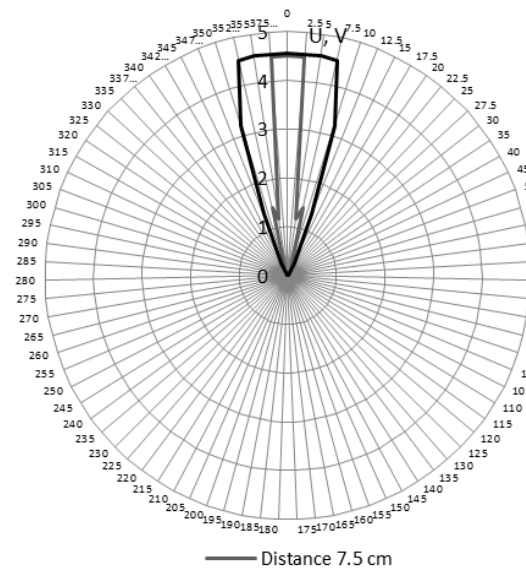


Figure 3. IVAC LED directivity diagram in the horizontal plane, measured with IVAC IR sensor when the distances between lens centres are 7.5 cm and 2.7 cm respectively

This directivity diagram shows the efficiency and accuracy of the lens optics based drop sensor, but it works effectively only in the horizontal plane. If the drop camera is not vertical or the drop sensor is not mounted at a horizontal plane, the drop sensor will not detect drops correctly or will not register them at all. This sensor ensures high accuracy only when the drop camera is strictly upright, and the drop sensor is mounted in a horizontal position with a great precision.

Graphs in Fig. 4 illustrate the reliable IVAC 180 drop sensor (optical lens based) at the different drip-speed of 200 ml/h up to 1200 ml/h. Pulse amplitude and shape is stable, independent of the rate of infusion.

Oscilloscope graphs show that in many cases the drop causes a secondary voltage pulse, which is much smaller than the main one. We believe that it is due to the fact that a detached drop splits into two parts when falling, the main and the tiny drop formed from drop "tail". Additional pulses may be due to tiny droplets that eventually form on the inner walls of the drops chamber sides.

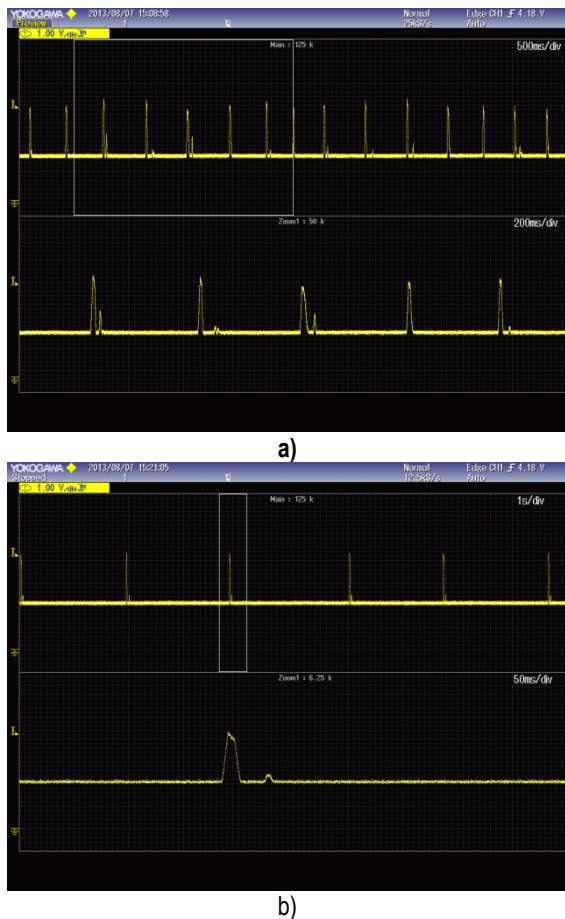


Figure 4. Oscilloscope waveforms of IVAC 180 drop sensor: a) the drip rate of 1200 ml/h (cell value in oscillogram is 500 ms), b) the drip rate of 200 ml/h (cell value in oscillogram is 1000 ms)

2.2. Electronics-based Drop Sensors

An electronic-based (without specialized optics) Daiwha drop sensor [5] LED's and IR sensor's directivity diagrams in the horizontal and vertical planes study is performed using ФД-263-01 IR sensor, and the built-in IR sensor.

The study was conducted with two different Daiwha drop sensors. The analysis evaluated the schematic diagrams, each differing slightly, but the sensor operating principle is identical. Both Daiwha drop sensors have the same IR LED sensors and IR sensors. In addition, they are symmetrical, so these sensor's LED's vertical and horizontal planes of the directivity diagram are the same and are suitable for both Daiwha drop sensors. Directivity diagrams normalized by the maximum value of the voltage (Fig. 5) are presented.

Directivity diagram width established is approximately 50° (with ФД-263-01 IR), and approximately 70° (with Daiwha IR). The resulting directivity diagram leads to the conclusion that LEDs in Daiwha

drop sensors emit infrared beams in a much wider angle (Fig. 5) than the IVAC 180 (Fig. 2, Fig. 3) and IR sensor accepts IR beams in wide angle as well.

Daiwha drops sensor oscillograms captured monitoring the out signal of the operational amplifier of the drop sensor are presented Fig. 6.

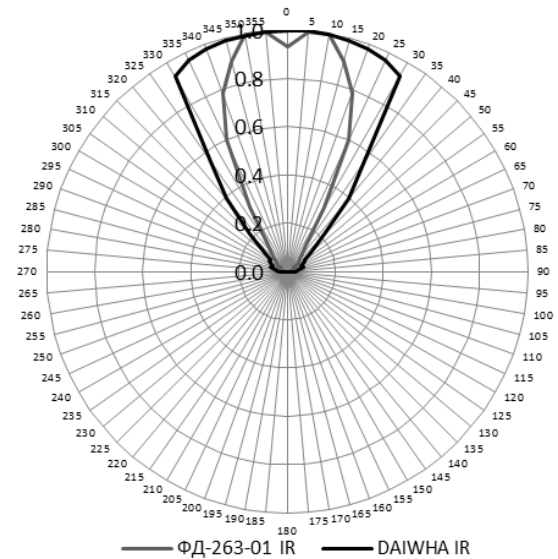


Figure 5. Daiwha LED directivity diagram measured with ФД-263-01 IR sensor and with Daiwha IR sensors in the horizontal plane (normalized values by the maximum value).

Figure 6 shows that the Daiwha sensors able to capture drops dripping at different speeds: 400 ml/h ... 1200 ml/h. However, when the drip rate is high, it is clear that each drop falling causes two voltage pulses whose amplitude varies very little. The drop about to let splits into two parts when fallen, the main one, and the tiniest drop formed from drop "tail". Due to the sensor electronics features a small and a large drop evoke the same amplitude pulse, but with different pulse duration.

This problem disappears at low (<400 ml/h) drip speed. The study found that the operational amplifier signal is fed with noise (50 Hz and 120 kHz). The same noise (120 kHz) in the output signal is observed (Fig. 6). Possible cause may be the lack of filtered mains of voltage converter noise in the power supply.

2.3. IR Optical Pair without Electronics

Research showed that the drop sensor can operate in the absence of the electronic part. In this case IR sensor and IR LEDs are sufficient. The signals are obtained with the noise, but with proper selection of LEDs and IR sensor detection of the flow of fluid dripping are possible. (Fig. 7).

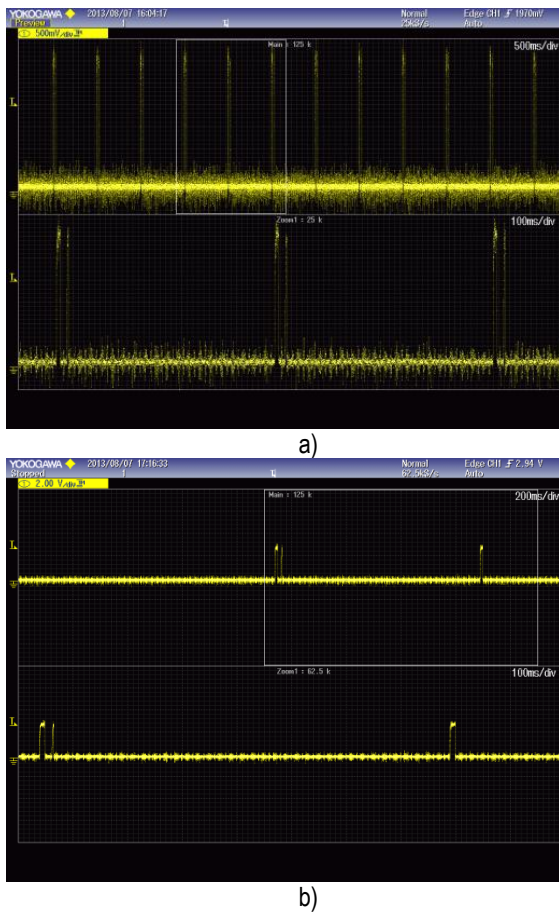


Figure 6. Daiwha drop sensor oscillograms: a – the drip rate of 1200 ml/h (cell value of 500 ms), b – drip rate of 400 ml/h (cell value of 200 ms)

Daiwha drop sensor LED on IR the couple signal is presented in Fig. 7.

These oscillograms raise suspicion that the Daiwha [5] drops sensor scheme is misleading, or at least misspelled because after removing the electronic part from the sensor, and leaving only the IR LEDs and IR sensors, it still works. Signals are obtained with a very high noise level (from the power transformer) and one drop falling creates several voltage pulses (Fig. 7). Interestingly, even without the electronic part, the generated voltage pulse amplitude and duration is almost the same as with the electronic part and the peristaltic pump is operating normally.

3. PATENT ANALYSIS

Summarising the study carried out, analysis of patents associated with the drop sensors is presented (Table 1) [6] – [12], highlighting the principle of operation as well as the advantages and disadvantages.

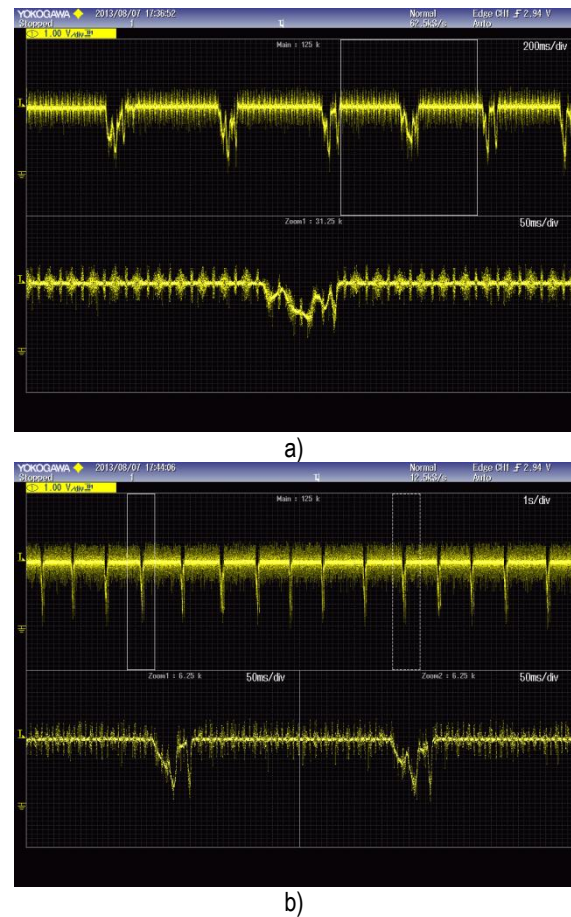


Figure 7. Daiwha drops sensor oscillograms without electronics: a) – the dripping rate of 1200 ml/h (cell value of 200 ms), b) – the dripping rate of 600 ml/h (cell value of 1000 ms)

4. DISCUSSION

Usually each manufacturer adds a drops sensor at its peristaltic pump, which is designed specifically for that peristaltic pump model. The main problem is that most of these sensors operate reliably only when they are mounted precisely vertically. The sensors are usually not working in horizontal position or at an angle. Such sensors are not valuable in busy environments such as an ambulance, even though drops sensors would be very useful in such an environment, since it is often very difficult, if not impossible to administer the appropriate dose of the medication to the patients in such circumstances.

When the speed is very low (0.3 to 0.6 ml/h), the drops are also difficult to capture for the sensor because it is unable to distinguish whether the drops fall very slowly, or do not fall at all, so often at a slow dripping rate, drops sensors report an empty drops tank or discontinued supply of drugs, although this is not true.

Table 1. Summary of patent analysis

<i>Patent No.</i>	<i>Operating principle</i>	<i>Advantages and disadvantages</i>
US 4,181,130	Electronic based. There are five IR LEDs that illuminate phototransistors on the other side of the drops tank.	Production costs of such drops sensor are not small because an optical lens is required. Its accuracy is pretty good. Would not be able to capture drops in slow dripping rate.
US 4,583,975	Based on electronics. Piezoelectric sensors responsible for the drop detection feel the vibrations that occur when a single drop falls in the liquid of the drops chamber.	Such drops sensor production costs are high, but it is not very accurate, because the piezoelectric sensors detect vibrations caused by the drops when they fall, but those vibrations can easily be the result of many external stimuli. It is small and easily fixed.
US 4,680,977	Based on expensive optics. Lenses focus infrared light exactly in the centre of drops container and to the IR sensor. Only the width of the drop IR beam is allowed to enter the sensors.	Drops sensors described in this patent are highly accurate, but they are among the most expensive ones, because they are based on complex optics. The sensor is designed so that it can be mounted and removed very conveniently and simply. The only disadvantage of such drop sensors is that they are very expensive.
US 4,703,314	Operates on electronic basis. On one side of the drop sensor is the IR LED, which emits beams to the other side in the straight line to the IR sensor.	This drops sensor is quite simple. Its production costs are not high, but accuracy is also low. Daiwha drops sensors operate on this basis.
US 7,918,834	Operates on electronic basis. Contains a number of IR LED's and IR sensor layout options. The point is that one IR sensor captures the IR beam going through the drop, and the other reflected from the drop.	Drops sensors described in that patent can be placed on the number of drops containers. They are easy to make, simple in their construction, manufacturing costs are low. Accuracy is good enough due to the arrangement of IR LEDs and IR sensor described in the patent.
EP0198909 B1	Based on mirrors. On one side of the drops sensor is the IR LEDs and IR sensors. Using one large or three smaller mirrors, the IR beam is directed into the sensor.	Such drops sensors are accurate, but they are difficult to produce. Their production costs are high; in addition they need a lot of time to accurately calibrate the mirrors, because these sensors are working only through them. Evaluating cost and time of production of these sensors relatively to their accuracy, they are hardly worthwhile to produce.
Str. A61M5/14	Operates on electronic basis. Basically formed from three IR LEDs arranged at different heights, and sensors located before them at the same height.	These drops sensors are easy to produce. They are quite accurate, and the production cost is not high. However, these sensors are large and unwieldy.

5. CONCLUSIONS

Drops sensors are available in different designs, but all of their principle of operation is similar, and the goal is the same. It was found that:

- Almost all of the drops sensors are based on the use of optical IR pairs;
- Lenses and mirror systems are used to increase reliability;
- Most of the sensors have a convenient fastening on the drops chamber mechanism;
- Most of the sensors have a simple or more complex electronic part;
- Specialized or standard connectors are used to connect to peristaltic pump;

- Most sensor designs ensure that the Sun's rays are prevented from entering the sensor active area.

The study distinguished two main weaknesses of peristaltic drips:

- At high dripping speed, drops form a sort of continuously flowing faint trickle so the individual droplets cannot be identified with any drops sensor;
- At low dripping rates drop formation can take a long time. It is very difficult for drops detection, because it is difficult to determine whether the dripping rate is very low, or there is no drip at all. In general, this is the problem of not only drops sensors, but of the pump PI algorithms as well.

References

- [1] R. C. Gupta, S. R. Taneja, K. K. Thariyan, S. Verma, "Design and implementation of controlled drug infusion system", *Journal of Scientific & Industrial Research*, vol. 64, pp. 761-766, 2005.
- [2] R. J. Bowman, D. R. Westenskow, "A microcomputer-based fluid infusion system for the resuscitation of burn patients", *IEEE Transactions on Biomedical Engineering*, vol. 28, no. 6, pp. 475-479, 1981. DOI: 10.1109/tbme.1981.324822
- [3] K. Park, J. Lee, S. Kim, J. Kim, I. Kim, S. P. Choi, S. Jeong, S. Hong, "Infusion volume control and calculation using metronome and drop counter based intravenous infusion therapy helper", *International Journal of Nursing Practice*, vol. 19, pp. 257-264, 2013.
- [4] R. Ilan, R. A. Fowler, N. D. Ferguson, C. S. Parshuram, J. O. Friedrich, S. E. Lapinsky, R. Biason, R. Pinto, E. E. Etchells, "Prolonged time to alarm in infusion devices operated at low flow rates", *Critical Care Medicine*, vol. 36, no. 10, pp. 2763-2765, 2008. DOI: 10.1097/CCM.0b013e31818698e3
- [5] *Daiwha flow sensor data sheet*. Online: <http://www.acimedical.com.co/descargas/euiposMedicos/Bombalnfusion.pdf>
- [6] Wilber H. Bailey. Ivac Corporation. Drop discriminator system. PAT. US 4,181,130. 1977.
- [7] Michael O. Pekkarinen, Ludwig Wolf, Jr., Walker Woodworth. Baxter Travenol Laboratories, Inc. Indirect piezoelectric drop counter and method. PAT. US 4,583,975. 1985.
- [8] Ronald S. Conero, Terry L. Landis. Ivac Corporation. Optical flow sensor. PAT. US 4,680,977. 1985.
- [9] Wayne M. Spani. Fisher Scientific Group, Inc. Empty container detector with drop sensor. PAT. US 4,703,314. 1986.
- [10] Morten Mernoe, Morten Thing. T3M. Drop counter. PAT. US 7,918,834. 2009.
- [11] Kamen, Dean, L. Drop detection system with mirror element. PAT. EP0198909. Europe. 1985.
- [12] Robert J. Bowman. University of Utah Research Foundation. Self-compensating optical drop count apparatus for measuring volumetric fluid flow. PAT. US 4,314,484. 1979

EXPERIMENTAL INVESTIGATION ON SPACE CONFIGURATION AND INFLUENCE OF ELECTROMAGNETIC FIELD OF MICROWAVE APPARATUSES IN MEDICAL THERAPY

Veska M. Georgieva

Faculty of Telecommunications, Technical University of Sofia, Bulgaria
1000 Sofia, "Kl. Ohridsky" str.8
T. (+359 2) 965-3293; E-mail: vesg@tu-sofia.bg

Antoniya P. Petrova

Faculty of Telecommunications, Technical University of Sofia, Bulgaria
1000 Sofia, "Kl. Ohridsky" str.8
E-mail: tony.petrova@gmail.com

Abstract

The application of microwave equipment in medical therapy is well known. The frequency band of these devices is 2 to 3 GHz. These frequencies and wavelengths are most effective and allow for a much deeper and more reliable results. In the experimental set-up used an antenna with a circular emitter. The antenna system provides the effect of the electromagnetic field of a small part of the human body. Because the distance between the antenna system and the living tissue is very low, it is difficult to determine the electromagnetic field distribution of values and the power of the field in the region of the patient. It's difficult to be provided one exact mathematical description of electromagnetic field in this area taking in account deformation of this field because of live tissues additionally. Because of that one experimental investigation of electromagnetic field in the patient's area would be useful in this case.

The obtained results can be connected with X-ray images of respective alive tissues. X-rays are especially useful in the detection of pathology of bony structures. These images are no truly isotropic and its quality varies depending on penetration of X-rays in the anatomical structures and on the technologies of their obtaining. In most cases they need to be enhanced. This investigation is also the goal of the paper.

1. INTRODUCTION

At the high frequencies of electrical field, the polarizing molecules fail completely to change their spatial orientation and vibrations occur of the dipoles around neutral position. This process is associated with generate the heat. In microwave therapy, the patient is set in electromagnetic fields with frequencies a few GHz, which means that the wavelength is from 10 to 70 cm. The energy of microwaves, absorbed from the body tissues, is converted into heat, significantly more effective than the energy of longer wavelengths.

2. THEORETICAL SOLUTION

The effects of microwaves on the patient's body can be achieved by dipole antennas with hemispherical or semi-cylindrical reflector. Reflectors are placed directly on the area, which has to be heated, or at some distance from it. Reflectors can be closer or further away, so they can adjust their distance to the skin, which must be 2-10 cm. When determining the shape of the area of the plane, which the simulation is performed, the main consideration is the

reporting of the configuration of the antenna's system, and its deployment of the appropriate part of the patient area. [1]

Figures 1a, 1b, 1c illustrate the most commonly used antennas in microwave physiotherapy. Figure 1a depicts the antenna, which the research is doing, namely comical antenna or "circular field" antenna, which is used mainly for localized joint (e.g. elbow, wrist, knee, instep) and pediatrics applications. Figure 1b shows rectangular antenna or "long rectangular field" antenna: used for treatment of larges areas (rachis, upper and lower limbs, etc.) and figure 1c: three dimensional antenna or "surrounding field" antenna: mainly used for shoulders, neck and rachis.

It is apparent that the reflector radiator may have an arbitrary location in the space according to the treatment area of the patient's body. In order to facilitate and accelerate the sampling, streamline and simplify the calculation is appropriate the area of space to be approximated by regular geometric figure. This would allow using the available symme-

try for an optimization the developed algorithms for sampling and calculation. We also use geometric figure should cover the maximum radiating surface. If we use the formal requirement of symmetry suitable plane figures are rectangle, square, circle. This coincides with the usual forms of radiation surfaces. The following figure 2 shows the change of the power density in a plane transverse to the axis of the transmitter (antenna) in a nearby area where the black dots are the maximum of the directional diagram. [4]

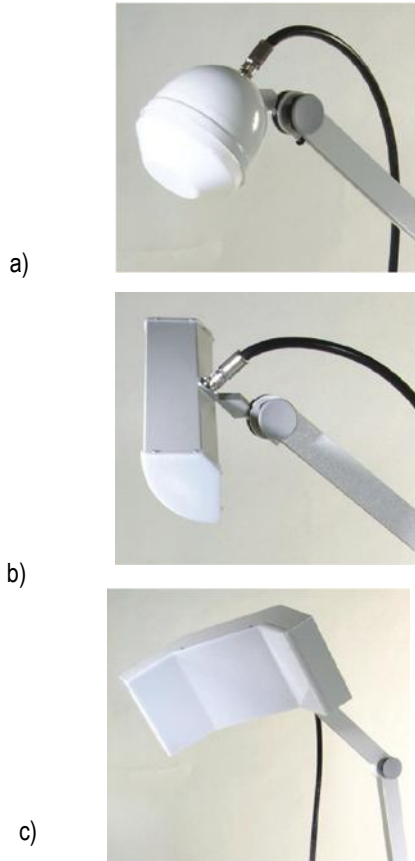


Figure 1. Antennas for microwave therapy

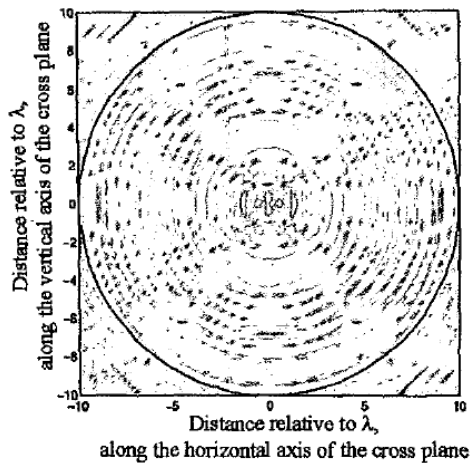


Figure 2. Modification of the power density

3. RESULTS AND ILLUSTRATION OF THE EXPERIMENTAL INVESTIGATION OF THE ELECTROMAGNETIC FIELD

Experimental measurements of the physical power of the electromagnetic in nearby area under real clinical conditions were incurred in connection with the article. Measurements were performed in the usual regimens used in the process of therapy, namely continuous transmission mode of the electromagnetic field. Figure 3 shows the experimental setup for these measurements. To facilitate the measurement and interpretation of the results was used and graphical representation.



Figure 3. The image of the experimental set-up

The measurements of power density were held at various points along the patient bed. The aim of the measurements was to study the spatial configuration of the electromagnetic field in the near zone of antenna's system (patient area). In this sense, it can be handled with relative units of power. Of course these values are related to the absolute values with an accuracy of one coefficient. In Table 1 are shown in relative units of the measured power values of the field along the length of the patient bed in parallel to the measuring antenna, and Figure 4 shows the measurement results graphically of the field, enhancement at 20dB and 29dB, with parallel placement of the measuring antenna.

Table 1. Relative values of the measured power P

Length, cm	-30	-27.5	-25	-22.5	-20	-17.5	-15	-12.5	-10	-7.5	-5	-2.5	0
Power P, relative units, 20 dB gain	1.75	2.5	4.2	4.7	7.1	10	11.9	9.8	7.2	4.7	4.2	7	9.4
Power P, relative units, 29 dB gain	3.6	4.7	3.6	3.8	4.4	6.9	7.45	11.1	10.2	10.3	14.75	19.7	19

Length, cm	2.5	5	7.5	10	12.5	15	17.5	20	22.5	25	27.5	30
Power P, relative units, 20 dB gain	7.1	4.2	4.8	7	10	12	10	7	4.5	4.3	2.5	1.7
Power P, relative units, 29 dB gain	19.8	14.7	10	10	11	7.5	6.9	4.5	4	3.7	4.7	3.5

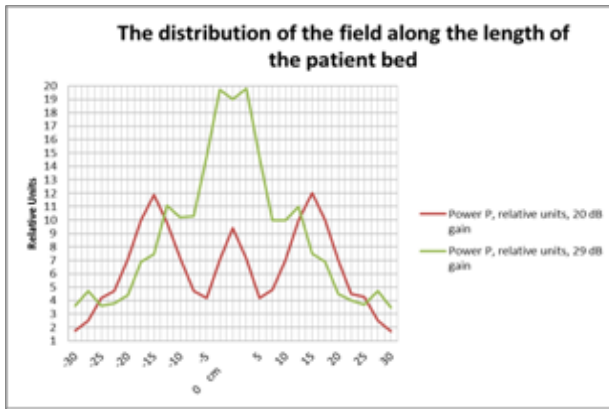


Figure 4. Graph of the measured values of the power P

Normal applications of the heat treatment are generally used to treat the following conditions: reduction of pain, improvement in collagen extensibility, reduction in articular rigidity, reduction of oedema and inflammatory exudates and increase in blood flow. [2]

4. X-RAY IMAGE ENHANCEMENT

The results of magneto therapy can be seen below, using X-ray images.

An "artifact" on a diagnostic X-ray image may appear as light or dark spots, lines, fogging, specks, etc. They can be caused by motion, poor contact between the film and the cassette that holds the film, and so on. The quantum noise is dominant and comes from the quantization of energy into photons. It is Poisson distributed and independent of measurement noise. The measurement noise is additive Gaussian noise and usually negligible relative to the quantum noise.

An integrated adaptive approach is presented to enhance the quality of the X-ray image. The algorithm consists of three basic stages [4].

The first stage is increasing of contrast based on contrast limited adaptive histogram (CLAHE). It is a generalization of ordinary histogram equalization and adaptive histogram equalization. CLAHE does not operate on the whole image works like ordinary Histogram Equalization (HE), but it works on small areas in images, named tiles. Each tile's contrast is enhanced, so that the histogram of the output area roughly matches the histogram determined by the 'Distribution' parameter. This parameter can be selected depending on the type of the input image. The presented algorithm proposes to select this parameter adaptively on the base on PSNR. For limiting the maximum slope is to use a clip limit contrast factor that prevents over-saturation of the

image specifically in homogeneous areas. These areas are characterized by a high peak in the histogram of the particular image tile due to many pixels falling inside the same gray level range. The procedure of CLAHE can be applied to Y component of the selected image that is processing in YUV system as more effectiveness. The second stage is morphological processing for detail preservation capabilities. Local structures can be eradicated or local geometry of the inspected object can be customized by appropriate selection of opening and closing filtration, top and bottom hat filtration and proper form of structuring elements and its parameters. All these elements of the procedure of morphological processing can be determined on the base of the calculated estimation parameters.

The third stage of the algorithm is noise reduction. It is based on the 2D wavelet packet methods and adaptive threshold. The classical entropy-based criterion is a common concept for optimal decomposition. It is used spatial adapted threshold that allows to determinate the threshold in three directions: horizontal, vertical and diagonally. In addition the threshold can be hard or soft. The noise reduction is applied on Poisson distributed noise components, which can be presented as an additive noise model for each pixel.

All adaptive procedures in the proposed algorithm are made automatically, based on calculated estimation parameters such as PSNR, Signal to noise ratio in the noised image (SNR_Y), Signal to noise ratio in the filtered image (SNR_F), Effectiveness of filtration (E_{FF}) Noise reduction ratio (NRR) in the different stages of the algorithm. PSNR and E_{FF} values are higher for better denoised X-ray image where the value of NRR is lower.

The formulated stages of processing are presented by computer simulation in MATLAB, version 7.14 environment with using the IMAGE PROCESSING and WAVELET TOOLBOXES. The obtained results for the investigated X-ray image of the foot are presented in Table 2.

Table 2. Simulations results

Method of processing	Estimations Parameters				
	PSNR [dB]	NRR	SNR_Y [dB]	SNR_F [dB]	E_{FF} [dB]
CLAHE	24.325				
Morphological processing	27.684	0.5	14.949	16.556	1.607
Noise reduction based on WPT	29.688	0.3	16.556	18.471	1.915

Visual presentations of the original and processed X-ray images are given on Figure 5.



Figure 5. Original and processed X-ray images

The corresponded histograms of the original and processed by CLAHE method image are presented in Figure 6 and Figure 7.

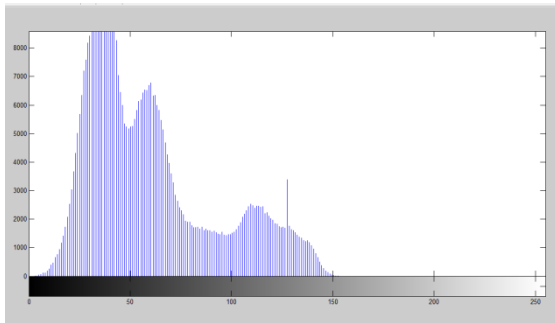


Figure 6. Histogram of the original X-ray image

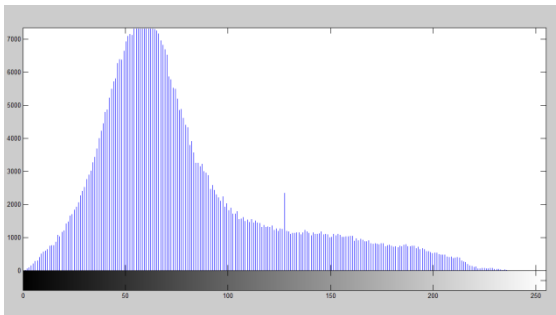


Figure 7. Histogram of the processed X-ray image

5. CONCLUSION

We can say that the study of the characteristics of electromagnetic field in the nearby area along with the study and optimization of the space-time configuration of the electromagnetic field are very important and crucial for achieving the desired therapeutic effect. X-rays are widely used in medicine for various graphics and scopic studies in order to obtain an image. In our case, they are used for the representation of the bone structure in the patient. For the improvement of their quality, different methods were used, one of them is shown in the article.

References

- [1] D.Dimitrov, Medical systems for influence of electromagnetic fields on human, education book, TU-Sofia, 2007
- [2] W.Y. Riadh, "Electromagnetic Fields and Radiation (Human Bioeffects and Safety)", Marcel Dekker Inc. Canada, 2001, ISBN 0-8247-0877-3
- [3] Schwan, H. P., Interaction of Microwave and Radio Frequency Radiation with Biological Systems, IEEE Transactions on Microwave Theory and Techniques 10, 2001
- [4] V.Georgieva, R. Kountchev, I. Draganov, "An Adaptive Enhancement of X-Ray Images", Advances in Intelligent Analysis of Medical Data and Decision Support Systems, Springer, Heidelberg, New York, Dordrecht, London, 2013, pp. 79-88.

GUI FOR CONTRAST ENHANCEMENT IN MEDICAL IMAGES

Veska M. Georgieva

Faculty of Telecommunications, Technical University of Sofia, Bulgaria
1000 Sofia, "Kl. Ohridsky" str.8
T. (+359 2) 965-3293; E-mail: vesg@tu-sofia.bg

Virginia A. Mileva

Faculty of German Engineering Education and Industrial Management, Technical University of Sofia, Bulgaria
1000 Sofia, "Kl. Ohridsky" str.8
E-mail: v.at.mileva@abv.bg

Abstract

In the paper is presented software for contrast enhancement in medical images and its graphic user interface (GUI). It works in the MATLAB environment and uses IMAGE TOOLBOXES defined functions. Different contrast enhancement techniques such as increasing the contrast, histogram equalization (HE) and contrast limited adaptive histogram equalization (CLAHE) can be used, regarding to process different medical modalities of grayscale and color images. The GUI proposes also an interactive option to choose the type of the specific function and its parameters. It can be applied to real medical images attempt to make diagnostic more precise. The GUI is suitable also to engineering education for studying of this processing.

Some results of the experiments are presented, which were made by computer simulation in MATLAB environment.

1. INTRODUCTION

Image contrast enhancement is one of the categories of medical image processing, attempt to make diagnostic more obvious. Contrast enhancement is based on emphasizing the difference of brightness in an image to improve its perceptual quality [1]. Most of these techniques are based on global histogram modifications or local contrast transformations. The current state-of-the-art method for automatic display is a variation of the technique of histogram equalization [2]. Histogram equalization (HE) is a nonlinear transformation scheme that maps image intensity values across the entire range of a display device.

CLAHE is basic local histogram-based contrast-enhancement techniques. It divides the original image into several non-overlapped sub-blocks, performs a HE of each sub-block and merges the sub-blocks using bilinear interpolation [3]. This method usually produces an undesirable checkerboard effect near the boundaries of the sub-blocks. To counter this effect, sub-blocks are overlapped generally at the expense of increased computation and memory usage. Increasing the contrast by a `imadjust` function in Matlab maps the intensity values of the image such that 1% of data are saturated at low and high intensities. It fails to achieve any contrast enhancement but does not introduce luminance shift or saturation. The HE and CLAHE tech-

niques emphasize the details, but introduces saturation artifacts and color shift. Most of the image contrast enhancement techniques are applied to grayscale medical images. Techniques for color contrast enhancement are similar to those for grayscale images. Color imaging may be considered as a channel-by-channel intensity image processing scheme. This is based on the assumption that we can process each of the monochrome channels separately and finally combine the results. Independent equalization of RGB leads to a hue shift. Another approach to color enhancement is to transform the image from the RGB space to other color spaces such as the CIELAB, LHS, HSI, HVS, etc.

In the paper is presented software for contrast enhancement in medical images and its GUI. Different contrast enhancement techniques such as increasing the contrast, HE and CLAHE can be used, regarding to process different medical modalities of grayscale and color images.

The software is created in MATLAB 7.14 environment by using IMAGE PROCESSING TOOLBOX.

The graphic user interface consists of checkboxes, buttons, edit boxes, pop-up controls, which make it easy to use. Users enter or choose input data in a single form, because input information changes and visualizations are easier and faster in this way. The processed image can be saved on the disk and so

can be used to another processing or its visualization.

2. THE GUI FOR CONTRAST ENHANCEMENT

The GUI for contrast enhancement of medical images is shown on Fig.1. It is divided in several areas, where the user applies different settings, concerning image contrast enhancement techniques and their parameters and areas for universal application.

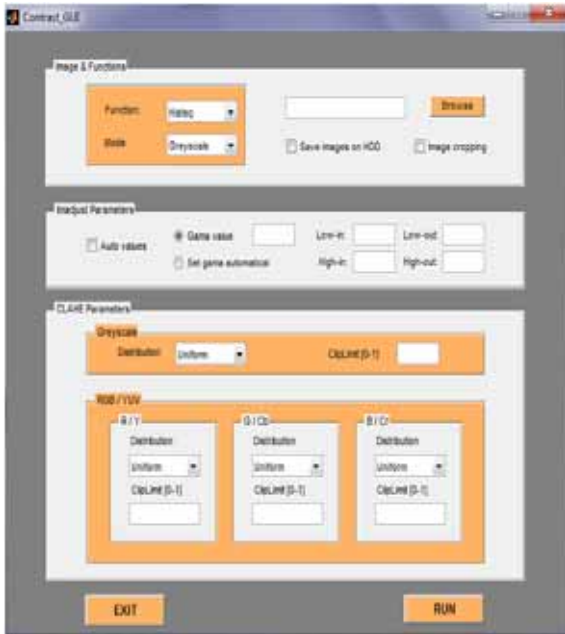


Figure 1. GUI for contrast enhancement of medical images

The area "Image and Functions" is shown on Fig.2. It is for entering an image file name with an image file extension. The user can navigate among the folders in the work folder and choose image by using "Browse" button and view the image. The user can select the contrast enhancement function from the pop-up menus and the mode for color (RGB or YCbCr) or grayscale format of the image, which will be processed. The selected image can be processed as region of interest (ROI) image, too. The user can choose in this case the function "Image cropping". "Save Image on HDD" is checked to save results from contrast enhancement in image files in 'jpg' format.

The user can select the imadjust or histogram equalizations parameters, from the area "Imadjust parameters", which is presented in Fig.3. The important parameters of these methods are minimum and maximum intensity difference (threshold) and gamma parameter's value with values between 0 and 1. It can be input automatically or manually.



Figure 2. Area "Image and Functions"



Figure 3. Area "Imadjust parameters"

The area "CLAHE Parameters" is shown on Fig.4. The CLAHE contrast enhancement technique can be applied on grayscale or on color medical images, too. The desired histogram shape for the image tiles can be selected by pop-up menu. There are 3 possibilities of distribution functions: 'uniform' for flat histogram; 'Rayleigh' for bell-shaped histogram; 'exponential' for curved histogram.

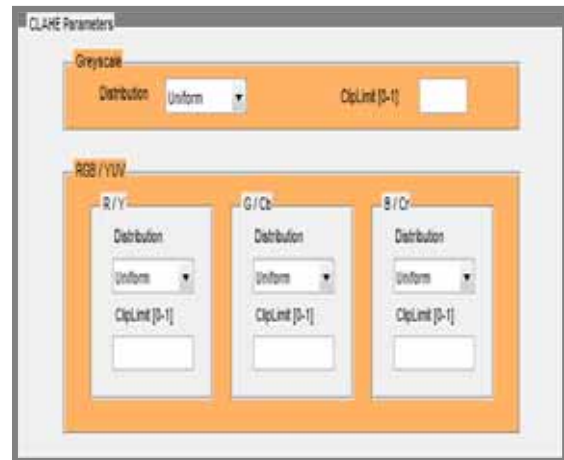


Figure 4. Area "CLAHE Parameters"

The other important parameter is 'ClipLimit' factor. It is a contrast factor that prevents over-saturation of the image specifically in homogeneous areas.

After choosing all input information the procedure of processing begins, when the user clicks on button "Run Process". Then the final result is shown – original image, and processed images. When button "Exit" is pressed the program can be closed.

3. TASKS CARRIED OUT FROM THE MAIN PROGRAM

The basic algorithm that works behind is shown in Fig. 5.

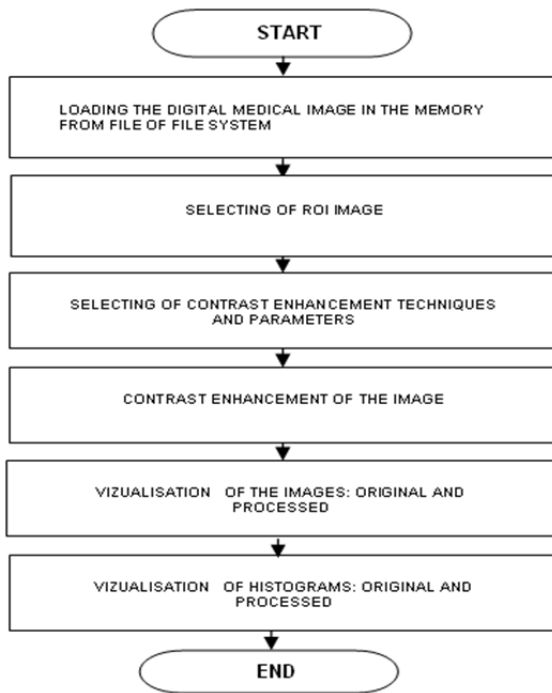


Figure 5. Block diagram of the algorithm

By acting of component from GUI can be implemented a callback-function from the main program. Every graphic component can be treated to object. Every object can be referred to handle. The objects referred a complex of attributes, which can be manipulated from the software. The multifarious attributes can be leaved for using in MATLAB environment, such as "Enabled", "Value", "Visible", "On", "Off" etc. [4]. Every attribute can be enabling in the presence of corresponding handle or reference to the object. Every graphic component can be reiterated to a cycle of events for the MATLAB environment by initialization of the graphic application.

It submits addresses of the callback-functions, associated to a given event, which are important. By its identification can be called out a corresponding callback-function. One of the important tasks that the main program has is input data validation. The execution is canceled if an error concerned with wrong information occurs. Another essential purpose of is presenting the input information in appropriate data structures. It is necessary for the next steps in the processing strategy, in this step the processing is made with appropriate input data. Wrong information prevents contrast enhancement from carrying out or may lead to wrong output.

Some results from simulation, which illustrate the working of the program, are presented in the next figures below. In Fig.6 is shown the original X-ray image of hand of size 640x480 pixels and its computed histogram.

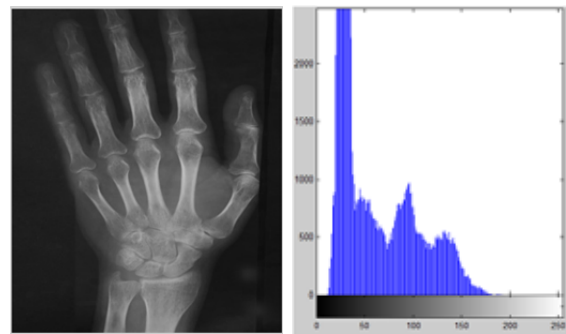


Figure 6. Original X-ray image and its calculated histogram

In Fig.7 are presented the modification of the X-ray image, obtained by HE, in Fig. 8, obtained by 'imadjust' function and in Fig.9. by CLAHE and the corresponding computed histograms.

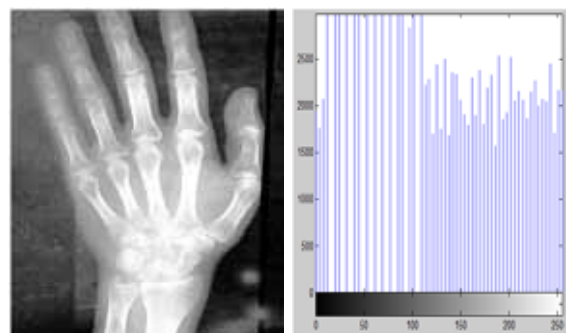


Figure 7. Processed by HE X-ray image and its calculated histogram

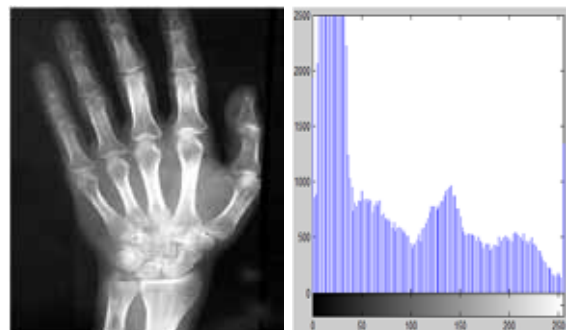


Figure 8. Processed by 'imadjust' X-ray image and its calculated histogram

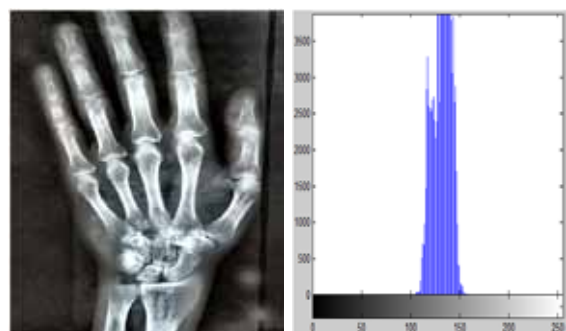


Figure 9. Processed by CLAHE X-ray image and its calculated histogram

4. CONCLUSION

In the paper is presented a GUI for contrast enhancement of medical images. It uses MATLAB defined function and works in MATLAB 7.14 environment. The GUI can be used in engineering and education for studying this process. It can be used also in real time to provide important anatomical information in medical images to physicians and specialist upon which can be made diagnoses of different diseases.

References

- [1] Gonzalez RC, Woods RE, Digital Image Processing Prentice Hall, Upper Saddle River, NJ; 2002.
- [2] Saleem A., Beghdadi A., Boashash B., Image fusion-based contrast enhancement, EURASIP Journal on Image and Video Processing, 1-17, 2012.
- [3] Lamberti F, Montrucchio B, Sanna A, CMBFHE—a novel contrast enhancement technique based on cascaded multistep binomial filtering histogram equalization. IEEE Trans Consum Electron, 52(3): 966-974, 2006.
- [4] MATLAB User's Guide. Accessed at: www.mathwork.com

DEACTIVATION OF STAPHYLOCOCCUS AUREUS AND ESCHERICHIA COLI USING PLASMA NEEDLE AT ATMOSPHERIC PRESSURE

¹Hamad Raheem H., ²Maha Adel Mahmood

¹Department of Physics, College of Science, Baghdad University, Baghdad, Iraq

²Department of Basic Science, College of Dentistry, Baghdad University, Baghdad, Iraq

E-mail: dr.hammad6000@yahoo.com

Abstract

Non-thermal (low-temperature) plasma may act as an alternative approach to control superficial wounds and skin infections when the effectiveness of chemical agents is weak due to natural pathogen or biofilm resistance. In this paper an atmospheric pressure plasma needle jet device local made which generates a cold plasma jet 1mm diameter and about 30 mm in length sustained by low-frequency excitation was used to study the deactivation of two bacterial isolates Escherichia coli and Staphylococcus aureus. Escherichia coli and Staphylococcus aureus were used as a model system to optimize the conditions for bacterial destruction. Plasma working gas flow rate, treatment time and needle to sample distance are varied. Plasma treatment of Escherichia coli results in formation of inhibition zone of 25 mm and Staphylococcus aureus in 29 mm inhibition zone respectively. Prolongation of treatment time improves the destruction efficiency. Sample treatment during plasma treatment has been monitored. The temperature can reach up to 32°C at shortest needle-to- sample distances and 80 s treated time where the ambient temperature was 29°C.

Keywords: Plasma needle, plasma bacteria deactivation, non-thermal plasma

1. INTRODUCTION

Some major drawbacks of the conventional sterilization techniques are the high processing temperatures (ovens and autoclaves) which makes it impossible to sterilize heat-sensitive materials like polymers, the use of toxic chemicals and the long sterilization times needed approximately 12 hours in the case of ethylene oxide exposure[1]. Another interesting sterilization method

is the use of gamma irradiation, but this is an expensive technique and may cause the material to undergo undesirable changes during sterilization.

It has been known for a long time that ionized gases have biotical effects, but only in 1996 successful killing of bacteria with plasma was reported [2].

One of the attractive features of non-equilibrium plasmas is the ability to achieve enhanced gas phase chemistry without the need for elevated gas temperatures. This is because these plasmas exhibit electron energies much higher than that of the ions and the neutral species. The energetic electrons enter into collision with the background gas, causing enhanced level of dissociation, excitation, and ionization. Because the ions and the neutrals remain relatively cold, the plasma does not cause

any thermal damage to articles it comes in contact with.

In physics plasma is considered the fourth state of matter next to solids, liquids and gases. On the basis of their high bactericidal effectiveness plasmas are also used to sterilize medical devices and in packaging of food stuffs. The development of diverse, usually non-thermal atmospheric-pressure plasma sources makes its use also in the (bio) medical field possible. While in the past only the thermal properties of plasmas ($> 80\text{ }^{\circ}\text{C}$) were utilized – cauterization, sterilization of heat-resistant instruments or for cosmetic, reconstructive procedures – current research is directed primarily at the non-thermal effects of plasma [3].

These plasma-generated active species are useful for several bio-medical applications such as sterilization of implants and surgical instruments. Sensitive applications of plasma, like subjecting human body or internal organs to plasma treatment for medical purposes, are also possible.

Biomedical applications of plasmas have recently been summarized as “Plasma medicine.” Within this context, there is an increasing interest on the development and characterization of flexible plasma sources which can be used under atmospheric pressure conditions. Plasma jets, barrier dischar-

ges, and other micro plasma devices are therefore under intensive investigation [4,5].

The aim of this work was to use *Escherichia coli* and *Staphylococcus aureus* as a model system to optimize the conditions, Plasma working gas flow rate, treatment time and needle to sample distance for bacterial destruction.

2. EXPERIMENTAL WORKS

2.1. Plasma Needle Apparatus

Non-equilibrium plasma generated by a plasma needle was used for the treatment of bacteria. The plasma torch shown in Fig.1 local made is consisting from 10cc glass syringe adapted to a hallow stainless steel needle with inner diameter 1.04mm from one side and the working gas (Ar) into other side through Teflon gas fitting. The needle is powered by high voltage of sinusoidal shape of 7.5kV and frequency of 28 kHz peak to peak generated by high voltage transformer. The Ar gas is directed to the needle through the syringe and mixes with ambient air around the tip of the needle. The Ar gas was flowing at 1slm (standard liters per minute) flow rate through the needle. The jet length depends on argon gas flow rate and it can reach 3.5 cm in air at gas flow rate 1slm.



Figure 1. Plasma needle torch [6]

2.2. Sample Preparation

Two bacterial isolates (*S. aureus* and *E. coli*) were obtained from Al-Yarmook Teaching Hospital. They were activated by cultivating *S. aureus* on blood agar and *E. coli* on MacConkey agar for 20 h at 37°C. Sub-cultures on solid nutritional media were incubated under the same conditions.

Bacterial suspension was prepared according to no.5 McFarland standards tube whose density corresponds to an approximate cell density of 1×10^8 colony forming unit per milliliter (cfu ml^{-1}), from this initial suspension, other suspensions in cfu /ml were made with cell density 1:10, 1:100 and 1:1000 of the original. Plastic Petri dishes were filled to a depth of 4 mm with agar, which is an aqueous growth medium with a jelly-like consistency. After cooling and solidification, the bacterial inoculum was uniformly spread using sterile cotton swab on a

sterile Petri dish of nutrient agar forming a bacterial lawn. (from antibiotic original)

2.3. Plasma treatment

There were three adjustable parameters for our plasma treatment against the studied isolates. The exposure time was varied in a range from 20 to 80 s, the needle-to-sample separation d from 2 to 6 mm, and the gas flow from 1 to 5 slpm.

At first, the plasma torch was raised, installed a Petri dish with its center immediately below the needle, and then lowered the plasma torch to the desired separation d . Next, plasma treatment was start by positioning the Petri dish so that the plasma impinged on a desired spot in the inoculated portion of the dish. At the end of the exposure time, the dish was moved to treat another spot. This step was repeated to treat a total of three spots on the dish, as shown in Fig. 2. The fourth spot was the control for the experiment; it was exposed to the gas flow without plasma glow. The control spot indicates the effects of argon flow without any plasma-generated species.

2.4. Incubation and imaging

To visually observe the effect of plasma treatment, the treated samples were incubated so that visible colonies formed. Petri dishes were covered to prevent atmospheric contamination. All plates were then incubated in an incubator at 37°C for 48 hours so that bacteria multiplied. And the inhibition diameter zones were observed and measured in mm. (from antibiotic original). After incubation we imaged the dishes with a digital color camera using white photographer's lights for illumination.

2.5 Temperature tests

For the purpose of measuring temperature increase during the plasma treatment, the temperature was monitor by infrared thermometer.

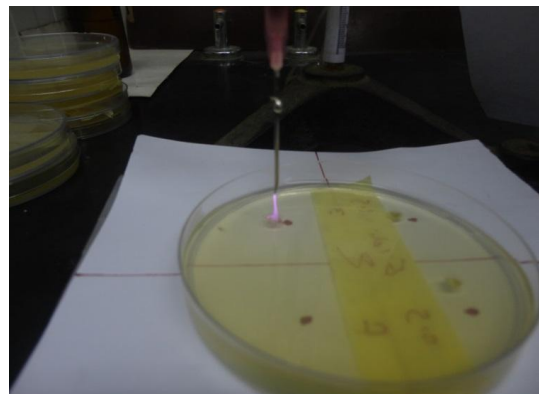


Figure 2. Plasma samples treatment

3. RESULTS AND DISCUSSION

Susceptibility to the argon plasma treatment was determined by applying plasma to planktonic bacterial cells plated on nutritive agar plates. To check the effect of non-ionized argon gas, it was applied to parallel samples. As a control, bacterial plates were left untreated. The bactericidal effect was determined as the diameter of inhibition zones (Diz) in millimeter after treatment with plasma or non-ionized argon compared with the untreated control. Figure 3 showed the (Diz) in millimeter for *S. aureus* cultivated on agar plate versus plasma exposed time using three different distances between the needle end and agar surface (2, 4, 6 mm), three different gas flow rates (1, 2.5, 5 slpm) and exposure time ranged between 20- 80s. Figure 4 showed the (Diz) in millimeter for *E. coli* at the seam condition. Figure 3 and 4 shows that an increase in inhibition zones when the distances between needle end and agar surface was increased from 2mm to 6mm for all argon gas flow rate. Also show increase in inhibition zones with increasing plasma exposure time for all flow rate and for all distances. The maximum increase in inhibition zone for *S. aureus* was seen at 4 mm distance, 2.5 slpm, 80 s. or at 6mm distance, 2.5 slpm, 80 s (29 mm) respectively.

The exposure of *S. aureus* to plasma work at gas flow rate of 2.5 slpm for 80 seconds at distance of 4 or 6 mm was the best killing condition where the inhibition zone of 29 mm. From this result we can conclude that the gas flow doesn't affect the inhibition zones rather what the role will due to the time which play a great role in this case. The most favorable conditions in *E. coli* inactivation was the exposure of *E. coli* to either 5 slpm at 2mm distance for 80 s (25mm) or 2.5 slpm at 4 and 6mm distance for 80 s and this corresponds with the results obtained for *S. aureus*.

The diameter of inhibition zone of both bacteria (*S. aureus* and *E. coli*) was increased as the time increased from 20 to 80 s for each gas flow and for each distance used in this investigation. The inhibition zone of both bacteria (*S. aureus* and *E. coli*) was increased with an increase of distances at gas flow 1 or 2.5 slpm but this is not the case with 5 slpm. Under most conditions, in our temperature tests, the agar temperature remained below 32°C. The agar temperature did not exceed 32°C for all experiment conditions even increased the exposure time to 80 s. From this result we conclude that

it is possible to operate a plasma needle so that there is no killing due to heat [7,8].

To summarize, all conditions are most attractive for possible clinical applications, and these are achieved at short exposure time but large separation between plasma needle and Petri dish. The 80 s treatment proves to be efficient even at a low flow rate whereas higher flow rate appear to be less efficient for shorter treatment times.

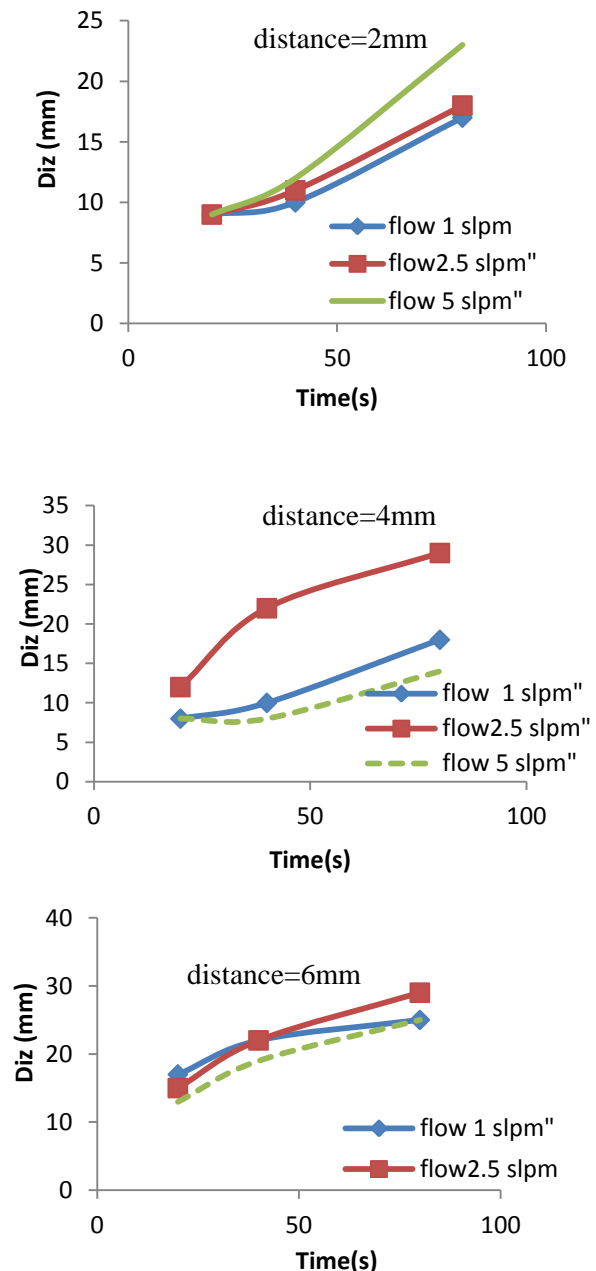


Figure 3. The diameter of inhibition zones (Diz) in millimeter for *S. aureus* cultivated on agar plate versus plasma exposed time

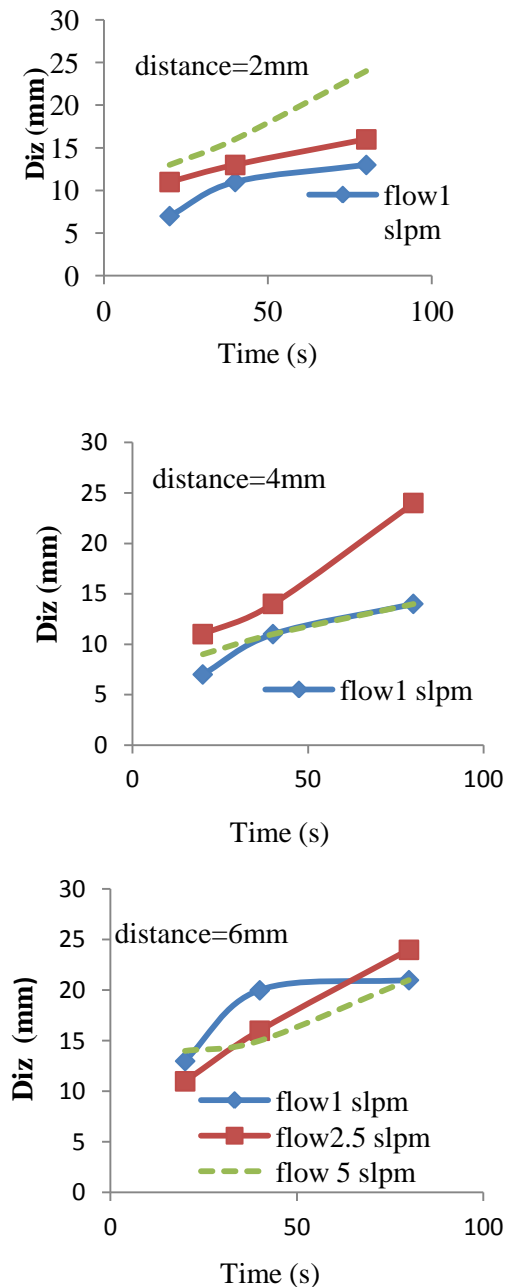


Figure 4. The diameter of inhibition zones (Diz) in millimeter for *E. coli* cultivated on agar plate verse plasma exposed time

The flow of the Argon gas plays an important role in the resulting concentrations of bacteria. This is presumably due to different resulting concentrations of reactive particles (radicals) where the flow of the inert Argon gas pushes atmospheric gases further away from the plasma core, and while the densities of UV photons could remain unperturbed, the densities of chemically active radicals would be reduced because of the increasing gas flow. This is, on the other hand, a simplified explanation as operating conditions may be quite different depending on the percentage of atmospheric gases. *E. coli* is a Gram-negative bacteria, which means that it has an addi-

tional outer membrane made of lipopolysaccharides and protein. If mechanical erosion of the bacterial membrane is one of the factors responsible for its inactivation, we can assume that *E. coli* will suffer less damage in the same treatment conditions, as compared to *S. aureus*[7]. The damage induced by plasma in the case of *E. coli* consisted of punctured, eroded and morphologically transformed bacteria, while for *S. aureus*, the bacteria were ruptured with their cellular contents released onto the substrate surface.

Another very strong disinfectant is UV radiation but its role in atmospheric plasma sterilization goes from modest to highly effective depending on the type and concentration of bacteria or spores, the amount and composition[10,11].

4. CONCLUSIONS

The plasma needle is capable of treatment under conditions that are attractive to clinical uses as it is capable of killing *S. aureus* and *E. coli* with a treatment time of seconds, and without an elevated temperature. It found that the plasma needle can be operated under conditions where the bactericidal effect is attributable to atmospheric chemical species produced by the plasma and not due to heat. Most importantly, the treatment time proved to be more important than merely the gas flow rate and the distance between plasma needle and petri dishes within the plasma jet length.

References

- [1] B. J Park, D. H. Lee, J. C. Park, I. S. Lee, K. Y. Lee, S. O. Hyun, M. S. Chun, and K. H. Chung, "Sterilization using a microwave-induced argon plasma system at atmospheric pressure", *Physics of Plasmas*, 10, 2003, pp. 4539-4544.
- [2] M. Laroussi, "Sterilization of contaminated matter with an atmospheric pressure plasma", *IEEE Trans Plasma*, 24, 1966, pp. 1188-91.
- [3] M. G. Kong, G. Kroesen, G. Morfill, T. Nosenko, T. Shimizu, J. Van Dijk, and J. L. Zimmermann, "Plasma Medicine: an Introductory Review", *New J Phys*, 11, 2009, pp. 115012-14.
- [4] M. Moreau, N. Orange, and M. G. J. Feuilleux, "Nonthermal plasma technologies: new tools for bio-decontamination", *Biotechnol Adv* 26, 2008, pp. 610-617.
- [5] Hammad R. Humud, Ahmad S. Wasfi and Wafaa Abd Al-Razaq, "A low temperature atmospheric pressure plasma jet", *International Review of Physics (I.RE.PHY)*, 7, 1, 2013, pp. 40-43.

- [6] Hammad R. Humud, Ahmad S. Wasfi, Wafaa Abd Al-Razaq, and Mazin S. El-Ansary, "Argon plasma needle source", *Iraqi Journal of Physics*, 10,17,2012, pp.53-57.
- [7] J. Goree, B. Liu, D. Drake, and E. Stoffels, "Killing of *S. mutans* bacteria using a plasma needle at atmospheric pressure", *IEEE Trans. Plasma Sci.*, 34, 4, Aug. 2006, pp.1317-1324.
- [8] Hammad R. Humud, Maha Adel Mahmood, and Wafaa Abd Al-Razaq, "Strain specificity in antimicrobial activity of non-thermal plasma", *Iraqi Journal of Physics*, 11,20, 2013, pp.110-115.
- [9] K. Y. Lee, B. Joo Park, D. Hee Lee, I. S. Lee, O. S. Hyun, K. H. Chung and J. C. Park, "Sterilization of *Escherichia coli* and MRSA using microwave - induced argon plasma at atmospheric pressure" *Surf. Coat. Technol.*, 193, 2005, pp.35-38.
- [10] F. Iza, G. J. Kim, S. M. Lee, J. K. Lee, J. L. Walsh, Y. T. Zhang, and M. G. Kong, "Microplasmas: sources, particle kinetics, and biomedical applications," *Plasma Process. Polym.*, 5, 4, Jun. 2008, pp.322-344.
- [11] T. Nosenko, T. Shimizu and G. E. Morfill "Designing plasmas for chronic wound disinfection", *New J. Phys.* 11, 2009, pp.115013-32.

METHOD FOR DESIGN OF SYSTEM FOR MAGNETOTHERAPY USING "RUNNING" RANDOM LOW FREQUENCY SERIES OF SIGNALS

Atanas Dimitrov, Kalin Dimitrov

Technical University of Sofia, Bulgaria,
Faculty of Telecommunication, TU-Sofia, "Kl. Ohridsky" str. 8, 1000 Sofia, Bulgaria

Abstract

The systems for magnetotherapy, which use running low frequency magnetic field are new generation of systems for magnetotherapy. It is well known that familiarization of patients with parameters of external influence is a big disadvantage of systems for physiotherapy. This problem can be avoided in systems for low frequency magnetic field by running of this field around the human body. The possibility for simultaneously influence of low frequency magnetic field on different part of the human body is one additional advantage of systems for magnetotherapy, using moving magnetic field. The basic requirements and method for design of above mentioned system for magnetotherapy is described in the paper.

1. INTRODUCTION

The main component of systems for magnetotherapy using low frequency magnetic field is generator for rectangular electrical impulses with special parameters. Now more and more digital systems are applied to therapy. The use of digital elements for their construction offers greater flexibility, economy and more functions in one system. The data which pass through various digital modules can be saved in memory, subject to various digital processing, and also can be displayed on digital display. In the design of pulse generators can be used and one-chip microcomputers, characterized by low consumption and a limited number of external components. Great advantage over the basic generators is the programmable logic. Any functional change can be implemented easily without any hardware changes (making a new board, adding/replacing components).

2. THEORETICAL SOLUTION OF THE SYSTEM FOR MAGNETOTHERAPY BY RANDOM "RUNNING" MAGNETIC FIELD

The system for magnetotherapy with the "running wave", the subject of this paper is achieved through a combination of analog and digital elements. Management system is implemented using a microprocessor PIC18F452 Microchip. The output of the processor signals are close to perfect form rectangular signals with extremely low and falling and rising edge amplitude of 5V. This allows for easy and extremely accurate control of analog compo-

nents connected to the processor, as well as precise control of output signals for the system. The block diagram of the system for magnetotherapy by a "running" low frequency magnetic field is shown in Figure 1.

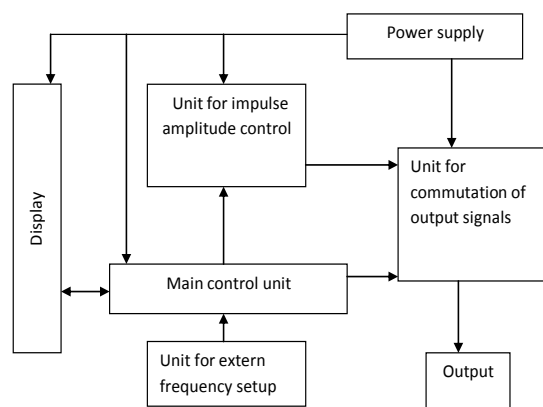


Fig.1 Bloc-diagram of systems for magnetotherapy with running magbetic field

The block diagram of the system for therapy by "running" magnetic field is mainly composed of seven functional blocks. Principle of operation of each of them will be discussed in detail below in the paper. Modes of therapy system can be described as follows: The output of the control unit generates a series of rectangular digital pulses that are submitted to "block for switching the output signals." Amplitude of the output is determined by the "control box for switching the amplitude of the pulse train." Management and operation mode of the system is possible through therapy, "Block external frequency control." For real-time visualization of the parame-

ters of output pulses for the system using liquid crystal display.



Fig. 2

The system can be build as apparatus for magneto-therapy which outputs are connected with many coils for local applications (Fig.2).



Fig. 3

The coils can be put on special medical bed for magnetotherapy, which has mobile carriage. A half of coils can be put on the bed and the rest coils cab put on the mobile carriage (Fig. 3).

3. BASIC COMPONENTS OF SYSTEM FOR MAGNETOTHERAPY BY "RUNNING MAGNETIC FIELD"

Control unit:

The control unit serves to control the behavior of the system, controlled by digital signals "block switching the amplitude of the pulse train", "block switching of output", "Block external frequency control." Powered by a microprocessor is pre-programmed with suitable software. This block sets: the time for

generating periodic pulses, the maximum operating frequency, amplitude and rate of filling of the system output signals. Change the operating mode of this module is possible by detecting the signals coming from "external control unit of frequency." Modes of the block is monitored in real time by sending data to a digital liquid crystal display.

Because the requirements for the system required an appropriate program for proper and precise control of the synthesized sound. Created for this purpose is a program allows you to generate different delays and thus realize pulses with different frequency and duty cycle. Especially used for the system processor that is all one byte instructions are performed by a single instruction cycle. Exceptions are cases where there is a condition for branching in the program or the program counter changes its state following the instructions. In this situation, execution takes two instruction cycles, the second run by NOP /no operation/. Two-byte instructions are performed in two cycles, one cycle consists of four periods of the oscillator. Time for one command at frequency of 20 MHz clock generator is equal to 0.2s. In the presence of branching in the program or the program counter is changed as a result of the instructions, the time needed for implementation will be 0.4s. Therefore making delays of 1ms is necessary to make 5000 operatsii in the microprocessor.

The frequency of pulses at the terminals of micro-computer specified and outputs can be easily changed by appropriate subroutine. Manually changing the frequency via external buttons is also possible to realize the only way software. Providing this type of user control requires constant monitoring of the findings which relate buttons to change the status of signals.

One algorithm for implementation of this function is assigned to fig. 4. The block generating a pulsed output of a given frequency is a counter which counts up to a certain value. Thus, time-delay that occurs as a result of counting corresponds to the period of repetition of pulses. Before starting the count output, that which generates pulses with an initial level set "1" after counting to prevent that outcome again be reset, which in this case is a logical "0". Fig. 5 shows an example functional diagram of pulse generator realized with single-chip microcomputer. With two buttons, the user can adjust the frequency output of the device. The first button is used to increase the frequency and the

second reduction. The outputs of the microcomputer is applied the inputs for power circuit switching

voltages and different target specific outputs of the synthesis apparatus.

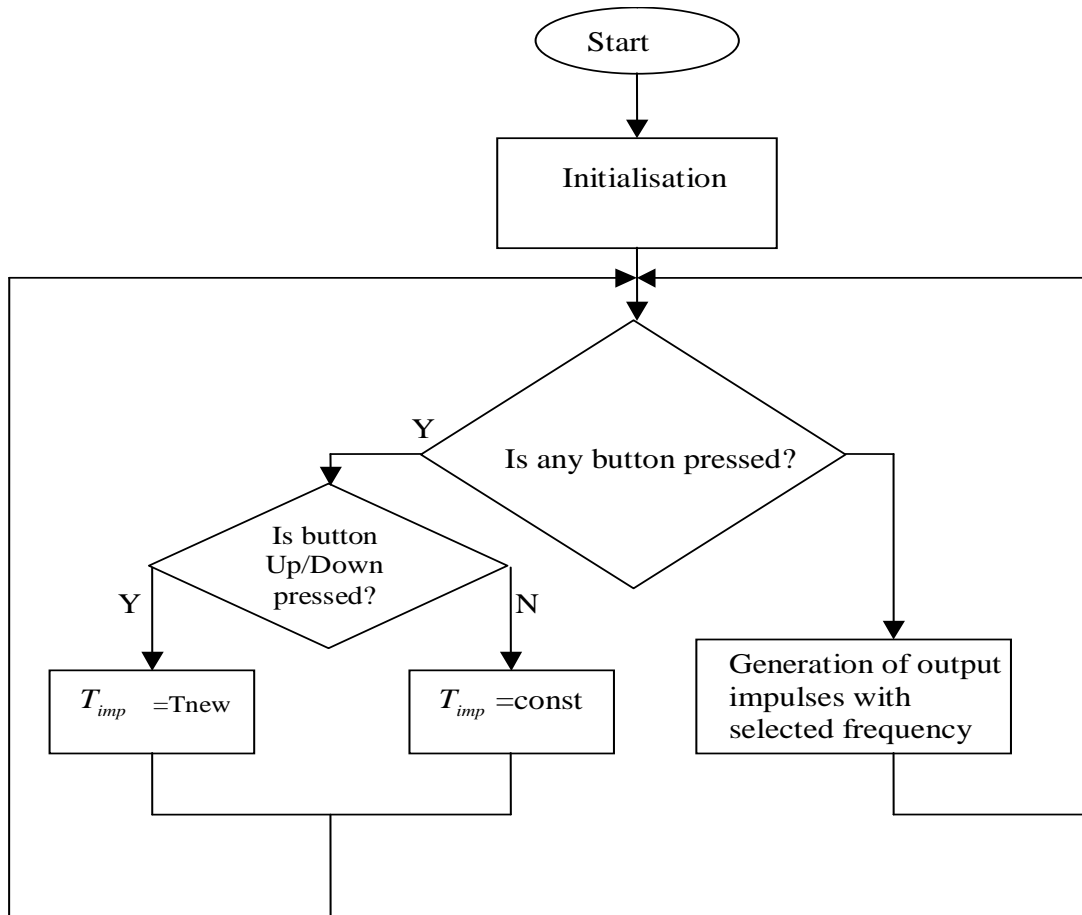


Fig. 4

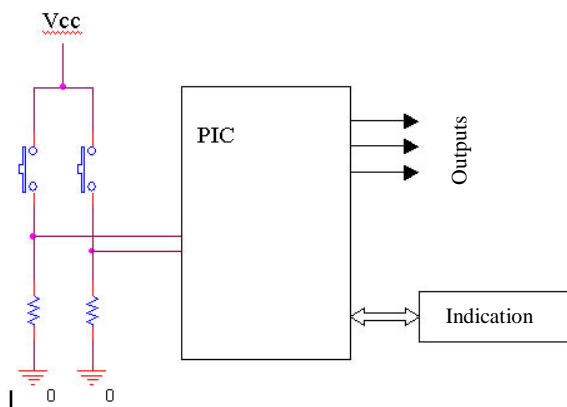


Fig. 5

The outputs of the microcomputer is applied the inputs for power circuit switching voltages and different target specific outputs of the synthesis apparatus. This is necessary because the outputs of the circuit can not provide the required output power and serve only as a logical control scheme. Providing feedback to the user device to be carried out by liquid crystal (LCD) also connected to the micro-processor. Thus it is possible to monitor the current

frequency and amplitude of the output device. The successful combination of analog power components with micro-electronic integrated circuits offers a modern and easy way to precisely control, monitor and generate low-frequency analog signals with high power. The advantage of using such a combination consists of low power consumption and relatively simple hardware solution. Similar systems with traveling wave therapy in the manner described can be easily implemented in portable cans. By the user that makes the system convenient and easy to use.

External control unit of frequency

This block allows the user to influence the process of the system. By timing buttons displayed on the front of the device is easy to make changes in the parameters of the synthesized output signals for the system.

Block switching output

This unit carried out successively shift the generated pulse train to one of the outputs of the device.

Switching signal a "running wave" is done automatically using appropriate software solution. Principle of action can be explained by the fact that continuous time monitor which output is a logical unit. When an output is high level, all others are low. For the realization of a series of impulses running /"running wave"/ a walk therefore all conclusions in this case the duty cycle of pulses depends inversely on the number of outputs.

Control unit amplitude pulse train

Thanks to this unit it is possible to perform manipulation of amplitude output signal for the device. Provides precise control of amplitude of output signal for the system.

Output unit

Represents the synthesized output interface system. It consists of appropriately selected connector box mounted to the apparatus. Provides smooth and reliable connection between the device and external to the system inductive load.

Liquid-crystal display

Allows monitoring of pulse parameters and feedback from users. Visualization of the computer is deliberately avoided, because in this case functions, will be limited in the absence of a computer connected to projection device. Seven segment display is a good choice because of the need to use a large number of terminals to display a symbol. The ability to simultaneously monitor multiple parameters using a small number of conclusions and low power consumption due to the advantages that the use of the LCD-display the most appropriate choice.

Power supply

The power supply consists of a special transformer for medical equipment and a group of voltage straightening, maximum filtration and stabilization of the interference with the mains voltage. The main task of the unit to ensure proper working pressure of all the elements constituting the system. Input-output signals used for communication between management and individual blocks are:

- Power supply should work with the input output voltage $\sim 220V/50Hz$. Voltages of secondary windings usually must be 60,80,110 V AC.
- The output of power supply usually must be maintained straight and stable voltages +12 and +5 V. Used are voltage 7805 and 7812.

- Block external impact of the output signals chestoia filed with TTL level / 0 and 5V inputs to certain microcomputer. After identification of the signals is done processing and software programming decision-making.
- By microcomputer management of hill-switch relays various secondary windings of power transformer. At precisely that moment in time, to an output device is made from selected AC voltage secondary winding of the transformer.
- To manage the unit is switching signals to TTL level to the microcomputer connected to it triacs. These signals serve to control the output signals and directing them to an exit. Provide mode "running magnetic field"
- Communication between the liquid crystal display and microcomputer is done by bus. It consists of a 4-bit data channel signal and 2 service configuration.

System therapy "running magnetic field" is synthesized by the successful combination of analog and digital components and appropriate software.

4. A REAL SYSTEM FOR MAGNETOTHERAPY BY "RUNNING" RANDOM LOW FREQUENCY MAGNETIC FIELD



Fig. 6

A real system for magnetotherapy by "running" random low frequency magnetic field can be seen on Fig. 6. The outputs of apparatus for magnetotherapy are connected with five independent coils. The pulses of electrical current in the independent pairs of coils can be seen on fig. 7 It's possible to be provided not only "running" of magnetic field on the length of the bed ,but "rotation" of magnetic field, also. This rotation can be provided due to the coils situated on the mobile carriage.

Note: Publication of this paper is on the base of financial support of contract No. 122ПД0019-07 of Scientific- Research Centre of Technical University- Sofia

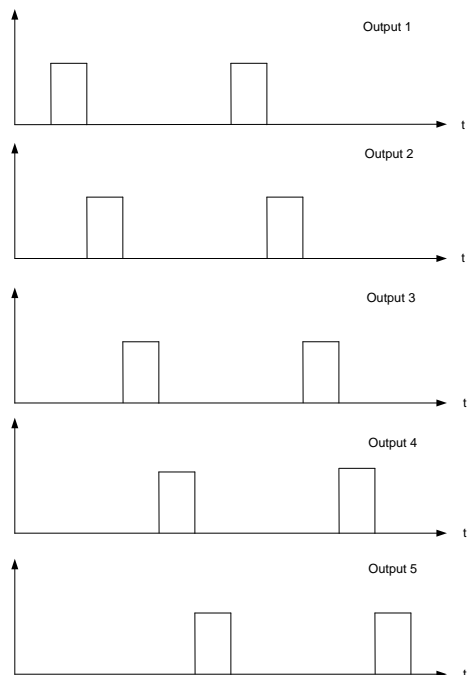


Fig. 7

5. CONCLUSION

1. A method and basic requirements for design of systems for magnetotherapy by running low frequency magnetic field are described in the paper.
2. A real system for magnetotherapy by running low frequency magnetic field is done , also/

References

- [1] "Електротехника и Електроника", списание на съюза по електроника, електротехника и съобщения, София, януари/февруари 2002
- [2] К. Конов, М. Димитрова, А. Попов, Импулсни схеми, Техника, 1984.
- [3] Microchip- спецификация на PIC18F452
- [4] Philips – спецификация на PCF8583
- [5] SHENZHEN JINGHUA DISPLAYS CO.,LTD., LCD AC162A
- [6] Н. Стефанов, Токоизправители и стабилизатори, София, Техника, 1981
- [7] Fairchild Semiconductor Corporation, спецификация на MJE340
- [8] К. Конов, М. Димитрова, А. Попов, Импулсни схеми, Техника, 1984

AN ALGORITHM FOR VISUALIZATION OF LOW-FREQUENCY MAGNETIC SIGNALS IN SYSTEMS FOR MAGNETOTHERAPY

Bogdan Kudrin

St. Petersburg State University, Faculty of Math. & Mech.,
198504, SPb, Universitetsky pr.28,

Atanas Dimitrov,

Technical University of Sofia, Bulgaria
Faculty of Telecommunication, TU-Sofia, "Kl.Ohridsky" str. 8, 1000 Sofia, Bulgaria

Abstract

It's well known that mathematical description of magnetic field created by several non-coaxial coils is enough complicated. Therefore the calculation of magnetic induction of this magnetic field in different points is also complicated. Because of that digital methods for calculation of magnetic induction around the coils would be more user friendly. An algorithm for simulation and visualization of magnetic induction in different points of magnetic field generated by several non-coaxial coils is described in the paper. The package Para View has been used for computer calculation of magnetic induction as one convenient software. Some results of numerical experiments and the optimization by using parallel computations are given in the paper, also.

1. INTRODUCTION

Visualisation of space temporal configuration of the vectors of magnetic induction around and in the human body is very important requirement for obtaining of good results in magneto-therapy. This visualisation can be obtained using one preliminary mathematical description of space temporal configuration of the vectors of magnetic induction around and in the human body.

As first step we should use mathematical description of the vectors of magnetic induction around and in the human body in the case of magnetic field created by single coil. Then we use mathematical description of the vectors of magnetic induction around and in the human body in the case of magnetic field created by several coils with parallel axis (or/and non-parallel axis).

The basic mathematical formulas (1) and (2) for calculation of components of magnetic induction of single coil in cylindrical coordinate system are well known [1], but they are too complicated:

$$B_{\rho} = \frac{\mu_0 i}{2\pi} \frac{z}{\rho \sqrt{(R+\rho)^2 + z^2}} \left(\frac{R^2 + \rho^2 + z^2}{(R-\rho)^2 + z^2} L - K \right) \quad (1)$$

$$B_{z_{cyl}} = \frac{\mu_0 i}{2\pi} \frac{1}{\sqrt{(R+\rho)^2 + z^2}} \left(\frac{R^2 - \rho^2 - z^2}{(R-\rho)^2 + z^2} L + K \right) \quad (2)$$

Here

K and **L** are complete elliptic integrals of 1 and 2 sort as functions of **k**;

$$k^2 = \frac{4\rho R}{(R+\rho)^2 + z^2} \quad (3)$$

i - current value in the present single current loop;
R - radius of the current loop;
 $\mu_r(x, y, z, t) = const$ is relative magnetic permeability;
 ρ - radius of the circle lying in a plane;
z - this is z-coordinate of the point

As the second step we should use mathematical description of the vectors of magnetic induction around and in the human body in the case of magnetic field created by several coils. As the coordinates of any point **M** both in GCS (global coordinate system) and LCCS (local coordinate system) are uniquely determined, it is possible to choose an arbitrarily LRCS. The same coordinates ρ and **z** of **M** can be used for the transition chain GCS → LRCS → LCCS and in the case of vice versa, for the chain LCCS → LRCS → GCS the same coordinates in GCS can be obtained.

It's should to be considered that such a LRCS results in the reducing of calculations because the transition from one Cartesian coordinate system to another is coordinate shift and multiplication on a fixed transition matrix. In this way the transition and inverse transition matrix can be calculated only once for every coil.

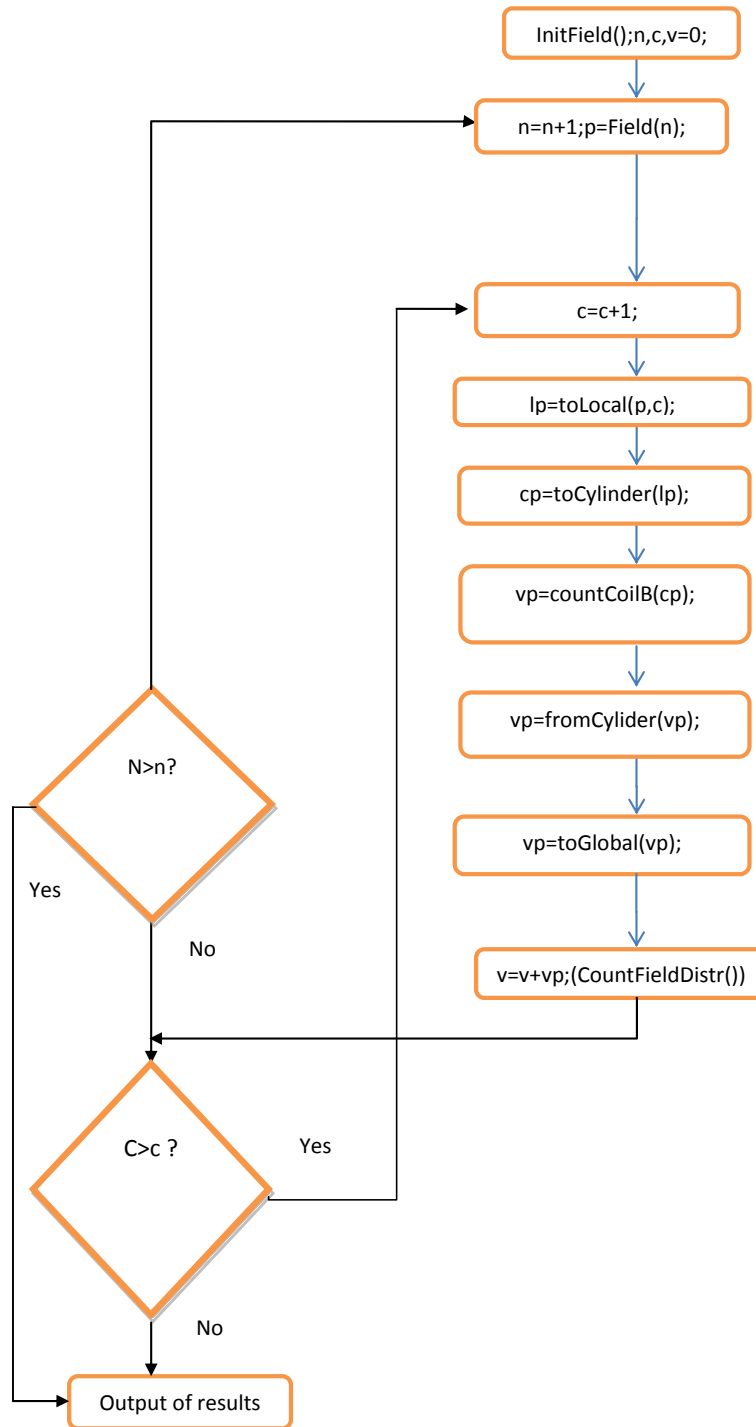


Fig. 1

The transition matrix has the form (1):

$$T = \begin{pmatrix} x1 & x2 & x3 \\ y1 & y2 & y3 \\ z1 & z2 & z3 \end{pmatrix} \quad (4)$$

Here columns are basis vectors of LRCS in the GCS basis (

$$\mathbf{O}_x=(x_1,y_1,z_1), \mathbf{O}_y=(x_2,y_2,z_2), \mathbf{O}_z=(x_3,y_3,z_3).$$

The main parts of algorithm for this calculation dur-

ing the process of transition chain GCS ->LRCS for the point *M* of the mesh are i the following:

1. Transition chain GCS->LRCS;
2. Transition chain_LRCS ->LCCS;
3. Calculation of module of magnetic induction *B*;
4. Transition chain LCCS->LRCS;
5. Transition chain LRCS->GCS;

2. ALGORITHM –PROGRAM DESCRIPTION AND SCHEME

The algorithm (Fig.1) has been implemented on Java language. To visualize results the package ParaView was used. The program contains the following classes and methods:

Main – the class that contains the method `main()`, where all the methods for calculation of magnetic field and output of results into a file *.vtk (for the following visualization by ParaView) are called.

I – contains the methods `eK()` and `eE()` to obtain interpolated values of elliptic integrals. Tabular data and finite differences are in a text file.

MainForm – contains methods for a work with the graphic interface and corresponding event handlers.

Coil – the class of coil that contains the following methods:

`Coil()` – this is the constructor of the class. It has parameters such as the direction of the coil axis, the origin of local coordinate system of the coil, current value, the number of contours etc. The coil axis is taken as Oz. When a copy of coil is created an arbitrary vector is chosen, and the vector product of the vector and Oz is taken as Ox, then vector product of Oz and Ox is taken as Oy. Basis vectors are normalized. In the copy of coil direct and inverse transformation matrix (from global to local coordinate system and inversely) are calculated and saved.

`toLocal()`– transformation from global coordinate system to the local one;

`toCylinder()`–transformation from local coordinate system to the cylindrical one;

`fromCylinder()` — transformation from cylindrical coordinate system to the local one;

`toGlobal()` —transformation from local coordinate system to the global one. The library Java3D is used.

`countLoopB()`– calculation of electromagnetic induction vector in cylindrical coordinate system for one contour of the coil;

`countCoilB()` – calculation of electromagnetic induction vector in cylindrical coordinate system for a given coil (in a given point of space) as the superposition on all the contours.

Counter – contains method `initField()` to initialize 3-dimensional array of values of electromagnetic field vectors and `countFieldDistr()` that calculates the vector of electromagnetic field for a given point as the superposition on all the coils in the configuration. (For one coil there is the method `countCoilFieldDistr()` that calculates electromagnetic induction in every point of the given array of points.)

Introduce the following notations: *Field* -the 3D array of points in which the calculation will be performed;

N – the number of points in Field;

C – the number of coils;

p – a current point of the lattice;

c – the current coil number;

lp – local coordinates of the point;

cp –cylindrical coordinates of the point;

vp – value of magnetic induction (MI) in a given point relative to the current coil;

v – the sum of vectors of magnetic induction created by all the coils in the current point.

3. OPTIMIZATION RESULTS

The magnetic induction should be calculated in many points around the coils. The number of these points depends on the resolution of computer images and the space configuration of the field of magnetic induction. It is clear that the increasing of resolution of computer images would need increasing of number of points. To optimize running time a variant of the algorithm using parallel calculations has been implemented: for every coil calculation of magnetic induction has been performed in a separate flow. The results can be seen in the Table1 and on Fig.2 and Fig.3. The time includes running time and the result file generation time.

Table 1

№	Number of coils	Number of points	Time (sec)	Optimization time (sec)
1	1	400000	21	21
2	2	400000	35	21
3	3	400000	50	24
4	4	400000	64	29
5	5	400000	78	32
6	6	400000	92	35
7	7	400000	107	55
8	8	400000	121	61
9	9	400000	135	46
10	10	400000	150	48
11	2	100000	9	6
12	2	200000	18	11
13	2	300000	26	16
14	2	400000	35	21
15	2	500000	44	26
16	2	600000	53	32
17	2	700000	61	37
18	2	800000	71	42
19	2	900000	79	47
20	2	1000000	88	57

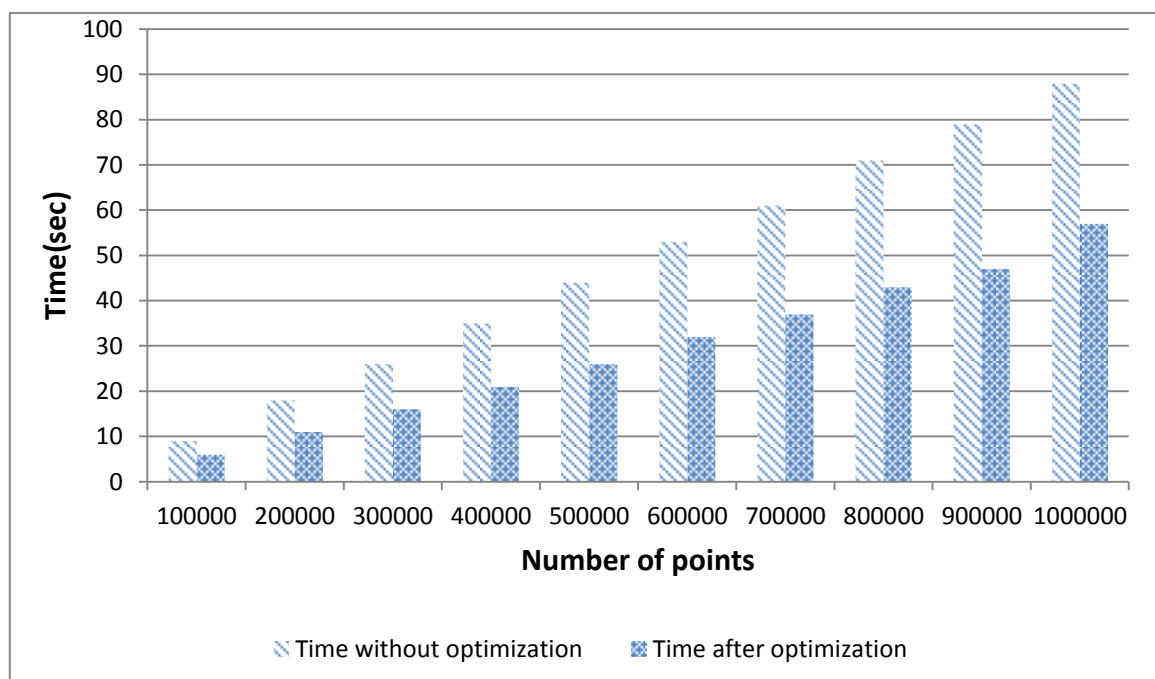


Fig. 2. Optimization results for two active coils

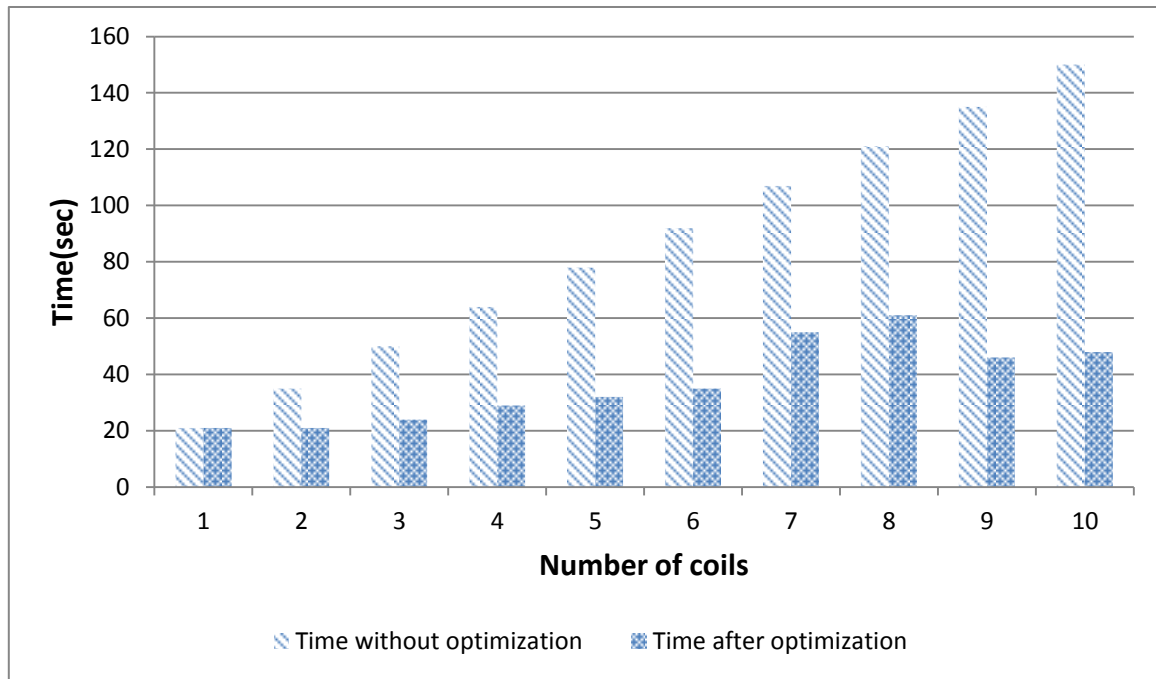


Fig. 3 Optimization results for 10 coils

4. CONCLUSION

An algorithm for calculation of the values of magnetic induction of low frequency magnetic field around and in the human body in the process has been created. Some results of optimisation of the time for calculation of space configuration of magnetic field in the patient's area are also presented. The optimisation has been done both for different numbers of coils for calculation of magnetic induction and for different number of points of the space lattice.

5. ACKNOWLEDGMENTS

The work was partially supported by the grant RFBR 13-01-00782

References

- [1] Nataly Ampilova, Dimitar Dimitrov, Bogdan Kudrin, "Mathematical investigation on calculation of magnetic induction of low frequency magnetic field in systems for magnetotherapy" Proceedings of 8th INTERNATIONAL CONFERENCE on Communications, Electromagnetics and Medical Application (CEMA'13), Sofia, 2013
- [2] Bekiarski Al., Sn. Pleshkova, Microphone Array Beamforming for Mobile Robot, The 8th WSEAS International Conference on CIRCUITS, SYSTEMS, ELECTRONICS, CONTROL & SIGNAL PROCESSING, (CSECS'09), Puerto De La Cruz, Spain, 2009, pp.146-150
- [3] Alexander Bekiarski, Snejana Pleshkova, Svetlin Antonov, "Real Time Processing and Database of Medical Thermal Images", 4rd INTERNATIONAL CONFERENCE on Communications, Electromagnetics and Medical Application (CEMA'11), Sofia, 2011, pp.101-106

COMPUTER VISUALIZATION OF LOW FREQUENCY MAGNETIC SIGNALS IN SYSTEMS FOR MAGNETOTHERAPY WITH VARIABLE PARAMETERS

B. Kudrin

St. Petersburg State University, Faculty of Math. & Mech., Postgraduate student at Comp. Sci.
Dept, 198504, SPb, Universitetsky pr.28, Russia

Atanas D. Dimitrov

Technical University of Sofia, Faculty of Telecommunication,
8, Kliment Ohridski str., 1000 Sofia, Bulgaria

Abstract

The systems for magneto-therapy often are with variable parameters. In this case both temporal parameters and space parameters of low frequency magnetic signals are variable. Therefore the space-temporal configuration of these magnetic signals is very complicated. In the same time the system for magneto- therapy can to provide many different programs for therapy of different diseases taking in account the specific status of every patient. One important requirement in the process of application of these systems is optimization of space-temporal parameters of magnetic signals for every procedure for therapy. Therefore the visualization of space configuration of magnetic signals is would be very useful for physicians.

One investigation on visualization of space configuration of the field of magnetic induction of one flexible system for magneto-therapy with variable parameters is described in the present paper.

The result of computer visualization of space configuration of the field of magnetic induction of one flexible system for magneto-therapy with variable parameters is done in the paper.

1. CONFIGURATION OF SYSTEM FOR MAGNETO-THERAPY AND TASK DESCRIPTION

A new flexible multifunctional system for magneto-therapy with variable space-temporal parameters of the field of magnetic induction in the patient's area has been designed (Fig. 1). The basic unites of this system are bed, mobile carriage, microprocessor unit and unit for providing of movement of the carriage. The coils for excitement of low frequency magnetic field are situated on the bed and on the mobile carriage. During the therapy, the human body is on coils of the bed and under the coils of the carriage. The changes of space-temporal parameters of low frequency magnetic signals in the patient's area can be provided by microprocessor's unit using special software. These changes can be provided not only by movement of carriage, but by switching of different coils of both bed and carriage, also. A cross-section of carriage of the flexible multifunctional system for magneto-therapy with variable space-temporal parameters can be seen on Fig. 2.

The scheme of the cross-section contains 6 equal coils: A1, A2, B1, B2, C1 and C2. The centers OA1

and OA2 of the coils A1 and A2 are on the small base of trapezium. The distance between their axes is 232mm. The centers OC1 and OC2 of coils C1 and C2 are on the big base of trapezium. The coils A1 and C1 and coils A2 and C2 have common axis. On the plane the sizes of trapezium are shown. The centers of the coils B1 and B2 are situated on the middles of the trapezium edges. The axes of coils B1 and B2 are perpendicular to the edges of the trapezium. The angles between axes of coils B1, B2 and the big base of the trapezium is α . This angle can be easy calculated using the sizes of trapezium. The trapezium is in the plane XOY. The origin O of 3D coordinate system is the bottom left angle of trapezium. The plane of the coil in two projections and the sizes of coil can be seen at the upper right angle of the plan.

3D coordinates (in mm) of centers of all the coils in the coordinate system X,Y,Z are:

OA1 (184, 500,0); OA2(416,500,0); OB1(50,250, 0);
OB2(550, 250,0);

OC1(184,0,0); OC2(416,0,0).

The task of present investigation is to be calculated and visualized magnetic fields created by the following pairs of coils:

1. A1 and C1.
2. A1 and C2.

3. B1 and C1.
4. A1 and B1.
5. B1 and B2.

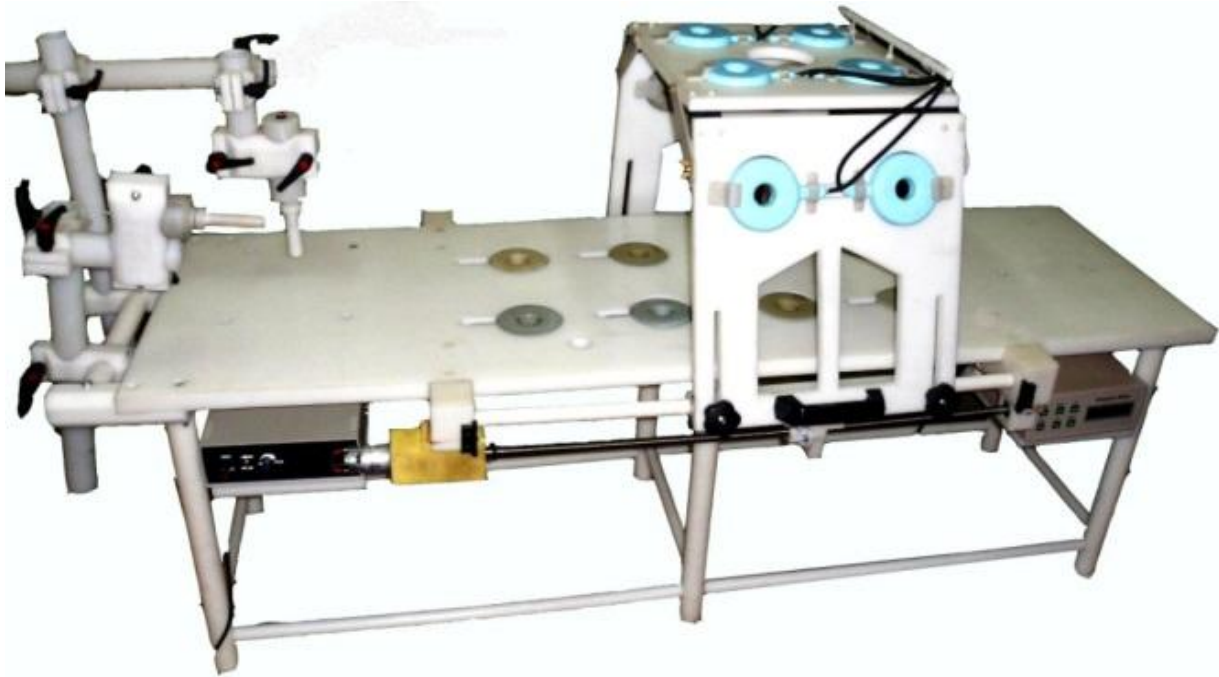


Fig.1 multifunctional system for magneto-therapy with variable space-temporal parameters

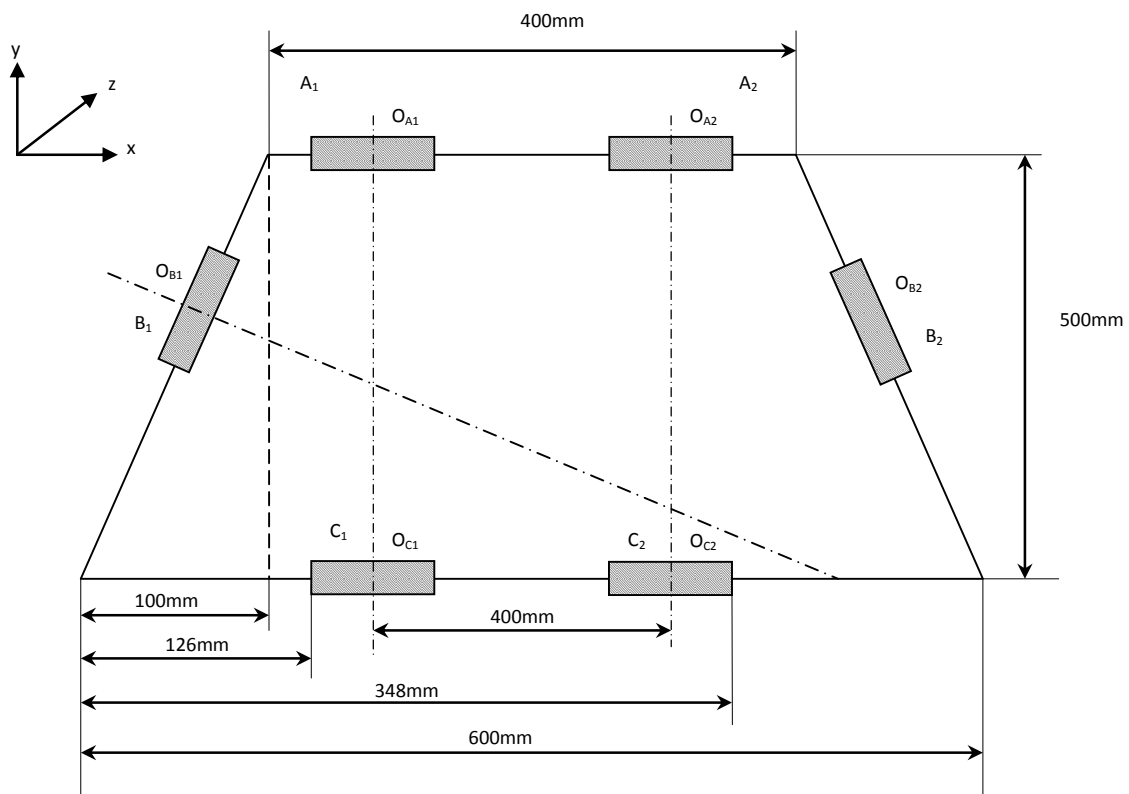


Fig. 2. A cross-section of carriage of the flexible multifunctional system for magneto-therapy

2. VISUALIZATIONS OF SPACE CONFIGURATION OF LOW FREQUENCY MAGNETIC FIELD IN THE PLANE OF CROSS-SECTION OF CARRIAGE

Usually there is an influence of low frequency magnetic field only on the part of human body during the process of therapy. Because of that often there is a movement of the mobile carriage on the bed's axis. There is an additional movement of magnetic field in the plane of cross-section of carriage of the flexible multifunctional system for magneto-therapy (Fig. 2), also. This movement of magnetic field can be provided by microprocessor's unit. In fact this is one movement (rotation) of pair of coils in the plane of cross-section of carriage around the part of human body. The basic steps of this movement of pair of coils can be provided by switching of above mentioned combinations for pairs of coils namely:

1. A1 and C1.
2. A1 and C2.
3. B1 and C1.
4. A1 and B1.
5. B1 and B2

Therefore the visualizations of space configuration of low frequency magnetic field in the plane of cross-section of carriage can be presented as separate visualizations of space configuration of low frequency magnetic field in the plane of cross-section of carriage for the above mentioned pairs of coils. These separate visualization can be obtained using appropriate mathematical methods [1] and appropriate algorithms [2]. These methods and algorithms have been used for respective combinations for pairs of coils. A computer visualization of space configuration of low frequency magnetic field of every one of above mentioned separate pair of coils A1 and C1, A1 and C2, B1 and C1, A1 and B1, B1 and B2 can be seen on the Figure 3, Figure 4, Figure 5, Figure 6 and Figure 7.

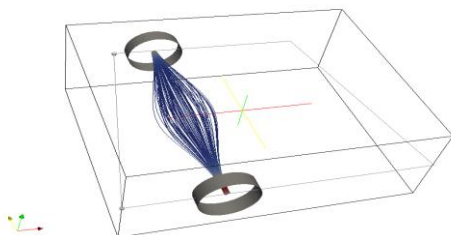


Figure 3. Space configuration of low frequency magnetic field of pair A1 and C1 in the plane of cross-section of carriage

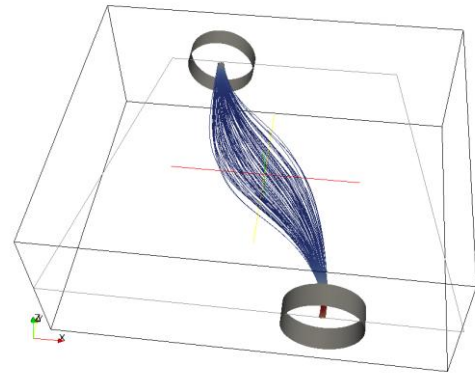


Figure 4. Space configuration of low frequency magnetic field of pair A1 and C2 in the plane of cross-section of carriage

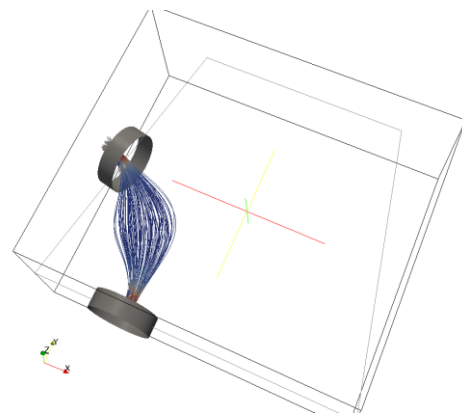


Figure 5. Space configuration of low frequency magnetic field of pair B1 and C1 in the plane of cross-section of carriage

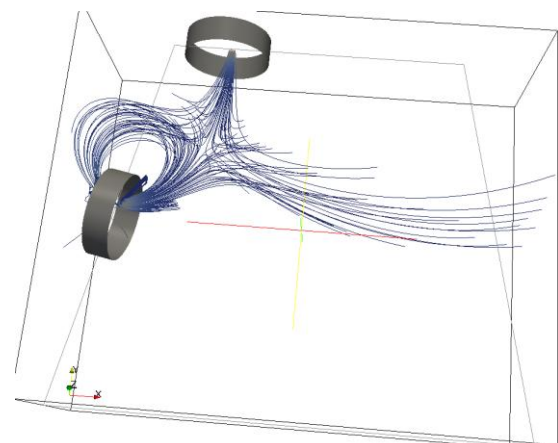


Figure 6. Space configuration of low frequency magnetic field of pair B1 and A1 in the plane of cross-section of carriage

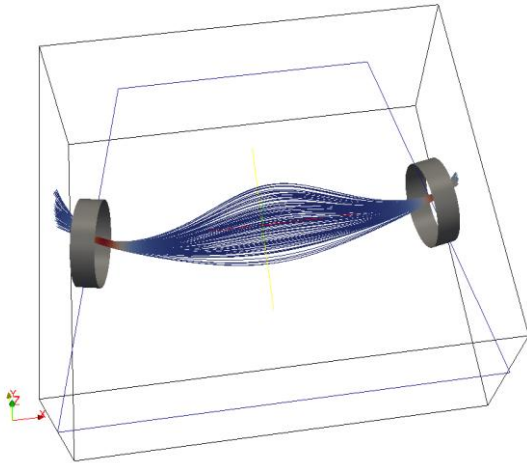


Figure 7. Space configuration of low frequency magnetic field of pair B1 and B2 in the plane of cross-section of carriage

7. CONCLUSION

One periodical change or rotation of direction of the vectors of magnetic induction in cross-section of carriage can be obtained step by step in time using switching of coils. These changes of space configuration of magnetic field can be done by appropriate software for of microprocessor's unit. Usually [3],[4] the vectors of magnetic induction and vector of blood's velocity should be orthogonal. It's clear that it would be obtained for different part of human body in cross-section of carriage by above mentioned switching of pairs of coils. This is the reason for obtaining of fast effect of therapy.

5. ACKNOWLEDGMENTS

The work was partially supported by the grant RFBR 13-01-00782

References

- [1] N. B. Ampilova, D. Dimitrov, B. Kudrin, "Mathematical investigation on calculation of magnetic induction of low frequency magnetic field in systems for magnetotherapy" 6th International Conference "Communications, Electromagnetics and MedicalApplication" (CEMA'13), Sofia, 2013, October 17-19.
- [2] B. Kudrin, A.Dimitrov, "Algorithm for visualization of low-frequency magnetic signals in systems for magnetotherapy", 6th International Conference "Communications, Electromagnetics and MedicalApplication" (CEMA'13), Sofia, 2013, October 17-19.
- [3] Bekiarski Al., Sn. Pleshkova, Microphone Array Beamforming for Mobile Robot, The 8th WSEAS International Conference on CIRCUITS, SYSTEMS, ELECTRONICS, CONTROL & SIGNALPROCESSING, (CSECS'09), Puerto De La Cruz, Spain, 2009, pp.146-150
- [4] Alexander Bekiarski, Snejana Pleshkova, Svetlin Antonov, "Real Time Processing and Database of Medical Thermal Images", 4rdINTERNATIONAL CONFERENCE on Communications, Electromagnetics and Medical Application (CEMA'11), Sofia,2011, pp.101-106

EXPERIMENTAL INVESTIGATION ON SPACE CONFIGURATION AND INFLUENCE OF ELECTROMAGNETIC FIELD OF SHORT WAVE APPARATUSES IN MEDICAL THERAPY

Antoniya P. Petrova, Dimitar Dimitrov

Faculty of Telecommunication, TU-Sofia,
Kl. Ohridsky str.8, Sofia, Bulgaria, E-Mail: tony.petrova@gmail.com

Abstract

The usage of short waves in the medical therapy started to become quite popular in the recent decades. The space-time configuration research of the electromagnetic field in the patient area within the UHF range is really important for the treatment used in physiotherapy methods. Based on the results of this study are defined the system's mode which induce the electromagnetic field in the patient area, the number of the therapeutic procedures and duration of each of them. The radiators (antennas) in the physiotherapy are often in proximity to the patient's body, i.e it is necessary to consider the impact of the body to the patient, the parameters of the antenna and to the research of the area in the near field. In this paper are presented and described in graphic form the conducted studies for electromagnetic field strength in the very near field in real clinical conditions.

At high frequencies, polarizing molecules are in the patient's body completely failed changing their spatial orientation and appear vibrations of the dipoles around neutral position. This process is related to the generation of heat. A characteristic feature of UHF waves impact on the body that the heat is produced within the body itself. In physiotherapy are used transmitters, which excited the electrical field for the induction of these frequencies. A pair of two "electrodes" usually acts as antenna system on these devices. The antenna system is ensuring the influence of the electromagnetic field of a small part of the human body.

1. INTRODUCTION

In the theory of antennas and the distribution of electromagnetic waves are defined three areas: the first area (far field) in which the angular distribution of the field is independent of the distance from the antenna and the emitted wave is spherical. The second zone is the very near radiating field (Fresnel zone) in which the angular distribution of the field depends on the distance from the antenna. In this area radiated wave, which is actually a plane wave, is gradually becoming a spherical wave. The third area is the near reactive field, which is located at a distance between 0 and $\lambda/2\pi$ from the antenna where the reactive field dominates. It is the area of interest in medical systems for the physiotherapy [4]. For an antenna with a maximum size, which is small compared to the wavelength, the energy in the very near field is mostly reactive. This stored energy is transmitted periodically from the antenna to the near field. The reactive near field extends from the antenna to a distance "R" from the antenna. The formula for calculation of this distance is:

$$R = \frac{\lambda}{2\pi} \quad (1)$$

where λ is the wavelength.

2. EXPERIMENTAL INVESTIGATION ON THE SPACE CONFIGURATION OF THE ELECTROMAGNETIC FIELD

For exploring the space-time configuration in the patient area in the measurements, a transmission frequency of the device is used, which is close to the used frequency, namely – 29.5 MHz with a wavelength 10.1 m approximately. In our case, the very near field extends at a distance $R = 1.62$ m from the antenna, considered in the formula (1).

The definition of the two components \vec{E} and \vec{H} of the electromagnetic field at the relevant points of the patient area is necessary for making the desired measurements. When determining the shape of the area of the space / the plane, which the simulation is performed, the main consideration is the reporting of the mutual position of the electrodes (antennas) of the system and its emplacement to the treatment area of the patient's body. A common case in physical therapy is the used of an apparatus with a pair of emitters. It can be seen the measured antenna system with the exact location of the disc nozzle in Figura 1. [1]

In order to facilitate and accelerate the sampling and the calculation (simplification of the algorithms based on the use of symmetry) is appropriate the

space area to be approximated by a regular geometric figure. This would be allowed using the available symmetry for optimization the developed algorithms for sampling and calculation. The used geometric figure should also cover the maximum radiating surface. If we use the formal requirement of symmetry, the suitable plane figures are rectangle, square and circle. This matches with the usual forms of radiation surfaces. In the case of a circle can be selected algorithm which completes the circle of points situated in concentric circles starting from the center. In the case of a circle can be selected algorithm which completes the circle with points, situated in concentric circles, starting from the center. [2]



Figure 1. The used antenna system with disc nozzles of each of the emitters during the study of space-time configuration of the electromagnetic field

To facilitate the measurement and interpretation of the results was used a graphical representation of the antenna system (placement of the vibrators relative to one another) in the vertical plane (Figure 2). Formally the figure can be considered as a trapezoid, which is in accordance with the usual position of the electrodes (antennas) of Figure 1. The mid-segment of the trapezoid (Figure 2) is the axis between the centers of the antennas. It is important to know the location of the vibrators, as they can be located closer or further away, the distance should be between 2 and 10 centimeters. And depending from their size and location, can determine the distribution of the field and the change of the temperature on the patient.

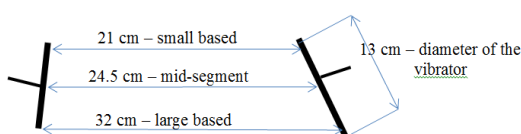


Figure 2. A graphical representation of the antenna system (position of vibrators relative to one another in the vertical plane).

3. RESULTS AND ILLUSTRATION OF THE INVESTIGATION OF THE ELECTROMAGNETIC FIELD

The measurements of the electrical intensity were made at different points in small base, large base and mid-segment on the trapezoid, and in the points of the radius of one emitter.

The measured values are in relative units, as for the electric strength and the magnetic induction. These values are related of course with the absolute values with an accuracy of one coefficient. The magnetic induction in the respective sections was calculated was calculated by the following expression:

$$\frac{E}{H} = \eta = 120\pi \approx 377\Omega \quad (2)$$

where η is the characteristic impedance. [3]

In Table 1 are given in relative units the obtained values for the electric intensity and magnetic induction in the various items of the bases and the mid-segment of the trapezoid (Figure 2) and the radius of one of the emitters in parallel placement of the measured antenna of electrical in parallel placement of the antenna in the patient area. In Table 2 are given in relative units the obtained values for the electric intensity and magnetic induction in the various items of the bases and the mid-segment of the trapezoid (Figure 2) and the radius of one of the emitters when the measured antenna measurement is perpendicular of electrical line of force.

Table 1. Relative values of the measured levels of electric intensity E and magnetic intensity H in parallel placement of the antenna in the patient area

Small base		Mid-segment		Large base		Radius	
E	H	E	H	E	H	E	H
77,1	0,204	64,1	0,17	77,3	0,205	75,5	0,2
77,8	0,206	67,4	0,179	78,3	0,208	74,5	0,198
77,7	0,205	65,7	0,174	77,8	0,206	72,5	0,192

Table 2. Relative values of the measured levels of electric intensity E and magnetic intensity H in perpendicular placement of the antenna in the patient area

Small base		Mid-segment		Large base		Radius	
E	H	E	H	E	H	E	H
78,1	0,2072	61,9	0,1642	77,6	0,2058	77,8	0,2064
78,5	0,2082	64,5	0,1711	78,2	0,2074	76,2	0,2021
78,2	0,2074	62,4	0,1655	78	0,2069	75,2	0,1994

Of Figure 3 is illustrated a screen of the spectrum analyzer for measuring the relative level of the electrical intensity. The tick is for a broadcasting frequency, together with significant harmonic of the radiation to the right of the main tick. These harmonics appear, as the apparatus is operated in the mode of the amplitude manipulation. The amplitude

manipulation is a method often used in the physiotherapy, in order to avoid the adaptation of the patient to the parameters of the influence electromagnetic field and thus to provide, if necessary, a longer course of treatment for more severe disease. The screen of the spectrum analyzer can be seen in figure 4, where is the oscillogram of the broadcasting amplitude manipulated signal.

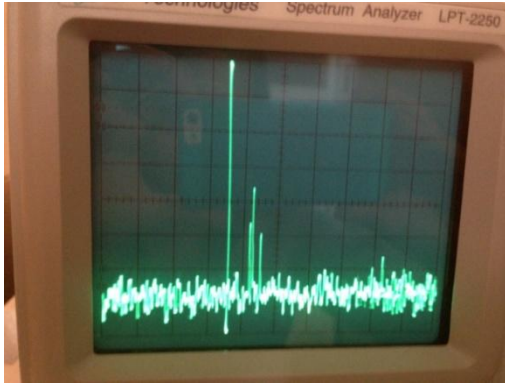


Figure 3. A screen of spectrum analyser at measurement of the relative level of electric intensity

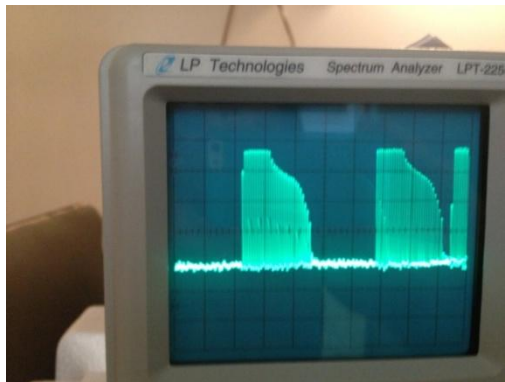


Figure 4. The oscillogram of the broadcasting amplitude manipulated signal

In graphical form are the results of the measurements are given in Table 1 and Table 2 below. The results, from the measurement of the electric intensity and the calculated values of the magnetic induction on the three bases of the trapezoid small, large and mid-segment in parallel placement of the measured antenna and the electrical line of force in the near field, are present in Figure 5 and Figure 6. Figure 7 and Figure 8 shows the results, from the measurement of the electric intensity and the calculated values of the magnetic induction on the three bases of the trapezoid small, large and mid-segment in perpendicular placement of the measured antenna and the electrical line of force in the near field. Figure 9 and Figure 10 shows the results, from the measurement of the electric intensity and the calculated values of the magnetic induction on the three bases of the trapezoid small, large and

mid-segment in parallel and perpendicular placement of the measured antenna and the electrical line of force in the near field. The functions shown in the figure from 5 to 10 were obtained as discrete values in the result of the measurements of the electrical intensity in a finite number of points. If the obtained discrete values of the functions are connect with the segment, could be regarded that the made a simple interpolation, so that they can take into account the relative values of the variables and between points of measurements. This is shown by points 1 and 2 on the charts. In mathematics certainly has quite analytical methods for interpolation, which may be used in the requirement for greater accuracy in the interpolation.

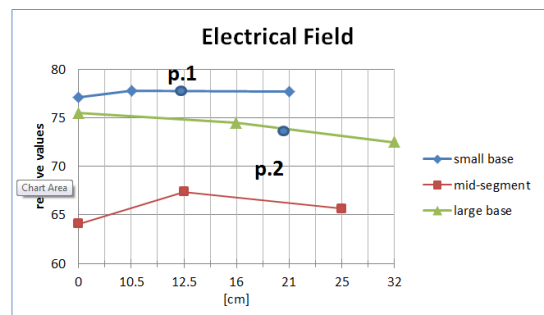


Figure 5. Relative values of the electrical intensity of the three axes: small, mid and large segment in parallel placement of the measured antenna

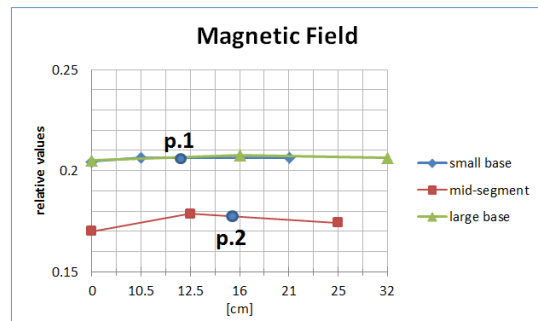


Figure 6. Relative values of the magnetic induction of the three axes: small, mid and large segment in parallel placement of the measured antenna

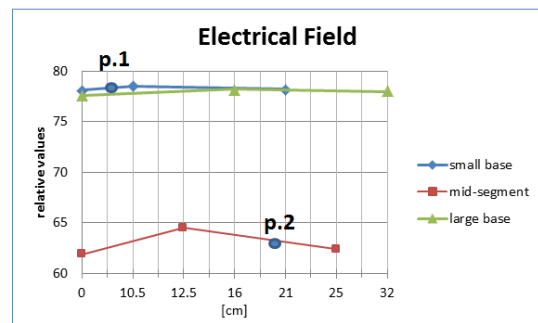


Figure 7. Relative values of the electrical intensity of the three axes: small, mid and large segment in perpendicular placement of the measured antenna

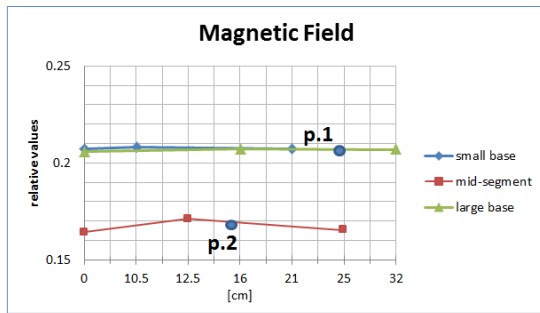


Figure 8. Relative values of the magnetic induction of the three axes: small, mid and large segment in perpendicular placement of the measured antenna

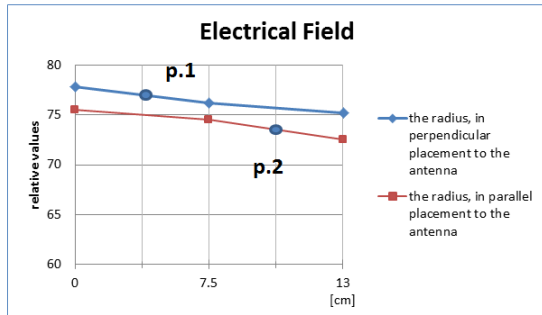


Figure 9. Relative values of the electrical intensity at the radius in parallel and perpendicular to the measured antenna

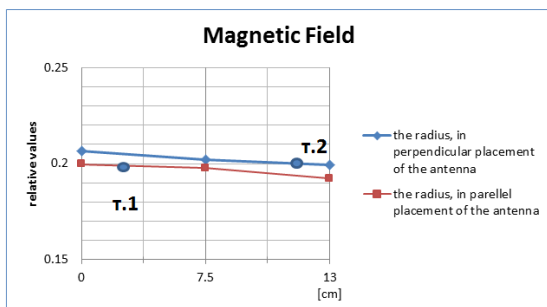


Figure 10. Relative values of the magnetic induction at the radius in parallel and perpendicular to the measured antenna

Experimental measurements of the strength of the electric field in the very near field in actual clinical conditions were made in the conventional mode, used in the course of therapy, namely, continuous transmission mode and a mode of amplitude manipulation of the electromagnetic field.

4. CONCLUSION

In conclusion we can say that the study of the characteristics of electromagnetic field in the nearby area along with the study and optimization of the space-time configuration of the electromagnetic field are very important and crucial for achieving the desired therapeutic effect. These waves have similar physiological action with the other high frequencies currents, but they penetrate to greater depths. Ultra-high frequency waves have a good therapeutic effect in: transient disorders of cerebral circulation, stroke, vascular incidents in the central nervous system, chronic arterial insufficiency of lower extremities. Improves microcirculation, rheological properties of blood, detection of shunting, increased cell permeability.

References

- [1] D. Dimitrov, Medical systems for influence of electromagnetic fields on human, education book, TU-Sofia, 2007
- [2] W. Y. Riadh, "Electromagnetic Fields and Radiation (Human Bioeffects and Safety)", Marcel Dekker Inc. Canada, 2001, ISBN 0-8247-0877-3
- [3] S. Laybros and P. F. Combes, "On Radiating Zone Boundaries of Short, $\lambda/2$ and λ Dipoles", IEEE Antennas and Propagation Magazine, 45, 5, October 2004, pp. 53-64.
- [4] Boyadzhiev S., Lazarova V., Rassovska M., Yordanova I., Yordanov R, Comparison between RF and DC Magnetron Reactive Sputtered Molybdenum Oxide Thin Films for Gas sensors, Journal of Optoelectronics and Advanced Materials – Rapid Communications (OAM-RC), Vol. 4, ISS. 10, October 2010, pp. 1485 – 1488, ISSN: 1842-6573.

STRUCTURAL ENTROPY BASED PROCESSING OF COLORECTAL POLYP IMAGES

András Fehér, Ádám Békefi, Szilvia Nagy

Széchenyi István University
Egyetem tér 1, H-9026 Győr, Hungary
T. +36 96 613 693; F. +36 96 613 694; E. nagysz@sze.hu.

Abstract

The colorectal tumors are the third or fourth most common cancers in the world, and colonoscopy or virtual colonoscopy are the methods for diagnosing this illness. Most of the colorectal polyps are not malignant and do not have the potential to develop into an adenoma, thus taking samples of these polyps and biopsy of these tissue samples are unrequired inconvenience for the patients and unnecessary cost for the medical institutions. Usually a specialist of gastroenterology can distinguish the potentially malignant polyps from the benign ones by visual diagnosis, as the topologies are different.

The Rényi entropies based structural analysis is a method for characterizing the topologies of any kind of distribution. It is mostly used in solid state physics. With some examples we show, that the structural entropy can be capable of distinguishing polyps, thus determining the localization type of the polyp can help to draw the attention of the gastroenterologist to a possibly malignant polyp, or later be a characterizing quantity in genetic or neural network-based algorithms.

1. INTRODUCTION

During colonoscopy a CCD or fiber optic camera, which is placed to the end of a flexible tube, takes live images about the wall of the large bowel. Besides optical visual diagnosis it is also possible to take tissue samples for biopsy and remove malignant polyps.

Unfortunately, the images got from colonoscopy are not of very good quality, as the inflated bowel moves continuously, the light-source reflects from the wet surfaces and the lining of the bowel and the polyps are shades of pink colour. Narrow band imaging (NBI) can increase the contrast between veins and the other tissues, and spraying of blue paint - chromoendoscopy - can enhance the topological unevenness [1], as it can be seen in Figure 1.

Colorectal polyps have more types, and only biopsy can decide the true class of the polyp, but usually morphological characteristics give a very good initial guess [2]. Besides Colonoscopy capsular colonoscopy is also used [3], during these takes, the live video pictures are usually necessary in order to get distance and size information, from single pictures these informations can not be taken, thus any image processing applied during this diagnostic method should be live or last not longer than a couple of seconds.



Figure 1. White-light, narrow-band imaging and chromoendoscopy pictures of a patient's colon. Picture taken at the Petz Aladár Hospital Győr.

2. STRUCTURAL ENTROPY AND LOCALIZATION

The structural entropy-filling factor based localisation measure was developed by Pipek and Varga [4] for characterizing quantum mechanical electron density distributions [5-7].

The most straightforward method for introducing structural entropy is the following. The n th Rényi entropies

$$S_n = \frac{1}{1-n} \ln \left(\sum_{i=1}^N I_i^n \right). \quad (1)$$

of a distribution $\{I_i | i = 1, \dots, N\}$ are the generalizations of the Shannon entropy

$$S = - \sum_{i=1}^N I_i \ln I_i. \quad (2)$$

The distribution should fulfil the properties of a probability distribution

$$I_i \geq 0 \quad \text{for } i = 1, \dots, N, \quad (3)$$

$$\sum_{i=1}^N I_i = 1, \quad (4)$$

thus if images are studied, the quantities I_i is the - according to Eq. (4) - normalized pixel intensity corresponding to the i th pixel.

The differences of various level Rényi entropies characterize the structure of the distribution. The quantity

$$S_{str} = S_1 - S_2 \quad (5)$$

is the structural entropy, it consists of two parts, the S Shannon entropy gives the general disorder in the studied image, whereas the second Rényi entropy gives the entropy of a system that has a two-valued distribution and the same square-norm as the original system. This results that the structural entropy of two-coloured systems is zero. The difference of the second and zeroth Rényi entropy

$$-\ln q = S_0 - S_2 \quad (6)$$

is also needed for proper characterisation of the structure: images with e.g. an overall Gaussian or exponentially decreasing characteristic are situated on a given line at the $S_{str}(S_2-S_0)$ plot. Each type of decreasing has different lines. The variable q is known in solid states physics as the filling factor. These $S_{str}(\ln q)$ maps are used also for characterising scanning microscope images and separating superstructures in these pictures [8, 9].

Note, that this type of localization study does not take into account the position of the pixels, just their intensity values, so an image with one large (e.g. Gaussian) structure can have the same dot on the $S_{str}(\ln q)$ map as an image with several smaller structures.

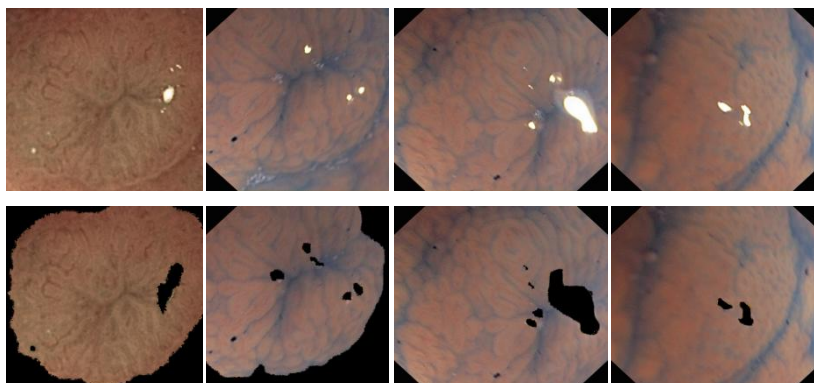
3. SAMPLES

The images were taken at the local hospital from two patients. Both patients were on a control examination after removal of pre-malign or malign polyps. The polyps were photographed in the colon with various zoom options, by white-light and NBI, with and without paint liquid, as it can be seen in Fig. 1.

From the images the polyps were cut out and a solid black colour was used to mask out the background bowel tissue, the bubbles and the light reflections. No other image processing method was carried out, except for the normalizing according to (4).

4. RESULTS

The sample images are shown in Fig. 2. Both the masked and the unmasked images were studied, in all the three colour channels. Note, that the bowel tissue is visible only on a very small part of the image, and it is approximately of uniform colour.



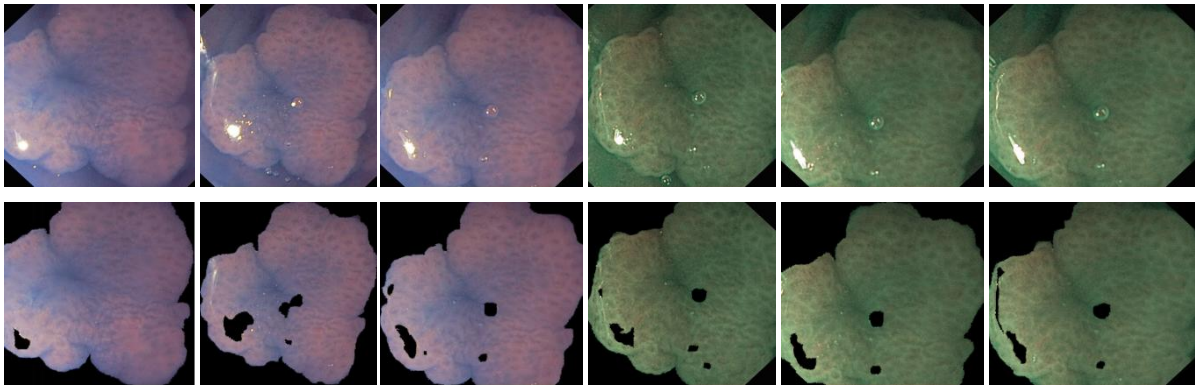


Figure 2. Endoscopy pictures of two patient's colonic polyps. The picture numbers are in the upper row *s1i15* (white light image), *s1i22*, *s1i24* and *s1i28* (dyed white-light images), in the lower row *s2i12*, *s2i17*, *s2i19* (dyed white-light images), *s2i23*, *s2i24* and *s2i25* (NBI images). Pictures taken at the Petz Aladár Hospital Győr.

4.1. Localization type of the images

The structural entropy vs. filling factor images can be seen in Fig. 3.

In case of the white-light image *s1i15*, the red channel gives practically no information about the localization type of the image probably because of the very low variation of the intensity, thus very small localization factor. The blue and green channels are more informative. In case of the dyed images the two types of polyps can be distinguished, the first has a more slope localisation - it fits to a lower line on the $S_{str}(S_2-S_0)$ map - than the second,

especially in the blue and green images, both in the background masked and the non masked cases. The NBI positions the image to a more favourable part of the $S_{str}(S_2-S_0)$ map, where the tendencies are more distinguishable, so it seems to be the ideal candidate for basis of structural entropy calculations.

All the calculations were carried out in Matlab environment and the calculation time is for the 20 images was less than 3 seconds on a 2.27 GHz processor with a code including the plotting.

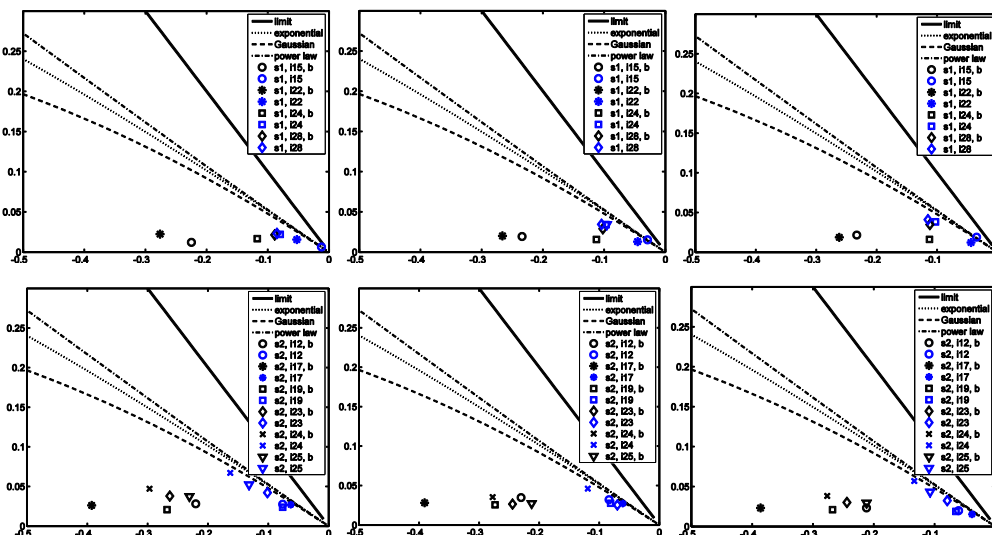


Figure 3. Structural entropy S_{str} vs. the filling factor S_0-S_2 maps of the images from Fig. 2. The results for one set of images (*s1* and *s2*) are plotted into the same row, the three colour channels *r*, *g*, and *b* are in the first, second and third column subplots. The blue markers indicate the original images, the black markers the masked ones.

5. CONCLUSION

Localization types of the studied colonic polyp images are slower than Gaussian. The different colour channels of the images give different information, thus it is worth to keep all the three channels for

calculations. Usually the NBI images are the best candidates for further processing, especially in the blue and red colour channels. Preprocessing of the images significantly alter the localization type of the image, and increases the calculation time.

As the calculation time is significantly less than the time needed for taking a still image from the live colonoscopic feed, and it has a possibility to distinguish polyp types, the method seems to be a good candidate for helping the medical staff.

6. ACKNOWLEDGMENTS

The authors gratefully thank Professor István Rácz and his group at the Division of Gastroenterology at the Petz Aladár County Educational Hospital for the guidance and the images. Fruitful discussions with Professor Zoltán Horváth and his co-workers from the Széchenyi University are also gratefully acknowledged.

References

- [1] J. J. W. Tischendorf, H. E. Wasmuth, A. Koch, H. Hecker, C. Trautwein, and R. Winograd, "Value of magnifying chromoendoscopy and narrow band imaging (NBI) in classifying colorectal polyps: a prospective controlled study", *Endoscopy*, Volume 39, Thieme, Stuttgart-New York, 2007, pp. 1092-1096.
- [2] J. R. Jass, "Classification of colorectal cancer based on correlation of clinical, morphological and molecular features", *Histopathology*, Volume 50, Wiley, 2006, pp. 113-130.
- [3] I. Rácz, M. Jánoki, and H. Saleh, "Colon Cancer Detection by 'Rendezvous Colonoscopy': Successful Removal of Stuck Colon Capsule by Conventional Colonoscopy", *Case Rep. Gastroenterol.*, Volume 4, Karger, 2010, pp. 19-24.
- [4] J. Pipek and I. Varga, "Universal classification scheme for the spatial localization properties of one-particle states in finite d -dimensional systems", *Phys. Rev. A*, Volume 46, APS, Ridge NY-Washington DC, 1992, pp. 3148-3164.
- [5] J. Pipek and I. Varga, "Scaling behavior of energy functionals of highly complex distributions", *Int. J. Quantum Chem.*, Volume 70, Wiley, 1998, pp. 125-131.
- [6] I. Varga and J. Pipek, "Rényi entropies characterizing the shape and the extension of the phase space representation of quantum wave functions in disordered systems", *Phys. Rev. E*, Volume 68, APS, Ridge NY-Washington DC, 2003, 026202.
- [7] I. Varga, E. Hofstetter, and J. Pipek, "One-parameter Superscaling at the Metal-Insulator Transition in Three Dimensions", *Phys. Rev. Lett.*, Volume 82, APS, Ridge NY-Washington DC, 1999, 4683-4686.
- [8] L. M. Molnár, Sz. Nagy, and I. Mojzes, "Structural entropy in detecting background patterns of AFM images", *Vacuum*, Volume 84, Elsevier, Amsterdam, 2010, pp. 179-183.
- [9] A. Bonyár, L. M. Molnár, G. Harsányi, "Localization factor: a new parameter for the quantitative characterization of surface structure with atomic force microscopy (AFM)", *MICRON*, Volume 43, Elsevier, Amsterdam, 2012, pp. 305-310.

R – radius of the current loop

O – center of the current loop and the beginning of the cylindrical coordinate system;

M – arbitrary point, in which is calculated the magnetic induction

m – projection of the point M in the plane of current loop;

O_1 – center of the circle lying in a plane parallel to the plane of the current loop and passing through the point M ;

ρ – radius of the circle lying in a plane

parallel to the plane of the current loop and passing through the point M ; dl - elementar segment of the current loop; елементарен участък от токовия контур;

2α – angle between two symmetrical parts of the elementary current loop

r – distance from any of the two basic parts of the current loop to the point M ;

Every coil has its own coordinate system (local). The system from several coils is considered in a global coordinate system. For an arbitrary point of the area the magnetic field in this point is obtained as the sum of magnetic fields concerning to every coil. To calculate the magnetic field in the point concerning to a coil it's necessary to be defined the point's coordinates in a local coordinate system of the chosen coil. The next step should be calculation of magnetic induction magnetic field in this local system. Then should be transformation of result of calculation in local coordinat system to the global system. The calculation of magnetic induction in local coordinat system is described in [1].

Visualization of results f calculation can be performed using ParaView package.

2. CALCULATION OF MAGNETIC FIELD FOR SEVERAL COILS

The calculation of total magnetic field for several coils is performed in the area bounded by a rectangular parallelepiped. The area is divided on cells with the same size, which are also rectangular parallelepipeds. The calculation is performed in the nodes of the constructed mesh. The origin of global coordinate system (GCS) is supposed to be in the left bottom angle of the area (Fig.2).

The position of every coil is defined by the coordinates of intersection point of the coil axis (z_{loc}) with the bottom base of the coil and the coordinates of z_{loc} vector. Coils may be located both inside the area and outside it. Magnetic field values are calculated only inside the area. The direction of the coil axis is defined in accordance with the direction of current.

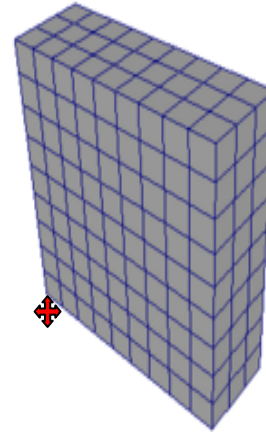


Fig.2

In the local cylindrical coordinate system (LCCS) of coil the coordinates of the point M are ρ (the distance from M to the coil axis) and z (the distance to the coil base plane). Hence, for fixed coil the coordinates of point M in LCCS are uniquely determined. For every coil a local rectangular coordinate system (LRCS) with 3 mutually orthogonal basis vectors ($z_{loc}, x_{loc}, y_{loc}$) has been used, where x_{loc}, y_{loc} are mutually orthogonal and lie in the coil's base plane.

As the coordinates of any point M both in GCS and LCCS are uniquely determined, it's possible to be choosed an arbitrarily LRCS. The same coordinates ρ and z of M can be used for the transition chain GCS \rightarrow LRCS \rightarrow LCCS and in the case of vice versa, for the chain LCCS \rightarrow LRCS \rightarrow GCS the same coordinates in GCS can be obtained.

It's possible to be considered that such a LCRS to reduce calculations – the transition from one Cartesian coordinate system to another is coordinate shift and multiplication on a fixed transition matrix. In this way the transition and inverse transition matrix can be calculated only once for every coil.

The transition matrix has the form (1):

$$T = \begin{matrix} x1 & x2 & x3 \\ y1 & y2 & y3 \\ z1 & z2 & z3 \end{matrix} \quad (1)$$

Where columns are basis vectors of LRCS in the GCS basis $\mathbf{O}_x=(x_1, y_1, z_1)$, $\mathbf{O}_y=(x_2, y_2, z_2)$, $\mathbf{O}_z=(x_3, y_3, z_3)$.

In going from LRCS to LCCS and inversely the coordinate on z axis does not change, coordinates m_x and m_y are transformed in m and inversely: vector B_ρ is decomposed on the basis (m_x, m_y) .

It's clear that before the calculation of magnetic induction \mathbf{B} in the point \mathbf{M} one preliminary transition chain GCS \rightarrow LRCS should be provided. The algorithm for this calculation during the process of transition chain GCS \rightarrow LRCS for the point \mathbf{M} of the mesh (Fig.2) is the following:

1. TRANSITION CHAIN

GCS \rightarrow LRCS

In the case when the global coordinates of an arbitrary point be \mathbf{M} are (x_M, y_M, z_M) , the basis vectors LRCS in GCS are $\mathbf{v}_1 = (x_1, y_1, z_1)$, $\mathbf{v}_2 = (x_2, y_2, z_2)$, $\mathbf{v}_3 = (x_3, y_3, z_3)$, the origin of LRCS is point $\mathbf{O}(x_0, y_0, z_0)$. The vector of coordinates of point \mathbf{M} in LRCS can be determined, using the following equation:

$$(\mathbf{m}_x, \mathbf{m}_y, \mathbf{m}_z)^T = \mathbf{T}(\mathbf{M} - \mathbf{O}) \quad (2)$$

Where:

\mathbf{M} and \mathbf{O} are radius vectors of corresponding points; \mathbf{m} is the projection of the point \mathbf{M} on the base plane of the coil;

2. TRANSITION CHAIN

LRCS \rightarrow LCCS

The radius ρ of the circle lying in a plane can be calculated using the equation (3):

$$\rho = \sqrt{m_x^2 + m_y^2} = m_z \quad (3)$$

3. CALCULATION OF MAGNETIC INDUCTION \mathbf{B}

The vector of magnetic induction \mathbf{B} in the point \mathbf{M} has two components, taking in account Fig.1. These components can be calculated in LCCS according to [1]:

$$B_\rho = \frac{\mu_0 i}{2\pi} \frac{z}{\rho \sqrt{(R+\rho)^2 + z^2}} \left(\frac{R^2 + \rho^2 + z^2}{(R-\rho)^2 + z^2} L - K \right) \quad (4)$$

$$B_{z_{cyl}} = \frac{\mu_0 i}{2\pi} \frac{1}{\sqrt{(R+\rho)^2 + z^2}} \left(\frac{R^2 - \rho^2 - z^2}{(R-\rho)^2 + z^2} L + K \right) \quad (5)$$

In equations (4) and (5) K and L are complete elliptic integrals of 1 and 2 sort as functions of k .

Where:

$$k^2 = \frac{4\rho R}{(R+\rho)^2 + z^2} \quad (6)$$

It's well known [1] that the equation (1) can be taken in account for the air environment and approximately for the alive tissues, also. Therefore the total value of magnetic induction \mathbf{B} in every point in the case of several coils can be calculated as sum of partial values of magnetic induction in the same point, created by respective coils.

The above mentioned calculations of the value of vector of magnetic induction can be used for every point, but often it would be too difficult because of long time for computer calculation [3],[4]. Because of that, some times the values of magnetic induction can be calculated for limited number of points using equations (4), (5) and (6), which are very complicated. Then the values of magnetic induction for every additional point can be obtained using more simple approximately method for calculation, using the results of preliminary exact calculations. In the process of approximately method a simple linear interpolations can be used.

The table values of magnetic induction in the additional points and values of limited differences (first order) can be obtained for instance from [2].

4. TRANSITION CHAIN

LCCS \rightarrow LRCS

$$B_{z_{loc}} = B_{z_{cyl}} \quad (7)$$

$$B_{x_{loc}} = B_\rho \times \frac{m_x}{\sqrt{m_x^2 + m_y^2}} \quad (8)$$

$$B_{y_{loc}} = B_\rho \times \frac{m_y}{\sqrt{m_x^2 + m_y^2}} \quad (9)$$

$$\mathbf{B}_{loc} = (B_{x_{loc}}, B_{y_{loc}}, B_{z_{loc}}) \quad (10)$$

5. TRANSITION CHAIN LRCS \rightarrow GCS

$$\mathbf{B}_{glob} = \mathbf{T}^{-1} \mathbf{B}_{loc} \quad (11)$$

The calculations 1-5 are should be repeated for the value of magnetic induction of every coil. As it has been above mentioned the total value of magnetic induction in point \mathbf{M} can be obtained as the sum of partial values of magnetic inductions of respective

coils. This procedure should be performed for all the points of the mesh and the results can be saved in 3-dimension array and written in a file *.vtk for visualization in ParaView package.

7. CONCLUSION

A mathematical investigation on methods for calculation of the value of magnetic induction of low frequency magnetic field created by several coils in one point is described in the present paper. This is typical situation for the modern systems for magneto-therapy. Usually there is an influence of magnetic magnetic field created by several coils on the human body. The axis of these coils can be parallel or not parallel. Usually the system for magneto-therapy contain one microprocessor unit, which can switch different coils according to the special software during the process of therapy. The number of "active" coils and their space dispositions are different in every moment. This configuration is determined by microprocessor's unit in every moment. Therefore the results of investigations in the present paper would be useful not only for physicians for optimisation of process of therapy, but for engineers in the process of design of systems for magneto-therapy, also.

Acknowledgements

The work was partially supported by the grant RFBR 13-01-00782.

References

- [1] D. Dimitrov. Medical Systems for Influence of Electromagnetic Field on the Human Body (in Bulgarian), Sophia, Technical University, 2008.
- [2] Е. Ямке, Ф. Эмде, Ф. Леш. Специальные функции. Москва, изд. Наука, 1964.
- [3] Bekiarski Al., Sn. Pleshkova, Microphone Array Beamforming for Mobile Robot, The 8th WSEAS International-Conference on CIRCUITS, SYSTEMS, ELECTRONICS, CONTROL & SIGNALPROCESSING, (CSECS'09), Puerto De La Cruz, Spain, 2009, pp.146-150
- [4] Alexander Bekiarski, Snejana Pleshkova, Svetlin Antonov, "Real Time Processing and Database of Medical Thermal Images", 4rd INTERNATIONAL CONFERENCE on Communications, Electromagnetics and Medical Application (CEMA'11), Sofia, 2011, pp.101-106

A NOVEL CLOSED – FORM ANALYTICAL SOLUTION TO THE RADIATION PROBLEM FROM A VERTICAL SHORT DIPOLE ANTENNA ABOVE FLAT GROUND USING SPECTRAL DOMAIN APPROACH

S. Sautbekov**, P. Frangos* Ch. Christakis* and K. Ioannidi*

*School of Electrical and Computer Engineering,
National Technical University of Athens,
9, Iroon Polytechniou Str., 157 73 Zografou, Athens, Greece
Tel. +30 210 772 3694, Fax. +30 210 772 2281, E-mail: pfrangos@central.ntua.gr

**Eurasian National University, 5, Munaitpassov Str., Astana, Kazakhshtan, E-mail : sautbek@mail.ru

Abstract

In this paper we consider the problem of radiation from a vertical short (Hertzian) dipole above flat ground with losses, which represents the well – known in the literature ‘Sommerfeld radiation problem’. We end - up with a closed – form analytical solution to the above problem for the received electric and magnetic field vectors above the ground in the far field area. The method of solution is formulated in the spectral domain, and by inverse three – dimensional Fourier transformation and subsequent application of the Stationary Phase Method (SPM) the final solutions in the physical space are derived. To our knowledge, the above closed – form solutions are novel in the literature for the Sommerfeld radiation problem. Finally, preliminary numerical results showing comparison of our derived new analytical solutions for the EM field scattered from the ground and corresponding EM field based on K. A. Norton’s approximate solution [3] are provided in this paper.

1. INTRODUCTION

The so - called ‘Sommerfeld radiation problem’ is a well – known problem in the area of propagation of electromagnetic (EM) waves above flat lossy ground for obvious applications in the area of wireless telecommunications [1,2]. The classical Sommerfeld solution to this problem is provided in the physical space by using the so- called ‘Hertz potentials’ and it does not end – up with closed form analytical solutions. K. A. Norton [3] concentrated in subsequent years more in the engineering application of the above problem with obvious application to wireless telecommunications, and he provided approximate solutions to the above problem, which are represented by rather long algebraic expressions for engineering use, in which the so – called ‘attenuation coefficient’ for the propagating surface wave plays an important role.

In this paper the authors take advantage of previous research work of them for the EM radiation problem in free space [4] by using the spectral domain approach.

Furthermore, in Ref. [5] the authors provided the fundamental formulation for the problem considered here, that is the solution in spectral domain for the radiation from a dipole moment at a specific angular

frequency (ω) in isotropic media with a flat infinite interface. At that paper, the authors end – up with integral representations for the received electric and magnetic fields above or below the interface [Line of Site (LOS) plus reflected field – transmitted fields, respectively], where the integration takes place over the radial spectral coordinate k_ρ . Then, in the present paper the authors concentrate to the solution of the classical ‘Sommerfeld radiation problem’ described above, where the radiation from a vertical dipole moment at angular frequency ω takes place above flat lossy ground [this is equivalent to the radiation of a vertical small (Hertzian) dipole antenna above the flat lossy ground]. By using the Stationary Phase Method (SPM method [6]) integration over the radial spectral coordinate k_ρ is performed and novel, to our knowledge, closed – form analytical solutions for the received electric and magnetic fields in the far field zone (where SPM method is applicable) are derived. Finally, physical interpretation of these novel closed – form analytical expressions are provided in Ref. [7], where a variant version of the present paper of ours can be found.

2. PROBLEM GEOMETRY

The geometry of the problem is given in Fig. 1. Here a Hertzian (small) dipole with dipole moment p directed parallel to positive x – axis, at altitude x_0 above the infinite, flat and lossy ground, radiates time – harmonic electromagnetic (EM) waves at angular frequency $\omega=2\pi f$ [exp(-i ωt) time dependence is assumed in this paper]. Here the relative complex permittivity of the ground (medium 2) is $\epsilon'_r = \epsilon'/\epsilon_0 = \epsilon_r + ix$, where $x = \sigma/\omega\epsilon_0 = 18 \times 10^9 \sigma/f$, σ being the ground conductivity, f the frequency of radiation and $\epsilon_0 = 8.854 \times 10^{-12}$ F/m is the absolute permittivity in vacuum or air. Then the wavenumbers of propagation of EM waves in air and lossy ground, respectively, are given by the following equations :

$$k_{01} = \omega / c_1 = \omega \sqrt{\epsilon_1 \mu_1} = \omega \sqrt{\epsilon_0 \mu_0} \quad (1)$$

$$k_{02} = \omega / c_2 = \omega \sqrt{\epsilon_2 \mu_2} = k_{01} \sqrt{\epsilon_r + ix} \quad (2)$$

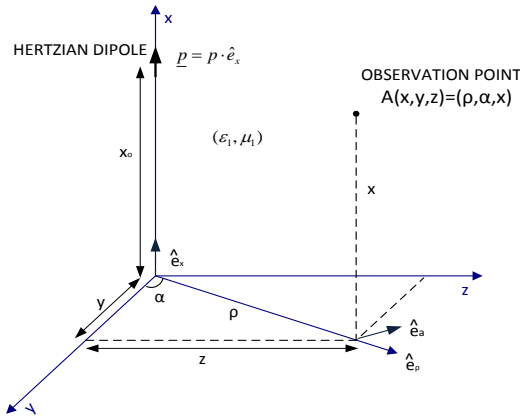


Figure 1. Geometry of the problem

3. ANALYTICAL CLOSED – FORM EXPRESSIONS FOR THE SCATTERED EM FIELDS OBTAINED THROUGH THE APPLICATION OF THE STATIONARY PHASE METHOD (SPM)

Following [5], [7], [8], and by using the Stationary Phase Method (SPM) [6,7], we finally end - up with the following expressions for the reflected fields (in the higher half - space, $x>0$), as given below :

$$\underline{E}_{x>0} = \underline{E}^{LOS} - \frac{ip}{8\pi\epsilon_o\epsilon_{r1}} \underline{I}_1 \cdot \hat{e}_\rho - \frac{ip}{8\pi\epsilon_o\epsilon_{r1}} \underline{I}_2 \cdot \hat{e}_x \quad (3)$$

$$\underline{H}_{x>0} = \underline{H}^{LOS} - \frac{i\omega p}{8\pi} \underline{I}_3 \cdot \hat{e}_\alpha \quad (4)$$

where

$$I_1 = \frac{i2}{k_{01}\rho^{1/2}} \frac{1}{(x+x_0)^{1/2}} \kappa_{1s}^{3/2} k_{\rho s}^{3/2} \cdot \quad (5)$$

$$\frac{\epsilon_2 \kappa_{1s} - \epsilon_1 \kappa_{2s}}{\epsilon_2 \kappa_{1s} + \epsilon_1 \kappa_{2s}} e^{ik_{\rho s}\rho} e^{i\kappa_{1s}(x+x_0)}$$

$$I_2 = \frac{i2}{k_{01}\rho^{1/2}} \frac{1}{(x+x_0)^{1/2}} \kappa_{1s}^{1/2} k_{\rho s}^{5/2} \cdot \quad (6)$$

$$\frac{\epsilon_2 \kappa_{1s} - \epsilon_1 \kappa_{2s}}{\epsilon_2 \kappa_{1s} + \epsilon_1 \kappa_{2s}} e^{ik_{\rho s}\rho} e^{i\kappa_{1s}(x+x_0)}$$

$$I_3 = \frac{i2}{k_{01}\rho^{1/2}} \frac{1}{(x+x_0)^{1/2}} \kappa_{1s}^{1/2} k_{\rho s}^{3/2} \cdot \quad (7)$$

$$\frac{\epsilon_2 \kappa_{1s} - \epsilon_1 \kappa_{2s}}{\epsilon_2 \kappa_{1s} + \epsilon_1 \kappa_{2s}} e^{ik_{\rho s}\rho} e^{i\kappa_{1s}(x+x_0)}$$

and

$$k_{\rho s} = \frac{k_{01}\rho}{\left[(x+x_0)^2 + \rho^2\right]^{1/2}} = \quad (8)$$

$$= k_{01} \frac{1}{\left[1 + \left(\frac{x+x_0}{\rho}\right)^2\right]^{1/2}} = k_{01} \cos \phi$$

is the (unique) stationary point [7], while ϕ is the angle defined by the image point of the radiating dipole, the observation point and the horizontal line drawn from the above mentioned image point [8].

Furthermore, regarding eqs. (5)-(7) above, the following quantities have been introduced :

$$\kappa_{1s} = \sqrt{k_{01}^2 - k_{\rho s}^2} = k_{01} \sin \phi \quad (9)$$

where angle ϕ has been defined just above, and

$$\kappa_{2s} = \sqrt{k_{02}^2 - k_{\rho s}^2} \quad (10)$$

Then our final closed-form analytical solution consists of eqs. (3) - (10).

Furthermore, note in the derivation of our analytical solution above, the following restriction holds [8] :

$$\frac{(x+x_0)^2}{\rho^4} + \frac{1}{\rho^2} \ll k_{01}^2 \quad (11)$$

For wireless telecommunication applications, which are of primary interest in this paper, condition (11) appears to be a rather weak condition, especially for frequencies $f=100$ MHz (radio FM) and above.

4. PRELIMINARY NUMERICAL RESULTS – COMPARISON WITH THE APPROXIMATE RESULTS PREVIOUSLY DERIVED IN THE LITERATURE

Below are provided preliminary numerical results showing comparison of the scattered electric field based (i) on our novel analytical solution, eqs. (3) – (10), and (ii) the approximate solution by K. A. Norton [3], where the 'space wave' and the approximate formula for the 'Norton surface wave' are involved (the latter rather 'dominating', in a sense, for relatively low transmitter and receiver antenna heights). Both results show excellent accuracy between the two methods. Note that the problem parameters in Figs. 2 and 3 below (except the parameters directly shown in these figures) were selected as following : current of the radiating Hertzian dipole $I=1A$, frequency of radiation $f=80$ MHz (wavelength $\lambda=c/f=3.75$ m), length of radiating Hertzian dipole $2h=0.1m$. Note here that the relation between current I and dipole moment p of the radiating Hertzian dipole is : $I(2h)=i\omega p$, where $\omega=2\pi f$ and i is unit imaginary number.

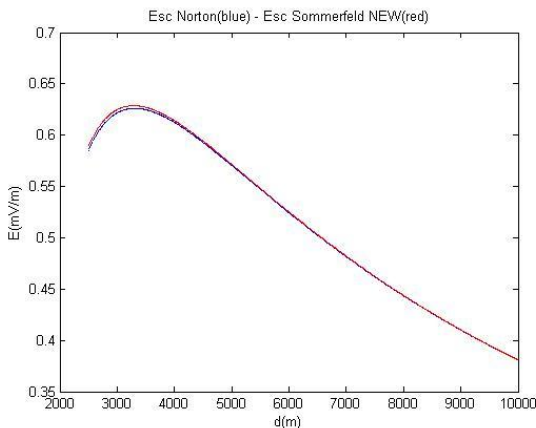


Figure 2

Comparison of electric field scattered from the ground as a function of the horizontal distance $\rho=d$, based on (i) our novel analytical solution (red curve), (ii) Norton's approximate solution (blue curve) [8]. Here both transmitter and receiver antenna heights (x_0 and x , respectively) equal to 150 m. Note that in this case Norton's 'space wave' dominates over his corresponding 'surface wave' [8].

Similarly with Fig. 2 above, except that here both transmitter and receiver antenna heights (x_0 and x , respectively) equal to 1 m. In this case Norton's 'space wave' and 'surface wave' are comparable (not shown here).

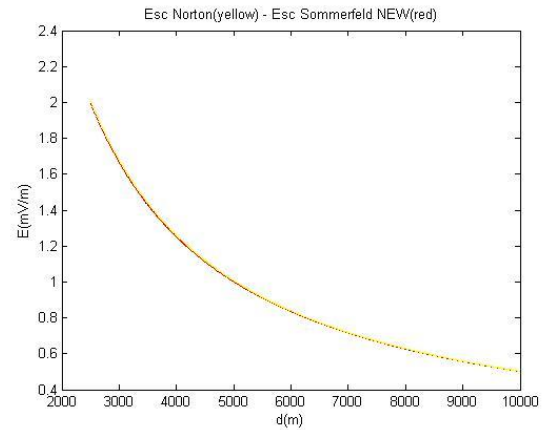


Figure 3

Further clarifications about the above presented numerical results will be provided during the Conference.

5. CONCLUSIONS – FUTURE RESEARCH

In this paper we have derived analytical closed - form solutions for the received electromagnetic (EM) field for the problem of radiation of vertical Hertzian (small) dipole antenna above infinite, flat and lossy ground. To our knowledge these expressions are novel in the literature, and they have been derived here from a formulation in the spectral domain [4,5]. Furthermore, very interesting remarks regarding the physical interpretation of the analytical expressions mentioned above can be found in [7], including wavenumbers of propagation (in horizontal and vertical directions), surface wave behavior and formula for the Fresnel reflection coefficient in the problem examined here, as well as in the limiting case of 'space waves' (where the usual expression for the Fresnel reflection coefficient is obtained). Finally, preliminary numerical results based on our novel analytical solution are provided in this paper.

Related research in the near future by our research group will include : further (detailed) comparison of values for the received EM field with K. A. Norton's results [2], derivation of corresponding EM field expression for the transmitted EM field (region $x < 0$), solution of the corresponding problem for horizontal radiating Hertzian dipole above flat and lossy ground, propagation in isotropic and anisotropic crystals with interface (at $x=0$) etc.

References

- [1] A. N. Sommerfeld, "Propagation of Waves in Wireless Telegraphy", *Ann. Phys.*, 28, pp. 665–736, March 1909; and 81, pp. 1135 – 1153, December 1926.
- [2] T. K. Sarkar et. al., "Electromagnetic Macro Modeling of Propagation in Mobile Wireless Communication: Theory and Experiment", *IEEE Antennas and Propagation Magazine*, Vol. 54, No. 6, pp. 17 – 43, Dec. 2012.
- [3] K. A. Norton, "The Propagation of Radio Waves Over the Surface of the Earth", *Proceedings of the IRE*, 24, pp. 1367 – 1387, 1936; and 25, pp. 1203 – 1236, 1937.
- [4] S. Sautbekov, "The Generalized Solutions of a System of Maxwell's Equations for the Uniaxial Anisotropic Media", Chapter 1 in book 'Electromagnetic Waves Propagation in Complex Matter', edited by A. A. Kishk, Croatia, pp. 3 – 24, June 2011.
- [5] S. Sautbekov, R. Kasimkhanova and P. Frangos, "Modified solution of Sommerfeld's problem", 'Communications, Electromagnetics and Medical Applications' (CEMA'10), National Technical University of Athens (NTUA), Athens, Greece, 7-9/10/2010, pp. 5 – 8.
- [6] C. A. Balanis, 'Antenna Theory : Analysis and Design', Appendix VIII : Method of Stationary Phase, pp. 922 – 927, J. Wiley and Sons Inc., New York, 1997.
- [7] <http://arxiv.org/abs/1303.1171>
- [8] S. Sautbekov, P. Frangos, Ch. Christakis and K. Ioanidi, "A closed – form analytical solution to the radiation problem from a short dipole antenna above flat ground using spectral domain approach", ICEAA Conference, Torino, Italy, September 2013.

FLICKER NOISE IN HARMONIC REJECTING CURRENT COMMUTATING PASSIVE FET MIXERS

Ludwig Lubich

Technical University of Sofia, Faculty of Telecommunications
1000 Sofia, 8 Kl. Ohridski Blvd
lv@tu-sofia.bg

Abstract

The paper examines the flicker noise contribution of different FETs in harmonic rejection mixers (HRM) to the total mixer noise, using simple physical models. There are several different mechanisms which transfer the FETs' flicker noise to the mixer output. Equations for the level of flicker noise due to each noise transfer mechanism have been derived. Comparison between HRM and ordinary double balanced mixers in terms of flicker noise level has been made.

1. INTRODUCTION

Harmonics in the waveform of the local oscillator (LO) make the heterodyne receivers susceptible to interference from signals with frequencies $f = nf_{LO} \pm f_i$, where f_i is the intermediate frequency (IF) used. Traditionally high-order preselect filters are used to solve this problem. However, they are difficult or impossible to integrate on-chip.

In the recent years, harmonic rejection mixers (HRM) have gained in popularity as they allow to considerably relax the requirements on the receivers' preselect filters.

An HRM consists of several parallel operating elementary mixers, driven by multiphase LO. Their output signals, multiplied by different weighting factors, are summed. An HRM is equivalent to a single mixer, driven by an effective LO waveform from which some harmonics are excluded [1]. Usually, the effective LO waveform is based on a sampled sinusoid with N samples per period. Then the effective LO contains only harmonics of orders $kN \pm 1$.

There are various implementation alternatives for the elementary mixers in HRM. Current commutating passive mixers are a good choice, especially for zero-IF receivers, because of their lower $1/f$ noise and better linearity [2].

A conceptual diagram of a current commutating passive HRM is shown in Fig. 1. In order to avoid large voltage swings at the outputs of the transconductance amplifiers (TCA), their outputs should be connected to the ground in the time intervals, in which they are not used. This can be performed by

dummy switches, but it is more rational to use the temporarily idle TCAs to create a quadrature channel and additional IF/baseband (BB) outputs (Fig. 2). Such outputs can be useful when more sophisticated techniques for improved harmonic rejection are employed as in [1].

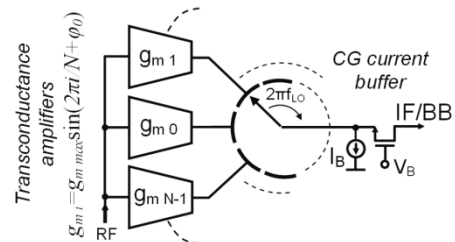


Figure 1. HRM operation principle

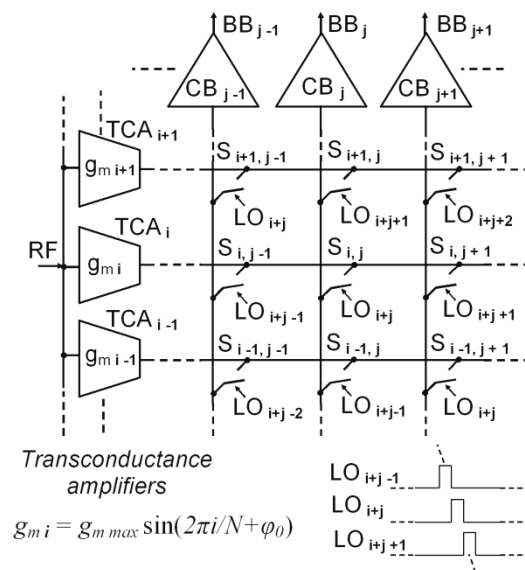


Figure 2. HRM with multiple outputs (single ended implementation).

Current buffers (CBs) can be implemented as FETs in a common gate (CG) circuit. Transimpedance

amplifiers (TIA) can be used instead of CBs. The paper assumes that the input resistance of CBs (or TIAs) is much lower than switch resistance.

The discussions will be mainly focused on direct conversion receivers, as they are most affected by flicker noise.

Also, ordinary mixers will be called “simple mixers” (SM) in contrast to HRM.

In this paper we extend the SM analysis described in [3] over the HRM, which is shown in Fig. 2. The equations are derived for even N only, as the odd values are not practical. All equations apply to balanced HRM implementation.

What was found in [3] for flicker noise of CB bias sources and CB loads as well as for TCA flicker noise of SMs also applies for HRMs, which is why it will not be discussed here.

The rest of the paper is organized as follows: Sections 2 and 3 focus on flicker noise originated by the switches and by CG FETs in the CBs, respectively. Section 4 compares HRMs and SMs in terms of flicker noise level.

2. SWITCH FLICKER NOISE

The slowly varying gate-referred flicker noise of the switching FETs of the mixer randomly modulates the commutation instants. This results in a train of noise pulses which add to the ideal square-wave commutation waveforms. As a consequence, flicker noise appears at the output under certain conditions [3].

In order to examine the changes of the effective LO waveform of the HRM caused by switch flicker noise, it is appropriate to apply a DC voltage $V_{in} = 1/g_{mmax}$ to the HRM input. Then the output signal of the HRM will be numerically equal to the effective LO waveform.

Further discussion is based on the following assumptions:

1. The gate referred flicker noise voltage V_n of the FET is independent of V_{GS} [4].
2. V_n is nearly constant even within a large number of LO cycles.
3. The LO waveform transitions are linear functions of the time:

$$V_{LO} = V_{LOmin} + S t \text{ or } V_{LO} = V_{LOmax} - S t, \quad (1)$$

where S is the slope of LO transitions.

4. FET switches are in the deep triode region, so the square-law model is accurate enough for our purposes [3]. Hence, switch conductance can be expressed as

$$g = \beta(V_G - V_B - V_{th} + V_{LO}) = \beta(V_{eff} + V_{LO}), \quad (2)$$

where V_G and V_B are the gate and source bias voltages, respectively, V_{th} is the threshold voltage of the FETs, V_{eff} is the dc effective voltage of the switch, and $\beta = \mu C_{ox} W/L$. In the last equation μ is the channel mobility, C_{ox} is the gate oxide capacitance, and W and L are the width and the length of the switch.

We examine the commutation of the TCA_i output current from the CB_{j-1} input to the CB_j input. The other currents have no influence, as the CB inputs act as virtual grounds. Commutation begins at time instant t_1 when $S_{i,j}$ starts to conduct and finishes at t_2 when $S_{i,j-1}$ is completely turned off (Fig. 3). Switches $S_{i,j-1}$ and $S_{i,j}$ form a current divider with current division ratios varying from 1 to 0 for the CB_{j-1} input and from 0 to 1 for the CB_j input linearly in the time.

Now let us consider the case when a nonzero noise voltage is present at $S_{i,j}$ gate only.

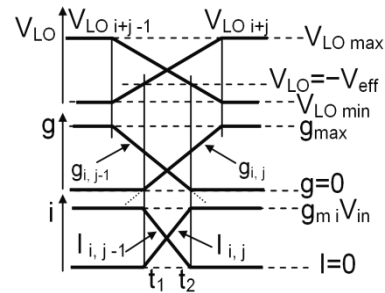


Figure 3. Commutation of TCA output from CB_{j-1} input to CB_j input.

The increase of gate voltage by V_n is equivalent to a time shift $\Delta = V_n/S$.

Depending on the V_n sign, this time shift increases or decreases the “on” time of the switch. As a result, modifications of the current waveforms occur. The difference between the ideal waveform and the “noisy” waveform is a pair of narrow error pulses shown in Fig. 4(a). If there is also a noise voltage at $S_{i,j-1}$ gate, the shape of error pulses changes as is

shown in Fig. 4(b) or Fig. 4(c) depending on the signs of $V_{n i, j-1}$ and $V_{n i, j}$.

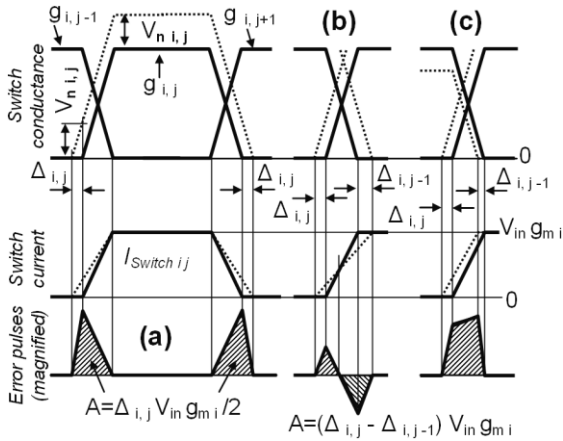


Figure 4. Error pulses at CB_j input, caused by commutation of TCA_i output current

Along with the commutation of TCA_i current from CB_{j-1} input to CB_j input another commutation in progress: The TCA_{i-1} current is redirected from CB_j to CB_{j+1} . This causes a second error pulse in the CB_j input. So a sum of two error pulses flows in the CB_j input. It is convenient to combine these two pulses in one resultant error pulse $P_{i,j}$. Thus, each CB receives N different error pulses $P_{0,j} \dots P_{N-1,j}$ per LO cycle, spaced approximately by T_{LO}/N . According to assumption 2, the error pulse train is approximately periodic with period T_{LO} . So, the spectrum of this error pulse train contains components with frequencies $k f_{LO}$, where $k = 0, 1, 2$ etc. So, the switch flicker noise degrades the harmonic rejection ratio (HRR) of the HRM. Furthermore, the noise voltage variations in time result in changes in the LO spectrum, therefore these components are modulated by the flicker noise. In other words, switch flicker noise is up-converted to frequencies $k f_{LO}$. If there is a strong blocker at some of these frequencies, it will cause downconversion of the switch flicker noise to baseband.

In order to evaluate the level of the flicker noise penetrating to baseband, we will derive an expression for the mathematical expectation of squared harmonics of the error pulse train.

The harmonics of interest have numbers from 1 to $N-2$. The harmonic $N-1$ is not rejected by HRM, so blockers at $f_{Bl} \geq (N-1)f_{LO}$ are suppressed by the preselect filter of the receiver.

As the error pulses are relatively short, we replace them by time-shifted delta functions, multiplied by the area of respective error pulses. We performed Matlab simulations, which showed errors of the calculated spectra within 1.5 dB for pulse durations up to $0.25T_{LO}/N$.

After some geometrical considerations, based on Fig 4, we express the areas A_i of the pulses.

Further we express the Fourier series coefficients $C_{k,j}$ of the error pulse train and take the expectation of $C_{k,j}^2$. We assume that the flicker noise voltages $V_{i,j}$ are uncorrelated random variables with variances $\sigma_{i,j}^2$. The latter are inversely proportional to the FET area [2], so if the switch widths are scaled according the values of g_{mi} , then $\sigma_{i,j}^2 = \sigma_{n\min}^2 / |\sin(2\pi i/N + \varphi_0)|$, where $\sigma_{n\min}^2$ is the variance of the flicker noise voltage of the "unity" switch.

After doing substitutions and mathematical simplifications we obtain:

$$E[C_k^2] = 8 \left(2 + \cos \frac{2\pi k}{N} \right) \frac{\sigma_{n\min}^2}{T_{LO}^2 S^2} \cdot \frac{\cos(\pi/N - \varphi_0)}{\sin(\pi/N)}. \quad (3)$$

If the width of the switches is equal,

$$E[C_{k\text{eq sw}}^2] = 2N \left(2 + \cos \frac{2\pi k}{N} \right) \frac{\sigma_{n\min}^2}{T_{LO}^2 S^2} \quad (4)$$

or about 1 dB lower than $E[C_k^2]$.

Equations (3) and (4) were verified by Matlab simulations.

Now we can find the signal to noise ratio at the HRM output as a function of the blocker power P_{bl} :

$$SNR = \frac{P_{in}}{P_{bl}} \frac{C_1^2}{E[C_k^2]} \approx \frac{P_{in}}{P_{bl}} \frac{\pi}{8N} \frac{T_{LO}^2 S^2}{\sigma_{n\min}^2} \left(2 + \cos \frac{2\pi k}{N} \right)^{-1}. \quad (5)$$

The extent, to which the switch noise can cause a concern, is shown by an example. Let us assume that $N=12$, $TS=4$ and the RMS flicker noise voltage $\sigma_{n\min}$ is 100 μV . On the basis of eq. (5) we can calculate that a blocker to signal ratio of about 70 dB at the mixer input will cause 0 dB SNR at the mixer output. The HRR of the best HRMs is limited to 60-70 dB due to amplitude and phase mismatches. Therefore such a blocker will jam the desired

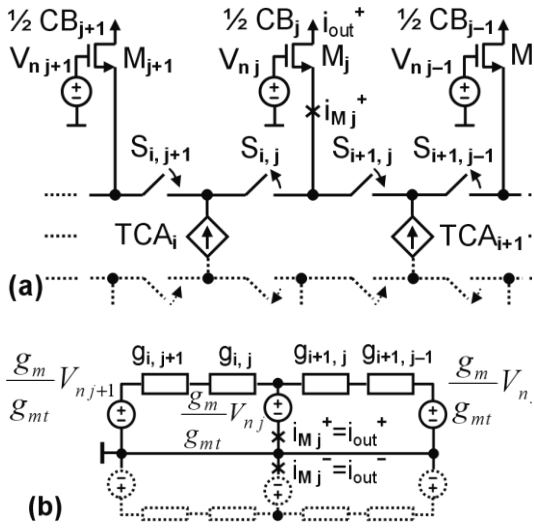


Figure 5. Commutation of CB_j from TCA_i to TCA_{i+1} (a) and corresponding equivalent circuit (b).

signal even without this noise transfer mechanism. So, the discussed mechanism can be a concern only in the best HRMs.

3. BUFFER FLICKER NOISE

The flicker noise contribution of the common gate (CG) FETs of the buffer depends on the operation of the preceding switching core [3]. Therefore, in an HRM it will be different from that in an SM, so, it will be discussed here. For their own gate referred flicker noise these FETs operate in a common source circuit. As the sources are connected to the large impedance of the bias current sources, the gain for the flicker noise should be very low. However, because the switches do not commute instantly and there is a nonzero parasitic capacitance at the TCA outputs, the flicker noise of the CG FETs appears at the output [3]. As in [3], we will call the noise transfer mechanism which is due to imperfect commutation “direct” and that which is due to parasitic capacitance “indirect”.

3.1. Buffer flicker noise, Direct

It is recommended to ensure some overlap between the “on” times of the switches [3]. As a result, during the transition time of the LO pulses, there are $4N$ switches in conductive state, which form low-ohmic paths between the CB inputs. Therefore, the gain of the buffer FETs for their own gate referred flicker noise will be increased. As the CB_{j-1} and CB_{j+1} inputs are virtual grounds, only 8 of these $4N$ switches should be taken into account for CB_j (Fig. 5). In addition, the FETs M_{j-1} and M_{j+1} act as source followers for their own gate referred noise and can be replaced by voltage sources.

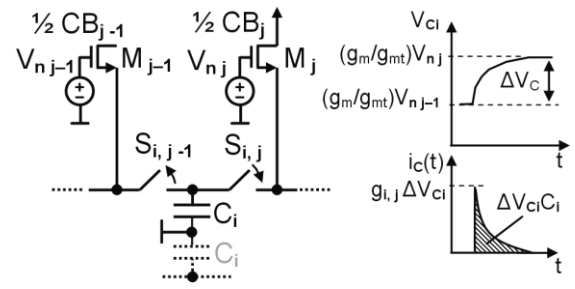


Figure 6. Arousal of noise spikes due to the indirect mechanism

The equivalent circuit is shown in Fig. 5 (b), where g_m and g_{mt} are transconductance and total transconductance (including that due to body effect) of CG FETs, respectively.

It is straightforward to express the currents i_{out}^+ and i_{out}^- for one commutation. The differential flicker noise current in BB is equal to the difference of their time-averaged sums:

$$i_{oav} = \frac{1}{T_{LO}} \int_0^{T_{LO}} \sum_{i=0}^{N-1} i_{out}^+ dt - \frac{1}{T_{LO}} \int_0^{T_{LO}} \sum_{i=0}^{N-1} i_{out}^- dt. \quad (6)$$

We take expectation of i_{oav}^2 . After doing substitutions and mathematical simplifications, we obtain:

$$E[i_{oav}^2] = \frac{64}{3} \frac{\beta_{max}^2 V_{eff}^4}{S^2 T_{LO}^2} \frac{\cos^2(\pi/N - \varphi_0)}{\sin^2(\pi/N)} \frac{g_m^2}{g_{mt}^2} \sigma_n^2 \approx 2.2 \beta_{max}^2 V_{eff}^4 \frac{N^2}{S^2 T_{LO}^2} \frac{g_m^2}{g_{mt}^2} \sigma_n^2. \quad (7)$$

If the switches are equal, the noise power will be about 4 dB higher.

3.2. Buffer flicker noise, Indirect

Even if the switches commute instantly, the flicker noise of the CG FETs appears at the buffer outputs due to the parasitic capacitance at the inputs of the switches (Fig. 6).

We assume that the time constants C_i/g_i are small enough to allow complete charging of the parasitic capacitances. When the switch $S_{i,j-1}$ is “on”, the FET M_{j-1} act as a source follower and charges the parasitic capacitance C_i up to $V_{n,j-1} g_m/g_{mt}$ through the conductance $g_{i,j-1}$ of $S_{i,j-1}$. When the switch $S_{i,j}$ turns on, the source current of M_j will charge C_i up to $V_{n,j} g_m/g_{mt}$, producing a noise current spike at the CB_j output.

The corresponding charge, flowing through M_j , is $Q_i = C_i(V_{ni} - V_{ni-1})g_m/g_{mt}$. There are N such spikes per LO cycle. The flicker noise in baseband (for the half of the circuit) is:

$$i_{oav} = \frac{1}{T_{LO}} \sum_{i=0}^{N-1} C_i (V_{nj} - V_{n,j-1}). \quad (8)$$

If the parasitic capacitance is proportional to the g_{mi} values, then $C_i = C_{\max} \sin(2\pi i/N + \varphi_0)$.

We take expectation of i_{oav}^2 . After doing mathematical simplifications, we obtain:

$$\begin{aligned} E[i_{oav}^2] &= \frac{16C_{\max}^2}{T_{LO}^2} \frac{\cos^2(\pi/N - \varphi_0)}{\sin^2(\pi/N)} \frac{g_m^2}{g_{mt}^2} \sigma_n^2 \approx \\ &\approx 1.6 \cdot \frac{N^2 C_{\max}^2}{T_{LO}^2} \frac{g_m^2}{g_{mt}^2} \sigma_n^2 \end{aligned} \quad (9)$$

If C_i values are equal, the noise power will be about 4 dB higher.

Equations (7) and (9) were verified by Matlab simulations.

4. COMPARISON BETWEEN HRM AND SM AND DISCUSSION

In order to compare HRMs and SMs, we derived the necessary equations for SMs. They seem different from these in [3]. This is primarily because we take into account the noise of all involved FETs.

The equations for the switch noise and the CB direct and indirect noise in SMs are

$$E[C_k^2] = 64 \sigma_n^2 / (T_{LO}^2 S^2) \quad (10)$$

$$E[i_{oav}^2] \approx 57 \sigma_n^2 (g_m^2 / g_{mt}^2) \beta_{\max}^2 V_{eff}^4 / (S^2 T_{LO}^2) \quad (11)$$

$$E[i_{oav}^2] \approx 32 \sigma_n^2 (g_m^2 / g_{mt}^2) C^2 / T_{LO}^2. \quad (12)$$

Note that these equations are not obtained substituting N by 2 in eq. (3), (7) and (9). The SM is different from a degenerated HRM with $N=2$.

Furthermore, for the TCA in the SM it should be selected $g_m \approx (\pi/4) g_{\max}$ to ensure equal conversion gains of the both compared mixers. The other parameters of SM should be scaled accordingly.

Switch flicker noise: HRMs have lower flicker noise than SMs for $N < 10 \div 32$, depending on the harmonic number.

Buffer flicker noise: For $N \geq 4$ (i.e. for all useful values of N) CB noise level in HRMs is higher than

that in SMs and increases with increasing LO frequency.

It seems that CB noise can be decreased using smaller switches, but for a given large signal performance the g_{mi} values of TCAs should be scaled down accordingly, lowering the signal level. So, the SNR will be the same.

S can be increased, but it is limited by the HRM power budget at least.

Another way to reduce noise is to decrease N/T_{LO} . N depends on the required harmonic rejection. Generally, the higher the frequency of the desired channel, the lower the needed value of N . If N was variable, it could be decreased with increasing received frequency, keeping the noise level unchanged. This raises the question of finding HRM architectures with a variable N .

If the width of the switches is scaled according to g_{mi} values, the noise level is about 4 dB lower than in the case of equal switches.

If N is big, dummy switches between the CBs can be used. Then the CB noise will be caused only by the noise voltage V_{nj} .

CB FETs flicker noise can be reduced using large devices. As they operate at BB frequencies, the corresponding rise of their parasitic capacitance is largely tolerable.

4. CONCLUSION

We derived equations for flicker noise in HRM and made comparison between HRM and SMs.

In general HRM have higher flicker noise than SMs. So, it is desirable to look for new HRM architectures with lower flicker noise.

References

- [1] Zhiyu Ru et al., "Digitally-Enhanced Software-Defined Radio Receiver Robust to Out-of-Band Interference", *IEEE Journal of Solid-State Circuits*, vol. 44, 15 Dec. 2009, pp. 3359–3375.
- [2] B. Razavi, *RF Microelectronics*, Prentice Hall PTR, 2011.
- [3] S. Chehrizi, A. Mirzaei, A. A. Abidi, "Noise in Current-Commutating Passive FET Mixers", *IEEE Transactions on Circuits and Systems I: Regular Papers*, vol. 57, Feb. 2010, pp. 332–344.
- [4] H. Darabi, A. A. Abidi, "Noise in RF-CMOS mixers: a simple physical model" *IEEE Journal of Solid-State Circuits*, Vol.35, Jan. 2000, pp. 15 – 25.

WHITE NOISE IN HARMONIC REJECTING CURRENT COMMUTATING PASSIVE FET MIXERS

Ludwig Lubich

Technical University of Sofia, Faculty of Telecommunications
1000 Sofia, 8 Kl. Ohridski Blvd
lv@tu-sofia.bg

Abstract

This paper examines the white noise contribution of different noise sources in the harmonic rejection mixers (HRM) to the total mixer noise, using simple physical models. Equations for the level of noise due to each of the separate noise transfer mechanisms have been derived. A comparison in terms of white noise level between HRM and ordinary double balanced mixers has been made.

1. INTRODUCTION

In the recent years, harmonic rejection mixers (HRM) have gained in popularity due to their suitability for highly integrated RF receivers. The use of HRM alleviates the harmonic mixing problem and thus relaxes the pre-select filtering requirements.

A current commutating passive HRM with multiple outputs is presented in Fig. 1. The RF signal is applied to the inputs of N transconductance amplifiers (TCAs) with transconductance values $g_{mi} = g_{m\max} \sin(2\pi i / N + \varphi_0)$. The output currents of the TCAs flow into the switching core, consisting of FET switches, driven by multiphase local oscillator (LO). Note that each column, as each row of switches can be viewed as an N -position rotary switch doing one revolution per LO cycle. The switching core is followed by current buffers (CBs), ideally with zero input impedance.

In principle, it is possible to implement an HRM with one I and one Q output only. However, in this case the TCA outputs will not be used over the whole LO cycle and should be connected to the ground by dummy switches when they are not used. Otherwise, undesirable large voltage swings at the TCA outputs will occur. On the other hand, the presence of additional outputs makes possible the implementation of techniques for improved harmonic rejection as those proposed in [1].

An HRM is equivalent to an ordinary mixer, driven by an effective LO waveform from which some harmonics are excluded [1]. It is easy to realize that the effective LO contains only harmonics of orders $kN \pm 1$.

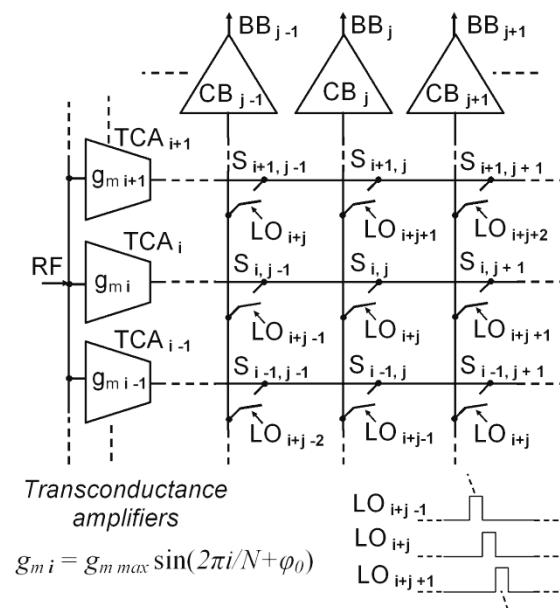


Figure 1. HRM with multiple outputs (single ended implementation).

In contrast to HRM, we will use the term “simple mixers” (SM) for ordinary double-balanced mixers without harmonic rejection capability.

In this paper we extend the analysis, made for SMs in [2] to the case of an HRM like the one shown in Fig. 1, but in a balanced implementation. Furthermore, the number of TCAs is $N/2$ as each differential TCA replaces two TCAs with transconductances of equal absolute values and opposite signs. The equations are derived for even values of N only, as the odd values are not practical.

The paper assumes that CB input resistance is much lower than switch resistance.

The discussions will be primarily oriented to direct conversion and low-IF receivers, as they are very suitable for highly integrated implementation.

The rest of the paper is organized as follows: Sections 2, 3, and 4 present noise contributions of transconductors, switches, and current buffers, respectively. Section 5 compares HRM and simple mixers in terms of white noise level in baseband (BB).

2. TCA WHITE NOISE

From the viewpoint of the succeeding blocks, the TCA noise is indistinguishable from the input RF signal. Therefore, the noise components, centered around the LO harmonics, will be down-converted to baseband. The total noise power is sum of the power of the down-converted noise components, since they are uncorrelated. So, the total single-sided PSD of the noise, converted to baseband is:

$$S_0 = N_0 F g_{m\max}^2 \sum_{k=1}^{\infty} C_k^2 / 2, \quad (1)$$

where N_0 is the thermal noise PSD, F is the TCA noise factor, and C_k are the Fourier series coefficients of the effective LO waveform. Then we can express the ratio between the PSD of the TCA noise converted to baseband by a real mixer and by a perfect multiplier driven by pure sinusoidal LO.

$$S_0/S_{0\text{perfect}} = \sum_{k=1}^{\infty} C_k^2 / C_1^2 \quad (2)$$

For an HRM we have found that

$$S_0/S_{0\text{perfect}} = \frac{\pi^2}{N^2 \sin^2(\pi/N)}, \quad (3)$$

whereas for an SM driven by a symmetrical square-wave LO this ratio is $\pi^2/8$ or 0.9 dB. In fact (2) gives an equivalent increase of the TCA noise factor due to LO harmonics. Fig. 2 presents eq. (3) for N between 5 and 16.

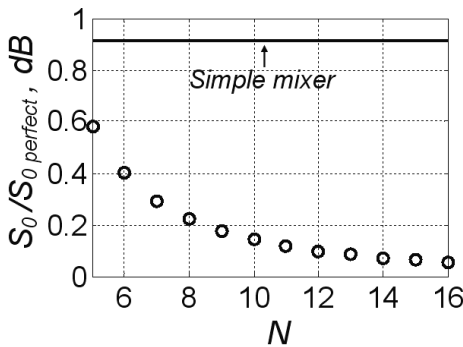


Figure 2. Plot of eq. (3) in dB

3. SWITCH WHITE NOISE

The switching FETs in a passive current commutating mixer operate in the deep triode region when they are in “on” state. The transistor can be replaced by a Norton equivalent circuit, consisting of the drain-source conductance in parallel connection with a noise current source. The single-sided PSD of its noise current is

$$S_n = 4kT\gamma g_{ds}, \quad (4)$$

where γ is the excess noise factor of the transistor and g_{ds} is its “on” conductance [3].

At first glance, it seems that the switches cannot generate noise, as the mixer output current is fixed by the TCAs. However, because the switches do not commute instantly and there is a nonzero parasitic capacitance at the TCA outputs, the white noise of the switches appears at the output [2]. As in [2] we will call the noise transfer mechanism which is due to imperfect commutation “direct” and that which is due to parasitic capacitance “indirect”.

3.1. Switch white noise, Direct

It is recommendable to ensure some overlap between the “on” times of the switches which are turning on and the switches which are turning off [2]. As a result, 4N switches are in a conductive state during the ON overlap. They form low-ohmic paths at the CB inputs. So the noise current of the switches can flow into CB inputs.

Let us examine the noise current flowing in the CB_j input during the commutation from TCA_i to TCA_{i+1} (Fig. 3a). As the CB_{j-1} and CB_{j+1} inputs are virtual grounds, only 8 of these 4N switches should be taken into account for CB_j . The corresponding equivalent circuits are presented in Fig. 3b.

The conductance of the switch is

$$g = \beta(V_G - V_B - V_{th} + V_{LO}) = \beta(V_{eff} + V_{LO}), \quad (5)$$

where V_G and V_B are the gate and source bias voltages, respectively, V_{th} is the threshold voltage of the FETs, V_{eff} is the dc effective voltage of the switch. $\beta = \mu C_{ox} W/L$, in which μ is the channel mobility, C_{ox} is the gate oxide capacitance, and W and L are the width and length of the switch.

We assume as in [2] that LO waveform transitions are linear functions of the time, i. e.

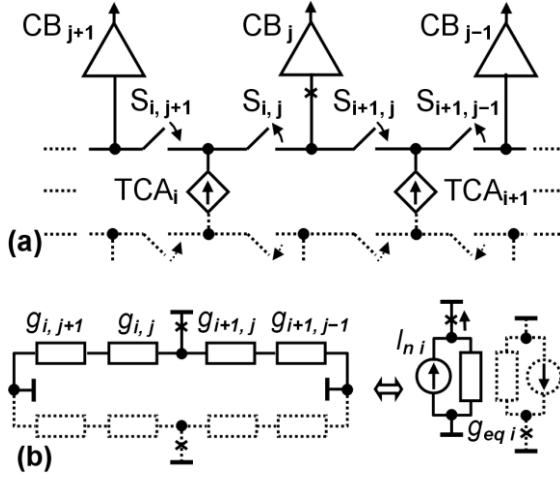


Figure 3. Commutation of CB_j from TCA_i to TCA_{i+1} (a) and corresponding equivalent circuit (b).

$$V_{LO} = V_{LO\min} + S t \quad \text{OR} \quad V_{LO} = V_{LO\max} - S t, \quad (6)$$

where S is the slope of LO transitions.

Then the equivalent conductance connected to CB_j input during the overlap time of the i -th commutation is

$$g_{eqi} = (\beta_i + \beta_{i+1}) \frac{V_{eff}^2 - V_{LO}^2}{2V_{eff}}, \quad (7)$$

where $\beta_i = \beta_{\max} \sin(2\pi i / N + \varphi_0)$ and β_{\max} is the β value of the "unity" switch.

As g_{eqi} varies periodically with the time, the noise current produced by the periodical commutation of each pair of TCAs, can be considered as white noise, multiplied by a periodical signal. Its PSD can be found as product of their respective PSD and power:

$$S_{ni} = 4kT\gamma(\beta_i + \beta_{i+1}) \frac{1}{T_{LO}} \int_{t_1}^{t_2} \frac{V_{eff}^2 - V_{LO}^2}{2V_{eff}} dt \quad (8)$$

In the last equation t_1 and t_2 are the borders of the overlap time interval.

Since the noise currents produced by the N separate commutations in each LO cycle are uncorrelated, the total PSD at CB_j input is the sum of their PSDs.

After performing the necessary mathematical operations and simplifications, we obtain for the total differential PSD at HRM output:

$$S_{odiff} \approx 4kT\gamma \frac{16}{3} \frac{N}{\pi} \frac{\beta_{\max} V_{eff}^2}{ST_{LO}} \quad (9)$$

If the switch widths are not scaled according to the transconductance values of the corresponding TCAs, the PSD of the direct switch noise will be about 2 dB higher.

3.2. Switch white noise, Indirect

Due to the parasitic capacitances at the TCA outputs, the switch white noise will appear at the HRM output even in the case of instantaneous commutation. Let us consider the role of the parasitic capacitance at the non-inverting TCA_i output for the white noise at the CB_j output. The corresponding part of the HRM is presented in Fig. 4a. The equivalent circuit of the highlighted part of Fig. 4a is shown in Fig. 4b. As the resistor is a memoryless component and all N switches connected to TCA output have the same "on" conductance, the resistors in Fig. 4b can be replaced by one resistor. In addition, since the values of the white noise are uncorrelated in time, the noise current sources can be replaced by a single noise source. We have assumed that the CB input resistance is low, so the CB inputs can be considered as virtual grounds. All these considerations lead to the equivalent circuit in Fig. 4c.

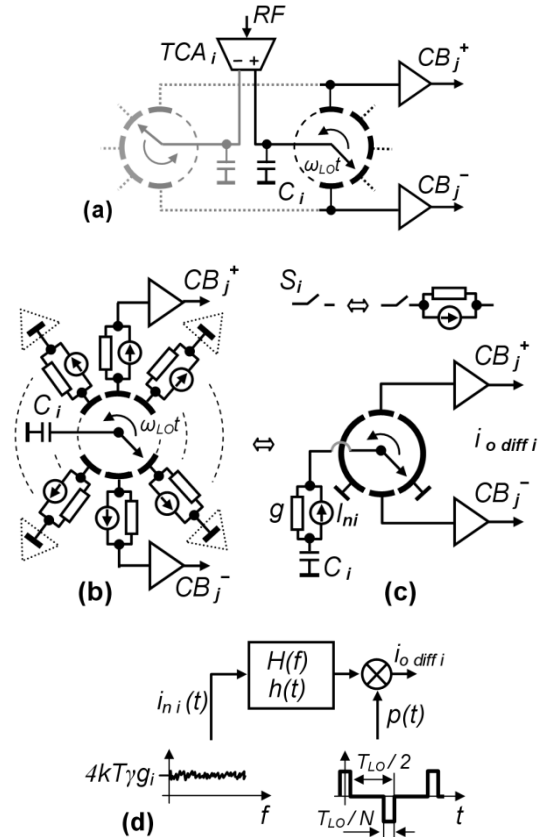


Figure 4. Indirect switches noise due to parasitic capacitance C_i

The switch conductance g_i and C_i form a high-pass filter with a transfer function

$$H(f) = \frac{j f / f_0}{1 + j f / f_0}, \quad (10)$$

where $f_0 = 1/(2\pi C_i / g_i)$ is the corner frequency. The corresponding impulse response is $h(t)$. The values of the corner frequency f_0 should be the same for all TCAs in a well designed HRM, so the transfer function and the impulse response of the individual TCAs are the same.

This filter causes a frequency-dependent attenuation for the components of the noise current. When the TCA_i output is connected to CB_j, the filtered noise current flows into its input. Over the rest of the LO cycle, the filtered noise current continues to flow to the ground, so from the viewpoint of the noise source and the filter, the circuit is unchanged. Therefore the circuit in Fig. 4c can be modeled by the system shown in Fig. 4d.

The differential noise current, produced by this system is

$$i_{odiff i}(t) = [i_{ni}(t) * h(t)]p(t). \quad (11)$$

Following some mathematical simplifications, we obtain the single-sided baseband PSD of (11) presented in a form comparable to that in [2]

$$S_{odiff i} = \frac{8}{\pi^2} S_{swi} \sum_{m=0}^{+\infty} \left[\frac{\sin^2\left(\frac{(2m+1)\pi}{N}\right)}{(2m+1)^2} |H((2m+1)f_{LO})|^2 \right], \quad (12)$$

where $S_{swi} = 4kT\gamma g_i$ is the single-sided PSD of the noise current produced by any of the switches connected to TCA_i and

$$g_i = g_{\max} \sin(2\pi i / N + \varphi_0).$$

Since the noise currents, originating from the switches at the two TCA_i outputs are uncorrelated, the total noise power related to TCA_i is two times as large as in (12). The noise currents produced by the switches belonging to the separate TCAs are uncorrelated, so the total PSD for one HRM output is

$$S_{odiff} = 2 \sum_{i=1}^{N/2} S_{odiff i} = 4kT\gamma g_{\max} \frac{\cos\left(\frac{\pi}{N} - \varphi_0\right)}{\sin\left(\frac{\pi}{N}\right)} \times \frac{16}{\pi^2} \sum_{k=0}^{+\infty} \left[\frac{\sin^2\left(\frac{(2m+1)\pi}{N}\right)}{(2m+1)^2} |H((2m+1)f_{LO})|^2 \right]. \quad (13)$$

We found an expression for PSD in closed form, but it is somewhat awkward. Fortunately, it turned out that many of its terms are negligible, so we obtained a very good approximation, which works well for all f_{LO}/f_0 values:

$$S_{odiff} \approx (4kT\gamma g_{\max}) \frac{2N}{\pi^2} \times \frac{f_{LO}}{f_0} \left[1 - \exp\left(-\frac{2\pi}{N} \frac{f_0}{f_{LO}}\right) \right]. \quad (14)$$

For $f_{LO}/f_0 > 2\pi/N$ this expression approaches $(4kT\gamma g_{\max})4/\pi$. On the other hand, for $f_{LO}/f_0 \ll 2\pi/N$ eq. (14) tends to

$$(4kT\gamma g_{\max}) \frac{2N}{\pi^2} \frac{f_{LO}}{f_0}.$$

If the switches are not scaled according to the transconductance values of the corresponding TCAs, the noise PSD will be about 2 dB higher.

As $\sin(\pi - x) = \sin(x)$ the number of TCAs can be further reduced to $N/4$. In this case, the first summation in (13) will be incorrect, as the pairs of symmetrical addends correspond to correlated noise currents. We examined this correlation. Without going into details, we found that it is significant only for the pair of addends with numbers $i = N/4$ and $i = N/4 + 1$ when f_{LO}/f_0 decreases. For $f_{LO}/f_0 < 3/N$ the sum of the powers of these two noise currents tends to the power of only one of them. In this case, the value calculated by (13) should be multiplied by approximately $(1 - \pi/N)$.

The equations derived in section 3 were verified by Matlab simulations.

4. BUFFER WHITE NOISE

The white noise of bias and load circuits of the CBs (Fig. 5) appears directly at the output [2]. The white noise contribution of the common gate (CG) FETs depends on the operation of the switches and the parasitic capacitances at the TCA outputs. As in [2] and [4] there are two mechanisms, which transfer the white noise of CG FETs to the mixer output: direct and indirect.

These components of the white noise, which are close to DC, appear at the output in the same way as the flicker noise in [2] and [4]. The components, which are centred around $k f_{LO}$, seem to be down-

converted to baseband. However, they will be shorted to ground by the large CB input capacitance and will appear at the HRM output unaffected by the operation of the switches. As a result, they will be outside the spectrum of the desired signal [2] and should not be taken into account. Therefore, the equations for the direct and indirect white noise of the buffer are the same as the equations for the buffer flicker noise derived in [4]. The only difference is that the squared voltage of the flicker noise has to be replaced by $4kT\gamma/g_m$.

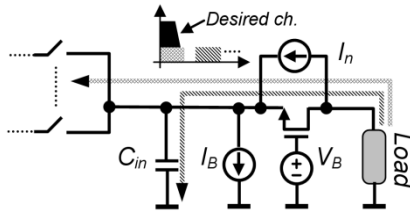


Figure 5. CB white noise

If the CBs are implemented as transimpedance operational amplifiers, the equations will be roughly the same. The RMS flicker noise voltage should be substituted by the input referred noise voltage of the amplifier.

5. COMPARISON BETWEEN HRM AND SM AND DISCUSSION

In order to make a comparison between HRM and SM, we should select $g_m \approx (\pi/4) g_{max}$ for the TCA in the SM. This ensures equal conversion gains of both compared mixers. The other SM parameters should be scaled accordingly.

HRMs perform better than SMs with respect to trans-conductor white noise. The advantage is fairly small and approaches 0.9 dB when N is large. In practice, increasing N above 10-12 does not result in a further noticeable reduction in the noise level (Fig. 2).

The direct white noise of the switches has a higher level than in a comparable SM when N is above 4 (i.e. for all useful values of N).

The indirect white noise of the switches in an HRM has a higher PSD than in an SM when $f_{LO} < f_0$. On the other hand, for N up to 20 and practically any f_{LO} value, the HRM noise is no more than 6 dB higher than that of the SMs.

What was discussed in [2] and [4] about the CB flicker noise also applies for the white noise originated by them.

The analysis of the derived equations shows that the level of the *indirect* white noise of the switches and CG FETs can exceed the unavoidable white noise at the TCA outputs. This can result in a considerable degradation of the noise figure of the HRM. In order to prevent this, the parasitic capacitance at the TCA outputs should be minimized and too large values of N should be avoided. It is not appropriate to reduce the conductance of the switches, as this will result in a decrease of f_0 , which will counteract the noise level reduction. Moreover, the large-signal performance of the mixer will be impaired.

In practice, the *direct* white noise of the switches and CG FETs is lower than the white noise at the TCA outputs in any case. The direct white noise of the switches can be several times lower than the TCA white noise, while the direct white noise of the CG FETs can be made negligible. This can be achieved primarily by using LO with sharp transitions, as long as the power budget of the HRM allows it.

4. CONCLUSION

We derived equations for white noise in HRM and made comparison between HRMs and SMs with respect to noise level.

In general, HRMs have a higher white noise level than SMs. The increase of N alleviates the harmonic mixing problem, but it also increases the level of the white noise, originating from the switches and the current buffers.

The white noise contributed by the switches and the CBs can be made lower than the TCA noise. Therefore, the noise figure of the entire HRM can be near the noise figure of the TCAs.

References

- [1] Zhiyu Ru et al., "Digitally-Enhanced Software-Defined Radio Receiver Robust to Out-of-Band Interference", IEEE Journal of Solid-State Circuits, vol. 44, 15 Dec. 2009, pp. 3359–3375.
- [2] S.Chehrizi, A. Mirzaei, A. A. Abidi, "Noise in Current-Commutating Passive FET Mixers", IEEE Transactions on Circuits and Systems I: Regular Papers, vol. 57, Feb. 2010, pp. 332–344.
- [3] T. H. Lee, The Design of CMOS Radio-Frequency Integrated Circuits, Cambridge University Press, 2004.
- [4] L. Lubich, "Flicker Noise in Harmonic Rejecting Current Commutating Passive FET Mixers", CEMA'13, Sofia, Bulgaria, October 17th -19th, 2013.

RECENT TRENDS AND FUTURE DEVELOPMENTS OF VEHICLE MOUNTED SATELLITE TRACKING COMMUNICATIONS SYSTEMS

Veselin Demirev

Radio Communications and Video Technologies Department, TU-Sofia,
Kl. Ohridski blv. № 8, 1756-Sofia,
e-mail:demirev_v@tu-sofia.bg

Abstract

Earth Stations mounted On Mobile Platforms are currently a strong growth market, driven chiefly by major projects to deploy vast regional or world-wide networks. One of the biggest technical problems here is the antenna system. The tracking of a satellite independently of mobile motion is an essential function for directional antenna systems in Ku and Ka frequency bands. The tracking function needs two capabilities – beam steering and tracking control.

Analytical review of the beam steering and tracking control methods, used in Earth Stations mounted On Mobile Platforms, is given in the report. The advantages and disadvantages of the Mechanical steering and Electronic steering methods, as well as the closed and open loop methods for tracking control are given too.

The proposed review of tracking antenna methods shows that the solving of tracking Earth Stations mounted On Mobile Platforms problems needs entirely new approach. The aim of this paper is to analyze the new technical proposal, named Spatial Correlation Processing, from satellite tracking techniques point of view. Special attention is given to the reasons for obtaining a very short acquisition time period during the starting procedures. Proposal for parallel code acquisition procedures is given too.

1. INTRODUCTION

The growing satellite communications market makes it more and more difficult to assign frequency resources in the commonly used frequency bands at 4-6 GHz and 11-14 GHz. Thus, frequency bands above 17 GHz are of increasing interest for future satellite communication links. Ka band satellite broadband applications present a number of advantages and some drawbacks in comparison with other broadband solutions, their suitability depending on the environment considered. For example, in rural and other isolated areas, where fibre links could be very expensive, satellite Ka band can be used to overcome first-mile connectivity gaps [1]. Improvements in Ka band technology include amongst others:

- Systems employ narrow “spot beams” rather than a single coverage area over a region. A far more efficient use of the available bandwidth resulting in a higher throughput and a much lower transmission cost per Mbytes. The contracted and planned Ka band satellites will use multiple tens and up to several hundreds of spot beams for broadband access systems. Spot beam apertures of less than 0.3° and advanced beam pointing error correction techniques are foreseen.

- High satellite Equivalent Isotropic Radiated Power (EIRP) and Figure of Merit (G/T) will allow to accommodate small-size user antennas (e.g. down to about 40 cm diameter dish) compatible with requirements on transportability.
- Improved spectrum efficiency in particular due to multispot frequency re-use.

Ka band satellite broadband services currently enable diverse applications such as:

- Internet: Provisioning of broadband access to small and medium enterprise, households as well as individuals in low density populated areas (more than 50% of European territory).
- Information & Entertainment: Broadcasting high quality of service (QoS) TV in high definition or even 3D format as well as emerging interactive broadcast services.
- Broadband service to mobile platforms such as aircrafts, ships, cars and trains.
- Business continuity: Provisioning of high QoS as well as reliable and dependable private communication networks for real time exchange of critical information between geographically distributed entities;
- Disaster management: Surveillance of critical or dangerous assets as well environ-

mental monitoring with data collection from sensors deployed in remote areas.

- National and international security domain.
- Feeder links for satellite data relay systems.

Satellite broadband services with advanced Ka band multi-beam antenna and payload technologies will be able to deliver up to 100 Mbps peak data rates on the downlink and up to 20 Mbps peak data rates on the uplink. Hence, satellite broadband can be qualified as a complementary Next Generation Access technology.

2. THE USE OF EARTH STATIONS ON MOBILE PLATFORMS OPERATING WITH GSO SATELLITE NETWORKS IN THE FREQUENCY RANGE 17.3-20.2 GHZ AND 27.5-30.0 GHZ

Recently there has been an increase in the use of Fixed-Satellite Service (FSS) networks by Earth Stations mounted On Mobile Platforms (ESOMP,s) to provide telecommunications services to aircrafts, ships, trains and other vehicles using both the C- and Ku-band. As the demand for these systems evolves, service providers are turning to other FSS bands, in particular Ka-band, to meet this growing need [2].

Advances in satellite antenna technology, particularly the development of stabilised antennas capable of maintaining a high degree of pointing accuracy even on rapidly moving platforms, have already allowed the development of mobile terminals with very stable pointing characteristics. The pointing accuracy performance of systems currently either in production or under development for use in Ka-band is equal to or better than that currently achieved by Ku-band systems operating on mobile platforms. These mobile terminals are designed to operate in the same interference environment and comply with same regulatory constraints as those for typical uncoordinated FSS earth stations. Ka-band satellite networks with mobile terminals are expected to be operated in Europe from early 2013.

To address potential interference with other co-frequency Geo Stationary Orbit (GSO) FSS networks, ESOMP,s should comply with the same constraints, such as off-axis EIRP limits, as those for other FSS earth stations. Such limits would be determined by both the inter-system satellite coordination agreements and the limits in the ETSI standard. In considering aggregate interference levels, it should be noted that there is no evidence

that FSS systems, supporting ESOMP,s, will have more spot beams or better frequency reuse than other FSS systems, thus by applying existing FSS rules the same level of protection will be provided to neighboring satellite networks as is currently the case. Hence, from the perspective of potential uplink interference to other satellite networks, these requirements will ensure that such earth stations are essentially equivalent to stationary FSS earth stations.

The design, coordination and operation of ESOMPs should be such that, the interference levels generated by such earth stations account for the following factors:

- Mis-pointing of the earth station antenna.
- Variations in the antenna pattern of the earth station antenna.
- Variations in the transmit EIRP from the earth station.

ESOMP,s that use closed loop tracking of the satellite signal need to employ an algorithm that is resistant to capturing and tracking adjacent satellite signals. Such earth stations must be designed and operated such that they immediately inhibit transmission when they detect that unintended satellite tracking has occurred or is about to occur. Such earth stations must also immediately inhibit transmission when their mis-pointing would result in off-axis EIRP levels in the direction of neighbouring satellite networks above those of other specific and/or typical FSS earth stations operating in compliance with Recommendation ITU-R S.524 or with any other limits coordinated with neighbouring satellite networks. These earth stations also need to be self-monitoring and, should harmful interference to FSS networks be detected, must automatically mute any transmissions.

3. EARTH STATION ANTENNA BEAM STEERING AND TRACKING METHODS

The tracking of a satellite independently of mobile motion is an essential function for directional antenna systems, used by ESOMP,s. The tracking function needs two capabilities – beam steering and tracking control [3].

There are two types of beam steering methods. The first is mechanical steering, which physically directs the antenna to the satellite. The second is electronic steering, which directs the antenna beam by electronic scanning. A typical example of electronic

steering is achieved through a phased array antenna. The main features of the two types of methods are listed below:

- Mechanical steering

Advantages: Technically easy to fabricate; Wide beam coverage; Good axial ratios in wide beam coverage.

Disadvantages: Low reliability; Low-speed beam scanning; Large in volume and heavy; Very high cost (in order of several thousands US \$).

- Electronic steering

Advantages: Light and low profile; High-speed beam scanning; High reliability.

Disadvantages: Technically difficult to fabricate; Narrow beam coverage, Narrow frequency working band; Poor axial ratios in wide scanned coverage; Excessive feeder loss; Extremely high cost (in order of hundred thousands US \$).

There are also two methods to control tracking. The first is the closed loop method, which uses a signal from the satellite to search for and maintain in satellite direction. The second method is the open loop method, which does not use signals from a satellite. It uses compasses and rate sensors and is not applicable for ESOMP,s in Ku and Ka frequency bands, where high gain narrow beam antenna systems are used.

The tasks, performed by the ESOMP,s satellite tracking system, include satellite acquisition and automatic tracking [4]. The acquisition system acquires the desired satellite by moving the antenna around the expected position of the satellite. Automatic tracking is initiated only after the received signal strength due to the beacon signal transmitted by the satellite is above a certain threshold value, which allows the tracking receiver to lock to the beacon. The automatic tracking ensures continuous tracking of the satellite. Figure 1 shows the generalized block schematic arrangement of the closed loop satellite tracking system. The ESOMP,s antenna makes use of the beacon signal to track itself to the desired positions in both azimuth and elevation. The auto track receiver derives the tracking correction data that is used to drive the antenna. The tracking techniques are classified on the basis of the methodology used to generate angular errors. Commonly used tracking techniques include Sequential Lobing, Conical Scan and Monopulse Tracking.

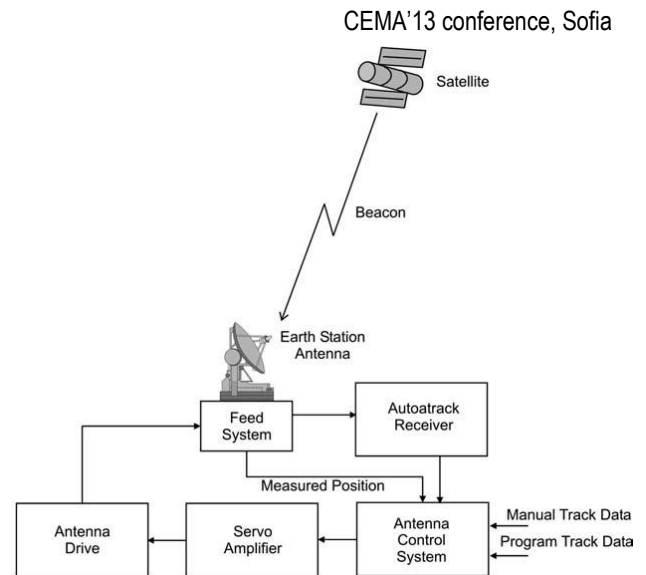


Figure 1. Block schematic arrangement of closed loop satellite tracking systems with mechanical steering

The main disadvantages of the above listed closed loop tracking methods when used in ESOMP,s are:

- The use of satellite signals as essential factor. This is because received signal levels from satellites are not stable because of the severe propagation environment, due to fading, blocking and shadowing.
- Long acquisition time period during the starting procedures, which is in order of one minute in real Ku band systems and several minutes in Ka band systems. The same acquisition time is needed after the loose of the signal due to blocking in urban environment.
- The listed methods can be used for tracking only one communication satellite. In some cases, where very high reliability is necessary, the space diversity approach is used. It includes simultaneous communications and tracking of several satellites.

4. THE SCP-RPSC APPROACH

The listed review of satellite tracking ESOMP,s methods shows that the solving of their main problems needs entirely new approach, proposed by the author ten years ago [5,6,7]. The name of the new proposal is SCP-RPSC (Spatial Correlation Processing – Random Phase Spread Coding) technology.

The SCP system objectives solve simultaneous the problems of antenna beam steering and closed-loop satellite tracking. SCP system could be defined as virtually electronic steering and multiple satellites closed-loop tracking system. The SCP approach is

base for the later developed Random Phase Spread Coding (RPSC, or SCP, transmit) approach, as well as for the RPSC-Multiple Access techniques.

The possibilities of SCP-RPSC approach to solve the regulatory ESOMP, s problems in Ku band were reported by the author in [8]. The same advantages could be declared for the SCP-RPSC systems in Ka band, as well as the additional advantages from acquisition and tracking point of view.

The SCP system architecture is shown in fig. 2, where the cooperative satellite is chosen for communications by means of the corresponding synchronized Pseudo-Noise (PN) code, using the well known Code Division Multiple Access (CDMA). This specific SCP-RPSC feature should be in the first place when short acquisition time of the ESOMP, s systems is of great importance. Code synchronization consists of two steps, acquisition and tracking [9].

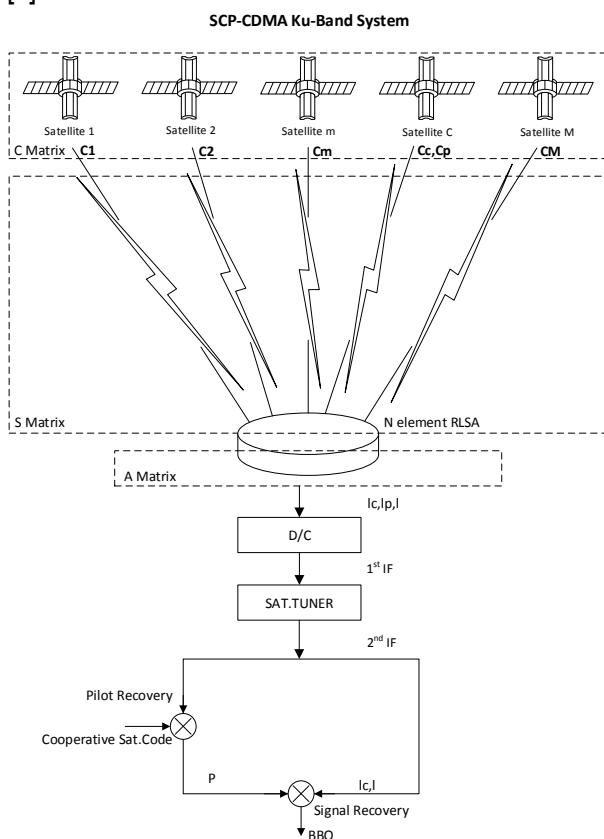


Figure 2. The basic SCP system architecture

The most widely used algorithm for code acquisition is the so-called serial search strategy. Here the phase of the local code is changed step by step, in equal increments, resulting in serial search of the code delay uncertainty region until the synchro position is found. For each value of the phase of the local sequence, a correlation between the input

signal and the local signal replica is formed and compared to a threshold. A high value of the correlation (above the threshold) indicates the synchro position. The acquisition time period is reduced in the modern CDMA systems by well developed methods of parallel and combined search up to several tenths milliseconds. It is incomparable with the acquisition time of the above mentioned, used in Ku and Ka frequency bands, classical methods.

The theory of code tracking in the modern CDMA systems is very well developed too. Similar to acquisition procedures, it is made by software and does not need multichannel RF coherent receiver as it is in classical monopulse tracking. This approach gives the possibility of simultaneous tracking of several cooperative satellites, insuring space diversity.

5. CONCLUSION

The recent and future developments of satellite communications in Ku and Ka frequency bands for fixed and mobile users will lead to new extremely important possibilities for the human mankind. They will improve quality of life of billion people. Very important part of this development is the practical implementation of the proposed by the author SCP-RPSC approach.

References

- [1] ECC Report 152, "The use of the frequency bands 27,5-30,0 GHz and 17,3-20,2 GHz by satellite networks", September, 2010.
- [2] ECC report 184, "The Use of Earth Stations on Mobile Platforms Operating with GSO Satellite Networks in the Frequency Range 17.3-20.2 GHz and 27.5-30.0 GHz", February 2013.
- [3] S. Ohmori, H. Wakana, S. Kawase, Mobile Satellite Communications, Artech House, Boston, 1998.
- [4] A. Maini, W. Agrawal, Satellite Technology – Principles and Applications, John Willey & Sons, Chichester, 2011.
- [5] Demirev V., "SCP technology – the new challenge of broadband satellite communications", ICEST'04, Conference Proceedings, 2004, pp. 159-162.
- [6] Demirev V., A. Efremov, "SCP-CDMA GSO's system proposal", ICEST'04, Conference Proceedings, 2004, pp. 163-166.
- [7] Demirev V., "Review of SCP-RPSC technology", ICEST'05, Conference Proceedings, V.2, 2005, pp.630-633.
- [8] Demirev V., "The regulatory aspects of SCP-RPSC technology – could they solve the VMES problems", Journal of Applied Electromagnetism, vol.13, Number 1, June 2011, pp. 33-38.

THE INVESTIGATION OF OPTICAL – WIMAX HYBRID ACCESS NETWORK

Lina Narbutaitė

Rasa Brūzgienė

Tomas Adomkus

Mindaugas Ruočkus

Stasys Kasetas

Kaunas University of Technology
Department of Telecommunications
Studentų str. 50-452, Kaunas, Lithuania, LT- 51368
E-mail: rasa.bruzgiene@ktu.lt

Abstract

Optical – WiMAX network provides the transfer rate in a different level, which shows an appropriate hierarchy of the capacity. The integration of Optical network with WiMAX is regarded as a promising solution for the access in realizing the convergence over fixed and mobile networks. The integration of Optical – WiMAX hybrid access network allows the allocation of the connecting bandwidth and a packet transfer scheduler, that better supports quality of service and improves the bandwidth of the network. The complementary features of such network can bring the economic efficiency to the network providers also. Therefore, the task of this paper is to investigate the traffic of services in the hybrid ONU/BS unit of the access network, evaluating the effect to the services of different type flows, which are provided over the Optical – WiMAX hybrid access network. Due to this, the mathematical model was created and the hybrid ONU/BS unit was divided into two parts: the unit of the optical network and the base station. The service's time in ONU/BS was estimated using the formation and description system of M/M/n/n for the queues of non-preemptive and preemptive priorities. The QoS parameters of uplink and downlink traffic of services in the hybrid ONU/BS unit was analysed using the created model in the environment of Java Modelling tool. The method of selection the queuing behaviour in the QoS scheduling, when the incoming traffic is dependent on the different distribution of the various classes of the services are as the result of this investigation.

1. INTRODUCTION

The hybrid optical – WiMAX network is a broadband network with a wide bandwidth and network coverage, the high reliability of the quality of service (QoS), the more cost effective network deployment and the lower prices of the network operating [1]. The integrated architectures of the hybrid optical – WiMAX network are based on the broadband antennas. Their base stations are sending the same wireless signals to mobile stations at the same time within the coverage areas [2]. Optical and WiMAX networks provide the transfer rate in different levels. The integration of these networks allows to combine the allocation of the transmission bandwidth and the planning of the packets transmission. This affects the higher QoS and improves the network throughput [3]. However, such processes as the control, data transmission or management [3,4] increase the impact of the hybrid network's parameters to the provision of the services of different types. The search of solutions for the effective management of these processes is a subject to a various investiga-

tions for the dependence of the network parameters, such as: the probability for the packets loss versus load [5]; the power use versus data bandwidth [6]; the packets' delay versus the transmission bandwidth [7] and traffic load, when the duration of the cycle (CT) is different [8]. Nevertheless, the main problem is the gateway ONU/BS node, which affects the processes of the control, data transmission or management. The hybrid ONU/BS node influences the processing time of the services at the user's side.

Due to this, the investigation of the traffic of services in the hybrid ONU/BS node, evaluating its impact to the processing time of the services of different type flows in the optical – WiMAX hybrid access network are presented in this paper.

2. THE PROPOSED ALGORITHM FOR THE INVESTIGATED ONU/BS OPERATION IN THE HYBRID OPTICAL – WIMAX ACCESS NETWORK

The integration of the hybrid optical – WiMAX access network nodes can be in different variants

(Fig. 1). The variant, when the optical network unit (ONU), WiMAX base station (BS) and the connection controller (CC) is in one place, was selected for the investigation. The optical network was the Ethernet passive optical network (EPON). The network management is centralized, because the optical line terminal (OLT) manages the flows from the subscribers' stations (SS) and the data transmission of WiMAX network. The quality parameters of the different services strongly depend on the processes of such management.

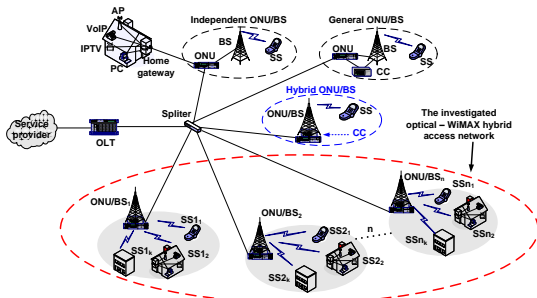


Figure 1. The structure of ONU/BS nodes in the investigated hybrid EPON – WiMAX access network

The relation between the centralized management of the data flows in the hybrid EPON – WiMAX network and QoS classification is presented in Fig. 2.

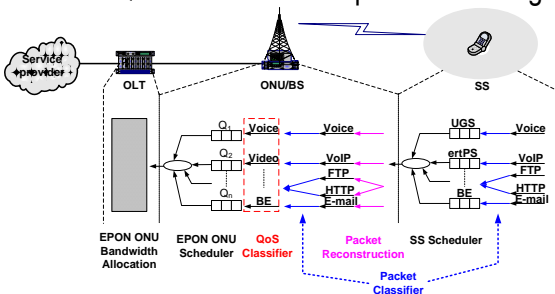


Figure 2. The relation between the centralized management of the data flows in the hybrid network and QoS classification

According to the centralized management of the data flows in the hybrid EPON – WiMAX network the authors proposed the algorithm for the effective ONU/BS operation (Fig. 3). First, the subscribers' stations (SS) create a log queries over WiMAX generator. The WiMAX requests' aggregator collects all these queries using the messages of the bandwidth requests. Then the queries are sent to the ONU/BS and classified according to the five classes of QoS: the unsolicited grant service (UGS), the extended real time polling service (ertPS), the real time polling service (rtPS), the non-real time polling service (nrtPS), the class of best effort (BE). The classification depends on the bandwidth management table (BMT).

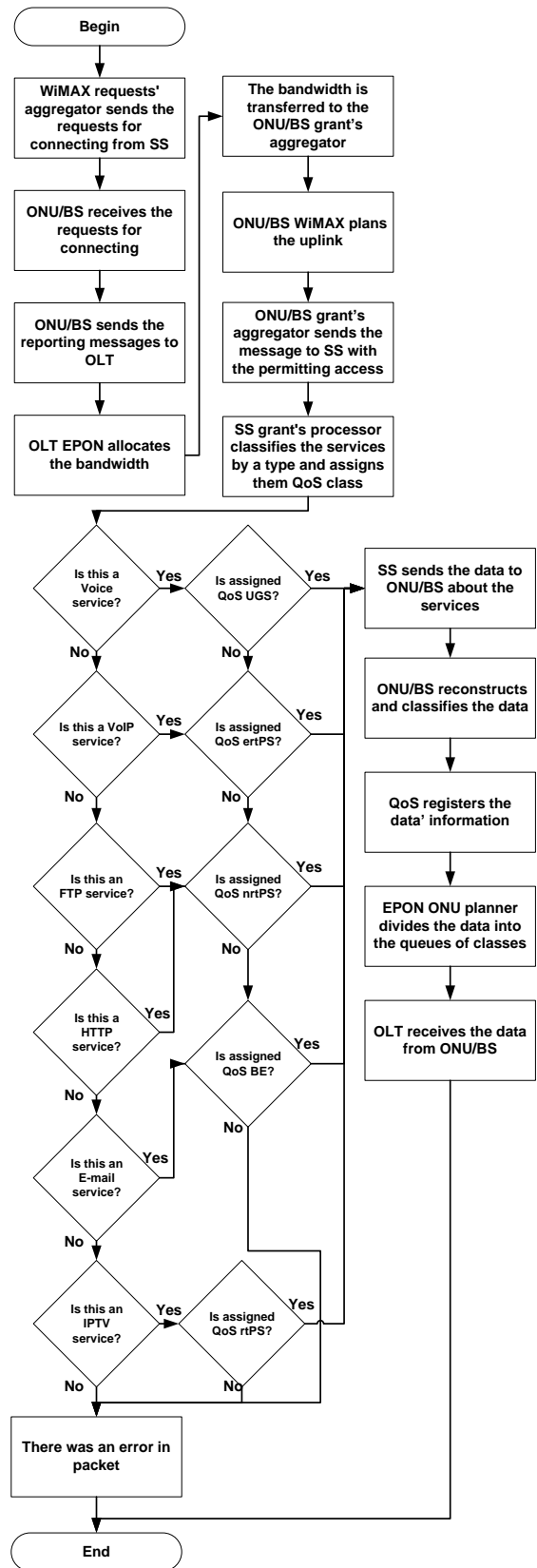


Figure 3. The proposed algorithm of ONU/BS operation in the hybrid EPON – WiMAX access network

The EPON services' classes have given bandwidth, which is transmitted using the GATE messages into the EPON grant processor. When the bandwidth is assigned to the ONU/BS, the scheduling of WiMAX uplink provides the bandwidth to the subscribers'

stations according to the BMT instructions. The uplink data transmission and the classification of the different types of services are executed in the subscribers' stations (SS). The planned data traffic from UGS to BE reaches only the ONU/BS node. The data is multiplexed into the queues' priorities after the quality classification. EPON ONU planner transmits the data traffic with the QoS records to the OLT. At the end of the transmission, the data traffic is transmitted from the SS directly to the OLT, thus reducing the delay of the data packets transmission.

3. THE MATHEMATICAL MODEL FOR THE HYBRID ONU/BS NODE

The mathematical model of the hybrid ONU/BS was created in order to evaluate the processing delay of the data packets in this node. The proposed algorithm for the delay evaluation of the packets transmission is presented in Fig. 4. The model is applied for the hybrid ONU/BS of the centralized planning. The mechanism of the centralized planning starts later than the packets leave the ONU/BS node. In this case, the instantaneous transfer of the data is approaching during the cycle or a frame. All reservation of the bandwidth is performed through the SS and the ONU/BS. The duration of the cycle (CT) or the frame (FT) varies from 2 ms to 5 ms [8]. The packets' delay T of the hybrid optical – WiMAX access network can be calculated [8]:

$$T = T_{poll} + T_{grant} + T_{queue}; \quad (1)$$

here T_{poll} – the time between the packet arrival and the next request from ONU; T_{grant} – the time between the request from ONU and the permission from OLT; T_{queue} – the queuing delay after the permissions from OLT.

The time between the packet arrival and the next request from ONU is evaluated using

$$T_{poll} = \frac{T_{max}}{2}; \quad (2)$$

here T_{max} is the maximum polling during the cycle (3).

$$T_{max} = N_{BS}^{ONU} \cdot \left(G + \frac{W_{max}}{R} \right); \quad (3)$$

here N_{BS}^{ONU} marks the number of ONU and BS; G is the guard time between the transmission windows; W_{max} is the maximum size of the transmission window; R is the uplink transmission rate of EPON.

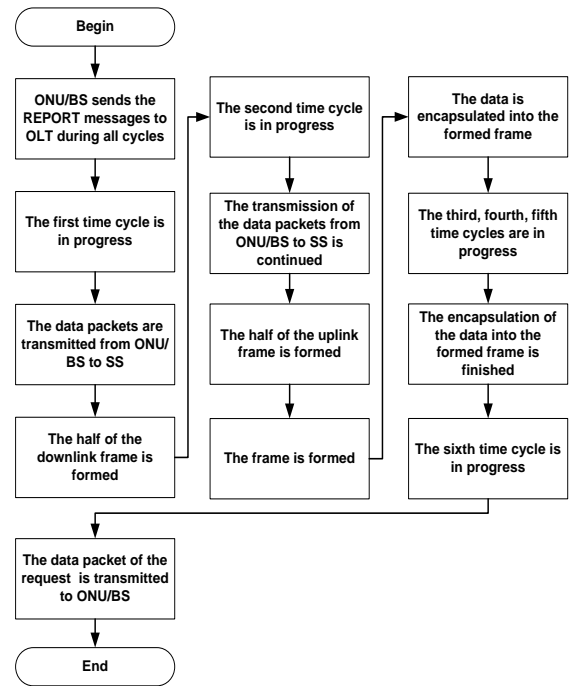


Figure 4. The proposed algorithm for the delay evaluation of the packets transmission

4. THE INVESTIGATIONS OF THE PROCESSING TIME OF UPLINK AND DOWNLINK DATA TRAFFIC OF THE DIFFERENT SERVICES

The simulation tests of the processing time evaluation of uplink and downlink data traffic of the different services were carried out using the software of Java Modelling Tools v.0.8.0. The structure of the simulated uplink hybrid ONU/BS node is presented in Figure 5 and the structure of the simulated downlink hybrid ONU/BS node - in Fig. 6. The characteristic, that was analyzed, is the delay analyzed as the dependence of the services' processing time on the load of the ONU/BS.

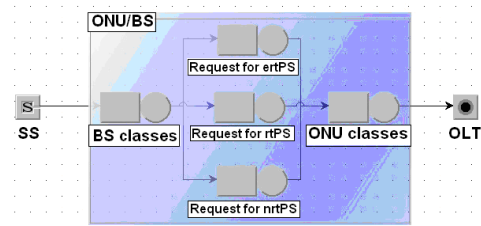


Figure 5. The structure of the simulated uplink ONU/BS

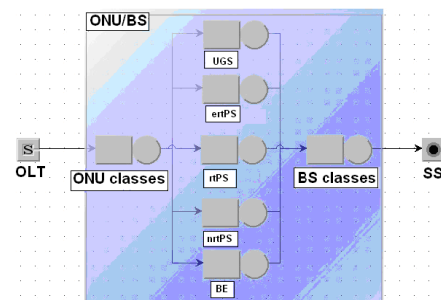


Figure 6. The structure of the simulated downlink ONU/BS

The uplink ONU/BS is when the users send the requests for the service to the OLT. The downlink ONU/BS is when the OLT transmits the services to the users. The investigation of the hybrid optical – WiMAX access network was carried out in two ways: a) when there is one hybrid ONU/BS node in the network; and b) when there are N hybrid ONU/BS nodes in the network. The initial data, used in simulation, are presented in Table 1. The investigation of one hybrid ONU/BS node in the network was carried out when the intensity of the data packets' flow λ was described in the different laws of the different types of services: the exponential distribution – for the UGS and ertPS; the Pareto distribution – for the rtPS and nrtPS; the burst normal distribution – for the BE services.

Table 1. Parameters used in simulation

Parameter	Value
The number of ONU/BS nodes N	16
The guard time G	5 μ s
The maximum size of the transmission window W_{max}	750 B
The uplink transmission rate of EPON R	10 Mbps
The duration CT	5 ms
The length of the queue Q	600 packets
The length of the waiting permission W_P	250 B
The intensity of the data packets' flow λ , packets/s	UGS – 10 ertPS – 15 rtPS – 25 nrtPS – 15 BE – 35
The intensity of the processing of data packets' flow μ , packets/s	UGS – 550 ertPS – 550 rtPS – 550 nrtPS – 750 BE – 750

The intensity of the processing of data packets' flow μ was described in the exponential distribution with the limited capacity of the buffer.

The results of this investigation are presented in Figures 7 and 8.

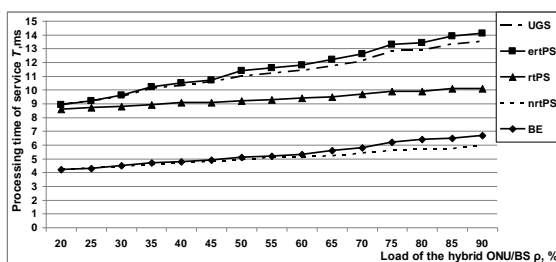


Figure 7. The service's processing time versus the load of ONU/BS in the uplink

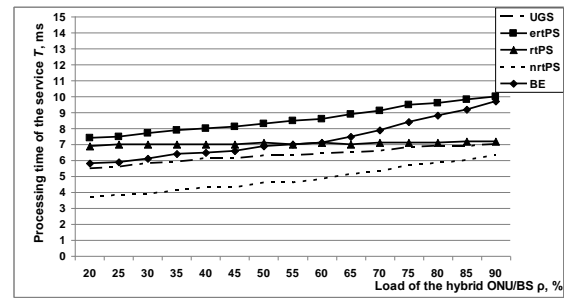


Figure 8. The service's processing time versus the load of ONU/BS in the downlink

According to the results from Fig. 7 and Fig. 8, it can be seen, that the uplink delay is longer than the downlink delay, except the BE service. The average processing time of the uplink services is longer in 1.9 times for UGS service, 1.4 times for ertPS and rtPS services, 1.1 time for nrtPS service in comparison with the downlink. The average processing time of the uplink service is shorter in 0.7 times only for BE. The processing time of BE service in the downlink ONU/BS varies from 5.8 ms to 9.7 ms, according to the load of the ONU/BS.

The results of the investigation, when there were N hybrid ONU/BS nodes in the network, are presented in Figures 9 and 10.

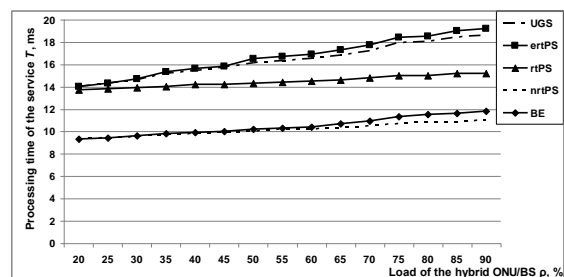


Figure 9. The service's processing time versus the load of ONU/BS in the uplink

According to the results in Fig. 9 – 10, when there are 16 hybrid ONU/BS nodes, it can be stated, that the uplink delay is longer than the downlink delay, except the BE service. The average processing time of the uplink is longer in 1.5 times for UGS service, 1.3 times for ertPS, and rtPS services; 1 time for nrtPS service in comparison with the downlink. It is shorter in 0.8 times for BE service.

The processing time of BE service in the downlink ONU/BS varies from 10.9 ms to 14.8 ms.

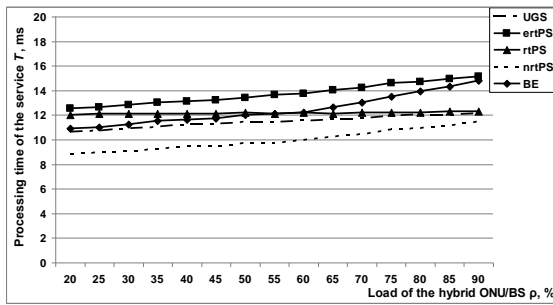


Figure 10. The service's processing time versus the load of ONU/BS in the downlink

5. CONCLUSIONS

In this paper, the authors investigated the optical – WiMAX hybrid access network and proposed the algorithm of the effective ONU/BS operation in this network. According to the obtained results, it can be stated, that using the proposed algorithm for the ONU/BS operation:

- the processing time in ONU/BS of rtPS and ertPS services are 29% shorter in the downlink than uplink, when was investigated one hybrid access node in the network;
- the processing time in ONU/BS of rtPS service is 19% shorter and the processing time of ertPS service – 21% shorter in the downlink compared with the uplink, when was investigated 16 hybrid access nodes in the network.

The obtained results of the investigation allow to state, that the proposed algorithm for the operation of the hybrid ONU/BS node enables to process more effectively the users' requests for the real – time services, such as VoIP or video, even with the increasing load of the access node in the hybrid optical – WiMAX network.

References

- [1] Shumao Ou, et al. "A control bridge to automate the convergence of passive optical network and IEEE 802.16 (WiMAX) wireless network", Proceedings of the 5 International Conference on Broadband Communications, Networks and Systems, September, 2008.
- [2] Kim, Min-Gon., et al. "Distributed antenna-based EPON-WiMAX integration and its cost-efficient cell planning", IEEE Journal on Selected Areas in Communications, vol. 28, no. 6, South Korea, 2010, pp. 808 – 817.
- [3] Gangxiang Shen, Rodney S. Tucker, Chang-Joon Cha. "Fixed Mobile Convergence Architectures for Broadband Access: Integration of EPON and WiMAX", IEEE Communications Magazine, vol. 45, no. 8, Melbourne, 2007, pp. 44 – 50.
- [4] Chowdhury, P., et al. "Hybrid wireless-optical broadband access network (WOBAN): prototype development and research challenges", IEEE Network, vol. 23, no. 3, California, 2009, pp. 41 – 48.
- [5] I-Shyan Hwang, Jhong-Yue Lee. "Performance Study of Homogeneous Uplink Scheduling in Hybrid ONU-BS Architecture", Proceedings of the International MultiConference of Engineers and Computer Scientists, March, 2011.
- [6] Ghazisaidi, N., Maier, M. "Fiber-Wireless (FiWi) Networks: A Comparative Techno-Economic Analysis of EPON and WiMAX", Proceedings of IEEE GLOBECOM, November and December, 2009.
- [7] Ranaweera, C. "Quality of service assurance in EPON-WiMAX converged network", Proceedings of the International Topical Meeting on Microwave Photonics, October, 2011.
- [8] Bokrae Jung, et al. "Centralized Scheduling Mechanism for Enhanced End-to-End Delay and QoS Support in Integrated Architecture of EPON and WiMAX", Journal of Lightwave Technology, vol. 28, no. 16, South Korea, 2010, pp. 2277 – 2288.

EXPERIMENTAL STUDY ON THE ATMOSPHERIC ATTENUATION EFFECTIVE ON AUDIO SIGNALS IN FREE SPACE LASER COMMUNICATION LINKS

Jassim Mohammed Jassim

Babylon University - College of Science for Women, Iraq
E-Mail: jassimm2007@yahoo.com

Abstract

In this work an experimental study on the effects of the atmospheric attenuation on audio signals carried by a laser beam in Free Space Laser Communication system. Both of the attenuation factors, absorption & scattering has been studied utilizing a frosted glass test cell for environment simulation conditions. The results show an effective change on the signals amplitude & pulse duration for different locations of the test cell with respect to the receiver. Far-field location produce defocusing effects while near field location show focusing effects which reflects on the received signal quality. Where an improvement of 200% has occurred due to low divergence. Assuming constant noise effects in all of the system, the experimental results show an effective reduction in the S/N ratio and increase in the bit error rates.

1. ATMOSPHERIC EFFECTS

Absorption is caused primarily by the water vapour (H₂O) and carbon dioxide (CO₂) in the air along the transmission path [1]. Gases in the atmosphere have many resonant bands, called transmission windows, which allow specific frequencies of light to pass through [2]. These windows occur at various wavelengths. Absorption is not generally a big concern in an infrared laser transmission system. Scattering has a greater effect than absorption. The atmospheric scattering of light is a function of its wavelength and the number and size of scattering elements in the air. The most common scattering elements in the air that affect laser beam transmission are fog and smog, rain, and snow [3].

2. NOISE IN FREE-SPACE OPTICAL COMMUNICATION

2.1. Bit error rate (BER) in Present of Atmospheric Absorption and Scattering

A laser beam propagation through the a atmosphere is attenuated by absorption and scattering due to the presence of aerosols , dust , smoke, fog, clouds, rain, snow and atmospheric molecules. In this paper we focus only to the optical propagation causing absorption and scattering. First calculate the received signal power for a lasercom system for a given range and extinction (combined absorption and scattering). Consider a laser transmitting a total power Transmitter the wavelength 650 nm. The signal power received at the communications detector can be expressed as [4]

$$P_R = P_T \frac{A}{(\theta_T L)^2} * \tau * \tau_R * \tau_T \quad \text{---1}$$

where A is the active area , θ_T is Beam divergence , τ is the atmospheric transmittance, τ_T is the transmitter optical efficiency and τ_R is the receiver optical efficiency. The detector noise that comes from the background power and the inherent detector noise, the amount of the generated current in photodetector (i_s) depends on the incident optical power on the photodetector P_r (μW), and the responsivity R_λ (A/W), the photocurrent induced by the received optical signal is given by

$$i_s = G * P_R * R_\lambda \quad \text{---2}$$

G is the photo detector gain ,for a Photodiode, we take G = 1.

There are 2 major detector noises in reception circuit: Thermal noise and Shot noise. Thermal Noise (Johnson or Nyquist noise), this is caused by a random electron movement in the load resistor R_L due to thermal energy. The value of thermal noise current, is given by [5]:

$$\langle i_{th}^2 \rangle = \frac{4kT \Delta f}{R_L} \quad [A^2] \quad \text{---3}$$

where K: Boltzmann's constant, T is the temperature in Kelvin, Δf is the spectral frequency. Finally, R_L is the loading resistor and i_d is the dark current.

And the Shot Noise (Quantum Noise), this is caused by a random fluctuation in electron-hole pair

generation in photodetector. The value Shot noise current, is given by [5]:

$$\langle i_{sh}^2 \rangle = 2e\bar{I}\Delta f \quad [A^2] \text{-----4}$$

where e = electron charge and \bar{I} = average current (dc current) = $I_{dc} + I_D$

2.2. Signal to Noise Ratio

The signal to noise ratio (S/N) is determined experimentally, as a ratio between the final output receiver voltage V_{ph} or current signal i_{ph} or photocurrent power P_{ph} and the voltage noise V_n (or current noise level i_n or noise photocurrent power P_n). The signal to noise ratio (S/N) is expressed in decibel [6].

$$SNR = \frac{(RP_r)^2 R_L}{2eR_L(I_D + RP_r)\Delta f + 4kT\Delta f} \text{-----5}$$

If the incident optical power is high. The dark current is very small compared to the average signal current, so that I_D can be dropped. Also, the shot-noise power is much larger than thermal power.

$$2eR_L(I_D + RP_r)\Delta f \approx 2eR_L(RP_r)\Delta f \gg 4kT\Delta f$$

Then we have

$$SNR = \frac{RP_r}{2e\Delta f} \text{-----6}$$

This is called "Shot-noise-limited" or "Quantum limited", but if the incident optic power is low. Thermal is dominating over the shot noise [7].

$$4kT\Delta f \gg 2eR_L(I_D + RP_r)\Delta f$$

$$SNR = \frac{(RP_r)^2 R_L}{4kT\Delta f} \text{-----7}$$

This is called "Thermal-noise-limited".

2.3. BER in digital modulation:

Bit Error Rate (BER) is a measurement of digital system quality. Noise makes it difficult to distinguish "0" from "1". BER is probability of error in "0" or "1" bit detection. In digital communication systems, $BER \leq 10^{-9}$ is good enough for many applications. The receiver will use a reference threshold current to decide whether it is "0" or "1" as

$\langle i_s \rangle > \langle i_{th} \rangle$ then assigns "1"

$\langle i_s \rangle < \langle i_{th} \rangle$ then assigns "0"

The BER can be expressed as [8]

$$BER = \frac{\exp(-SNR/2)}{(2\pi SNR)^{0.5}} \text{-----8}$$

3. EXPERIMENTAL DESCRIPTION

The general process of laser communications is to load information (speech, images) into the carrier, upon the transmitter processing (coding, modulation), the information contained in laser wave and transfer to reach the receiver, the receiver will process the received signal (amplification, decoding), the signal restored to the original information, as shown in fig. 1 The signal is modulated by the modulation circuit and loaded in a 80 KHz square wave on the other side to wave pulse width modulation, and thereby drive the semiconductor laser modulation signals, so that issuing a series of laser pulses of light modulation by the sound, the light pulse into the test cell (Frosted Glass), when the laser passes through the frosted glass with a rough surface its scattering or transmitting and the light beam interference, there will be randomly distributed bright spots and dark spots in different shape and size in the region near the space of the test cell surface, as show in fig.2 .The laser is received by photodiode receiver and restored back to electrical signals. At this time we can observe from the oscilloscope all signals. The parameters used in FSO calculations are shown in table 1.

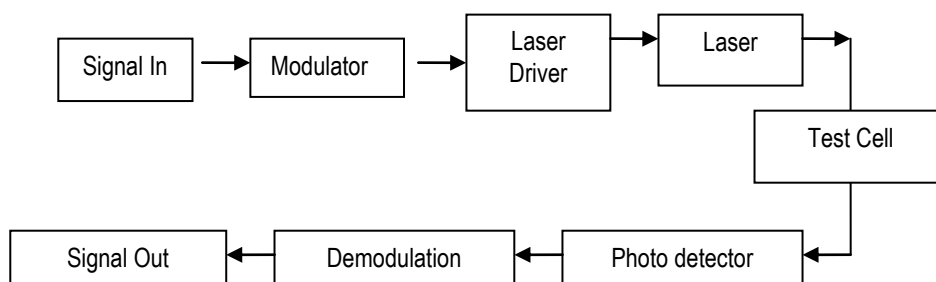


Figure 1. Block diagram of experiment setup

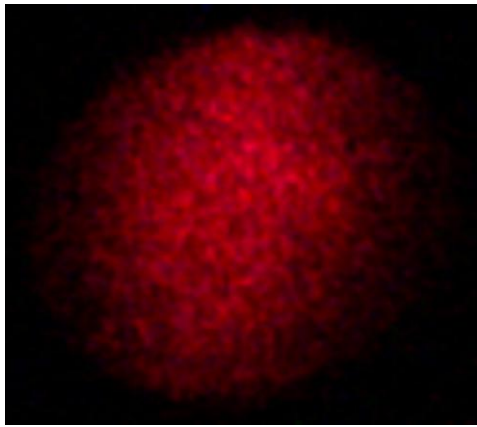


Figure 2. laser spot after passes through the frosted glass

Table 1. Parameters used in FSO calculation

Parameter	Values
Transmitter optical power(mw)	5
Laser Wavelength (nm)	650
Beam divergence	<2 mrad
Photodetector Spectral range	390 - 900 nm
Spectral sensitivity @ 650nm	0.50 A/W
Bandwidth	240 MHz
Active area	1 mm ²
Transmitter efficiency	1
Receiver efficiency	1
Background noise	0dB
Dark Current	0.35 nA
Total current noise	17.5 nA

4. RESULTS

4.1. Effective the test cell on beam propagation

The level of turbulence strength is controlled by placing the same frosted glass near and far away from the FSO transmitter. Ray tracing diagram in Figure 3 illustrates this concept. The optical beams shown in both Figure 3(a) and (b) could approximately experience the same degree of bending due to the same level-controlled turbulence source is used, however due to geometry configuration fluctuated in power will be collected at the receiver and desperation the pulse duration of signals shown in Figure 4(a,b and c).

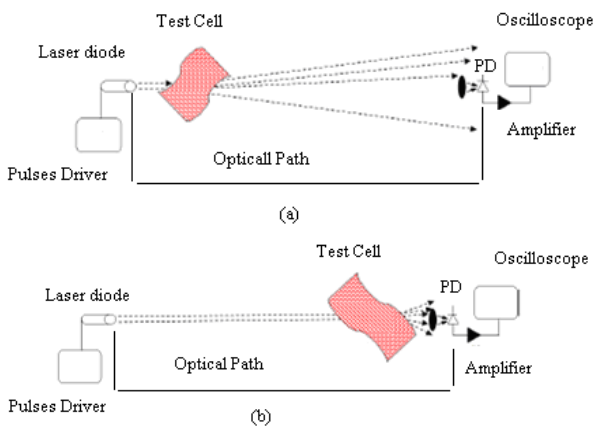
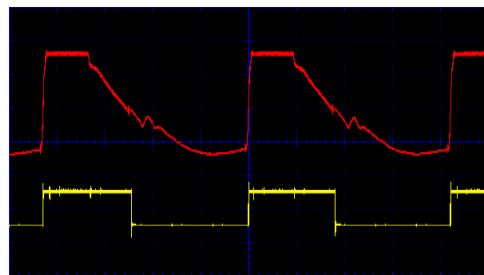
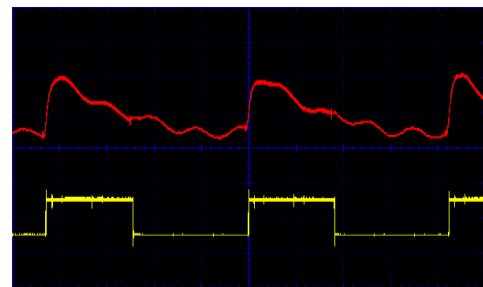


Figure 3. Sketch of diverted beams due to turbulence source positioned (a) near the transmitter and (b) near the receiver



(b)



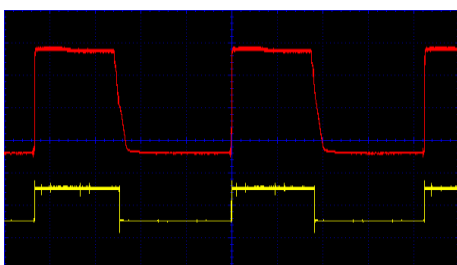
(c)

Figure 4. The measured eye diagram of received signal in the condition of (a) no turbulence, (b) medium turbulence (c) weak turbulence

4.2. BER as a Function of Received Power

The theoretical and experimental calculations of the received optical signal power and S/N variation with atmospheric transmittance of the system can be calculated by substitute the values from table (1) in equation (1), (2) and (7) we obtain the table (2).

Fig. 2 illustrates empirical result for the BER performance of FSO links for various of different of received power between (200 –1000) μ W this effective directly on SNR between (75 -90) dB. As the figure clearly illustrates, the improves BER with the increasing received optical power.



(a)

τ atmospheric transmittance	P_r (theoretical) μW	I_s (theoretical) μA	S/N (theoretical) dB	P_r (experimental) μW	I_s (experimental) μA	Table 2: The received power and S/N (theoretical and experimental) as a function of Atmospheric transmittance S/N (experimental) dB
0.3	375	187.5	80.5	208	104	75
0.4	500	250	83	370	185	80
0.5	625	312.5	85	450	225	82
0.6	750	375	86.6	553	276	84
0.7	875	437.5	88	648	324	85
0.8	1000	500	89	750	375	86.6
0.9	1125	562.5	90	887	443	88
1	1250	625	91	1012	510	89.3

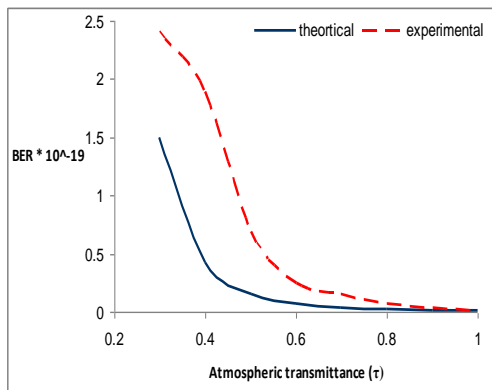
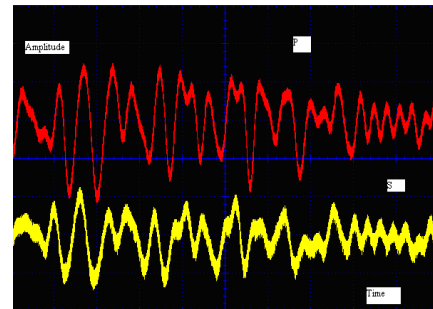


Figure 2. The theoretical and experimental of the BER as a function of atmospheric transmittance

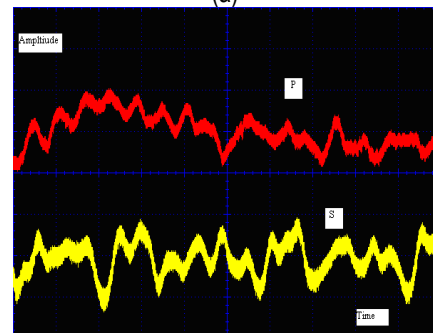
4.3. Effective the weather conditions on Quality speech

The speech 'input' and 'output' signals are illustrated in fig.4. It is evident that the synthesised speech signal at the receiver correlates well with the original analogue speech signal, under three different weather conditions (T of 100 %, 50 % and 30 %). the quality of the decoded speech signals at the receiver dependent on the error bit rate for $T = 100 \%$ the atmosphere no effective in power transmitter lead to low bit error rate and getting good quality speech but for $T = 50 \%$ and 30 %, respectively, thus indicating the considerable effect of atmosphere on the received signal quality lead to more bit error rate finally poor quality speech. The system is not capable of measuring bit error rate, its performance was assessed subjectively by applying an intelligibility test, which is the usual practice in speech communications trials, sometimes deciding on a comparison category rating. Many listeners were asked to judge the quality of the decoded speech signals at the receiver. As expected, they

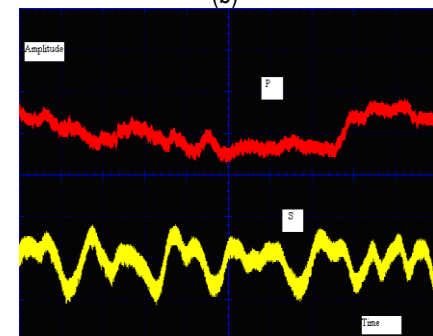
commented that the subjective quality between good and poor dependent on the weather conditions.



(a)



(b)



(c)

(p) synthesised speech signal at the receiver (s) Analogue speech signal for transmission

Figure 5. Speech Signal received at different weather conditions (a-T 100 %,b- 50 % and c-30 %).

4. CONCLUSION

From the results, it has been shown that the performance deteriorates with high values of BER. Also the maximum distance of free space optical link is limited by the noise and atmospheric attenuation. It is noticed that signal to noise ratio (SNR) decreases with the increase of the range and the bit error rate (BER) increases with increase of the range, the power budget increases, as the transmitted optical power increases, however it decreases, as the minimum detectable power increases.

References

- [1] Andrews L. C., "Free-Space Laser Propagation: Atmospheric Effects", IEEE Journal, Vol. 19, No. 5, P.6-8, October (2005).
- [2] H. Yuksel "Studies of the Effects of Atmospheric Turbulence on Free Space Optical Communications," Ph.D. Thesis, University of Maryland, 2005.
- [3] S. S. Muhammad, B. Flecker, E. Leitgeb and M. Gebhart, "Characterization of fog attenuation in terrestrial free space links," *Journal of Optical Engineering*, vol. 46, pp. 066001- 066006, 2007.
- [4] Air Fiber "The physical of Free Space Optics ", 2001.
- [5] A. Yariv, "Optical Electronics in Modern Communications" New York Oxford ,2007.
- [6] David G. Aviv "Laser Space Communications" Published by ARTECH HOUSE, 2006.
- [7] D. G. Baker, "Fiber Optic Design and Applications", Prentice-Hall, 1985.
- [8] Larry E. Andrews, Ronald L. Phillips, and Cynthia Y. Hoppen, *Laser Beam Scintillation with Applications*, SPIE Press, Bellingham, Washington (2001)

ON SOME ASPECTS OF THE FRACTAL SIGNATURE METHOD

N. B. Ampilova

Universitetsky pr.28, Faculty of Math.& Mech., Starii Peterhof, SPb, 198504,
Assoc. Prof. Comp. Sci. Dept, n.ampilova@spbu.ru

I. P. Soloviev

Universitetsky pr.28, Faculty of Math.& Mech., Starii Peterhof, SPb, 198504,
Assoc. Prof. Comp. Sci. Dept, i.soloviev@spbu.ru

Y. V. Shupletsov

Universitetsky pr.28, Faculty of Math.& Mech., Starii Peterhof, SPb, 198504,
Postgraduate student, shupaag@mail.ru.

Abstract

This work is devoted to a substantiation of the fractal signature method and an investigation of its applicability for digital images of different classes. The dependence on the color scale (grayscale and HSV) is demonstrated. The applicability of the method to the images with similar textures but belonging to different classes is also discussed.

1. INTRODUCTION

The main dimension in fractal analysis is the Hausdorff dimension, but in practice so called box computing (or box-counting) dimensions are used. The well-known capacity dimension [3] belongs to this class. To analyze digital images the Minkovsky dimension seems to be more preferable, because it is equal to capacity dimension for nonempty bounded sets in R^3 and is simple to calculate.

To analyze and classify textures the method of calculation of Minkovsky's dimension was proposed in [6]. It is based on the Mandelbrot idea [5] about the approximate calculation of the length of coastline by measuring the area of a strip that contains the line and has width 2δ , where δ is a fixed number. Then the length is approximately the area divided by 2δ . The authors applied this method to measure the area of a gray level surface constructed by a digital image. Then the sequence of special blankets is constructed over the surface. For every blanket its volume is calculated, the surface area and the so called "fractal signature" (the ratio of the log of the surface area to the log of the scale) is defined. The Minkovsky dimension of the area may be easily obtained from the fractal signature. So we have a sequence of areas and signatures in accordance with the number of blankets. For two images we can compare the obtained signature vectors: the closeness between vectors shows the textures adjacency. In [7] the authors applied the

method to calculate the document fractal dimension and called it the "modified fractal signature method". They used only two consecutive blankets. In such a variant the method demonstrated high reliability and was successfully used in [1] and [4] to classify both biomedical preparations and ISAR radar images.

In this work problems of substantiation and applicability of the method are discussed. Though empirical enough, this approach demonstrated good results in experiments described in [7], [1], [4]. The dependence experimental results on the color scale is demonstrated as well.

2. METHODS OF ANALYSIS

2.1. Mandelbrot task

When studying the problem of coastline length measurement B. Mandelbrot came to conclusion that such lines have complex geometry, a direct measurement is rather difficult, and hence one can find this value only approximately [5]. He suggested the following methods.

1. Take a stick of length δ (step) and walk along the coastline, i.e change the coastline by a polygon made from segments. If $N(\delta)$ – the number of steps then the length $L(\delta) \sim N(\delta)\delta$. The problem is that when the step size decreases, the observed length $L(\delta)$ increases without limit. The empirical study of the length changing per-

formed by L. Richardson showed that $(\delta) \sim F\delta^{-D}$, where F and D are constants depending on the type of the line. Then we have $L(\delta) \sim F\delta^{1-D}$. It is interesting to mark that the Richardson results count in favour of the main assumption which is introduced when the class of box-computing dimensions is considered, namely: $N(\delta) \sim \delta^{-D}$, where D is a fractal dimension.

2. Consider all the points with distances to the coastline of no more than δ . They form a strip of width 2δ . Then the strip area divided by 2δ is an approximation to $L(\delta)$. Here, too, the length increases as δ decreases. At the same time Mandelbrot noted that there is an interval for δ in which the value $L(\delta)$ becomes stable.

2.2. The approximation of a line length

In [6] the authors considered a modified variant of the second Mandelbrot method, namely: a) the approximation of a given curve by a piecewise constant function; b) the using a modified formula for calculation of the strip area.

To explain their method we consider the following example.

Let a piecewise constant function $x(i)$ be defined on intervals $[i, i+1)$, $i=1 \dots 10$. Let $\delta = 0$ and denote upper and low approximating boundaries for the initial curve $x(i)$ by u_δ and v_δ respectively. Construct the strip of width 2δ by the following formulas: following formulas:

$$u_\delta(i) = \max\{u_{\delta-1}(i) + 1, \max\{u_{\delta-1}(i+1), u_{\delta-1}(i+1)\}\},$$

$$b_\delta(i) = \min\{b_{\delta-1}(i) - 1, \min\{b_{\delta-1}(i+1), b_{\delta-1}(i+1)\}\},$$

$$u_0(i) = b_0(i) = x(i).$$

The strip area is calculated as

$S_\delta = \sum_{i=1}^{n-1} (u_\delta(i) - b_\delta(i))$. To calculate the approximate curve length we can use two formulas:

$$L(\delta) = \frac{S_\delta}{2\delta} \quad (1) \quad \text{or} \quad L(\delta) = \frac{S_\delta - S_{\delta-1}}{2}. \quad (2)$$

Formula (1) was supposed by Mandelbrot, formula (2) was used in [6] as a more appropriate variant. Let $x(i)$ be defined as $(1, -1, 1, 1, 1, 0, 0, 3, -2, 0)$, i.e. $x(1)=x([1,2))=1$, $x(2)=x([2,3))=-1$, etc. (See Figure 1.) Then for $\delta = 1$ we have

$$u_1 = \{2, 1, 2, 2, 2, 1, 3, 4, 3, 1\},$$

$$b_1 = \{-1, -2, -1, 0, 0, -1, -1, -2, -3, -2\},$$

$$S_1 = 31, L(1) = 15.5.$$

On this step the length values obtained according to (1) and (2) ($L^1(\delta)$ and $L^2(\delta)$) coincide.

For $\delta = 2, 3, 4$ we have $S_2 = 50$, $L^1(2) = 12.5$, $L^2(2) = 9.5$; $S_3 = 68$, $L^1(3) = 11.3$, $L^2(3) = 9$; $S_4 = 86$, $L^1(4) = 10.8$, $L^2(4) = 9$.

It is easy to check that the length of the initial curve is equal to 9, so the using (2) leads to the result faster.

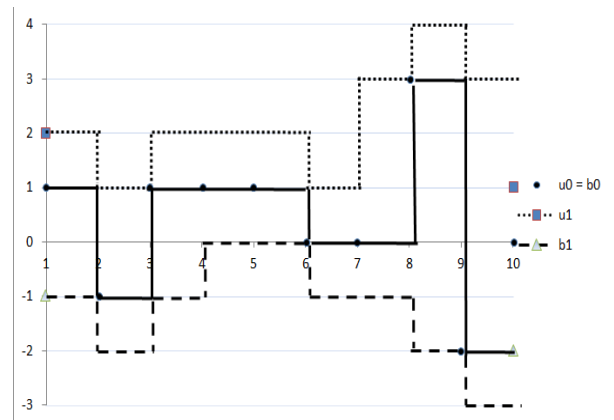


Figure 1. Covering blanket for one-dimensional case

2.3. The measuring a surface area

The described method may be applied to calculate approximately the area of gray level surface for an image. Let $F = \{X_{ij}, i = 0, 1, \dots, K, j = 0, 1, \dots, L\}$ be an image with multigray level and X_{ij} be the gray level of the (i, j) -th pixel. In a certain measure range, the gray-level surface of F can be viewed as a fractal. In image processing the gray level function F is a nonempty bounded set in R^3 . The surface area A_δ may be calculated using the volume of a special δ -parallel body — blanket with the thickness 2δ .

For $\delta=1, 2, \dots$ the blanket surfaces are defined iteratively as follows:

$$u_\delta(i, j) = \max \left\{ \begin{array}{l} u_{\delta-1}(i, j) + 1, \\ \max_{|(m,n)-(i,j)| \leq 1} u_{\delta-1}(m, n) \end{array} \right\},$$

$$b_{\delta}(i, j) = \min \left\{ \begin{array}{l} b_{\delta-1}(i, j) - 1, \\ \min_{|(m,n)-(i,j)| \leq 1} b_{\delta-1}(m, n) \end{array} \right\}.$$

The volume of the blanket Vol_{δ} is computed as

$$Vol_{\delta} = \sum (u_{\delta}(i, j) - b_{\delta}(i, j)).$$

By analogy with (1) and (2) one can use the following formulas for the surface area:

$$A_{\delta} = \frac{Vol_{\delta}}{2\delta} \quad (3)$$

and

$$A_{\delta} = \frac{Vol_{\delta} - Vol_{\delta-1}}{2}. \quad (4)$$

Fractal dimension of the surface is defined by the formula

$$D \approx 2 - \frac{\log_2 A_{\delta}}{\log_2 \delta}. \quad (5)$$

As it was noted in [6], the formula (3) is more preferable for pure fractal objects, whereas (4) is used both fractal and non-fractal surfaces. The application of (4) is necessary if Vol_{δ} depends on all smaller scales features: subtracting $Vol_{\delta-1}$ isolates those features that change from scale $\delta-1$ to δ . In what follows we use (4).

In [6] the authors calculated Vol_{δ}, A_{δ} and $S_{\delta} = \frac{\log_2 A_{\delta}}{\log_2 \delta}$ when δ changed from 1 to 49. For images I and J they computed the distance between them as the distance between obtained vectors $S_{\delta}(I)$ and $S_{\delta}(J)$:

$$\rho(I, J) = \sum_{\delta} (S_{\delta}(I) - S_{\delta}(J))^2 \log \frac{(\delta+0.5)}{(\delta-0.5)}. \quad (6)$$

For images having similar structures obtained vectors seemed to be close.

The authors also considered asymmetric method to calculate surface area, namely they use upper volume and low volume

$$Vol_{\delta}^{+} = \sum (u_{\delta}(i, j) - x(i, j)), \quad (7)$$

$$Vol_{\delta}^{-} = \sum (x(i, j) - b_{\delta}(i, j)), \quad (8)$$

and top area and bottom area respectively

$$A_{\delta}^{+} = Vol_{\delta}^{+} - Vol_{\delta-1}^{+}, \quad (9)$$

$$A_{\delta}^{-} = Vol_{\delta}^{-} - Vol_{\delta-1}^{-}. \quad (10)$$

Hence we have

$$S_{\delta}^{+} = \frac{\log A_{\delta}^{+}}{\log \delta}, \quad (11)$$

$$S_{\delta}^{-} = \frac{\log A_{\delta}^{-}}{\log \delta}, \quad (12)$$

and

$$\rho(I, J) = \sum_{\delta} ((S_{\delta}^{+}(I) - S_{\delta}^{+}(J))^2 + (S_{\delta}^{-}(I) - S_{\delta}^{-}(J))^2) 2 \log(\delta+0.5)(\delta-0.5). \quad (13)$$

For $\delta = 1, 2$ formulas (4) and (5) were used in [7] to estimate fractal dimension of different parts of text documents — text, graphic and background.

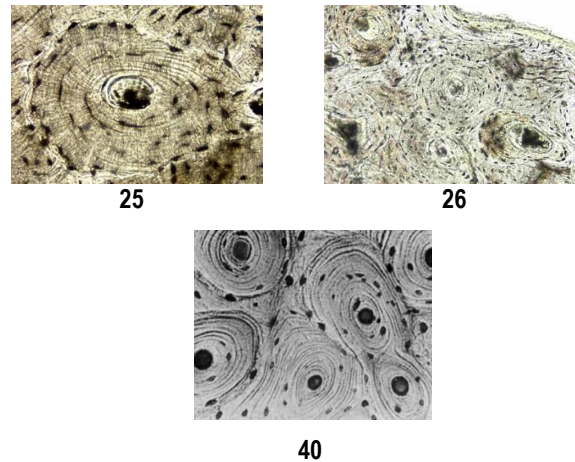
2.4. Color scale

It is known that the production of a color image is often a result of software application, whereas the image is monochrome (as in microscope, for example). The majority of mathematical methods of image analysis uses gray scale, but a transformation from one color scale to another may influence on the obtained results. It was shown in [2] that statistical characteristics calculated by the Haralick method do not allow classifying images from different classes when RGB is used. At the same time this classification was done for HSV palette.

3. EXPERIMENTAL RESULTS

It is easy to understand that the images having similar textures may have close vectors of features. The opposite is wrong: the similarity of textures not always follows from small distance between vectors, i.e. this is necessary but insufficient condition. Sometimes this situation may be corrected by the applying the asymmetric method or changing of palette (color). Consider some examples.

3.1. Health bone tissue (1)



The symmetric method gives the following results: $\rho(25,26)=0.09026$, $\rho(25,40)=0.06453$, $\rho(26,40)=0.07607$. Taking the minimal distance we

come to conclusion that 25 and 40 are close. The classification result is right. Moreover, in this case we could assume that these images belong to the same class (with the distance 0.09026).

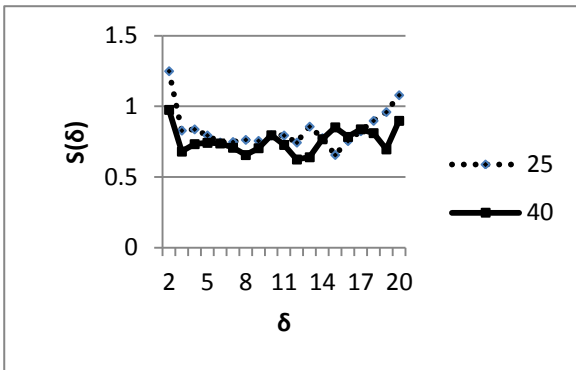
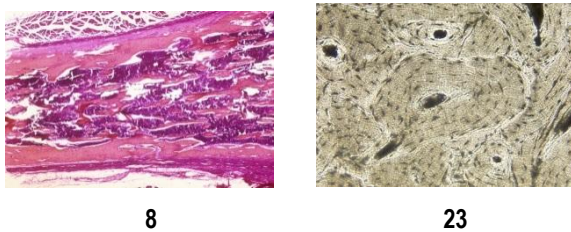


Figure 2. Close vectors for similar textures

3.2. Health bone tissue (2)



The result of symmetric method is 0.04113 (minimal in this class). As a misclassification occurred, asymmetric method was applied. The obtained distance 0.45156 seemed to be minimal in the set of images, hence a misclassification occurred again.

3.3. Affected bone tissue



The symmetric method showed the closeness of vectors – the distance 0.0649 is minimal for the given class. But it is easy to see that the pictures are quite different. The asymmetric method corrected the misclassification with the distance 0.235 which is not minimal. It is interesting to note that when using HSV palette we obtain the result by applying only symmetric method (Figure 5).

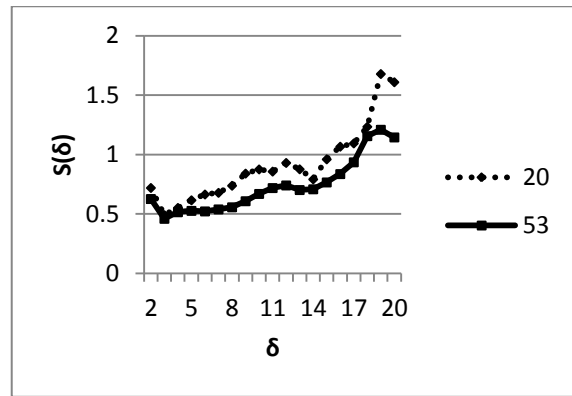


Figure 3. Close vectors for nonsimilar textures – symmetric method

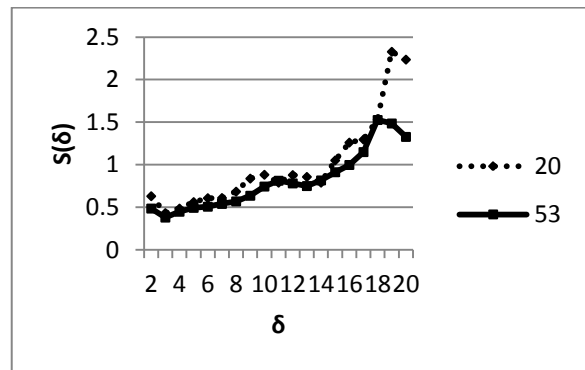
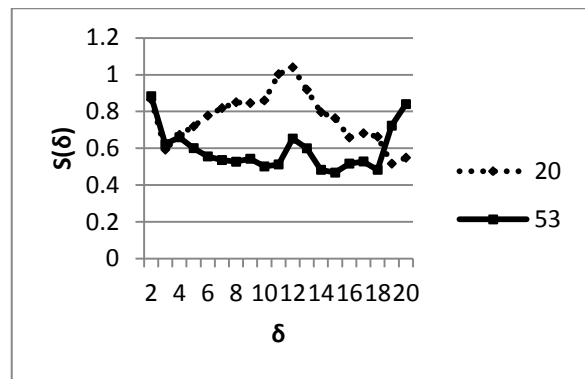


Figure 4. Nonsimilar textures – asymmetric method; S^+ (upper) and S^- (low)

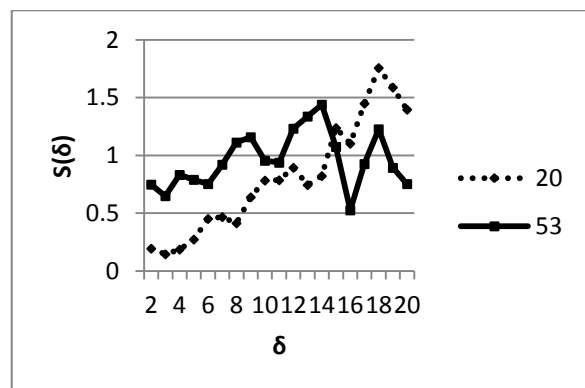


Figure 5. Symmetric method for HSV

3.4. Color scale

As we see in the case 3.2 misclassification occurred both symmetric and asymmetric method. Hence we used HSV scale (component h). The symmetric method in this scale showed the distance 1.92, not minimal. So, the images are not similar.

CONCLUSION

The fractal signature method is based on the Mandelbrot idea about the approximate measurement of the coastline length. In application to digital image analysis the construction of approximate surfaces is based on gray scale of pixels. The changing this scale by the definite rule (consecutive construction of blankets) may be considered as a changing of the image resolution. The application of the method to different classes of bone tissue images demonstrated that a primary classification have to be very accurate (size, color). Under these conditions it is sufficiently to use symmetric method. If a misclassification occurs symmetric variant or a color scale changing may help. But for more rigorous results it is necessary to apply additional methods.

Acknowledgements

The work was partially supported by the grant RFBR 13-01-00782.

References

- [1] N. Ampilova, E. Gurevich, I. Soloviev. Application of Modified Fractal Signature & Regny Spectrum Methods to the Analysis of Biomedical Preparations Images. Proc. 6 Int. Conf. CEMA11, 6-8 Oct. 2011, Sofia, Bulgaria. p. 96-100.
- [2] Batykov A.M. On the influence of color scale on the results of classification by the Haralick method. The collection of scientific papers SWorld. Materials of int. science-practical conference " Scientific investigations and their practical application. State-of-the-art and ways of development 2012". Odessa, 2012. V.3,N.3, p.103-107 (in Russian).
- [3] Falconer K.J. Fractal Geometry. Mathematical Foundations and Applications. John Wiley & Sons, 1990,288c.
- [4] Frangos P., Pandis C., Malamou A., Stefanias P.. Applying the modified fractal signature method to image classification: some preliminary results for ISAR radar images. Proc. 7 Int. Conf. CEMA12, 8-10 Nov. 2012, Athens, Greece . p. 50-52.
- [5] B. Mandelbrot. The fractal geometry of nature, W. H. Freeman and Co., 1982,480pp.
- [6] Shmuel Peleg, Joseph Naor, Ralph Hartley, David Avnir. Multiple Resolution Texture Analysis and Classification. IEEE
- [7] Xiaogang Mao, C. Y. Suen. Modified Fractal Signature (MFS): A New Approach to Document Analysis for Automatic Knowledge Acquisition. IEEE Trans. Knowledge and Data Eng., vol.9. no.5, 1997, pp. 742-762.

ON A NATURAL-SCIENCE INVESTIGATION OF THE ULTRALOW DOSES EFFECT

E. Y. Gurevich

Sofia & Jacobs Foundation, Italyanskaya str. 10/5, St. Petersburg 191186, info@organicproduct.ru

N. B. Ampilova

St. Petersburg State University, Faculty of Math. & Mech., Assoc. Prof. at Comp. Sci. Dept., 198504, SPb, Universitetsky pr.28, n.ampilova@spbu.ru

I. P. Soloviev

St. Petersburg State University, Faculty of Math. & Mech., Assoc. Prof. at Comp. Sci. Dept., 198504, SPb, Universitetsky pr.28, i.soloviev@spbu.ru

Abstract

Scientific and practical methods for studying ultralow doses effect are discussed. The importance of contemporary physics achievements in the construction of exact models is accentuated. The applicability of mathematical and computer modeling methods are also discussed.

1. INTRODUCTION

It is well known that any external factor (physical, chemical, etc.) acting on an organism in one way or another changes its functioning. As this takes place, a specific answer of the organism appears for any value (dose) of the action. Ultralow doses are used both in classical (acupuncture, electrophoresis) and homeopathic medicine, hence from this point of view the separation medicine on allopathic and homeopathic is artificial and conditioned by historical and economic reasons. As far as application of large doses of medicines may lead to side effects, many specialists suppose that low and ultralow doses provide` more delicate treatment.

Numerous researches show that in the network of the paradigm of classical medicine a study of ultralow doses effect is rather difficult. Recent advances in physics offer a clearer view of how these mechanisms work. Investigation in this area may promote considerably to the progress of so called conclusive medicine.

Many distinguished scientists made a contribution to the forming common approach to the study of complex biological systems. It was L. Boltzman who made an effort to reduce the biological evolution theory to thermodynamics and chemistry of 19 century and connected micro processes in an environment with its macro state. On this way he formulated the 2nd Law of thermodynamics (for a closed isolated system) in statistical form: the system en-

tropy S is proportional to the logarithm of the thermodynamic probability W of the system state, i.e. $S \sim \log W$. In fact he proposed to consider an integral characteristic of a system.

I. Prigogine, who investigated nonequilibrium processes in open systems (supposing that any system has an environment), also considered entropy as a system characteristic.

Russian biologist I. Shmalgauzen and physiologist P. Anohin asserted that the main property of an organism is the integrity that cannot be reduced to the sum of its elements. The founder of homeopathy H. Haneman also considered a man as a whole system and developed his treatment methods (based on ultralow doses application) in accordance with this approach.

Hence a system study of biological systems allows us to consider both qualitative and quantitative characteristics of common principles of their functioning. That leads to active application both mathematical and computer modeling.

From the point of view of modern science the occurrence of one or other macrophenomenon in a system (an organism) is a result of nonlinear interactions of its micro elements. Achievements in physics led to the elaboration and substantiation of these interactions, which are based on a special structure of water in alive tissues and the transfer of energy in biomolecula chains. It is important to note

that the supposed mechanism is the same for the processes generated by ultralow factors effect.

To analyze the results of ultralow effects one can use biotests (for example blood analysis, thermal imager data). It is the analysis of digital images that opens up possibilities to apply mathematical and computer methods to obtain comparative characteristics and classification signs of the images. In the paper we discuss the results of application both mathematical and computer methods to solve the problem concerning the methods of treatment using ultralow effects.

2. LOW AND ULTRALOW EFFECTS

In physics by low effects (or low signals) is meant both a measure of an action on an object and the value of the answer of the object. In classical sense the notion "experiment" means a purposeful action on an object that answers by a signal, and this signal should be measured. In this case it is implicitly assumed that when measuring only one acting factor is registered.

It should be noted that any effects, both low and ultralow, generate in a system a complex answer. But for low effects in the majority of cases the components of the answer are composed to a resulting signal, whereas for ultralow effects this does not take place.

In this situation we should estimate a change of a system state integrally and use biotests as indicators of such changes. The changes in biotest states really happen, are observed and may be experimentally registered.

3. ON A SUBSTANTIATION OF ULTRALOW DOSES METHOD

Basing on theoretical and experimental investigations of A. Sent-Dierdi, E. Burlakova [4], A. Kononov [7], L. Gall [6] and many others one can formulate the following:

- A set of biologically active substances, many of which are used as medicines, demonstrate in hyperweak solutions special properties that they have not in more concentrated ("classical") solutions. The answer of an organism on a drug substance action when consecutive decreasing its concentration is nonlinear and non-monotonic: for ultralow concentration the answer

may increase again. These properties are called "bimodal biological effect".

- These substances in hyperweak solutions show special physicochemical properties and form so called nanoassociates of rather large size (up to 200 nm).
- In addition these properties are observed only if solutions are saved no less than 18 hours in the magnetic field of the Earth, and not observed if the solutions are in a screening container.
- It is the magnetic field of the Earth that determines special properties of hyperweak solutions and acts the organizing role in all the structural processes concerning to water.

We note that used in homeopathy method of exponentiation of solutions gives the analogous properties to hyperweak solutions. Hence now the well-known ultralow doses method turns out to be explained and substantiated.

4. ON A PRACTICAL INVESTIGATION OF RESULTS

It should be noted that in the majority of cases in studies of complex biological system we cannot count on a mathematical model making. Hence we have to follow practical methods of investigation — experiments and measurements. Modern technologies put forward a wide spectrum of high-resolution hardware to measure and register processes elapsing in biological systems. The results of measurements may be obtained as digital images which are classified and analyzed by precise mathematical methods. The revealing an image structure and characteristics may considerably help a physician in diagnosing.

In analysis of such images statistical, texture, multifractal, morphological and spectral signs and their combinations are used. Many of these characteristics are invariant relative to wide class of image transformations, such as rotation, change of illumination, scaling. If there is a mathematical model of a process under investigation (described by a system of equations), one can use numerical methods to find a solution. All these methods may be applied to elaborate modern software and hardware instruments in investigations and treatment when using homeopathic medicines and other methods of conclusive medicine.

Consider examples of application of different mathematical methods.

4.1. Mathematical morphology

Investigation of blood crystal images obtained by "sensitive crystallization" by E.Pfaifer. The method is based on addition of blood to a solution of cuprum chlorides. In the book of A.Selavri [10] the method to study blood crystals to define malfunctions of organs and pathological processes has been described. For blood the crystallization by cuprum chlorides is a sensitive morphological test. The application of rigorous mathematical methods to different kinds of blood crystal allows us to extract many features such as regular areas, cavities and structures. In [11] such images were classified by the methods of mathematical morphology. Figure 1 shows typical blood crystal images [10]:

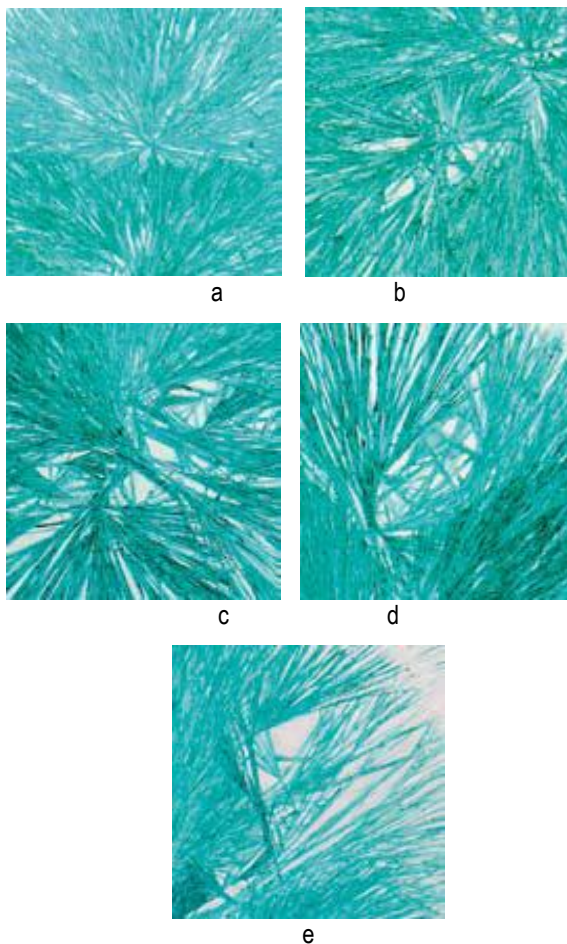


Figure 1. Blood crystals

- (a) crystallization in the star form, which is typical for acute inflammatory process;
- (b) crystallization in the star form with hole structure, which is typical for chronic inflammatory process;

(c) hole structure of crystals – typical for degenerative processes;

(d) hollow form of the crystal, benign tumor;

(e) hollow form of the crystal with transversal structures, malignant tumor.

4.2. Fractal analysis

To classify pharmacological solutions of Ag containing different (low) doses of the substance the authors of [3] used Regny spectrum. The images of solutions with different concentrations of Ag and corresponding Regny spectra are shown on Fig. 2.

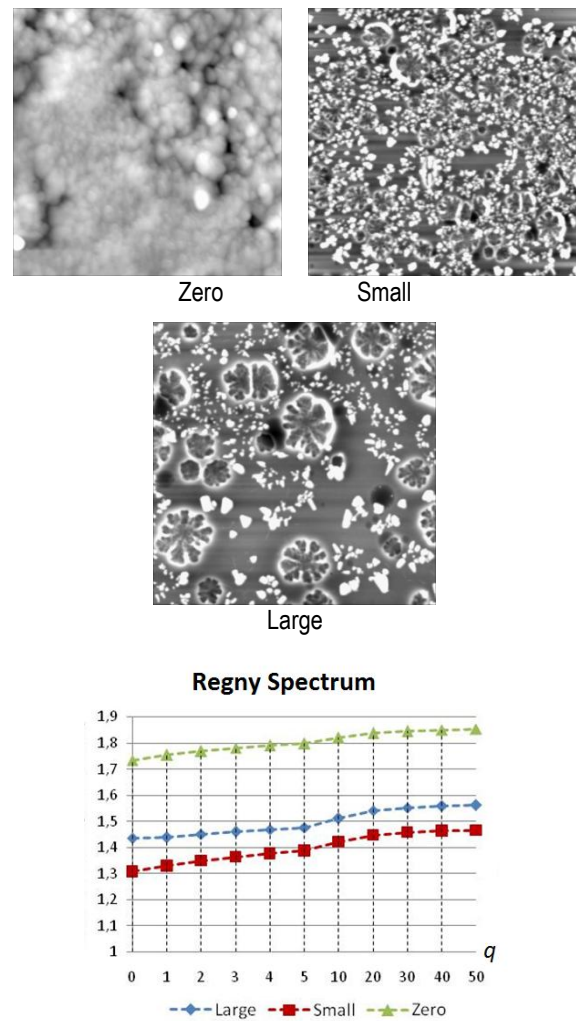


Figure 2. Fractal analysis of Ag solutions

4.3. Stationary processes on graphs

A method of a classification of images concerning to a substance propagation process was proposed in [1]. The image is considered as a lattice formed by pixels of given intensity. Then an oriented graph corresponding to the image is constructed in the following way: every vertex (pixel) is connected with N neighbours. For a given vertex all outgoing

edges have a value (pixel intensity/N), for boundary vertex – pixel intensity/(N-1). The constructed flow is normed. For obtained Markov chain by the Sheleikhovskiy-Bregman method a stationary distribution is constructed, which maximizes weighted entropy. It is weighted entropy that is used as a classifying sign when images with different doses of a substance are analyzed. In fact, weighted entropy may be considered as a time that is required for a distribution process to achieve a stationary state: the more concentration the more this time. For images shown on Figure 2 weighted entropy was equal to 0.0000025, 0.000013 and 0.000043.

4.4. Mathematical modeling

a) When a process may be described by a system of differential or difference equations, one can use numerical methods and the theory of dynamical systems to investigate the types of equilibrium states. In [5] the authors used differential equations with a small parameter and modeled the motion of ions in alive tissue under the influence of toroidal low frequency magnetic field. Studying the system behavior for various parameter values they obtained phase portraits. The conclusion of the physician concerning the effectiveness of treatment was based on both the results of measuring and corresponding phase portrait.

b) The study of the action of low frequency magnetic field in magnetotherapy devices is one of the most important problem in clinical practice. The papers [2,8,9] are devoted to the construction of space configuration of magnetic field for different configurations of the coils. The obtained numerical results and their visualization may be used to estimate the effectiveness of clinical procedure: changing the parameters of configuration a physician may choose a more appropriate regime.

CONCLUSION

Recent advances in physics, mathematics, computer science and their applications resulted in the substantiation of ultralow doses effect. There are various methods to measure states of a biological system when acting by such doses of medicines and other external factors. Numerical and experimental ways allows us to estimate the values of doses for which side effects would be minimal.

Acknowledgements

The work was partially supported by the grant RFBR 13-01-00782.

References

- [1] N. B. Ampilova. Stationary processes on graphs and image analysis. (in Russian). "Computer instruments in education", N.3 2013, p. 27-32.
- [2] N. B. Ampilova, D. Dimitrov, B. Kudrin. Mathematical modeling of low frequency magnetic field in systems for magnetotherapy. Proc. 8 Int. Conf. CEMA13, 17-19 Oct. 2013, Sofia, Bulgaria.
- [3] N. Ampilova, E. Gurevich, I. Soloviev. Application of Modified Fractal Signature and Regny Spectrum Methods to the Analysis of Biomedical Preparations Images. Proc. 6 Int. Conf. CEMA11, 6-8 Oct. 2011, Sofia, Bulgaria. p. 96-100.
- [4] E. Burlakova, A. Konradov, E. Maltseva. The action of ultralow doses of biologically active substances and low intensity physical factors. 4 Int. Symposium "Mechanisms of ultralow doses actions", 28-29 Oct. 2008, Moscow. Book of abstracts, p. 123-149.
- [5] Dimitrov, D. Dimitrov, S. Guergov, A. Savov. Investigation of motion of ions in alive tissue under influence of toroidal low frequency magnetic field. Proc. 7 Int. Conf. CEMA12, 8-10 Nov. 2012, Athens, Greece. p. 114-117.
- [6] L. N. Gall. Bioenergetica– the magic of life (in Russian), SPb, 2010.
- [7] Kononov. Effect of ultra-low concentrations and electromagnetic fields. Proc. of Int. Congress "Low and ultralow fields and radiations in biology and medicine", SPb, 2012, p.77.
- [8] Kudrin, A. Dimitrov The algorithm for visualization of low-frequency magnetic signals in systems for magnetotherapy. Proc. 8 Int. Conf. CEMA13, 17-19 Oct. 2013, Sofia, Bulgaria.
- [9] Kudrin, A. Dimitrov. Computer visualization of low frequency magnetic signals in systems for magnetotherapy with variable parameters. Proc. 8 Int. Conf. CEMA13, 17-19 Oct. 2013, Sofia, Bulgaria.
- [10] Selavri. Fuctional types of metals in Psychology and Medicine. (in Russian) v.2., SPb, Demetra, 2011.
- [11] Soloviev, N. Ampilova, E. Gurevich. On implementation of a neural network classifier for some classes of biological and medical preparation images. Proc. 7 Int. Conf. CEMA12, 8-10 Nov. 2012, Athens, Greece. p.94-97.

SYSTEM FOR MEASUREMENT OF MAGNETIC INDUCTION OF LOW FREQUENCY MAGNETIC FIELD

Vladimir Nikolov

Faculty of Telecommunication, TU-Sofia, Bulgaria

Postal address: Bulgaria

Sofia, PostCode 1000, Kliment Ohridski 8

T.+359 965 2278 ; F. .+359 965 2278; E. v_nikolov@tu-sofia.bg

Abstract

In this article is considered the construction of an apparatus for measuring the low-frequency magnetic fields in the range 0,1 Hz to 100 Hz. The construction of an apparatus for measuring the low-frequency magnetic fields in the range 0,1 Hz to 100 Hz is considered in this article. This instrument is capable of measuring low frequency magnetic fields used in many procedures in physiotherapy.

1. INTRODUCTION

During the past few decades, the advances in the theory and technology of modern electronics have led to improvements in medical diagnostic and therapeutic methods. As a result, bioelectric and biomagnetic phenomena have become increasingly important. Today it is not possible to imagine a hospital without electrocardiography and electroencephalography. The development of microelectronics has made the respective equipment portable and has increased its diagnostic power. Implantable cardiac pacemakers have made it possible for millions of people to return to normal life. The development of superconducting technology has provided the means to detect the weak biomagnetic fields induced by bioelectric currents. The latest advances in the measurement of electric currents flowing through a single ion channel of the cell membrane with the patch clamp have opened up completely new applications for bioelectromagnetism. With the patch clamp, bioelectromagnetism can also be applied to molecular biology, e.g. in developing new pharmaceuticals. These examples illustrate that bioelectromagnetism is a vital part of our everyday life. Modern bio-medical diagnostic technique involves two main groups of measuring instruments: ones for measuring bioelectric, biomagnetic, etc. signals and imaging systems. Registration systems are non-invasive bio-signals - with sensors and electrodes attached to the surface of the body in the form of implants, needle electrodes or chemical sensors.

The effect has been discovered in 1879 by Edwin Hall. There is a voltage between two sides of the

plate (semiconductor) when it is placed in a magnetic field. Voltage U_{hall} depends linearly on the magnetic induction field B (unit tesla T or gauss G, by $1\text{G} = 0,1\text{mT}$). This relationship is one of the great advantages of the Hall sensors, as it allows accurate measurements over a wide range of constant magnetic field through U_{hall} . The magnitude of U_{hall} is the sensitivity of the Hall element. Moreover, the expression of voltage U_{hall} is in force perpendicular to the magnetic field sensor and its value decreases when the field is at an perpendicular angle.

The output voltage of the Hall element is too small (amended by tens mV change in the magnetic field of 1mT), which is why their use alone is rare. An additional amplifier should be putted in the semiconductor in the case of measurement magnetic induction with small value. The positive supply voltage VCC has stabilized since REG, to reduce the impact of changes on its output voltage of the sensor. The transistor, which is NMOS in some ICs, is not mandatory. It is placed to provide enough current output. Due to the single power supply voltage output voltage is equal to 0,5 VCC where the semiconductor is out of magnetic field. This part is always one of the great sides of the hull of IC that is appropriately marked. The exact location of the sensor and the active thickness representing the distance between him and the marked side is given in the catalogs. The linear dependence of the magnetic induction B of V_{out} is valid only in a given part of its range, which. It corresponds to the minimum and maximum output voltage, which is shown in Fig. 1

Модел	Производител	V _{cc} , V	I _{cc} , mA	S, mV/mT	SN, dB	V _o , mV	W _o , Hz	T _a (T _o), °C	Размери, mm
A1301K	Allegro Microsystems	4.5 - 8	11max	25	20	150	2	-40 + +125	4,09x3,02x1,52
AH350	Drakes (Parsipat)	4.5 - 8	5	18	23	90	50	-20 + +85	4,19x3,1x1,57
EQ-41L	ARM Seonic	3 - 5.5	9	65	50	-	-	-30 + +100	3,9x3x1,2
OH5350U	TT Electronics	4.5 - 8	5.5	25	-	-	-	-40 + +150	4,57x4,55x0,52
A1395	Allegro Microsystems	2.5-3.5	3.2	100	10	80000	20	-20 + +85	3x2x0,75
MLX9026L	Meksis	4.5-5.5	4	4,1-340	1,3max	25000	8	-40 + +150	5,3x3,7x0x1,2
HALL 1820	Micronas	4.5-5.5	-	0.6x3 am ±20+160mT	1	-	-	-40 + +170	90T898

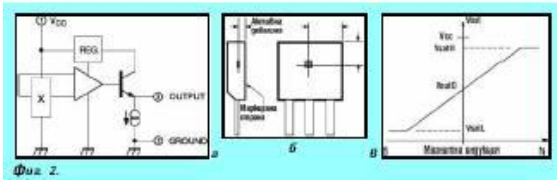


Fig.1

These voltages are usually given as parameters for the IC. The most important parameter is the sensitivity. It allows us to calculate the maximum value of magnetic induction B - to the graph of Fig. 2 for this south pole $BS = (V_{outO} - V_{satL}) / S$ and north pole $BS = (V_{satH} - V_{outO}) / S$, and usually both are equal and one is referred to as positive and the other as negative. For many applications it is essential that V_{outO} depends on temperature, which introduces an error in the measurement of C . Therefore, in most of the catalogs there is a graphics $V_{outO} (t^\circ)$. A note must be made that the voltage often increases in one direction of the magnetic field and decreases in the other. The temperature should be taken in account in the process of measurement of magnetic induction.

For our case we will be unable to apply the elements of Hall, because of the magnetic field, which measures a variable rather than a constant.

2. DESIGN OF A MAGNETIC INDUCTION MEASUREMENT SYSTEM

A small coil can be used as semiconductor for measurement of magnetic induction of low frequency magnetic field. The coil is made of dielectric on which reel is wound a copper wire with a thickness of 0,2 mm The coil is placed in a special housing with dimensions 15mm X 80mm. It has a cylindrical shape and is easy to use by the physician. The measurement coil is connected to the electronic unit of the described system. The connection between the probe and the meter is through a coaxial cable. It necessarily requires the use of shielded cable because signal interference is quite possible. The cable length is chosen as a compromise. On one hand the cable has to be as short as possible to reduce the interference and on the other, the medic should work normally and comfortably.

Gain stage is filled with an operational amplifier

We want to measure the intensity of the magnetic field over a wide range and high sensitivity of the

measuring device is required to use two measurement ranges. Ranging is performed by changing the feedback operational amplifier. The parameters of amplifier can be changed by change of the values of the elements in the feedback.

The operator must put the amplifier stage in order to amplify the signal to a level sufficient to "unblock" diodes in the detector to operate in linear mode.

Amplitude Detector

A classical scheme of amplitude detector, called successive can be used. It should be taken in account that successive amplitude detector has high input impedance to parallel amplitude detector. The aim is to have a high input impedance to avoid shunt operational amplifier. The integrated circuit is composed of a capacitor and resistor. The values of the elements are selected experimentally. The capacitor has a fairly large value to be obtained more good filtration. Integrated circuit is the load amplitude detector. The resistance in an integrated circuit is selected with great value, in order not to bridge the output of the detector. To provide feedback to the user using the standard liquid crystal display. It is a two-line, 16 characters per line (16h2). The display size is 85 mm x 30 mm x 13 mm, has a yellow backlight and uses the standard HD44780 interface, which is managed by a development board ARDUINO.

Power scheme is implemented by a classical scheme. The power operational amplifier needs 12 V. The power is bridge rectifier. Power consumption is consistent with the scheme, and used items are consistent with the medical device requirements. The selected transformer meets the requirement for continuous insulation between the primary and secondary coil capable 4KV.

3. MICROPROCESSOR CONTROL

Since we have 16 piece Sensor, it has to be controlled by a microcontroller. The sensor's outputs are connected to the input of amplifier. The microprocessor provides management of connection of different sensor's output to the input of amplifier. The amplifier's output is connected to the detector's input. The detector's output is connected to the input of integrated circuit.

In order to have more clarity and functionality after we file an analog input signal to the ADC board with the experimental ARDUINO it is processed by the microprocessor and is displayed on the LCD.

The principle of action described below diagram 2. The resulting voltage is amplified by the operational amplifier to a level necessary for the normal operation of the next-step detector. The detector detects the signal on its input as on its output remains only the enveloping curve of the signal. On the next step integrated circuit "smoothes" the detected signal. Already "pressed" is fed to one of the analog inputs of the development board ARDUINO. After the signal processing of the development board, its value is displayed.

The different probes which measure the magnetic field at various points in space can be switched with the microprocessor.

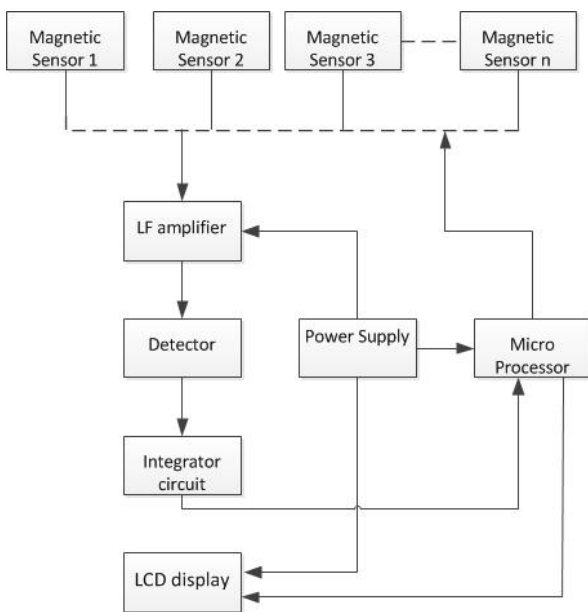


Fig. 2

4. ALGORITHM FOR GRADUATION OF SYSTEM FOR MEASUREMENT OF MAGNETIC INDUCTION

The adjustment of the measurement system can be provided using permanent magnetic field and low frequency magnetic field. The value of magnetic induction of permanent magnetic field should be the same as the amplitude of magnetic induction of low frequency magnetic field. The resulting value, which is measured, can be programmed in the memory of the microprocessor.

Table 1

Voltage	small range, mT	wide range, mT
1	0,5	10
3	1	20
5	1,5	30

Based on this table is built and graduation curve (Fig.3) by the method of least squares

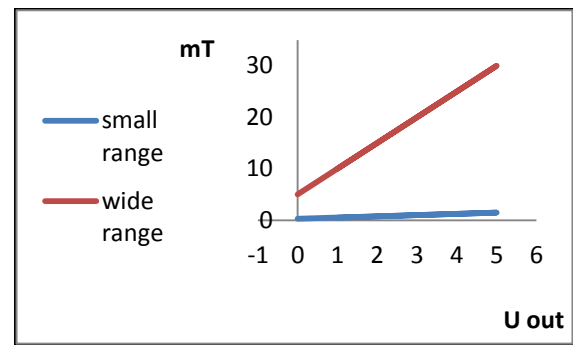


Fig. 3

5. CONCLUSION

The following processes are described in the paper. Invention device for measuring low frequency magnetic field is consistent with the requirement for electrical safety. Power supply unit is used which has a power transformer, for galvanic separation of the device from grid. Low frequency amplifier amplifies the signal to the level required for normal operation of Amplitude Detector. The detected signal is "smoothing" of the integrated circuit, which is selected through experiments. The advantage of the invention device to Hall sensor that is able to measure low-frequency magnetic fields.

References

- [1] Petsulev C., Siforov C, "Radio receiving devices", Technika, Sofia, 1979.
- [2] Stamboliev I., Medical equipment, Technika, Sofia, 1989.
- [3] Valkov S., "Impulse Technology", Technika, Sofia, 2002.
- [4] Stefanov N., Power Supply Technika, Sofia, 2002.

APPLICATION OF SPEECH TO TEXT AS CRITERION OF AUDIO QUALITY ESTIMATION IN MULTIMEDIA COMMUNICATION SYSTEMS

S. Pleshkova, K. Peeva

Department of Telecommunications,
Technical University - Sofia, Kliment Ohridski 8, Sofia
snegpl@tu-sofia.bg ; kala_peeva@yahoo.com

Abstract

In the multimedia communication systems is very important to guaranty not only the video quality, but also the quality of the sounds or speech, usually accompanying the video information. Additionally when the new speech coding methods are developed is necessary to test and estimate the quality of the decoded with the new method speech. There exists two main possible ways to estimate the speech quality in these above mentioned cases. First there are subjective methods based on subjective tests averaging of the individual estimations of each of the participants of these tests. The second possibility is to apply objective methods for speech quality determination. Most of these objective methods are the base of existing standards for audio quality measurements and estimations. It is necessary to underline, that each of two mentioned subjective and objective methods have appropriates advantages, but also the important disadvantages. Therefore, it is the goal of this article to propose and describe the new method combining the advantages of subjective methods to estimate the speech of receiving quality, changing the estimator to be not a person, but a speech to text system.

Keywords: Audio Quality, Speech to Text, Multimedia Communication System, Speech Quality Estimation

1. INTRODUCTION

The audio signal quality estimation is of leading importance in multimedia communication systems, in which generally there are two information sources: video and audio. There are several different group of methods [1, 2, 3] for subjective and objective quality measurements and estimation in multimedia systems of received and decoded speech signals, which are became the base of appropriates speech quality standards, known as ITU-T Recommendations [4, 5, 6]. Each of these methods or standards are very popular, but are prepared for specific cases of speech signals coding and concrete characteristics of communication channel in multimedia systems. The goal of this article is to propose the application of text to speech method in transmission part and speech to text method in receiving part of a multimedia system, as means to replace human as speaker in transmission part and human as listener in receiving part of the multimedia system. The main advantages from this proposition are to eliminate the human subjective factor in speech quality estimation process and to approach the precision of objective speech quality methods to the higher precision of subjective methods.

2. APPLICATION OF SPEECH TO TEXT AS CRITERION OF AUDIO QUALITY ESTIMATION IN AUDIO COMMUNICATION SYSTEMS

Fig. 1 presents the developed block diagram of objective quality estimation of speech signals in multimedia communications systems. The main difference of the proposed method for objective evaluation consists in the application of converting speech signals into text file.

As an initial component is used an original text (marked as block "Original text") from printed document or computer file, which is read into a microphone device connected to the computer system and is converted into a speech signal. The input speech signal is recorded as audio file (marked as block "Audio Record 1") in the computer system and simultaneously is converted into a digital text file (referred as block "Speech to Text Conversion 1"). The speech signal is transmitted via multimedia communication channel (block "Multimedia Communication System") and is received from the receiver part of the multimedia system and is reproduced by loudspeaker device (presented as "Speaker" in Fig 1). At the same time the received speech signal is recorded on the computer as audio file (marked as block "Audio Record 2").

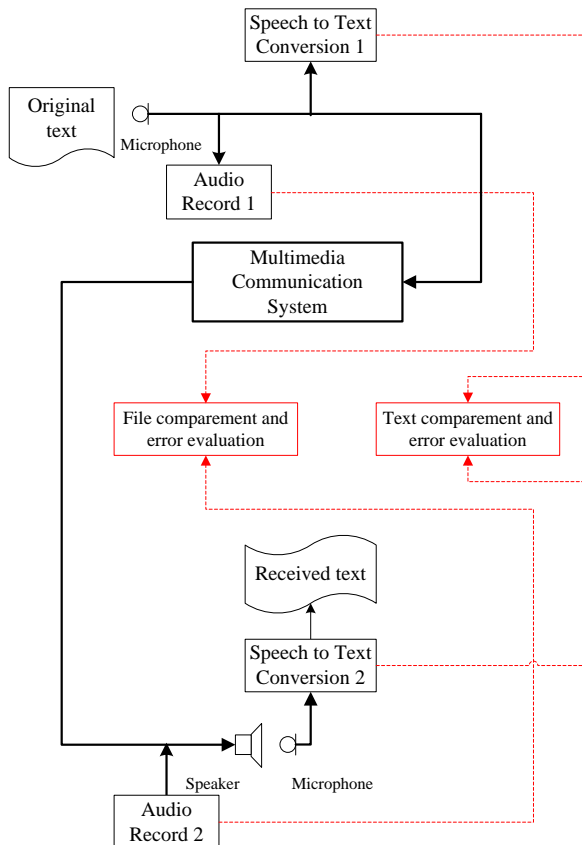


Fig. 1. Main functional block scheme of simulation model for objective speech quality assessment by conversion of speech signals into text file

In front of and nearby the speaker device is placed another microphone, which transmits the speech signal for conversion into a new text file (referred as block "Speech to Text 2").

The goal of the simulation model is the comparison between the two digital text files (block "Text comparement and error evaluation"), generated in the transmission and the receiver part and the detection and determination of the number of incorrect words in the text. As a result of error evaluation is defined an exact objective quality assessment of the speech signal. In addition of the main method in the proposed simulation model is also applied a comparison between the two audio records "Record 1" and "Record 2" (marked as block "Audio comparison and error evaluation") like an extra function for more precise objective speech quality assessment.

3. SIMULATION MODEL OF OBJECTIVE AUDIO QUALITY ESTIMATION IN MULTIMEDIA COMMUNICATION SYSTEMS, IMPLEMENTED ON MATLAB PROGRAM SYSTEM

On Fig. 2 is presented a general model of simulation program using Matlab Simulink system. The schema involve the transmission and receiving

parts of a multimedia communication system with the ability to choose the type of the communication channel (in this case it is shown on Fig. 2 an AWGN Communication Channel). There are presented on Fig. 2 two types of possibilities to choose the source of the speech signal: real speech signal direct from microphone (From Audio Device) or speech signal converted from a speech to text system (Data Type Conversion). In the transmission part the speech signal is saved as audio file (To Multimedia File) and in the same time is transmitted via communication channel of the Multimedia Communication System, in which is possible to define the level of noise and disturbances. In the receiving part are prepared similar operations like as in the transmission part. The received speech signal is saved back as audio file (To Multimedia File 1) and in the same time is reproduced with speaker (To audio device). With a microphone (From audio device 1), placed in front of the speaker is possible to made an inverse speech to text conversion (Data Type Conversion 2). This text is saved as a new received text document, which is used in the next step of the proposed method – the relative objective measures or estimations of speech quality in the multimedia system, described in next paragraph.

4. OBJECTIVE SPEECH QUALITY ESTIMATION BASED ON ORIGINAL AND RECEIVED TEXTS COMPARISON AND ERROR EVALUATION

The results from execution of the simulation program, presented in Fig. 2 are as following:

- received speech signal saved as speech file **rev.wav**;
- text document created after speech to text transformation in receiving part of the multimedia system and saved as text file **rev_stt.txt**;

Also in is known, that in the transmission part of the multimedia system (simulation model from Fig. 2) are available the corresponding speech information as saved files:

- original speech signal saved as speech file **orig.wav**;
- original text document **orig.txt**;
- text document created after speech to text transformation in transmission part of the multimedia system and saved as text file **stt.txt**.

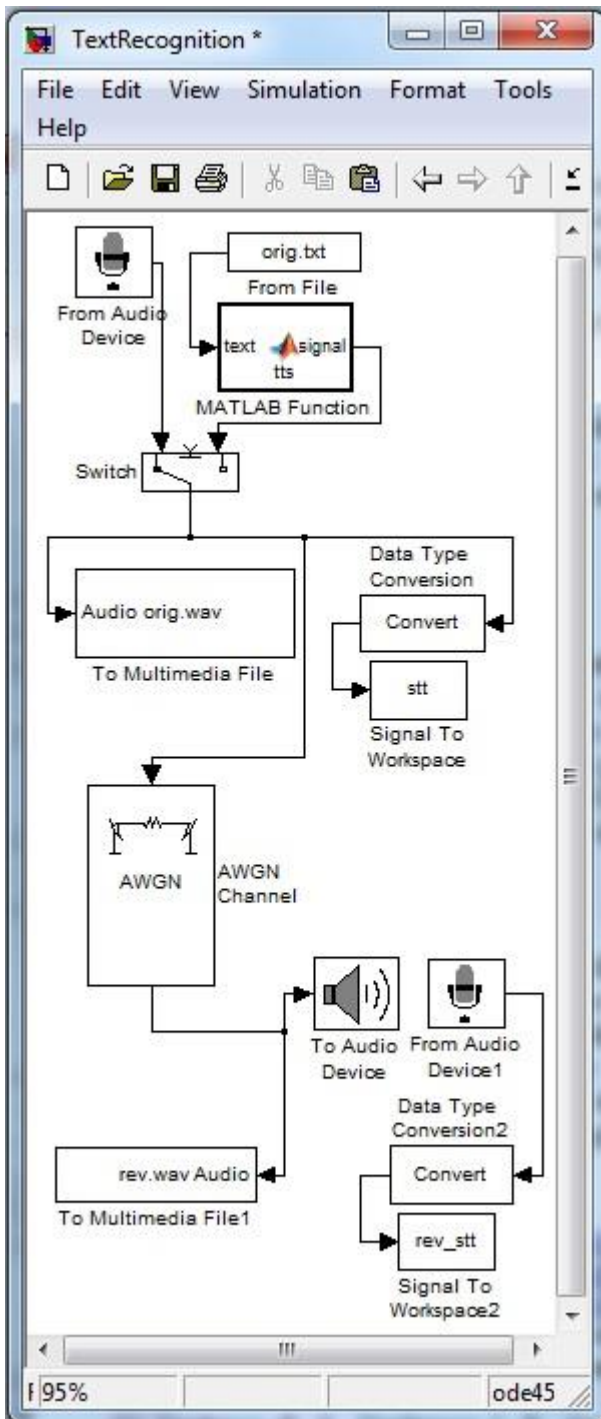


Fig. 2. Block scheme of the simulation program model for objective quality assessment of speech quality, by Speech to Text conversion

Usually each speech to text system gives some number of erroneous words when after the transformation spoken words are converted to corresponding text words. Therefore it can define the appropriate values of number of erroneous words in transmission ($NErW_{tr}$) and receiving ($NErW_{re}$) parts of the multimedia system. These definitions can be used to present the objective speech quality estimation (OSQE) as difference (DNErW) or as ratio (RNErW) between the number of erroneous

words in receiving ($NErW_{re}$) part and the number of erroneous words in transmission ($NErW_{tr}$) part of the multimedia system:

$$OSQE_D = DNErW = NErW_{re} - NErW_{tr} \quad (1)$$

or

$$OSQE_R = \frac{NErW_{tr}}{NErW_{re}} \quad (2)$$

The proposed above equations (1 and 2) are two possible relative objective measures or estimations of speech quality in the multimedia system. They can be compared with some of existing subjective methods of speech quality estimation in with are used the well-arranged speech databases. If in the simulations of the proposed here method are applied the same test speech signals from the mentioned above speech databases, then the results from the existing subjective speech quality estimation methods can serve as criterion of precision of the proposed in this article method and also, which is more important to calibration of the scale of values calculated from the equations (1 and 2).

5. SIMULATIONS AND EXPERIMENTAL RESULTS OF THE PROPOSED OBJECTIVE SPEECH QUALITY ESTIMATION BASED ON ORIGINAL AND RECEIVED TEXTS COMPARISON

The schema block of the simulation program model shown in Fig. 2 is used to carried out the experiments for objective quality assessment of speech quality, by speech to Text conversion. On Fig. 3 and Fig. 4 are shown as a simple example of one of the simulations: the original text after speech to text transformation **stt.txt** and text document created after speech to text transformation in receiving part **rev_stt.txt**

Get started ...

1. add the **text2speech** folder to your Matlab path

2. Test your new function:

Get started, if you use SAPI (before .NET)...

1. Make sure SAPI is **installed** on your computer

a) get the Speech SDK 5.1 (86MB) for free from Microsoft:

b) test your default computer voice

2. add the text2speech folder to your Matlab path

3. Test **your new** function: ('This is a test.')

I would like to thank "Desmond Lang" for his Text-To-Speech tutorial

and my wife for letting me play with the computer ;).

Fig. 3. Original text after speech to text transformation **stt.txt**

Get started ...

1. **add** the text2speech folder to your Matlab path
 2. Test your new function:
- Get started, if **you use** SAPI (before .NET)...
1. Make sure SAPI is installed on your computer
 - a) get the Speech SDK 5.1 (86MB) for **free from** Microsoft:
 - b) test your default computer voice
 2. add the text2speech **folder** to your Matlab path
 3. Test your new function: ('This is a test.')
- I would like to thank "Desmond Lang" for his Text-To-Speech **tutorial** and my wife for **letting me play** with the computer ;).

Fig. 4. Text document created after speech to text transformation in receiving part **rev_stt.txt**

It can be seen from Fig. 3 and Fig. 4, that there are differences of the number of erroneous words in the original text after speech to text transformation **stt.txt** and text document created after speech to text transformation in receiving part **rev_stt.txt**. This difference is used to calculate with the equations (1 and 2) the values the objective speech quality estimation (OSQE) as difference (DNErW) or as ratio (RNErW) between the number of erroneous words in receiving ($NErW_{re}$) part and the number of erroneous words in transmission ($NErW_{tr}$) part. For this example the concrete values of $NErW_{re}$ and $NErW_{tr}$ are:

$$NErW_{re} = 10 ; NErW_{tr} = 5 \quad (3)$$

Then from the equations (1,2 and 3) are calculated the values:

$$OSQE_D = DNErW = NErW_{re} - NErW_{tr} \quad (4)$$

$$= 10 - 5 = 5$$

$$OSQE_R = \frac{NErW_{re}}{NErW_{tr}} = \frac{10}{5} = 2 \quad (5)$$

The values calculated in equations (4 and 5) are only a demonstration of the methodology necessary to apply for the proposed method and in real simulation using the texts with larger number of words in the text the results are more realistic and precise. These results exists, but are not shown here a cause of limited size of this article.

6. CONCLUSION

In this article is proposed the application of text to speech method in transmission part and speech to text method in receiving part of a multimedia system, as means to replace human as speaker in transmission part and human as listener in receiving part of the multimedia system. The proposed method is developed as simulation model and a lot of simulations are prepared from which it is seen that the proposition of using text to speech and speech to text methods gives good results for objective speech quality estimation in multimedia system with the advantage of elimination the human subjective factor in speech quality estimation and of achievement of a near to in objective speech quality methods near to the precision of subjective methods.

Acknowledgment

This paper was supported by Technical University – Sofia inner program to support PhD research projects under Contract 132 PD0025-07: "Development of algorithms for quality estimation of audio-visual information in multimedia computer systems and networks".

References

- [1] L. Thorpe and W. Yang, "Performance of current perceptual objective speech quality measures," in Proc. IEEE Speech Coding Workshop, 1999, pp. 144–146.
- [2] A. Bayya and M. Vis, "Objective measures for speech quality assessment in wireless communications," in Proc. IEEE Int. Conf. Acoust., Speech, Signal Process., 1996, vol. 1, pp. 495–498.
- [3] V. Turbin and N. Faucheur, "A perceptual objective measure for noise reduction systems," in Proc. Online Workshop Meas. Speech Audio Quality Netw., 2005, pp. 81–84.
- [4] <http://www.itu.int/rec/T-REC-J.148-200305-I/>
- [5] <http://www.itu.int/rec/T-REC-J.143-200005-I/>
- [6] <http://www.itu.int/rec/T-REC-J.144-200103-S/>

MICROPHONE ARRAYS BEAMFORMING METHODS WITH LEAST MEAN SQUARE SPATIAL FILTRATION FOR NOISE SUPPRESSION

S. Pleshkova, K. Peeva

Department of Telecommunications,
Technical University, Kliment Ohridski, 8 Sofia
sneopl@tu-sofia.bg

Abstract

Beamforming is a group of methods with spatial filtering of sound signals captured from an array of sound sensors or microphones. The objective is to estimate the direction of arrival of sound source signal in the presence of noise and other interfering signals. A spatial filtering is prepared from beamformer to separates the signals with overlapping frequency content arriving from different directions. The goal of this article is to study the different beamforming methods using the algorithm of Least Mean Squares (LMS) filters for spatial filtering of sound signals from microphone array sensors. It is proposed to use a least mean square algorithm capable of iteratively adapting the weights of the sound sensor microphone array to minimize the noise in output microphone array signal. Two methods of microphone arrays are simulated and compared: the simple delay and sum beamformer and statistically optimum beamformer. The simulation results of are analyzed to estimate the SNR improvement of statistically optimum beamforming method in comparison to simple delay and sum beamforming method.

1. INTRODUCTION

The sound signals arriving to the microphone arrays are spatially propagating signals containing also interfering signals and noise. When the original sound signals and interfering signals are in the same temporal frequency band, it is not possible to use temporal filtering for separating the useful sound signal from the interfering signals [1]. Therefore it is necessary to apply the existence of different spatial locations to separate original sound signals from interfering signals and noise. This difference allow spatial separation the original sound signals from the interference signals using a microphone array beamforming methods. The microphone array contain a number of sound sensors and are made with different configurations. A simple way to use the microphone array beamforming is to apply signal filtering of each of sensor or microphones and to add up the filtered outputs of all the sensors. Here is proposed to study the different beamforming methods using the algorithm of Least Mean Squares (LMS) filters for spatial filtering of sound signals from microphone arrays.

2. THE BASIC PRINCIPLES AND DIFFERENCES BETWEEN BEAMFORMING METHODS

The different beamforming methods can be classified on two basic types: data independent and statistically optimum methods. In Fig. 1 is presented the simplest example of data independent beam-

forming method the delay and sum beamformer methods.

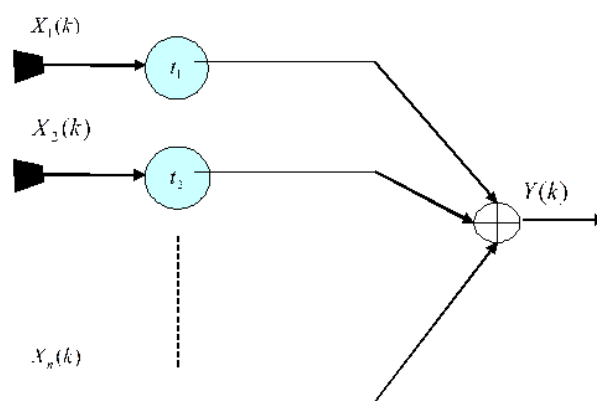


Fig.1. Delay and Sum Beamformer with “ n ” sound sensors or microphones

The major disadvantage of delay and sum beamforming method is the large number of sensors required to improve the SNR.

The main difference between shown in Fig. 1 simple delay and sum beamforming method and the statistically optimum beamforming method is the dependence on how the weights in the beamforming filters are chosen: the weights in data independent beamforming methods do not depend on the array data; the weights in a statistically optimum beamformer are chosen based on the statistics of the array data.

3. THE STATISTICALLY OPTIMUM BEAMFORMING METHODS

The statistically optimum beamforming method can be modeled as array processor shown in Fig. 2 with “ N ” sound sensors or microphones and “ J ” taps per microphone [2]. The delays after each sensor are not shown here.

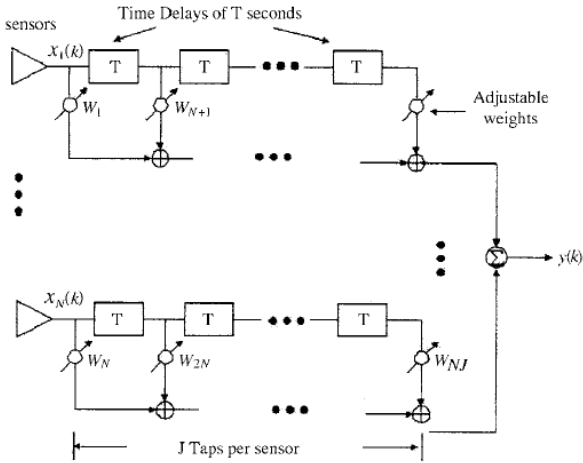


Fig. 2. Array processor with “ N ” sound sensors or microphones for statistically optimum beamforming method modelling

The presented in the Fig. 2 array processor work as a single tapped delay in which each weight is equal to the sum of the weights in the vertical column of the processor. These summation weights are set so as to determine the desired frequency response characteristic in the desired direction. The array processor is assumed to be steered to the required desired direction by appropriate delays after the sensors. Out of J weights of each N tap determine the desired direction frequency response. The remaining $NJ - J$ weights are used to minimize the total power in the array output, which is equivalent to minimizing the non- desired direction noise power because the signal and the noise is usually uncorrelated. The vector of tap values at the k -th sample is written as $X(k)$:

$$X^T(k) = [x_1(k), x_2(k), \dots, x_{KJ}(k)] \quad (1)$$

The tap values are the sums of the values due to desired-direction waveforms and the non- desired-direction noises:

$$X(k) = L(k) + N(k), \quad (2)$$

where

$L(k)$ and $N(k)$ are the KJ dimensional vectors of desired-direction and non-desired-direction at the k th sample, respectively:

$$L^T(k) = [l_1(k) \quad l_2(k) \quad \dots \quad l_{KJ}(k)] \quad (3)$$

$$N^T(k) = [n_1(k) \quad n_2(k) \quad \dots \quad n_{KJ}(k)] \quad (4)$$

The vector of weights at each tap is W :

$$W^T = [w_1 \quad w_2 \quad \dots \quad w_{KJ}], \quad (5)$$

With the equation:

$$E[N(k)L^T(k)] = 0 \quad (6)$$

is assumed that the condition of uncorrelation between desired direction vector and the vector of non-desired direction noise is satisfied. Therefore, the output of the array at the time of the k -th sample is:

$$y(k) = W^T X(k) = X^T(k)W \quad (7)$$

It is necessary to define and expressed the requirements of the weights on the j -th vertical column of the taps sum to a chosen number f_j with a KJ dimensional vector c_j , a constraint matrix C and a J dimensional vector F of weights of the desired-direction-equivalent tapped delay line:

$$c_j^T W = f_j \quad j = 1, 2, \dots, J \quad (8)$$

$$C = [c_1 \quad \dots \quad c_j \quad \dots \quad c_J] \quad (9)$$

$$F^T = [f_1 \quad \dots \quad f_j \quad \dots \quad f_J] \quad (10)$$

Now, the constraint can be written as:

$$C^T W = F \quad (11)$$

To achieve the optimal values of vector of weights W_{opt} the necessary minimization of equation (11) is carried out:

$$\min_w W^T R_{XX} W, \quad (12)$$

subject to $C^T W$

is proposed to use the algorithm of Least Mean Squares (LMS) filters [3] for spatial filtering of sound signals from microphone arrays. In the equation (12) is applying R_{XX} one of the existing in theory of statistically optimum beamforming method correlation matrixes defined as:

$$\begin{aligned} E[X(k)X^T(k)] &= R_{XX} \\ E[N(k)N^T(k)] &= R_{NN}, \\ E[L(k)L^T(k)] &= R_{LL} \end{aligned} \quad (13)$$

assuming that the equation (6) is satisfied. Therefore, the optimal values of vector of weights W_{opt} can be found as:

$$W_{opt} = -R_{XX}^{-1} C \lambda, \quad (14)$$

by the method of Lagrange multipliers λ :

$$H(W) = \frac{1}{2} W^T R_{XX} W + \lambda^T (C^T W - F) \quad (15)$$

From equation (15) is found the gradient with respect to W and is setting to zero:

$$\nabla_w H(W) = R_{XX} W + C \lambda = 0 \quad (16)$$

to calculate the optimal values of vector of weights W_{opt} as is shown in equation (14). In this equation R_{XX} can be considered as positive semi definite. Therefore, this give the reason to substitute equation (14) in equation (11):

$$C^T W_{opt} = F = -C^T R_{XX}^{-1} C \lambda \quad (17)$$

and find the Lagrange multiplier λ from the following equation:

$$\lambda = -[C^T R_{XX}^{-1} C]^{-1} F \quad (18)$$

Finally the optimum weight vector can be written as:

$$W_{opt} = R_{XX}^{-1} C [C^T R_{XX}^{-1} C]^{-1} F \quad (19)$$

In the calculated above optimal values of vector of weights W_{opt} from equation (19) the correlation matrix R_{XX} is not known. The direct substitution, when the correlation matrix R_{XX} is calculated, leads to a number of multiplications at each iteration proportional to the cube of the number of weights. Then, the adaptive algorithm [4], described briefly below, can be used to avoid this difficulties:

- initializing the vector of weights W

$$W(0) = C(C^T C)^{-1} F; \quad (20)$$

- at each iteration move the weight vector in the negative direction of the constrained gradient, scale by a constant μ and after k -th iteration calculate the next weight vector as:

$$\begin{aligned} W(k+1) &= W(k) - \mu \nabla_w H[W(k)] \\ &= W(k) - \mu [R_{XX} W(k) + C \lambda(k)]; \end{aligned} \quad (21)$$

- the Lagrange multipliers $\lambda(k)$ are chosen by requiring $W(k+1)$ to satisfy the constraint:

$$\begin{aligned} F &= C^T W(k+1) = \\ &C^T W(k) - \mu C^T R_{XX} W(k) - \mu C^T C \lambda(k); \end{aligned} \quad (22)$$

- calculating the Lagrange multipliers $\lambda(k)$ from equation (22);
- substituting multipliers $\lambda(k)$ into (21):

$$\begin{aligned} W(k+1) &= W(k) - \mu [I - C(C^T C)^{-1} C^T] \cdot \\ &R_{XX} W(k) + C(C^T C)^{-1} [F - C^T W(k)]; \end{aligned} \quad (23)$$

- defining vector \tilde{F} and matrix P :

$$\tilde{F} = C(C^T C)^{-1} F; \quad P = I - C(C^T C)^{-1} C^T; \quad (24)$$

- finally the iteration steps of adaptive algorithm is the following:

$$W(0) = \tilde{F} \quad (25)$$

$$W(k+1) = P[W(k) - \mu R_{XX} W(k)] + \tilde{F} \quad (26)$$

The statistical optimized LMS algorithm described above can be summarized in two main steps using the following equations:

- Initialization step (25)
- Iterative steps (26).

4. SIMULATION OF SIMPLE DELAY AND SUM BEAMFORMER AND STATISTICALLY OPTIMUM BEAMFORMER

Linear microphone sensor (Fig. 3) for are two types of beamformers are simulated: the simple delay and sum beamformer and statistically optimum beamformer. One of the speech signals, which are used in the numerous simulations is shown in Fig. 4 without and with added noise to test the ability of two simulated methods, the simple delay and sum beamformer and statistically optimum beamformer, to suppress the interfering signals and noise. The resultant simple delay and sum beamformer and statistically optimum beamformer diagrams are shown in Fig. 5.

Table.1 show that the values of SNR measured for statistical optimized with LMS algorithm for spatial filtering is higher, that these of simple delay and sum beamformer method.

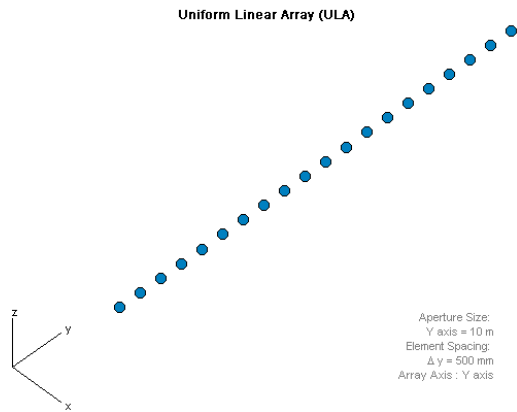


Fig. 3. Simulation model of linear microphone sensors

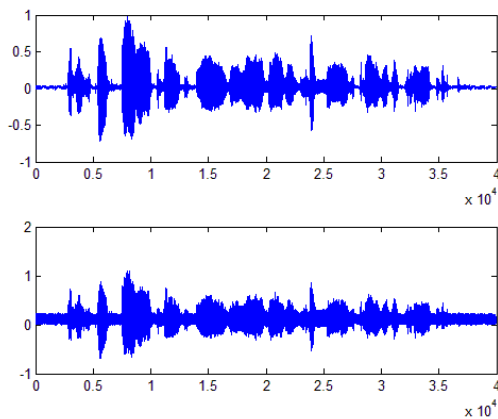


Fig. 4. One of the speech signals, used in the numerous simulations without and with noise

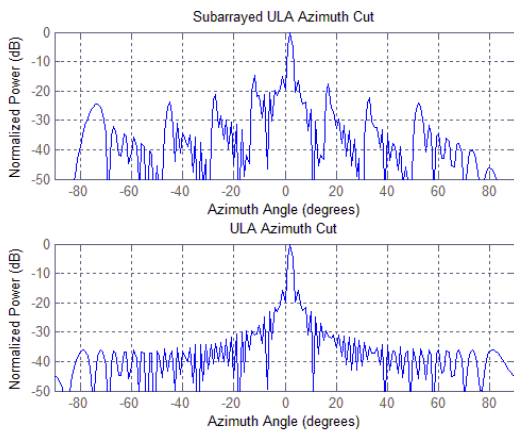


Fig. 5. The resultant simple delay and sum beamformer and statistically optimum beamformer diagram

Table. 1.

Simulation number	Delay and sum beamformer SNR(dB)	Statistical beamformer SNR(dB)
1	01.97	04.26
2	-06.04	01.23
3	-05.11	00.04
4	01.87	05.34
5	-06.02	02.34
6	-05.40	00.02

5. CONCLUSION

The results of simulations presented in graphics and tables shown the ability of the proposed least mean square algorithm to iteratively adapting the weights of the sound sensor to minimize the noise in output microphone array signal.

6. ACKNOWLEDGMENT

This paper was supported by Technical University – Sofia inner program to support PhD research projects under Contract 132 PD0025-07: “Development of algorithms for quality estimation of audio-visual information in multimedia computer systems and networks”.

References

- [1] Barry Van Veen, et. Al. “Beamforming Techniques for Spatial Filtering” 2000 CRC Press LLC. <http://www.engnetbase.com>
- [2] Raykar C.V. A Study of a various beamforming techniques of the Constrained Least Mean Squares (LMS) algorithm for Beamforming University of Maryland, College Park,2001
- [3] Simon S. Haykin, Bernard Widrow (Editor): *Least-Mean-Square Adaptive Filters*, Wiley, 2003
- [4] SPHSC 503, Adaptive directional microphones. Speech Signal Processing, UW – Summer 200.

MATHEMATICAL METHODS AND ALGORITHMS BASED ON ANALYSIS OF ECG AND EEG SIGNALS. NOISE REMOVAL FROM ECG AND EEG SIGNALS

¹Prof. Dr. Dimiter Dimitrov

²Deyan Milev

¹Faculty of Telecommunication, Technical University of Sofia
8, Kliment Ohridsky str., 1756 Sofia, Bulgaria
Phone: +359 2 9652278, E-mail: dcd@tu-sofia.bg

²Faculty of Telecommunication, Technical University of Sofia
8, Kliment Ohridsky str., 1756 Sofia, Bulgaria
Phone: +359 883 556 426, E-mail: dmilev@tu-sofia.bg

Abstract

This paper attempts to provide a comprehensive survey of different types of pathologies detection algorithms and their potential role in diagnostic and therapeutic applications. Major recent algorithms use electrocardiogram (ECG) and electroencephalogram (EEG) signals to detect the event. In these algorithms, various features are extracted from the EEG signal alone or in concert with the ECG signals. Noise sources increase the difficulty in analyzing the ECG and EEG to obtaining clinical information. For this reason, it is necessary to design specific filters to decrease such artifacts in ECG and EEG records. A new technique based on simple statistical parameters is proposed to solve this problem in this application. It is concluded that the proposed filter reduces the common artifacts present in EEG signals without removing significant information embedded in these records.

Keywords: ECG, EEG, noise removal, seizure detection algorithm.

1. INTRODUCTION

The mathematical modelling of the ECG is known as the forward problem of electrocardiography. It relies on three main ingredients: a model for the electrical activity of the heart, a model for the torso (extra-cardiac regions) and some specific heart-torso coupling conditions. Within each of these components, several options are possible, with different levels of complexity and realism. Although many works have been devoted to the numerical simulation of cardiac electrophysiology, only a small number addresses the numerical simulation of ECGs using a whole-heart reaction-diffusion model. Among them, only a very few provide meaningful simulations of the complete 12-lead ECG. The main ingredients of mathematical ECG model are standard: bidomain equations and phenomenological cell model for the heart, and a generalized Laplace equation for the torso.

The numerical methods proposed to solve the problem offer a good balance between efficiency, stability and accuracy. The PDE system made of the heart and torso models is solved using a finite element method and a second order semi-implicit time marching scheme. The coupling conditions at the

heart-torso interface are enforced by a Dirichlet-Neumann domain decomposition algorithm.

Technically an electroencephalography (EEG) consists of multiple channels that monitor neurons' activities in a region, each channel represent an electrode on a patient's scalp. A nerve axon may be stimulated and the activated sodium (Na^+) and potassium (K^+) channels produced in the vicinity of the cell membrane may lead to the electrical excitation of the nerve axon. The excitation arises from the effect of the membrane potential on the movement of ions, and from interactions of the membrane potential with opening and closing of voltage activated membrane channels.

A regular EEG can have from up to 20 electrodes and last more than an hour. Quite large areas of cortex –in the order of a few square centimetres - have to be activated synchronously to generate enough potential for changes to be registered at electrodes placed on the scalp [1] EEG plays a central role in diagnosis and management of patients with seizure disorders. Routine EEG is used in the following clinical circumstances: epilepsy, to distinguish epileptic seizures from other types of

spells, differentiate encephalopathy, neurodegenerative disorders, to evaluate comatose patients, to serve as an adjunct test of brain death.

2. MAIN TEXT

The reference model for the electrical activity of the heart is the so-called bidomain model. This macroscopic model is based on the assumption that, at the cell scale, the cardiac tissue can be viewed as partitioned into two ohmic conducting media, separated by the cell membrane: intracellular, made of the cardiac cells, and extracellular which represents the space between them. After a homogenization process, the intra and extracellular domains can be supposed to occupy the whole heart volume Ω_H (this also applies to the cell membrane). Hence, the averaged intra- and extracellular densities of current, j_i and j_e , conductivity tensors, σ_i and σ_e , and electric potentials, u_i and u_e , are defined in Ω_H . The electrical charge conservation becomes

$$\text{div}(j_i + j_e) = 0, \text{ in } \Omega_H,$$

and the homogenized equation of the electrical activity of the cell membrane is given by

$$A_m \left(C_m \frac{\partial V_m}{\partial t} + I_{ion}(V_m, w) \right) + \text{div}(j_i) = A_m I_{app}$$

Complemented with the Ohm's laws

$$j_i = -\sigma \nabla u_i, \quad j_e = -\sigma \nabla u_e.$$

Here, V_m stands for the transmembrane potential, defined as

$$V_m \stackrel{\text{def}}{=} u_i - u_e.$$

A_m is a constant representing the rate of membrane area per volume unit and C_m the membrane capacitance per area unit [8]. The term $I_{ion}(V_m, w)$ represents the ionic current across the membrane and I_{app} a given applied current stimulus. Both currents are measured per membrane area unit.

In general, the ionic variable w (possibly vector valued) satisfies a system of ODE of the type:

$$\frac{\partial w}{\partial t} + g(V_m, w) = 0, \text{ in } \Omega_H.$$

The definition of the functions g and I_{ion} depends on the considered cell ionic model [6].

To calculate brain rhythms a discrete Fourier (DFT) transformation is used:

$$\sum_{n=0}^{N-1} x_n \left(\sin \left(-\frac{2\pi}{N} kn \right) + i \cos \left(-\frac{2\pi}{N} kn \right) \right) \\ k = 0, \dots, N-1.$$

as well as the inverse discrete Fourier transformation (IDFT):

$$x_n = \frac{1}{N} \sum_{k=0}^{N-1} X_k e^{(2\pi i / N) kn} \quad n = 0, \dots, N-1.$$

To calculate the required brain rhythm DFT is applied over the signal. All the frequencies not corresponding to the required rhythm are set to zero. IDFT is applied over the resulting data [5].

After filtering out all the waves except the required rhythm we can calculate its power. To do this we use a statistical value – root mean square. Which is defined as:

$$RMS = \sqrt{\frac{x_0^2 + x_1^2 + \dots + x_{N-1}^2}{N}}$$

Here x is value of the signal at a discrete time. For every interval of EEG all of the brain rhythms and powers are calculated. Out of these a rhythm is said to be dominant in an interval if its power is the highest [7].

3. ILLUSTRATIONS

Action potential duration (APD) heterogeneity may be found at different myocardium locations, for instance: between base and apex, between septal and posterior sides, and transmurally[2]. Although not yet fully explained [3], experimental evidence suggests that transmural APD heterogeneity is likely to be the most important factor in the genesis of the normal ECG T-wave shape and polarity.

In the present work, cell heterogeneity is only considered as transmural variation of APD in the left ventricle [9]. Hence, we assume that epicardial cells have the shortest APD and that endocardial cells have the longest APD and that endocardial cells have an intermediate APD between mid-myocardial cells (M-cells) and epicardial cells[4]. The APD heterogeneity is modelled with a parameter τ_{close} varying across the left ventricle transmural direction: τ_{close}^{endo} near the endocardium, τ_{close}^{mcell} in the mid-myocardium (M-cells) and τ_{close}^{epi} near the epicardi-

um (figure 1 and figure 2). For simplicity, we take a constant value of τ_{close}^{RV} in the whole right ventricle. The values of the parameters are given in table 1.

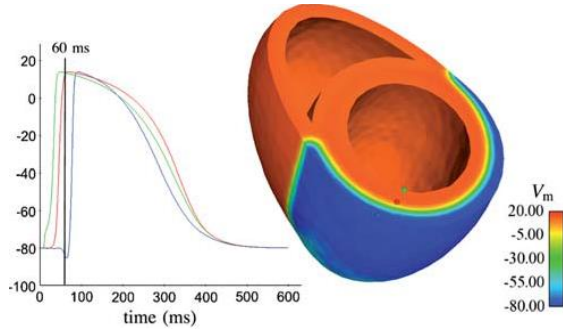


Figure 1. Transmural APD heterogeneity: comparison of the simulated transmembrane potential for endocardial cells (green), M-cells (red) and epicardial cells (blue). Snapshots of the transmembrane potential at times $t = 60$ ms.

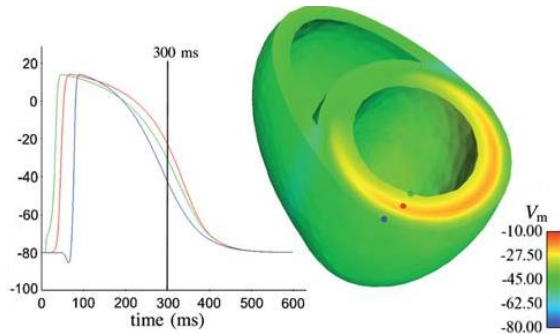


Figure 2. Transmural APD heterogeneity: comparison of the simulated transmembrane potential for endocardial cells (green), M-cells (red) and epicardial cells (blue). Snapshots of the transmembrane potential at times $t = 300$ ms.

Table 1. Cell membrane parameters

A_m (cm^{-1})	200
C_m (mF)	10^{-3}
τ_{in}	4.5
τ_{out}	90
τ_{open}	100
τ_{close}^{RV}	120
τ_{close}^{endo}	130
τ_{close}^{mcell}	140
τ_{close}^{epi}	90
V_{gate}	-67
V_{min}	-80
V_{max}	20

The membrane potential of EEG signal increases when the membrane is polarized with a net nega-

tive charge lining the inner surface and an equal but opposite net positive charge on the outer surface [10]. This potential may be simply related to the amount of electrical charge Q , using

$$E = \frac{Q}{C_m}$$

where Q is in terms of coulombs/cm², and E is in units of volts. In practice, in order to model the action potentials (APs) the amount of charge Q^+ on the inner surface of the cell membrane has to be mathematically related to the stimulating current I_{stim} flowing into the cell through the stimulating electrodes. The Hodgkin and Huxley model is illustrated in Figure 3.

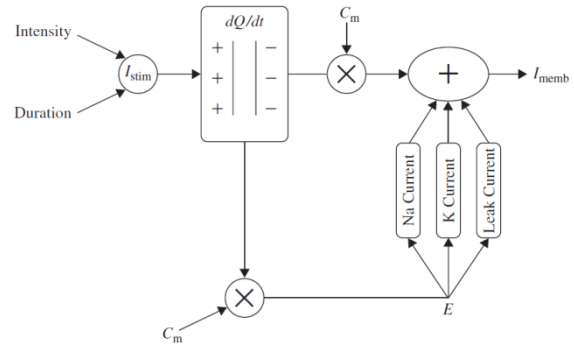


Figure 3. The Hodgkin-Huxley excitation model

In this figure I_{memb} is the result of positive charges flowing out of the cell. This current consists of three currents, namely Na, K, and leak currents. The leak current is due to the fact that the inner and outer Na and K ions are not exactly equal.

4. CONCLUSION

The electrical activity of the heart is based on the coupling of the bidomain equations with phenomenological ionic model, including anisotropic conductivities and transmural APD heterogeneity.

To further advance automatic EEG analysis these work items are planned for the future: develop methods for noise detection, high level analysis methods (i.e. epilepsy classification, a new drowsiness scale, etc.)

References

- [1] Aehlert, B. "ECGs Made Easy (3rd ed.)". Mosby Jems, Elsevier, 2006.
- [2] Antzelevitch, C. "Cellular basis for the repolarization waves of the ECG". *Ann. N. Y. Acad. Sci.* 1080:268-281, 2006.

- [3] Boulakia, M., M. A. Fernandez, J.-F. Gerbeau, and N. Zemzemi, "Direct and inverse problems in electrocardiography". *AIP Conf. Proc.* 1048(1):113-117, 2008.
- [4] Ethier, M., and Y. Bourgault. "Semi-implicit time-discretization schemes for the bidomain model". *SIAM J. Numer. Anal.* 46:2443, 2008
- [5] Krassowska, W., and J. C. Neu. "Effective boundary conditions for syncytial tissues". *IEEE Trans. Biomed. Eng.* 41(2):143-150, 1994.
- [6] W.O. Tatum, A.M. Husain, S.R. Benbadis, P.W. Kaplan, "Handbook of EEG Interpretation", *Demos Medical Publishing*, 2007.
- [7] S. B. Wilson, R. Emerson, Spike detection: "A review and comparison of algorithms", *Clinical Neurophysiology*, 113, pp. 1873-1881, 2002.
- [8] E. Niedermeyer, F.H.L. Da Silva, *Electroencephalography: Basis Principles, Clinical Applications, and Related Fields*, Lippincott Williams & Wilkins, 2004.
- [9] SJM Smith, "EEG in the diagnosis, classification, and management of patients with epilepsy", *Journal of Neurology, Neurosurgery, and Psychiatry*, 76, 2005.
- [10] A.T.Berg et al., "Revised terminology and concepts for organization of seizures and epilepsies: Report of the ILAE Commission on Classification and Terminology, *Epilepsia*", 51(4), pp.676-685, 2010.

A REAL TIME ECG AND EEG DATA TRANSMISSION FOR REMOTE PATIENT MONITORING SYSTEM

¹Prof. Dr. Dimiter Dimitrov

²Deyan Milev

¹Faculty of Telecommunication, Technical University of Sofia
8, Kliment Ohridsky str., 1756 Sofia, Bulgaria
Phone: +359 2 9652278, E-mail: dcd@tu-sofia.bg

²Faculty of Telecommunication, Technical University of Sofia
8, Kliment Ohridsky str., 1756 Sofia, Bulgaria
Phone: +359 883 556 426, E-mail: dmilev@tu-sofia.bg

Abstract

The recent year has witnessed a significant surge of interest in sensing and monitoring in healthcare. The monitoring and acquisition of patients' physiological information are quite crucial for the further treatment. The Electrocardiogram (ECG) aims to measure the cardiac rhythm and rate of a patient. It ensures that the QRS complex is intact for the diagnosis of cardiac arrhythmias.

The Electroencephalography (EEG) is used in the evaluation of brain disorders. Most commonly it is used to show the type and location of the activity in the brain during a seizure. Many patients can benefit from continuous monitoring as a part of a diagnostic procedure, optimal maintenance of a chronic condition or during supervised recovery from an acute event or surgical procedure.

These are challenges which include issues such as wireless networking protocols, power-efficient topologies, frequency, routing and security.

Keywords: ECG, EEG, Bluetooth communication.

1. INTRODUCTION

The electrical impulses within the heart act as a source of voltage, which generates a current flow in the torso and corresponding potentials on the skin. The potential distribution can be modelled as if the heart were a time-varying electric dipole. If two leads are connected between two points on the body (forming a vector between them), electrical voltage observed between two electrodes is given by dot product of the two vectors [1].

An accurate indication of the frontal projection of the cardiac vector can be provided by three leads/electrodes, one connected at each of the three vertices of the Einthoven triangle [2]. Generally, as many as twelve leads are used to monitor cardiac signals. The most prevalent and significant among these is Lead II for diagnosing rhythm problems. Signals from Lead II measure the variations in potential between the right arm and the left leg, with the electrode of the left arm acting as the ground.

Looking for a choice between Bluetooth and IEEE 802.11 protocols, various indicators point the superiority of 802.11 over Bluetooth protocol. For e.g., experimental results have shown better performance for 802.11b as compared to Bluetooth. Also,

the compatibility of 802.11b with existing LANs reduces the cost of extra hardware and the overhead of managing the Bluetooth network [4].

Smartphones with flexible software development environments have opened up the possibility of creating customized applications to facilitate emergency service. When designing a new systems, it is important to research and analyse any similar products that are already available. Application stores have created a market for both priced and free programs available for mobile download, and Apple's application store alone, there are nearly 12,000 applications related to health [5]. Among these are several applications dedicated to transmitting medical information. The application allows the user to take a picture of the ECG, sends it to the fast ECG website, and then generates a code that the sender can give to the intended recipient. The recipient enters the code on the fast ECG website to view the ECG. Cardiologists have approved the application for it is picture quality, reporting that it allows for normal interpretation of an ECG. The transmitted images are also only slightly compressed to 180kB, making transmission inefficient and slow. When the user presses send, fast ECG attempts to transmit the image only once rather than retrying for a speci-

fied amount of time. This decreases the probability of a successful transmission since it depends on having data service at one discrete moment. A vehicle may move in and out of strong service areas in a short amount of time, so a transmission is more likely to succeed if multiple attempts are made. A mobile application has potential to add value to the systems that are currently being used. All ECG devices available on the market produce 12-lead printouts; however some devices transmit ECG images to hospital servers, while others do not. Technology in camera phones has improved to take high resolutions images even in low quality lighting. Transmission using a smart phone is very different than using a proprietary system because applications on smart phones are developed to be flexible. Using a mobile application in the hospital workflow allows for customization with regards to probing for network activity and providing real-time feedback/results to users. Using the application could therefore provide more reliable feedback to users. In addition, the low cost of a mobile application would make ECG transmission accessible to rural EMS providers without funds for expensive systems.

2. MAIN TEXT

Wireless technology is ability to generate interactive healthcare utilizing modern technology and telecommunication. In telemedicine system is useful for absent of directly contact between the patient and doctor. The wireless device employ for the efficient remote monitoring system, using for real time, continuous and accurately information of patient heat condition.

The electrocardiogram is important role in the prevention, diagnose the abnormality of patients and rescue of heart disease. The development of a remote monitoring system for ECG signals, the deployment of packet data service over telecommunication network with new applications. Body area network where a certain number of sensors are acquire full range of biological signal and transmit them to remote base station for processing. Using wireless connection as medium, number of issue must be considered: ease of security, network generation, data throughput, data loss and power consumption.

3. ILLUSTRATIONS

The system divided in to the three parts. The first is the ECG and EEG acquisition part, the second part

is the wireless transmission of the data to the patient's computer transmission, and the third part is data acquisition, viewing and restore.

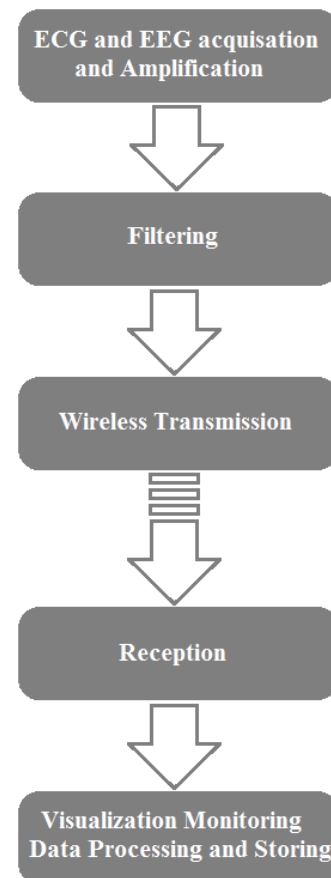


Figure 1. System work Flow

The analog signal portion has been simple, in order minimized space board. The raw signal- noisy ECG and EEG signals is acquire through disposable electrodes, attached to cables through a couple of standard clips. Filter circuit and then to wireless module for transmission. Wireless module based on IEEE 802.15.4 used for transmission and receiving the signal. ECG and EEG front end circuit connected with wireless module as remote base station.

The EEG test is non-invasive neurophysiology exploration usually needed in many neurological consultation to configure a final diagnose, together with the information from patient's clinic and neurological exploration. The EEG records the electrical activity of the brain to provide information used in the diagnosis of different clinical circumstances such as epilepsy or mental disorders. Moreover, it is used to analyse and control the treatment of patients with neurological damage. It is usually performed with an ambient video recording in order to clearly distinguish biological artefacts from neurological al-

terations and also to advice in advance epileptic seizures. Although the EEG test is a highly demanded medical technique, used in different medical fields like neurology, internal medicine and paediatrics, this service is not available in many primary or secondary hospitals. Thus, the introduction of a telemedicine system applied to acquire and transmit electroencephalographic signals in real time is presented as an attractive solution to avoid patient's transfer to tertiary hospitals and to provide them better access. In telemedicine field using transmission media and compression techniques to deliver bio such as ECG, EEG for long distance medical services has become reality and challenge. For the urgent treatment or ordinary healthcare or patient monitoring system, it is necessary to compress and transmit these data for the efficient use of bandwidth. In telemedicine application, transmitting a large amount of data through limited bandwidth and compressed form become a challenge [7]. While transmitting an EEG data, of data is compressed by compression techniques then it will reduce the data volume but significant features are preserved at the time of decompression. EEG data, being the acquired output from biological and physical systems, may possess various properties and characteristics that contribute to their diagnostic value [8].

3.1. Overview of algorithms

To meet the requirements of the research, the survey is carried out for the well-functioning of the developed applications. The survey carried comprises of comparison and transmission between various methods to achieve EEG data compression and transmission. For data compression the basic communication methods could give a best result. Methods like sampling, transforming, filtering and amplifying and coding can give the compression result and by using wireless network the transmission can be achieved.

Sangjoon lee, Jungkuk Kim, myoungho Lee [4] deals with the different methodologies for compression of bio signal. This paper focused on real-time algorithms for a periodic bio signal, which supports to e-health services. A mainly author introduces a real time compression and transmission algorithms. The proposed algorithms. Moreover, because the algorithm can compress and transmit data in real time, it can be served as an optimal bio signal data transmission method for limited bandwidth communication between e-health devices. The following evaluation factor of compression algorithm is

Table 1. Evaluation factor of compression algorithm

Sr No	Evaluation factor	Results
1.	Compression Ratio (CR)	21.30
2.	Percentage rms difference (PRD)	1.75
3.	Percentage rms difference normalize (PRDN)	24.93
4.	Signal to Noise Ratio (SNR)	13.10
5.	Quality of Service (QS)	12.18

In general, EEG data compression can be of two types

1. Lossless compression:

In the lossless processes the original data can be exactly reconstructed from their compressed form. Lossless compression is typically adopted for text compression. In the lossless compression all information is saved and the compression is reversible [9]. For typical biomedical signals lossless (reversible) compression methods can only achieve Compression Ratios in the order of 2 to 1 [10].

2. Lossy compression:

Other hand lossy (irreversible) techniques may produce CR results in the order of 10 to 1. In lossy methods, there is some kind of quantization of the input data which leads to CR which is defined as the ratio of the total number of bits used to represent the digital signal before and after Compression, higher CR results at the expense of reversibility. But this may be acceptable as long as no clinically significant degradation is introduced to the encoded signal. The CR levels of 2 to 1 are too low for most practical applications. Therefore, lossy coding methods which introduce small reconstruction errors are preferred in practice.

For the means of,

1. Effective and economic data storage.
2. Real time transmission of the signals.

The most efficient data compression technique from all the available lossless data compression techniques needs to be chosen.

4. CONCLUSION

There are several methods of recording and transmitting ECG and EEG signals. A classical recording in health centre, then ambulatory ECG and EEG recordings and telemetry monitoring the patient in and round medical centre. With the use of mobile phone in medical purposes, monitoring and recording of the ECG and EEG signals offer many ad-

vantages. It is possible to monitor a heart patient in a real time, immediately to give an advice and therapy, the covered area of movement of the patient is practically unlimited. The control monitor centre with trained medical staff enables 24 hour monitoring of few thousands patients. With pre-paid service we get more economical and efficient way of monitoring patients than with classical recording of the ECG and EEG signals.

References

- [1] "Bio signal and compression standard" by leontios J. Hadjileontiadis
- [2] N.Sriraan, C.Eswaran, "Performance Evaluation of Neural network and linear prediction for near lossless Compression of EEG signal." *IEEE transaction on Information Technology in biomedical*, Vol.12 No.1, 2011.
- [3] Ethier, M., and Y. Bourgault. "Semi-implicit time-discretization schemes for the bidomain model". *SIAM J. Numer. Anal.* 46:2443, 2008
- [4] Antzelevitch, C. "Cellular basis for the repolarization waves of the ECG". *Ann. N. Y. Acad. Sci.* 1080:268-281, 2006.
- [5] Benoit, Latre Bart Braem Ingrid Moerman Chriss Blondia, Piet Demeester. "A Survey on Wireless Body Area Network." 2012
- [6] Charles, B. L., "Telemedicine can lower costs and improve access", *Healthcare Financial Management*, 54(4), The Healthcare Financial Management Association, Oak Brook, Ill., 2000, pp. 66-69.
- [7] Bashshur, Rasid L., Teardon, Timothy G. and Shannon, Gary W., "Telemedicine: A new health care delivery system", *Annual Review of Public Health*, 21, Annual Reviews, Palo Alto, Calif., 2000, pp. 613-637
- [8] Huston, Terry L and Huston, Janis L., "Is telemedicine a practical reality?", *Communications of the ACM*, 43(6), Association for Computing Machinery, Baltimore, Md., 2000, pp. 91-95
- [9] BlueRadios, "BR-C30 Class1, Class2, and Class 3 Bluetooth ver1.2", 2005. Available: <http://www.blueradios.com/BR-C30.pdf>
- [10] J. Pan and W. J. Tompkins, "A real-time QRS detection algorithm," *IEEE Trans. Biomed. Eng.*, vol. BME-32, pp. 230-236, 1985.

APPLICATION OF AN AUTOFOCUSING ALGORITHM FOR SAR IMAGE QUALITY IMPROVEMENT AND APPLICATION OF THE MODIFIED FRACTAL SIGNATURE (MFS) METHOD FOR SAR IMAGE CLASSIFICATION FOR THE CASE OF REAL RADAR DATA

A. Malamou, C. Pandis, A. Karakasiliotis, P. Stefaneas, D. Kodokostas and P. Frangos

National Technical University of Athens
9, Iroon Polytechniou Str., GR 157 73, Zografou, Athens, Greece
Tel. +30 210 772 3694, Fax. +30 210 772 2281, E-mail : pfrangos@central.ntua.gr

Abstract

In the first part of this paper, the application of an autofocus algorithm is presented for the case of real field radar data, provided to us by SET 163 Working Group. This algorithm is named 'CPI-split-algorithm', where CPI stands for 'Coherent Processing Interval'. Numerical results presented in this paper show the effectiveness of the proposed autofocus algorithm for SAR image enhancement.

In the second part of this paper the Modified Fractal Signature (MFS) method is presented. This method uses the 'blanket' technique to provide useful information for SAR image classification. The MFS method is applied in real field data provided to us by SET 163 Working Group (comparison of a 'town' area, 'suburban' area and 'sea' area). In these results it is clearly seen that the type of area can be distinguished by the value of MFS signature for the real data.

1. INTRODUCTION

Synthetic aperture radar (SAR) can perform with high image resolution at long range, regardless the weather conditions. It is a radio frequency (RF) sensor and has been widely used as a tool for long-range imaging. The range-Doppler information collected by the SAR antenna leads to the synthesis of the SAR image of the target with high resolution [1], [2]. The targets of observation can be either stationary or moving ground objects. Moving targets are usually monitored as they are of great interest. However the reconstruction of the image of a moving target using SAR data is difficult because the obtained SAR image is usually degraded by defocus, distortion or displacement due to target movement. In this paper the post processing CPI-split autofocus algorithm [3] is applied to the case of real field data of a moving ship (airborne SAR), provided to us by SET 163 Working Group (see acknowledgement below for more details), in order to obtain a focused SAR image of a moving target.

Moreover, in this paper, the Modified Fractal Signature (MFS) is applied in real SAR radar images. This technique has already been used for document analysis, classification and pattern recognition [5], [6]. In this paper is applied in the classification of

SAR radar images and in particular in the discrimination of a real SAR radar image ('Oslo Fjord') to 'town' area, 'suburban' area and 'sea' area.

2. APPLICATION OF AN AUTOFOCUSING ALGORITHM FOR SAR IMAGE QUALITY IMPROVEMENT FOR THE CASE OF REAL RADAR DATA

In this section we incorporate the post processing CPI-split autofocus algorithm (briefly named "CPI-split auto-focusing") recently introduced by our research group [3], [4] in the case of real field radar data. This algorithm has already been tested for simulated data in the cases of SAR and ISAR geometry [3], [4]. The application of our proposed algorithm produced excellent focusing of SAR and ISAR images for several cases of moving targets [3], [4].

The real field radar data, which are examined here, were provided to us by SET 163 Working Group (see the 'Acknowledgement' below for more details). This radar transmits linear frequency modulated waveform (LFM), whereas in our simulation scenarios [3], [4] the radar antenna is assumed to emit Stepped Frequency (SF) pulses. These raw radar data yield ultimately (after appropriate SAR

signal processing) a moving ship target, which is being imaged by the SAR radar. In Fig. 1 three SAR images of consecutive CPI's are presented.

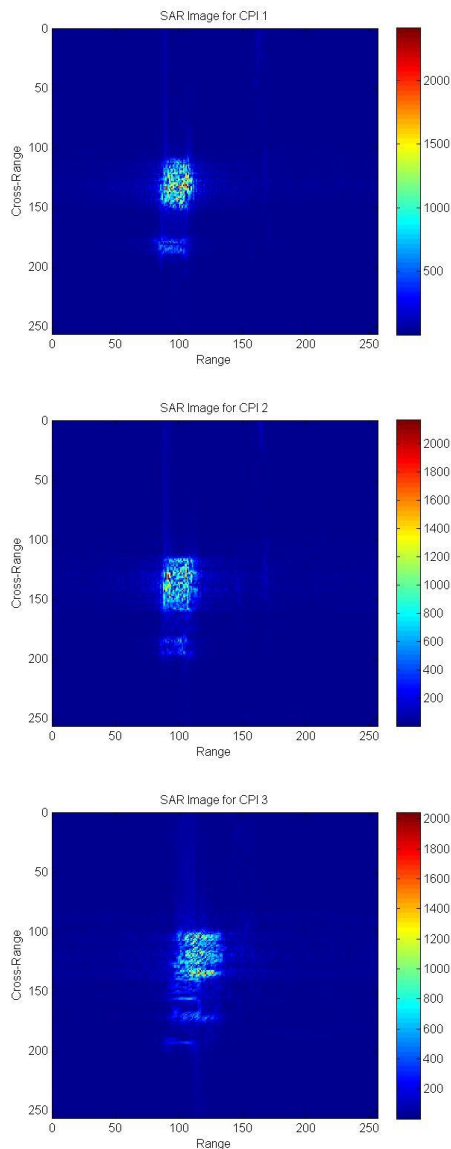


Figure 1. SAR images for three CPI's (real radar data provided by 'SET 163 Working Group')

In order to compare the quality of the above SAR images, the entropy value of each image is computed [3], [4]. In Table 1 the entropy values for the three SAR images presented above are listed. The CPI-split autofocusing algorithm is employed in the CPI which entropy value exceeds a threshold that represents an acceptable SAR image quality [3]. The images with entropy values below the entropy threshold are called "focused" images, while the images with entropy values over the threshold are called "unfocused". We have applied the autofocusing algorithm to the previously presented SAR images for four CPIs. As seen in Table 1, the 3rd CPI has the greater entropy value and therefore is the

"unfocused" CPI. The entropy threshold was set to 7.5.

Table 1. Entropy values

SAR Image	Entropy	Minimum Entropy Combination
1st CPI	7.1409	
2nd CPI	7.3497	
3rd CPI, unfocused	7.6694	
3rd CPI, focused	7.3948	stage 3, segment 2, combination 3 [3]

In Fig. 2 the SAR images for the 3rd CPI are presented, before and after the application of the autofocusing algorithm.

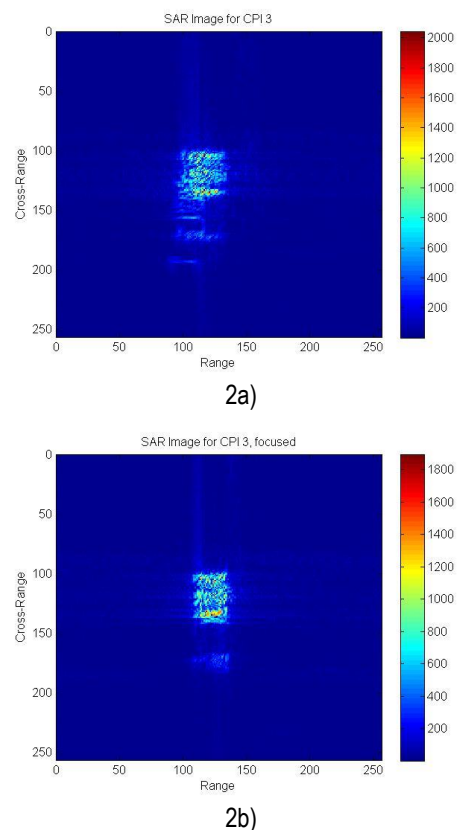


Figure 2. SAR image before (a) and after (b) the application of the proposed autofocusing algorithm.

The SAR image for the 3rd CPI after the application of the autofocusing algorithm is clearly more focused than the SAR image before the application of the autofocusing algorithm. This result is also validated by the entropy values presented in Table 1. The entropy value of the SAR image (3rd CPI) before the application of the autofocusing algorithm is greater than the entropy value of the SAR image (3rd CPI) after the application of the autofocusing algorithm. Moreover the entropy value of the 'focused' image is within the acceptable entropy values (below the entropy threshold).

The real-field data results presented above show that the proposed algorithm is effective in producing focused SAR images. Based on SAR image entropy minimization criterion, the proposed algorithm neglects data leading to ISAR images of poor quality and uses only data leading to ISAR images of superior quality. The simulations results verify the adaptiveness of the autofocusing procedure to different SAR imaging conditions.

3. APPLICATION OF THE MODIFIED FRACTAL SIGNATURE (MFS) METHOD TO SAR IMAGE CLASSIFICATION

In this section the implementation of the 'blanket' (MFS) method [5], [6] is described. Initially, the SAR image is converted to a gray – level function $g(x,y)$. Subsequently the whole SAR image is divided into several non-overlapping sub-images and the fractal signature is calculated for each sub-image. The overall fractal signature of the initial image is calculated ultimately by summation of the corresponding values of the sub-images [5]. In addition in order to compute the fractal dimension, we need to measure the area of the gray level surface.

In the blanket technique, all points of the three dimensional space at distance δ from the gray level surface $g(x,y)$ are considered. These points construct a "blanket" of thickness 2δ covering the initial surface. The covering blanket is defined by its upper surface $u_\delta(x,y)$ and its lower surface $b_\delta(x,y)$ as it is presented in Fig. 3.

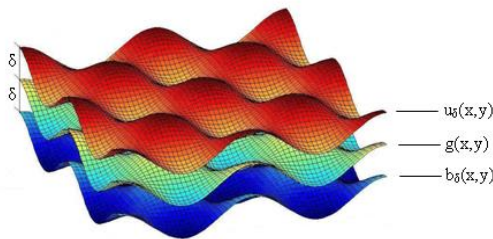


Figure 3. 'Blanket' of thickness 2δ defined by its upper $u_\delta(x,y)$ and lower $b_\delta(x,y)$ surface

The algorithm used to compute the upper and lower surface includes the following steps. Initially, the iteration δ equals zero ($\delta=0$), the gray-level function equals the upper and lower surfaces, namely: $u_0(x,y)=b_0(x,y)=g(x,y)$. For iteration $\delta=1,2,\dots$ the blanket surfaces are calculated through the following iterative formulae

$$u_\delta(x,y) = \max\{u_{\delta-1}(x,y) + 1, \max_{|(m,n)-(x,y)| \leq 1} u_{\delta-1}(m,n)\} \quad (1)$$

$$b_\delta(x,y) = \min\{b_{\delta-1}(x,y) - 1, \min_{|(m,n)-(x,y)| \leq 1} b_{\delta-1}(m,n)\}$$

Subsequently, the volume of the 'blanket' is calculated from $u_\delta(x,y)$ and $b_\delta(x,y)$ by:

$$Vol_\delta = \sum_{(x,y)} (u_\delta(x,y) - b_\delta(x,y)) \quad (2)$$

Furthermore, the fractal signature $A\delta$ is calculated by :

$$A_\delta = \frac{Vol_\delta}{2\delta} \quad \text{or} \quad A_\delta = \frac{Vol_\delta - Vol_{\delta-1}}{2} \quad (3)$$

Finally, concerning the calculation of the corresponding fractal dimension D , the following formula is used [5]:

$$A_\delta \approx \beta \delta^{2-D} \quad (4)$$

where β is a constant, from which the fractal dimension can be calculated from successive fractal signature values as following:

$$D \approx 2 - \frac{\log_2 A_{\delta_1} - \log_2 A_{\delta_2}}{\log_2 \delta_1 - \log_2 \delta_2} \quad (5)$$

where $\delta=1,2,\dots$ e.t.c.

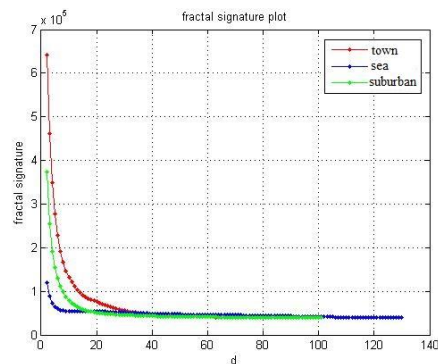
Subsequently, the application of the MFS method to Synthetic Aperture Radar (SAR) images from real radar data (SAR image of 'Oslo fjord') provided to us by SET 163 Working Group is presented. The SAR image examined here is shown in Fig. 4. Three sub images were obtained from the initial SAR image: the first includes a 'town' area, the second a 'suburban' area and the third a 'sea' area.



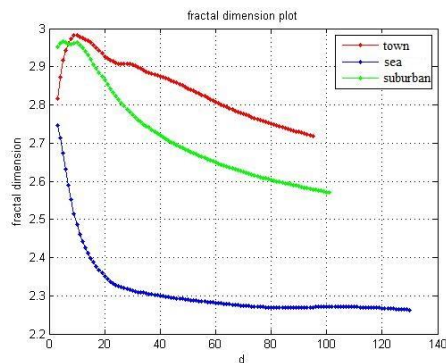
Figure 4. SAR image of 'Oslo fjord' (provided by 'SET 163 Working Group')

In Fig. 5, the fractal signature $A\delta$ as a function of iteration δ and the fractal dimension D as a function of iteration δ for the cases of three sub images: 'town' area, 'suburban' area and 'sea' area are presented.

It appears that the proposed algorithm provides interesting characterization results for the cases of 'town' area, 'suburban' area and 'sea' area.



5a)



5b)

Figure 5. (a) fractal signature A_δ as a function of iteration δ , (b) fractal dimension D as a function of iteration δ for the cases of 'town' area, 'suburban' area and 'sea' area.

4. CONCLUSION

In this paper, the 'CPI-split autofocusing algorithm' is incorporated for the case of real field radar data. The real-field data results presented above show that the proposed algorithm is effective in producing focused SAR images. The simulation results verify the adaptiveness of the autofocusing procedure to different SAR imaging conditions.

Furthermore, an iterative MFS technique [5], [6] is applied aiming in SAR radar image characterization (real data). As confirmed by the results presented above, the proposed algorithm provides interesting characterization results. It is apparent that the criteria of 'fractal signature' and 'fractal dimension' for SAR image characterization work in a satisfactory way. The type of area can be distinguished by the value of 'fractal signature' and 'fractal dimension' for the real field radar data.

Acknowledgments

The authors (AM, AK, PF) would like to acknowledge SET 163 Working Group, and its Chairman Dr. Luc Vignaud (ONERA, France) in particular, for providing to us the real field Synthetic Aperture Radar (SAR) data, which were used to reconstruct

the SAR images of moving ship shown in Fig. 1 above, as well as the SAR image of 'Oslo fjord' shown in Fig. 4. In particular, the radar data concerning the moving ship of Fig. 1 were provided to SET 111 and SET 163 Working Groups by Dr. William Miceli (ONR) and their origin is from a radar developed by 'Radar Branch of the Naval Command Control and Ocean Surveillance Center, Research Development Test and Evaluation Division (NRaD), San Diego, CA, USA. Furthermore, the 'Oslo fjord' image of Fig. 4 was produced by DLR, Germany (spaceborne image). To all the above institutes and involved scientists we express our sincere thanks for providing these real field radar data to us, in the framework of SET 163 Working Group.

This research has been co-financed by the European Union (European Social Fund) and the Greek National Funds through the Operational Program "Education and Lifelong Learning" of the National Strategic Reference Framework (NSRF) – Research Funding Program: THALES.

References

- [1] D. Wehner, High-Resolution Radar, London, Artech House, 2nd edition, 1995.
- [2] V. Chen, H. Ling, Time-Frequency Transforms for Radar Imaging and Signal Analysis, Artech House, London 2002.
- [3] E. Kallitsis, A. Karakasiliotis, G. Boultsadakis, P. Frangos, "A Fully Automatic Autofocusing Algorithm for Post-processing ISAR Imaging based on Image Entropy Minimization", Electronics and Electrical Engineering Journal, No. 4 (110), April 2011, pp. 125–130.
- [4] A. Malamou, A. Karakasiliotis, E. Kallitsis, G. Boultsadakis, P. Frangos, "Application of a Fully Automatic Autofocusing Algorithm for Post Processing of Synthetic Aperture Radar Images based on Image Entropy Minimization", Electronics and Electrical Engineering Journal, Vol. 19, No.6, June 2013, pp. 95–98.
- [5] Y. Tang, H. Ma, D. Xi, X. Mao, C. Suen, "Modified Fractal Signature (MFS): A New Approach to Document Analysis for Automatic Knowledge Acquisition", IEEE Transactions on knowledge and data engineering, Vol. 9, No. 5, Sept. – Oct. 1997, pp. 747-762.
- [6] N. B. Ampilova, E. Y. Gurevich, I. P. Soloviev, "Application of modified fractal signature and Regny spectrum methods to the analysis of biomedical preparation images", CEMA'11 Conference, Sofia, Bulgaria, October 2011, pp. 96 – 100.

PRAXIS: THE EUROPEAN CENTRE FOR PROJECT / INTERNSHIP EXCELLENCE

Nuno Escudeiro¹, Paula Escudeiro²

^{1,2}Instituto Superior de Engenharia do Porto
Rua Dr António Bernardino de Almeida, 431, 4200-072 Porto

²GILT
Rua Dr António Bernardino de Almeida, 431, 4200-072 Porto
T.+351 228 340 500; F.+351 228 321 159; E. ¹nfe@isep.ipp.pt; ²pmo@isep.ipp.pt.

Abstract

Project/Internship course units are particularly valuable to undergraduate degrees. It is through this type of courses that students have the chance to practice their technical skills in a real-world-like setting and experience soft skills that are a key factor for employability. There are many distinct flavors of Project/Internship courses throughout Europe. Nevertheless, there is a lack of foundation supporting innovation, development and dissemination of the field. The purpose of PRAXIS is to fill this gap and set a European dimension to this instructional paradigm. In this paper we describe the PRAXIS concept, its development plan and the foreseen outcomes.

1. INTRODUCTION

Project/Internship (PI) course units create an environment that is a unique cradle to forge students' soft skills and attitudes, such as, team work, leadership, communication, initiative, focus. Addressing and improving these skills in students efficiently and efficaciously is seldom done by any other type of instruction. A PI is probably the most efficient way to improve these skills in students since even a very short PI course unit has significant impact in students' competences. It is the appropriate setting to improve students' affective domain, an important domain in today's society, in any study area.

This type of instruction is very suited to the Bologna paradigm raising the interest of European Higher Education Area (EHEA) players into it.

Despite the relevance and added value of this type of instruction, despite the high interest that it raises in higher education institutions (HEI), there is no European cluster specifically addressing the field and there is no planned effort to improve and innovate in the field. The purpose of the PRAXIS network is to set a European dimension to PI instruction type.

PRAXIS' mission is to become recognized as the leading authority worldwide in the field of the PI instruction type by creating and maintaining an environment that promotes and supports innovation in the field aimed at improving students' employability, soft skills and attitudes.

Our goals are: (a) to promote a European Center for Excellence in the field of PI initiatives by leveraging common interests and promoting cooperation among stakeholders, bringing all of them together, creating an environment to discuss and to promote innovation in the field, joining efforts and exploiting synergies and results from each other; (b) set a European marketplace of PI maximizing students' chances to find a project course matching their needs and, at the same time, setting a place to deploy innovative project course units by making them visible and available to students.

The perception of this opportunity to contribute to the EHEA by providing foundation to support innovation in the PI field together with our strong convictions on these assumptions arose from our previous experience in PI related issues, from all the contacts and discussion around these subjects that we have been promoting in the last few years and from our former work on multinational project teams, mainly at the MUTW – Multinational Undergraduate Team Work, an Erasmus Multilateral Project, co-funded by the EU from October 2009 till December 2011[1].

In the rest of the paper we will briefly describe the motivations moving PRAXIS towards its goals, the work plan we are applying to deploy PRAXIS and some final considerations.

2. RELATED WORK

There are many distinct flavors of PI courses throughout the EHEA, such as:

- multinational teams of students working at their home institutions and communicating virtually (MUTW)
- multinational teams working at a host institution (European Project Semester from Copenhagen University College of Engineering)
- multidisciplinary teams (project course at the University of Minho in Portugal and the International Integrated Project from the Fontys University in Netherlands)
- capstone project courses developed in a company or at a research lab (most engineer universities)
- small project course units running at the end of the semester (LAPR course unit at Instituto Superior de Engenharia do Porto in Portugal)

Some European projects and other initiatives focused on students' skills show the interest motivated by the field:

- FS-Biotech - Future Skills for Biotechnology "Skills to transform the future"; an Erasmus project, coordinated by Universidade Católica do Porto, that fosters cooperation between companies and Universities and the adaptation of curricula to companies needs in terms of valued skills
- EUROPLACEMENT is another LLP project that focuses on the development of graduates' transferable skills, and provides them with procedures for quality work experience, adapted to improve their own existing competence sets

Although we have not found any direct competitor for PRAXIS – someone who is worried with a comprehensive study of the field and focused on innovation and on promoting students' employability – there are many institutions that offering internship to students.

The interest in PI and students' employability field is notorious. The issue is that there is no declared centralized hub to join all players together and to promote innovation and exchange of experiences in the field. PRAXIS will set such a facility with the aim of joining efforts, promoting awareness, taking ad-

vantage of synergies and encouraging innovation and dissemination of best practices.

3. MOTIVATIONS AND OBJECTIVES

The lack of foundation to support innovation in the field of PI is the main motivation for PRAXIS. There is an opportunity to fill in this gap and to bring a European dimension to the field, empowering students, HEI, companies and the EHEA in general with an extended set of opportunities to grow and profit from this instructional paradigm.

Establishing a center of excellence and a virtual marketplace for PI clearly marks a position and openly exposes this kind of instruction to all players assuring the European dimension that is required to empower the field. This European dimension will reach both students, who will have the chance to select the offer that is most suited to their needs, and teachers, who will have available the resources to discuss and bring to light their ideas in the field, a clear contribution to the development of EHEA.

There are already several distinct flavors of PI courses, with huge added value to the players, offered regularly in European HEI. However, these opportunities are not available neither known to all the students that might be interested in enrolling. Dissemination is a hard enterprise to take on one's own for several reasons, such as lack of resources and motivation. The benefits of these initiatives are not exploited given their local scope. Having the means to expose them worldwide will certainly generate economies of scale and encourage innovation in the field contributing to the exploitation of best practices in the field.

Student's employability is improved by PI courses to an extent that is not easily achievable by other instruction types. PI courses force students to develop soft skills and attitudes while training technical competence. This mix produces good results fast. Nevertheless, there is no cluster developing the field. There is a window of opportunity to set the agenda and to promote innovation in the field in Europe that PRAXIS intends to take, thus, incorporating new qualifications into the EHEA.

The frontend of both the European Center for PI Excellence and the PI market will be freely available online achieving a worldwide coverage. These facilities set a meeting point for players in the field. Operating them will enforce multilateral cooperation to discuss relevant issues and to organize mobility

for students selecting PI courses abroad. This cooperation is of high quality since it has a concrete goal in mind: improving student's value-to-labor-market.

Both the PI marketplace and the European Center for PI Excellence, two innovative outputs of PRAXIS, will be deployed through the internet and supported by ICT technologies. The comprehensive resource on PI materials, to be gathered and maintained by PRAXIS, including content and teaching materials, mainly directed to students, and technical materials, mainly directed to staff from the higher education institutions, to employers and to other stakeholders, will also be supported by ICT.

The PI instructional type, the focus of PRAXIS, is highly efficient; even a short PI course has high impact in students' competences. The conditions under which students do their assignment in PI courses is unique, significantly contributing to improve students' soft skills and attitudes and, as a consequence, their employability.

From the productivity point of view, PRAXIS promotes the reuse of the best practices in the field by making the most effective PI courses widely available thus contributing to the Europe 2020 Strategy.

3.1. Mission

Our mission is to become recognized as the leading authority worldwide in the field of Project/Internship instruction type aiming to improve students' employability and soft skills. Our activity, focused on achieving a widespread reputation and reach, will be based on the European Centre for Project/Internship Excellence and on the Project/Internship Virtual Market.

3.2. Goals

Our strategic goals are:

1. To promote a European Center for Excellence in the field of Project/Internship initiatives by leveraging common interests and promoting cooperation among stakeholders, bringing all of them together, creating an environment to discuss and to promote innovation in the field, joining efforts and exploiting synergies and results from each other.
2. To set a European market of Project/Internships maximizing students' chances to find a project course matching their needs and, at the same time, setting a place to

deploy innovative project course units by making them visible and available to students.

3.3. Added value

PRAXIS acts on a field closely related to the EU2020 flagships. The main outputs of PRAXIS, the PI market and the European Center for PI Excellence, provide means for students to take advantages of the global Europe wide offer by selecting the most appropriate PI course given their interests. This makes easier for them to get the right skills and competences.

The main issues of Bologna 2.0 are also addressed. PRAXIS provides a widening access to state of the art initiatives, it brings a global dimension to the field and deploys transparency tools.

Creating a cluster and the required framework to promote the PI instruction type and related issues will contribute to the EHEA in an area that can bring important benefits to all players at low cost. The PRAXIS vision is supported on the exposure of what already exists in the expectation that this exposure, in an appropriate scenario, will promote discussion and innovation. The PI market promotes reusing best practices. Reusing, in this sense, means saving, getting the benefits at low cost.

European cooperation is a sine qua non condition for PRAXIS. PRAXIS goals are not achievable without a representative group that has the power to influence opinion and generate the mood. The bigger the consortium, the better chances we have to succeed.

4. WORK PLAN

PRAXIS is a three years project co-funded by the EU, running between October 2011 and September 2014.

The focus of the project during the first year will be on the analysis of the field and design of the models and tools to describe and operate on it. During this first year we will map and model the target field of PRAXIS. When referring to the field we mean the broad area of project/internship and similar instruction types along with any initiatives related to them and to improving student employability. A detailed map of the field, clearly showing where we stand and what the market needs are, will allow us to identify opportunities for innovation and for improvement. The PRAXIS buzzwords for the first year of the project are exploring, mapping.

The second year will be focused on setting up and deploying the center for excellence in the field and the virtual PI market (PI stands for Project/Internship). Designing the market and the center for excellence as well as setting them up targeted for the opportunities previously identified, while assuring the required critical mass, will be the main achievements of the second year of the project. Our second year will be guided by headings acting, innovating.

The third and last year will be focused on exploitation and sustainability to assure the continuity of PRAXIS beyond funding. We will be focused on identifying opportunities for enlarging the consortium and on making PRAXIS a renowned brand in the EHEA and abroad. The third year of PRAXIS will be focused on exploitation, sustainability.

5. CONCLUDING REMARKS

At the PRAXIS consortium, we are deeply convinced that it is possible to improve the quality of most current curricula of undergraduate degrees without demanding for structural changes that force institutions to apply huge resources and that are very costly and time consuming. We refer to improvements in students' employability, in developing students' soft skills and attitudes which are rather important in today's economy and labor market as recognized by the EU. These are transversal to the majority, not to say all, of the study areas, so PRAXIS will be valuable to most study areas.

The cost/benefit ratio of initiatives in PI course units is probably one of the lowest in curriculum development, requiring small changes to provide big improvements. Almost all undergraduate degrees contain a PI course unit in their curricula. All we need is to take advantage of these course units to

make them provide to students, and also to their future employers and the society in general, all the benefits they can and which can be much more than those provided by today's common PI course units.

Offering valuable training to students, on one side, and being recognized by the society as a valuable higher education provider, on the other, are among the general objectives of any HEI. The PRAXIS network moves towards these objectives since it will create new conditions to improve students' skills at no additional cost and without requiring any structural changes in degrees' curricula. From this point of view, all that PRAXIS is doing is providing a distribution channel for the best practices in PI that will become available for use by any HEI without additional costs of any kind. With PRAXIS anyone will be able to benefit from best practices and contribute to innovation in the PI field.

6. ACKNOWLEDGMENTS

The work and the outcomes described in this paper are due to the PRAXIS consortium and to the dedication of all partners involved in it (www.praxisnetwork.eu).

This work has been funded with support from the European Commission under grant 518811-LLP-1-2011-1-PT-ERASMUS-ENW. This publication reflects the views only of the author, and the Commission cannot be held responsible for any use which may be made of the information contained therein

References

- [1] Multinational Undergraduate Team Work – Excellence in International Capstone Projects, Escudeiro, N.F., Escudeiro, P.M. Eds, IOS Press BV, Netherlands, 2011.

THE EVOLUTION OF ACTIVE PROSTHETICS

Viktor A. Nedialkov

Fakulty of Telecommunication, Technical University of Sofia,
8 Kliment Ohridski Blvd., 1000 Sofia, Bulgaria

Abstract

In their long history the prostheses have progressed from simple wooden legs through complex and heavy active research devices to state of the art mind driven robotic limbs. Many hurdles have been cleared during the years of research but still many challenges remain to be solved.

This article provides a summary of some of the active prosthetics projects, their advantages and disadvantages. This paper gives the reader some sense of perspective concerning the evolution of this field. The paper provides a discussion about the future of active prosthetics as well the problems still not solved.

1. INTRODUCTION

The origin of prosthetics dates back to the early civilizations of Egypt, Greece and Rome, when prosthetic limbs were made out of wood, iron, and bronze. Brutal war battles throughout world history have resulted in extraordinary mortality and morbidity, including grotesque injuries and the loss of limbs. During the 20th century world wars the number of amputees rose to unprecedented levels. The need for advancements in this field had been recognized by many institutions and many researches began.

Before that all prostheses were passive. They had no synchronization with the patient intended movement. This had resulted in altered gait for the patient, much more energy spent when walking and almost impossible hurdle passing (such as stairs). Also the unnatural gait that this prosthesis produces was the cause for many diseases to the remaining joints of the limb. This created the need for development of active prostheses, which had to provide more natural movement with less energy spent by the patient.

In this paper, we will present a review of the work done on some active prostheses projects.

The term 'active prosthesis' is typically used to describe a device intended to increase the ambulatory ability of a person suffering from a leg or hand pathology by providing some means of augmenting the power at one or more joints of the extremities.

Unlike passive prostheses, active orthotic devices have the potential of actively controlling the joints of the devices, rather than just simple mechanical coupling that exists with the most common com-

mercial assistive devices. Architectures in which power or torque is added at appropriate phases of the gait cycle might be able to enable users to walk who otherwise could not with passive devices, or allow them to walk more naturally and/or efficiently. Additionally, portable devices such as these have the potential of providing both assistance and therapy at the same time, an extremely desirable property in rehabilitation.

Active prostheses are generally classified as - 1. Active prostheses with state based control via Intrinsic sensing. 2. Active prostheses with biofeedback control or myoelectric prostheses. 3. Myoelectric prostheses with surgical interventions.

The state based designs use the sensors on the prostheses which activates the responding movement (e.g. when the sensor detects pressure on the toe edge of the foot a walking cycle is started).

Myoelectric prostheses collect EMG signals from residual muscles and nerves, process them and generate control signals to the prostheses. It is usually combined with the state based designs to give better results.

Myoelectric prostheses with surgical interventions again uses EMG signals for control, but patients undergo a surgical procedure for either nerves re-routing or implantable sensor placement. This techniques provide much better reliability and functionality than simple myoelectric prostheses.

2. ACTIVE PROSTHESES WITH STATE BASED CONTROL VIA INTRINSIC SENSING

The first controllable active orthosis that could be found is a patent for a hydraulically-actuated device from 1942 for adding power at the hip and knee joints. However, due to the state of the art in controls technology at the time, the device was "controlled" by the physical opening and closing of the hydraulic valves by a cable and linkage system that activates at certain joint angles in the gait cycle. Another early patent from 1951 describes a similar passive device that uses spring-loaded pins for locking and unlocking the joints of the brace at various stages of the wearer's gait [1].

2.1. Mihailo Pupin Exoskeleton

The pioneering work done with exoskeletons by Miomir Vukobratovic and his associates at the Mihailo Pupin Institute in Belgrade in the late 1960s and 1970s is some of the most extensive to date. The work started with a passive device for measuring the kinematics of walking and then quickly progressed to the development of powered exoskeletons. The earliest of these, the 'kinematic walker', featured a single hydraulic actuator for driving the hip and knee, which were kinematically coupled. In 1970, the so-called 'partial active exoskeleton' was developed, which incorporated pneumatic actuators for flexion/extension of hip, knee, and ankle, as well as an actuated abduction/adduction joint in the hip for greater stability in the frontal plane. This concept was later slightly modified into the 'complete exoskeleton' by extending the attachment at the torso to enclose the entire chest of the patient, providing greater trunk support (Fig. 1). More than 100 clinical trials were performed with this device, and a number of patients with varying degrees of paralysis mastered walking using the complete exoskeleton with support from crutches. These devices interfaced with the wearer via shoe bindings, cuffs around the calves and thighs, and a 'corset' on the torso. This corset also holds the 14 solenoid valves for the control of the pneumatic pistons. The total weight of the 'complete' exoskeleton, after incorporation of lighter valves, was 12 kg. This value does not include the power source and control computer, which are not located on the device

During operation, all of the above exoskeleton devices were driven through a predetermined reciprocating motion via an 'electronic diode' function generator. However, a set of three piezo-ceramic force sensors were soon incorporated into the sole of the

'complete' exoskeleton foot for use in determining the location and magnitude of the ground reaction force, which in turn was used in the control of the device.

In order to begin to address the problem of being energetically autonomous, a version of the exoskeleton actuated by DC motors was developed. Although the state of motor, battery, and computer technology limited the true portability of the device, this new actuation scheme offered further improvements such as smoother motion and better tracking ability.

One of the most lasting contributions of their work with exoskeletons is in control methods for robotic bipeds. Indeed, Professor Vukobratovic along with Devor Juricic are credited with developing the concept of the 'zero moment point' and its role in the control of bipedal locomotion [1].



Fig.1 Pupin institute exoskeleton

This type of prostheses use sensors in the foot surface to determine the current state of the movement. Below is a typical state chart of an active prostheses with state based control. The movement start when a threshold weight is applied to the heel.

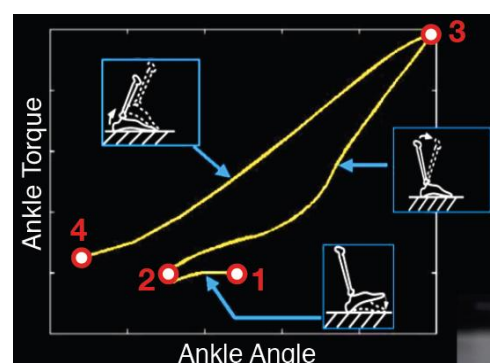


Fig.2. State chart of an active prosthesis with state based control

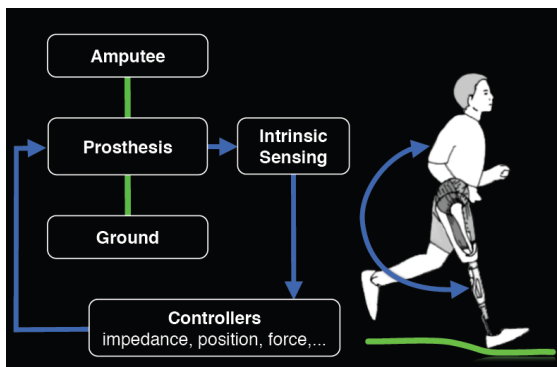


Fig.3. Block scheme of a typical active prosthesis

The advantages of this type of prostheses are the much lower price, the relatively secure interface with patient. They do not need extensive personalization from patient to patient and the process of patient learning is also short. The drawbacks are that these devices do not have any feedback of the actual patient intent, the few degrees of freedom and the absence of different modes of operation such as level walking, stairs climbing or descending. At best there is a manual control for these modes.

3. MYOELECTRIC PROSTHESES

The first myoelectric prosthesis was created in the period 1944-1948 by Reinhold Reiter, then a physics student at Munich University. Because the transistor had not been invented, Reiter was forced to use vacuum tubes for the electronic control system and it was not feasible to make the system portable. Instead this prosthesis was designed for use at a factory bench, powered from the nearest outlet. Even at this early date Reiter recognized the need to obtain maximum information from the myoelectric signal. His system controlled both opening and closing of an electronic hand from a single muscle [3].

There are many designs today that use myoelectric signal to control prosthesis.

The basic principle is to obtain a surface EMG from electrodes placed on the skin above a patient's residual muscles and use the signal from one muscle for flexion and from another for extension. When the muscle originally responsible for a given movement is not available, the myoelectric signal from another which is related also to the movement is used. In this case a more complex algorithm is needed.

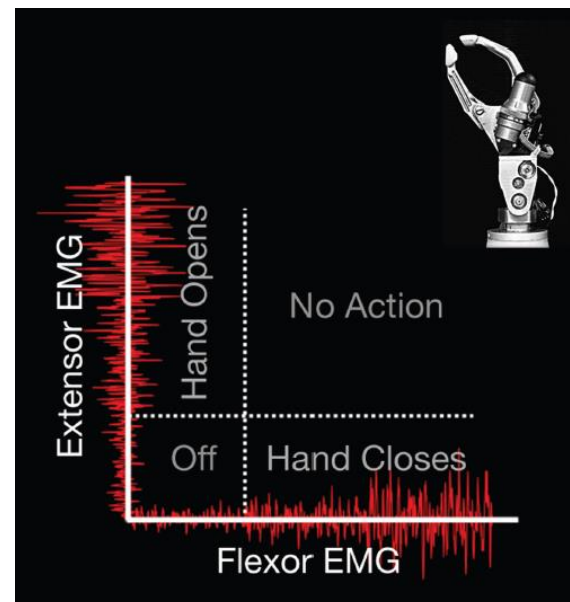


Fig. 4. Myoelectric prosthesis

The main advantages of myoelectric prosthesis are the voluntary movement of the artificial limb, the possibility to apply different force, depending on the strength of the EMG signal and also more degrees of freedom when extracting EMG signal from more muscles.

The disadvantages are that sometimes there are no residual muscles to extract the EMG signal for a given joint (e.g. when we have above the knee amputation we do not have the muscles responsible for the movement of the ankle). Other problems are the need for personalization and adaptation for every patient, since the levels of the EMG signals will be different. Another hurdle is the stability of the connection between the EMG electrode and the patient. If an electrode falls the prosthesis will become unusable. To meet some of these problems new surgical procedures were developed to improve the myoelectric prosthetics.

3.1. Targeted Muscle Reinnervation

In 2001 The Rehabilitation Institute of Chicago developed the targeted muscle reinnervation (TMR) prosthesis, which is an advancement of the myoelectric prostheses. In TMR the nerves from the amputated limb are rerouted to intact, healthy muscles in the body, such as chest muscles (when the prosthesis is for the upper limb), allowing for the movement of the prosthetic limb by thinking about the action to be performed. The nerve impulses generate a muscle contraction which generates EMG signal which in turn is sensed by surface electrodes attached to the surface of the muscle, where the nerves have been rerouted, and carried to the

artificial limb to generate movement. The targeted muscle acts as a natural amplifier for the neuronal signals produced by the transferred residual nerves [2].

EMG signal are recorded, then a high-pass filter is used to remove the body movement artefacts. Additional filtering is needed to eliminate crosstalk from other muscles and in case the prosthesis is for upper limb and a chest muscle is used as target muscle, the ECG signal needs to be eliminated from the EMG signal [6].

In November 2012 Zac Vawter successfully used his TMR myoelectric leg to climb 103 floors of Chicago's Willis Tower. This was an exciting event that validated the success of TMR technology.

The obvious advantages of this technology are the voluntary control of the prosthesis and the possibility of adding many degrees of movement.

The disadvantages are the surgical procedure needed, which prove to be unsuccessful sometimes or with side effects experienced by patients. Also the link between the prosthesis and the patient is with electrodes on the surface of the skin which can compromise the functioning of the prosthesis in the event of a bad contact.



Fig. 5 Rehabilitation Institute of Chicago Bionic leg, used by Zac Vawter to climb 103 floors of Chicago's Willis Tower

3.2. Myoelectric prosthetics with implanted sensors

Max Ortiz Catalan from the Chalmers University of Technology in Sweden has developed a new type of myoelectric prosthesis. He and his team use the Osseointegrated Prosthesis for the Rehabilitation of Amputees (OPRA) method developed by Rickard Branemark at Sahlgrenska University Hospital in Gothenburg [5]. This is a new type of method for anchoring prosthesis directly to the bone of the amputee. The method uses the recently discovered property of the titanium to fuse with the bone tissue. The new prosthesis uses a titanium screw implant for anchoring with the body [7].

Then this titanium screw acts as a bidirectional interface with implanted sensors directly attached to the patient nerves. It is a truer replication of how the arm was designed to work, with information from existing nerves being transferred to the limb and to the implant, where algorithms can translate thought-controlled instructions into movement.

The advantages of this method are the secure connection between the patient and the prosthesis. The implanted sensors give signals with much higher amplitudes and less noise. The disadvantages are the need for a more complex surgery for the titanium screw and the sensor implants. Also it is possible that the body will deny the implants.

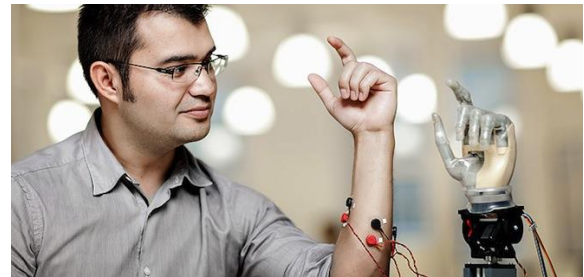


Fig. 6 Max Ortiz and his myoelectric prosthesis

4. DISCUSSION AND CONCLUSIONS

It is evident that the future belongs to the EMG driven prosthetics.

The main area for improvement, remain the development of a secure connection between the patient nerves and the active prosthesis. Also more complex algorithms are needed to process the signals, filter the noise and create the appropriate controls for the prosthesis. Multichannel signal processing will allow more degrees of freedom, hence more natural feeling for the patient. With the complexity

however the weight of the prosthesis will become a factor.

There are research ideas to acquire signals directly in the brain of the patient with implantable electrodes.

The targeted muscle reinnervation and the Osseo-integration also to stimulate the sensory nerves which can provide the patient with a sensitivity to the artificial limb.

The technologies being developed are not only restricted to the amputees, but they can also be used in the development of exoskeletons that can restore mobility to patients with Parkinson disease, stroke or other disorders that disrupt motor behaviors.

References

- [1] Aaron M. Dollar "Active Orthoses for the lower limbs: Challenges and State of the Art" Proceedings of the 2007 IEEE 10th International Conference on Rehabilitation Robotics, June 12-15, Noordwijk, The Netherlands
- [2] Francesco V. Tenore, and R.Jacob Vogelstein "Revolutionizing Prosthetics: Devices for Neural Integration"
- [3] R. N. Scott "Myoelectric Control Of Prostheses A Brief History" Proceedings of the 1992 MyoElectric Controls/Powered Prosthetics Symposium Fredericton
- [4] Stephanie Huang "Feedforward Myoelectric Control of Lower Limb Prostheses" O&P Educational seminar 10/19/2012
- [5] Ariola Bardhi, "Past, Present, and Future of Artificial Limb Design" The EJBM Blog
- [6] http://en.wikipedia.org/wiki/Targeted_reinnervation
- [7] <http://www.wired.com/wiredscience/2012/11/mind-controlled-robotic-arm/>